N°d'ordre NNT : 2017LYSEI087

THÈSE de DOCTORAT DE L'UNIVERSITÉ DE LYON

opérée au sein de
L'Institut National des Sciences Appliquées de Lyon

École Doctorale N° 162
Mécanique – Énergétique – Génie civil – Acoustique (MEGA)

Spécialité/discipline de doctorat :
Génie Mécanique

Soutenue publiquement le 11/10/2017,
par : **Fabien DUBOIS**
Ingénieur INPG-ENSE[3]

Tribological and vibratory approaches for amplified piezoelectric inertia motors

Devant le jury composé de :

DENAPE, Jean	Pr. ENIT, LGP, Tarbes	Rapporteur
BREGUET, Jean-Marc	Dr., PDG Alemnis AG, Thun, Suisse	Rapporteur
ROUCHON, Jean-François	Pr. ENSEEIHT, LAPLACE, Toulouse	Examinateur
BOHER, Christine	Dr. HDR, MCF Mines, ICA, Albi	Examinateur
STOICA, Gina	Pr. Université Polytechnique, Bucarest, Roumanie	Examinateur
BELLY, Christian	Dr., Cedrat Technologies, Meylan	Examinateur
CLAEYSSEN, Frank	Dr., DG Cedrat Technologies, Meylan	Invité
SAULOT, Aurélien	Dr. HDR, MCF INSA, LaMCoS, Lyon	Directeur de thèse
BERTHIER, Yves	DR CNRS, LaMCoS, Lyon	Directeur de thèse

Département FEDORA – INSA Lyon - Ecoles Doctorales – Quinquennal 2016-2020

SIGLE	ECOLE DOCTORALE	NOM ET COORDONNEES DU RESPONSABLE
CHIMIE	**CHIMIE DE LYON** **http://www.edchimie-lyon.fr** Sec : Renée EL MELHEM Bat Blaise Pascal 3ᵉ etage secretariat@edchimie-lyon.fr Insa : R. GOURDON	M. Stéphane DANIELE Institut de Recherches sur la Catalyse et l'Environnement de Lyon IRCELYON-UMR 5256 Équipe CDFA 2 avenue Albert Einstein 69626 Villeurbanne cedex directeur@edchimie-lyon.fr
E.E.A.	**ELECTRONIQUE, ELECTROTECHNIQUE, AUTOMATIQUE** **http://edeea.ec-lyon.fr** Sec : M.C. HAVGOUDOUKIAN Ecole-Doctorale.eea@ec-lyon.fr	M. Gérard SCORLETTI Ecole Centrale de Lyon 36 avenue Guy de Collongue 69134 ECULLY Tél : 04.72.18 60.97 Fax : 04 78 43 37 17 Gerard.scorletti@ec-lyon.fr
E2M2	**EVOLUTION, ECOSYSTEME, MICROBIOLOGIE, MODELISATION** **http://e2m2.universite-lyon.fr** Sec : Sylvie ROBERJOT Bât Atrium - UCB Lyon 1 04.72.44.83.62 Insa : H. CHARLES secretariat.e2m2@univ-lyon1.fr	M. Fabrice CORDEY CNRS UMR 5276 Lab. de géologie de Lyon Université Claude Bernard Lyon 1 Bât Géode 2 rue Raphaël Dubois 69622 VILLEURBANNE Cédex Tél : 06.07.53.89.13 cordey@univ-lyon1.fr
EDISS	**INTERDISCIPLINAIRE SCIENCES-SANTE** **http://www.ediss-lyon.fr** Sec : Sylvie ROBERJOT Bât Atrium - UCB Lyon 1 04.72.44.83.62 Insa : M. LAGARDE secretariat.ediss@univ-lyon1.fr	Mme Emmanuelle CANET-SOULAS INSERM U1060, CarMeN lab, Univ. Lyon 1 Bâtiment IMBL 11 avenue Jean Capelle INSA de Lyon 696621 Villeurbanne Tél : 04.72.68.49.09 Fax :04 72 68 49 16 Emmanuelle.canet@univ-lyon1.fr
INFOMATHS	**INFORMATIQUE ET MATHEMATIQUES** **http://infomaths.univ-lyon1.fr** Sec :Renée EL MELHEM Bat Blaise Pascal 3ᵉ etage infomaths@univ-lyon1.fr	Mme Sylvie CALABRETTO LIRIS – INSA de Lyon Bat Blaise Pascal 7 avenue Jean Capelle 69622 VILLEURBANNE Cedex Tél : 04.72. 43. 80. 46 Fax 04 72 43 16 87 Sylvie.calabretto@insa-lyon.fr
Matériaux	**MATERIAUX DE LYON** **http://ed34.universite-lyon.fr** Sec : M. LABOUNE PM : 71.70 –Fax : 87.12 Bat. Direction Ed.materiaux@insa-lyon.fr	M. Jean-Yves BUFFIERE INSA de Lyon MATEIS Bâtiment Saint Exupéry 7 avenue Jean Capelle 69621 VILLEURBANNE Cedex Tél : 04.72.43 71.70 Fax 04 72 43 85 28 jean-yves.buffiere@insa-lyon.fr
MEGA	**MECANIQUE, ENERGETIQUE, GENIE CIVIL, ACOUSTIQUE** **http://mega.universite-lyon.fr** Sec : M. LABOUNE PM : 71.70 –Fax : 87.12 Bat. Direction mega@insa-lyon.fr	M. Philippe BOISSE INSA de Lyon Laboratoire LAMCOS Bâtiment Jacquard 25 bis avenue Jean Capelle 69621 VILLEURBANNE Cedex Tél : 04.72 .43.71.70 Fax : 04 72 43 72 37 Philippe.boisse@insa-lyon.fr
ScSo	**ScSo*** **http://recherche.univ-lyon2.fr/scso/** Sec : Viviane POLSINELLI Brigitte DUBOIS Insa : J.Y. TOUSSAINT Tél : 04 78 69 72 76 viviane.polsinelli@univ-lyon2.fr	M. Christian MONTES Université Lyon 2 86 rue Pasteur 69365 LYON Cedex 07 Christian.montes@univ-lyon2.fr

*ScSo : Histoire, Géographie, Aménagement, Urbanisme, Archéologie, Science politique, Sociologie, Anthropologie

À mon père, parti trop tôt.
À ma mère, merci pour tout.

Abstract

SPA are amplified piezoelectric inertia motors. They operate by converting asymmetrical vibrations into μ-displacements by means of friction through stick-slip. These vibrations and this friction raise issues related to wear and noise. So, the present work investigates both *the tribological and vibratory behaviours of these motors.* First, a pin-on-pad tribometer, actuated by a SPA, was developed. It led us to observe, *in-situ* and in operation, interfacial solid flows: the 3rd body. These direct observations carried out in conjunction with *post-mortem* analyses resulted in decrypting the tribological solicitations and in increasing by ten the lifetime of the motors. Second, numerical and experimental considerations have been proposed to better grasp the vibratory behaviour of SPA. The existing lumped model was modified to a more versatile hybrid lumped-FEM model. The experimental tests made it possible to determine the main acoustic contributor and to reduce the noise level by sixteen dBA. Finally, this dual - tribology/vibratory - approach provided a better understanding of the SPA intricacies. In particular, it led to develop innovative structures such as a motor with three degrees of freedom and two rotary motors.

Keywords:

- SPA piezoelectric inertia motors

- Tribology:

    - *In-situ* observations of a friction contact,
    - 3rd body flows and tribological circuit.

- Vibration mechanics:

    - Hybrid - lumped-FEM - modelling,
    - Noise reduction.

Résumé

Les SPA sont des moteurs piézoélectriques inertiels amplifiés. Ils fonctionnent en convertissant des vibrations asymétriques en μ-déplacements par frottement, grâce au phénomène d'adhérence-glissement. Ces vibrations et ce frottement soulèvent des problématiques liées à l'usure et au bruit. Pour y répondre, ces travaux étudient *les comportements tribologique et vibratoire de ces moteurs*. Dans un premier temps, un tribomètre pion-plan, actionné par un SPA, a été développé. Il a permis d'observer, *in-situ* et en fonctionnement, les débits solides interfaciaux: le $3^{\text{ème}}$ corps. Ces observations directes, couplées à des analyses *post-mortem* ont permis de décrypter les sollicitations tribologiques et de multiplier par dix la durée de vie des moteurs. Dans un second temps, des analyses numérique et expérimentale ont été proposées afin de mieux appréhender le comportement vibratoire des SPA. Le modèle existant, à constantes localisées, a été modifié en une version hybride, constantes localisées-FEM, plus versatile. Les tests expérimentaux ont permis de déterminer le principal contributeur acoustique et de réduire le niveau de bruit de seize dBA. Finalement, la double approche tribologie/mécanique vibratoire a permis de mieux saisir les subtilités des SPA. Elle a notamment mené au développement de structures innovantes tels qu'un moteur à trois degrés de liberté et deux moteurs rotatifs.

Mots clés:

- Moteurs piézoélectriques inertiels SPA

- Tribologie:

  - Observations *in-situ* d'un contact frottant,
  - Circuit tribologique et débits de $3^{\text{ème}}$ corps.

- Mécanique vibratoire:

  - Modélisation hybride - constantes localisées-FEM -,
  - Réduction du bruit.

Table of Contents

Introduction

This CIFRE PhD research work about amplified piezoelectric inertia motors (SPA) is born from a collaboration between the Cedrat Technologies company and the team Tribology and Interface Mechanics (TIM) from Laboratory of Contact Mechanics and Structures (LaMCoS). It follows the PhD research work carried out by Christian Belly (2011), which led to the first SPA prototypes. It is partly supported by two successive European projects. The first one - Nepia - focused on tribological aspects. The second one - μ-Fast - focused on miniaturisation and vibratory aspects. It finally led to a third European project - Elvisa - in progress, focusing on the industrialisation of the innovative developments realised during this work.

Piezoelectric elements present the remarkable property to convert electrical energy into mechanical energy and conversely. If they were first used as sensors in sonar applications during the First World War, they become increasingly popular as actuators and motors in the last decades. Indeed, while electromagnetic, hydraulic and pneumatic actuation dominates the industry whenever large displacements or high force/torque outputs are relevant, piezoelectric actuation dominates the applications where compact size, fast response, μ-positioning accuracy or non-magnetic requirements are a priority. In particular, since their invention in the 70-80's, piezoelectric inertia motors became suitable solutions mainly for optics μ-positioning, cell manipulation and robotics μ-handling applications.

These motors generate asymmetrical vibrations converted into steps by means of a friction interface and by exploiting stick-slip phenomenon. They are made of a low number of parts to work, what makes them few bulky. However, it remains difficult to design such motors whose performances rely on piezoelectric, mechatronic, tribological, vibratory and acoustic inter-dependent parameters. Among the different inertia motors, Stepping Piezoelectric Actuators - SPA -, manufactured by Cedrat Technologies, are less sensitive to piezoelectric and mechatronic aspects. They take benefit from a leverage structure for amplifying the amplitude of vibrations before the conversion into steps. Thus, SPA are easy to electrically drive and reach high speed in low frequency range. However, issues relative to noise and wear that they generate remain to raise to make them fully reliable.

So, this work addresses several objectives. First, tribological investigation aims at understanding what happens at the friction interface in order to decrease wear generation while increasing lifetime of SPA. In particular, it consists in characterizing the flows of solid particles: the 3rd body, into the contact in the first operating cycles and until their nominal lifetime. Second, vibratory investigation are carried out from numerical and experimental approaches. On the one hand, it seeks to adapt and to improve the existing 1-D SPA-sizing Lumped model in order to take into account the main vibrations of the stator in the three directions of space. On the other hand, series of experiments are proposed in order to reduce the noise generated by the SPA. The progress of these two avenues was carried out in parallel and led to a new generation

1

of motors more versatile, less noisy and whose lifetime has been increased while maintaining stable performance. Finally, a complete design method, based on the lessons learned with the first two axes was formulated in order to promote their dissemination.

This thesis is organised in four parts, each with two chapters. First part describes the state of the art of piezoelectric motors (Chapter 1), and then focuses on amplified inertia-drive category to finally introduce the purpose of this PhD research work (Chapter 2). Second part is dedicated to the tribological approach. It introduces a new tribometer actuated piezoelectrically, reminds the fundamental notions of Godet's 3rd body approach and give an overview of experimental procedure (Chapter 3). This chapter is followed by the exploitation of measures and observations to decrypt the tribological solicitations (Chapter 4). Third part addresses the vibration mechanics approach. It presents a hybrid FEM-Lumped model (Chapter 5) and experiments for noise reduction (Chapter 6). At last, fourth part proposes a synthesis leading to a design methodology for SPA design (Chapter 7) and perspectives (Chapter 8) of this work.

Part I.

State of the Art

Those who cannot remember the past
are condemned to repeat it.
— G. Santayana

Piezoelectric motor overview

Since the discovery of piezoelectricity, research on piezoelectricity has been extremely active for being used either as sensors or as actuators. In particular, piezoelectric actuators can provide a motion with resolution down to sub-nanometre. But, because the generated motion is based on their deformation - about 1‰ -, stroke is limited, typically from 5 to 100μm. To overcome this limitation, on the one hand, mechanical amplification has been proposed, increasing strain to 1%. In spite of this, stroke higher than 1mm remains hard to reach, all the more in a compact design. On the other hand, a solution consists in piezoelectric motor which relies on a friction interface to generate steps in a theoretical infinite range. Modern linear piezoelectric motors became a valuable alternative to the other actuation technologies in low-size applications. They can generate large displacements, do not require a gear and develop force around a few Newtons at velocities in the range of a few cm/s. The purpose of this chapter is to give an overview of the piezoelectric actuation technology from its very beginning to the current motors. It starts with a short comparison with other actuation technologies and a brief glance at the history and the evolution of piezoelectricity. Then, the principle of energy conversion is introduced, leading to the different structures of existing motors, whose characteristics, pros and cons are recalled. Finally, focus on piezoelectric inertia motor is provided, from its operating principle based on stick-slip, to the current applications fields.

1.1 Piezoelectricity *vs.* other actuation technologies

Piezoelectricity plays nowadays a prominent role in actuator applications next to electromagnetic, hydraulic and pneumatic actuators (Uchino, 1996, 1998). While the latter actuation principles dominate the industry whenever large displacements or high force/torque output are relevant (Fig.1.1-a from Zupan et al. (2002)), piezoelectric actuation has dominated applications where compact size, fast response and high positional accuracy are of importance (Fig.1.1-b from Huber et al. (1997)). Indeed, Piezoelectric actuation is direct (no reduction component is needed), fast and controllable down to sub-nanometre range (Hemsel and Wallaschek, 2000). In addition, their (generally) simple structure makes them relevant for miniaturisation.
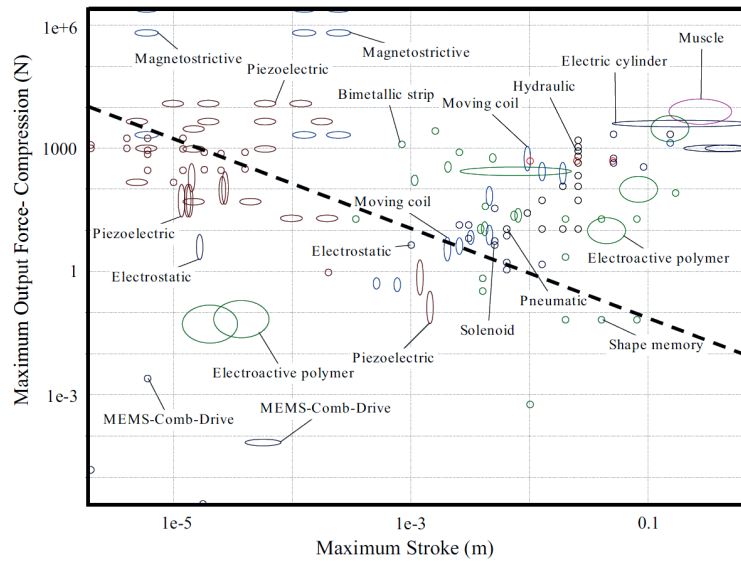
(a)
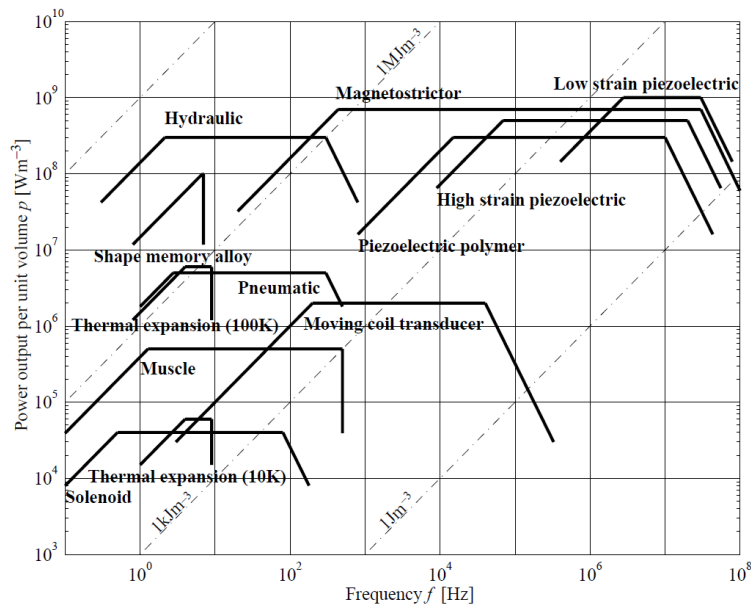
(b)

Figure 1.1 – Comparison of actuators based on different performance characteristics. (a) Plot of maximum actuator output force *vs.* maximum stroke - from Zupan et al. (2002). The dashed line describes a work capacity of 0.01Nm. (b) Plot of volumetric power *vs.* actuation frequency - from Huber et al. (1997).

1.2 Piezoelectricity: discovery and evolution

1.2.1 History

A piezoelectric material - from the Greek prefix *pies-* meaning squeeze or press - may convert a mechanical stress into electrical energy (called direct effect) or conversely, an electrical excitation into mechanical deformation (called converse effect). The abbot René Just Haüy was the first to speak about "pressure electricity" in 1817 about Iceland spath. But its works were then questioned due to the lack of rigour (Trainer, 2003). Direct effect (Fig.1.2-a) was described in 1880 by Pierre and Jacques Curie (Curie

and Curie, 1880). Its reversibility (Fig.1.2-b) was suggested the next year by Gabriel Lippmann (Lippmann, 1881). First application of piezoelectricity appeared during the First World War with sonar thanks to Paul Langevin (Zimmerman, 2002). In our everyday life, it led to use, for instance, quartz crystal to piezo-electrically power our watches.

(a)   **(b)**
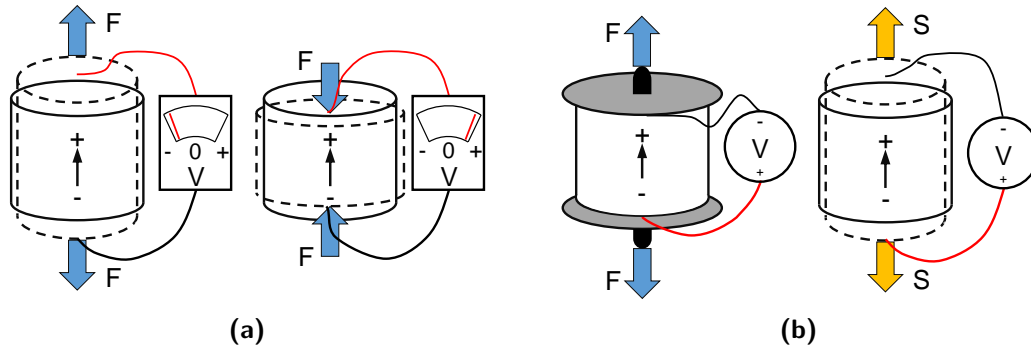
Figure 1.2 – Piezoelectric reversibility concept scheme (Adapted from Szufnarowski, 2013). (a) Direct effect. If an external tensile or compression force F is applied, the voltmeter indicates the polarity of induced potentials. (b) Converse effect. If the material is clamped, a force is generated, if not, it leads to strain S and distortion.

1.2.2 Today piezoelectric material

The discovery of oxides, such as $BaTiO_3$ and PZT (Lead Zirconate Titanate), led to improvements in existing applications and new developments (Heinzmann et al., 2002). Piezoelectricity depends mostly on the symmetry of the atomic arrangement in the crystal, typically with a Perovskite structure (Fig.1.3). These ceramics can be found in two different phases. Above a given temperature - called Curie temperature T_c, - their structure is cubic and they are paraelectric materials which do not exhibit piezoelectric properties. Below T_c, the Perovskite structure can adopt a tetragonal structure in which a metallic ion (Ti4+ or Zr4+ in the case of PZT) can find a stable off-centred position which leads to the polarisation of the material. By applying an electric field in the material, it is possible to invert the position of the ion and the remanent polarisation.
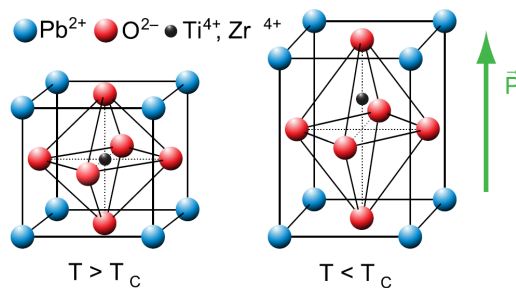
Figure 1.3 – Crystallographic structure of a piezoelectric material (From Leroy, 2013): Perovskite structure (ABO_3) of Lead Zirconate Titanate (PZT). On the left, above the Curie temperature T_c, the micro-structure is cubic and do not have piezoelectric properties. The electric behaviour of the crystal is paraelectric. On the right side, below the Curie temperature, the central titanium or zirconium ion can be off-centred within the oxygen octahedron resulting in tetragonal structure and a net polarisation of the crystal. The ferroelectric behaviour is the ability to change the position of the ion from the top to the bottom, resulting in an inverted polarisation.

1.2.2.1   Polarisation process

In a natural or synthetic form, these materials do not present a natural polarisation at a macroscopic scale. At a microscopic scale, material is not homogeneous but constituted of grains. Each grain is composed of domains called Weiss domains. The different domains (Weiss domains) have locally different electric polarisation, which cancel each other so that the total polarisation is zero. A process called polarisation of the material consists in applying a strong electric field to the ceramic - several $kV.mm^{-1}$ (Shifeng et al., 2004) - usually at high temperature - above Curie temperature T_c (Curie and Curie, 1880) - in order to reorient the polarisation of each domain and obtain a net macroscopic polarisation (Fig.1.4). Process is completed by fritting aiming at welding the grains in order to improve mechanical structure and decrease porosity.
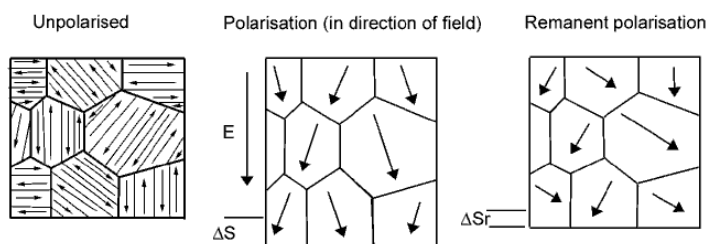
Figure 1.4 – Microscopic schematic view of a piezoelectric material. Diagram of the domains in lead zirconate titanate (PZT) before, during and after polarisation. ΔSr is the residual changing length from ΔS after the polarisation process (From Brevier Technical Ceramics website).

1.2.2.2   Soft vs. hard material

Two categories of ceramics exist today. They are called "soft" or hard" ceramics, depending on their propensity to depolarise. Soft ceramic presents good electromechanical coupling properties and a large frequency bandwidth but depolarise more easily. They are suitable for sensor applications such as hydrophones. Hard ceramic presents less mechanical and dielectric losses. They are rather suitable for piezoelectric motors. To get one or other category, PZT ceramics are doped by adding either donor or acceptor atoms in the material. This allows fine tuning of the material properties. Donor dopant such as La^{3+} or Nb^{5+} (Pereira et al., 2001) result in the formation of cation vacancies in the structure. It leads to the synthesis of the "soft" ceramics. Acceptor doped ceramics (*e.g.* with Fe^{3+}) result in the "hard" category. Synthesis of the advantages and disadvantages of respective categories are presented in table 1.1.

Table 1.1 – Characteristics of soft and hard piezoelectric ceramics (From American piezo website).

Characteristics	Soft ceramic	Hard ceramic
Piezoelectric Constants	larger	smaller
Permittivity	higher	lower
Dielectric constants	larger	smaller
Dielectric losses	higher	lower
Electromechanical coupling factors	larger	smaller
Electrical resistance	very high	lower
Mechanical quality factors	low	high
Coercive field	low	higher
Linearity	poor	better
Polasisation/depolarisation	easier	more difficult

1.2.2.3   One-layer and multi-layer actuators

Nowadays it is usual for piezo-ceramic plates, strips, rings, domes, small tubes and a large number of special geometries to be manufactured. Their compact form means that piezo-ceramic transducers take up little space, and use little energy when used as actuators (Uchino, 1990). Stroke of one-layer ceramics are a few $\mu\varepsilon$ (ppm). To obtain greater displacements, multi-layer ceramics are used. They consist in an assembly of several ceramics as shown in Fig.1.5. If a one-layer ceramic, of length $L_{ceramic}$, is subjected to an input voltage V, it produces a displacement d. Then for an assembly of n layers, of length $L_{ceramic}/n$, a voltage V/n will be required. Indeed, as detailed in section 1.3.1, the displacement is proportional to the applied electric field. The associated two main drawbacks are (i) a higher cost, because of manufacturing complexity, (ii) an electrical capacitance n^2 times higher leading to a higher current consumption.
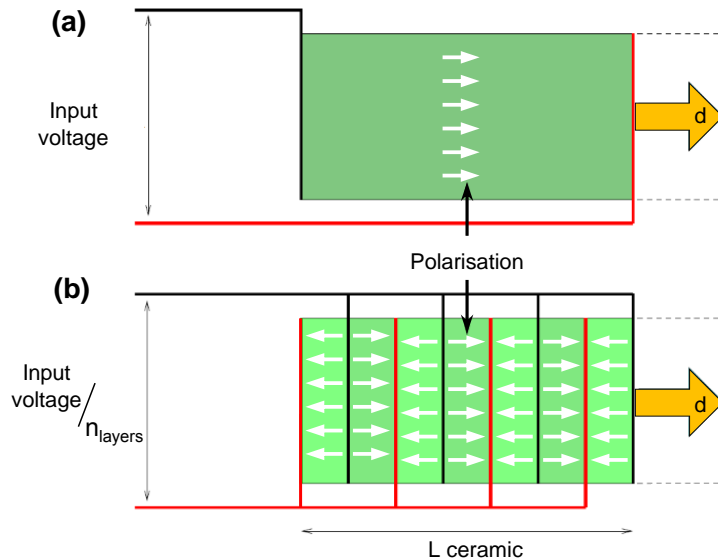
Figure 1.5 –   Schematic comparison between one-layer and multi-layer piezoelectric ceramics (Adapted from Garbuio, 2006). (a) One-layer. (b) Multi-layer. Same displacement d is represented by the blue arrow.

1.3   Piezoelectric based motor: electro-mechanical conversions

The concept of piezoelectric motor - introduced by Williams (1937) - is based on the combination of two energy conversion mechanisms (Fig.1.6). First, an electric signal is converted into mechanical deformation by means of piezoelectric converse effect (see section 1.3.1). These piezoactive elements are hereafter called piezoelectric actuators. The actuator is rigidly connected to a friction element. Second, the resulting vibratory oscillations are converted into linear or rotary displacements by means of a friction interface (see section 1.3.2). The overall system is designed as a piezoelectric motor.

ELECTRICITY   MECHANICAL VIBRATIONS   MECHANICAL MOTION
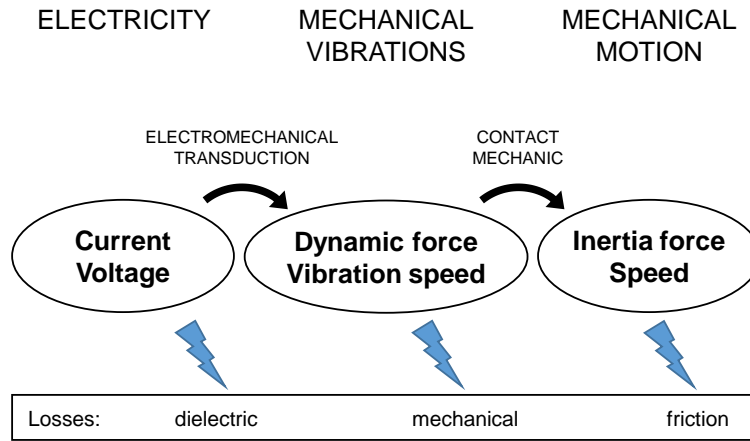
Figure 1.6 – Principle scheme of the double energy conversion leading to piezoelectric motor from a piezoelectric actuator (Adapted from Vanel, 1996).

1.3.1 1st conversion - actuator: from electrical to mechanical energy

Details about electromechanical equations can be found in any PhD manuscript focusing on piezoelectric material. Here, purpose is to recalled briefly the equations leading to use piezo-ceramic as actuators (polled in $\overrightarrow{3}$ direction in Fig.1.7).

1.3.1.1   High resolution actuator

A piezoelectric rod is used thereafter with associated directions (Fig.1.7). Characteristics of the material are given by the equations 1.1. The first one links the strain S [m/m] in the material to the electric field E [V/m] and to the applied stress T [N/m^2]. s^E [m^2/N] is defined as the compliance at constant electric field. d [m/V] is defined as the transposed piezoelectric constant tensor. The second equation links the electric displacement D [C/m^2] to the stress T and the electric field E in the material. ε^T is the permittivity of the material at constant stress. S and T are 6-components vectors, E and D are 3-components vectors.
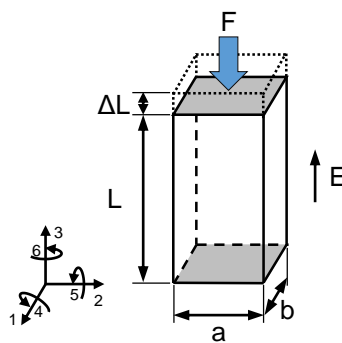
Figure 1.7 – Principle scheme of a piezoelectric rod polled in a longitudinal direction and stressing by a force F (From Belly, 2011).

$$\begin{cases} S = s^E.T + d.E \\ D = d.T + \varepsilon^T.E \end{cases} \tag{1.1}$$

Considering i-the notations of the Fig.1.7, ii-full boundary conditions at the bottom of the piezoelectric rod, iii-a vertical force F applied to the top of the rod (stressing it

in vertical direction), purpose is to calculate the strain relative to an applied voltage V. Resulting electrical field is $\|\overrightarrow{E}\| = \text{E}_3 = \text{V/L}$. By neglecting dynamic variations, stress becomes $\|\overrightarrow{T}\| = \text{T}_3 = \text{-F/a.b}$

Considering the ceramic has been poled along the $\overrightarrow{3}$ direction, Eq.1.1, can be simplified as followed - Eq.1.2:

$$
\begin{bmatrix} S_1 \\ S_2 \\ S_3 \\ S_4 \\ S_5 \\ S_6 \\ D_1 \\ D_2 \\ D_3 \end{bmatrix} = \begin{pmatrix} s_{11} & s_{12} & s_{13} & 0 & 0 & 0 & 0 & 0 & d_{31} \\ s_{12} & s_{11} & s_{12} & 0 & 0 & 0 & 0 & 0 & d_{32} \\ s_{13} & s_{12} & s_{33} & 0 & 0 & 0 & 0 & 0 & d_{33} \\ 0 & 0 & 0 & s_{44} & 0 & 0 & 0 & d_{15} & 0 \\ 0 & 0 & 0 & 0 & s_{44} & 0 & d_{15} & 0 & 0 \\ 0 & 0 & 0 & 0 & 0 & s_{66} & 0 & 0 & 0 \\ 0 & 0 & 0 & 0 & d_{15} & 0 & \varepsilon_{11}^T & 0 & 0 \\ 0 & 0 & 0 & d_{15} & 0 & 0 & 0 & \varepsilon_{11}^T & 0 \\ d_{31} & d_{31} & d_{33} & 0 & 0 & 0 & 0 & 0 & \varepsilon_{33}^T \end{pmatrix} \begin{bmatrix} T_1 = 0 \\ T_2 = 0 \\ T_3 = -F/a.b \\ T_4 = 0 \\ T_5 = 0 \\ T_6 = 0 \\ E_1 = 0 \\ E_2 = 0 \\ E_3 = V/L \end{bmatrix}
\tag{1.2}
$$

Considering D_3, piezoelectric ceramic can be characterized electrically, leading to Eq.1.3.

$$
D_3 = -d_{33}\frac{F}{a.b} + \varepsilon_{33}^T \frac{V}{L}
\tag{1.3}
$$

Electrical charge between two electrodes then comes - Eq.1.4:

$$
Q = \int_S D_3 \, \mathrm{d}S = -d_{33}.F + \varepsilon_{33}^T \frac{a.b}{L} V
\tag{1.4}
$$

With $\text{C}_0 = \varepsilon_{33}^T \frac{a.b}{L}$, so-called piezoelectric capacitance (Fig.1.10). It becomes possible to size the power supply for static operations in terms of current requirement (Eq.1.4).

Considering S_3 (strain in vertical direction), it leads to Eq.1.5. This expression emphasises the proportional relationship between applied voltage and strain, no matter the initial applied stress (Fig.1.8).

$$
\Delta L = -s_{33}^E . \frac{F.L}{a.b} + d_{33}.V
\tag{1.5}
$$

Free deformation at zero force stems from Eq.1.5 (Eq.1.6:

$$
\Delta L_{F=0} = d_{33}.V
\tag{1.6}
$$

Notice that previous equation must be multiplied by the number of layers in case of multilayer piezoelectric ceramic. The previous expression also highlights a maximal voltage. Related blocked force is defined for a null deformation - Eq.1.7:

$$
F_b = \frac{d_{33}.V_{lim}.a.b}{s_{33}^E.L}
\tag{1.7}
$$
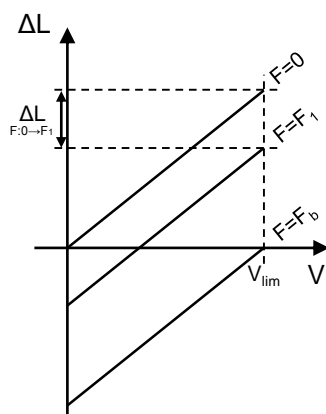
Figure 1.8 – Strain of the rod depending on the applied voltage for different initial applied stresses.

In a similar way, if the stress is applied by a spring, whose stiffness is k [N/m], ΔL is expressed as followed and depicted on Fig.1.9:

$$\Delta L = \frac{a.b}{a.b + s_{33}^E.k.L}.d_{33}.V \tag{1.8}$$
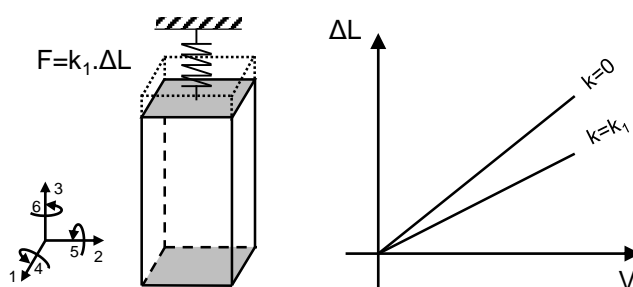
Figure 1.9 – Strain of the rod depending on the applied voltage for different initial applied elastic stresses.

Thus, high resolution features of piezoelectric actuator are better understood: very small displacements - around $1‰ L_{ceramic}$ - but high generated forces - >1kN for a 5×5 mm^2 section -. In addition, they are relevant in dynamic operation because of their quite short response time to an electrical excitation.

1.3.1.2 High dynamic actuator

As it will be shown in chapter 2, the performances of piezoelectric motors considered in this work depend on the fast transition between two voltage orders (stick → slip). Previous equations have to be completed to describe the dynamic operating conditions of the actuator and so its time response to such a voltage step. Electromechanical equivalent circuit (Mason scheme) - based on the equations of material mechanics - has been proposed to reach this goal (Mason, 1948). It considers a motional branch taking into account the external stresses applied to the piezoelectric element (Fig.1.10-c).
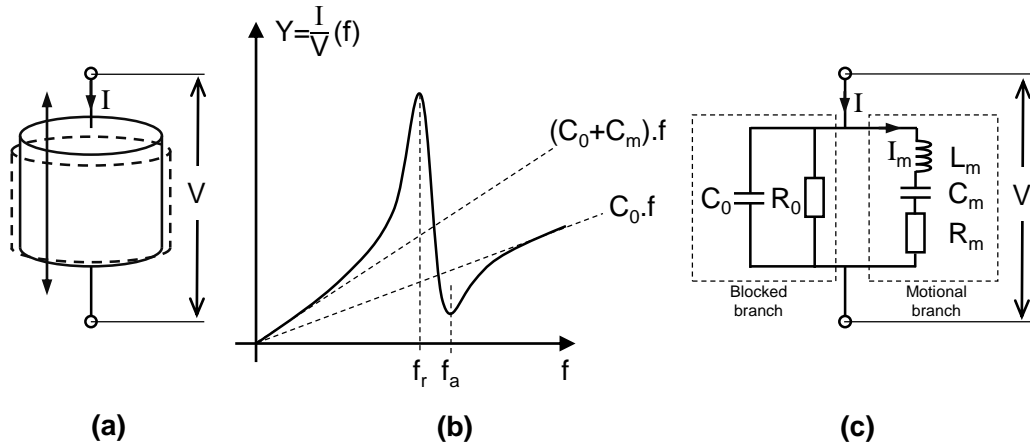
Figure 1.10 – Electrical representation of a piezoelectric ceramic. a) Considered resonance mode in d_{33} direction. b) admittance representation (current I / voltage V) for the associated resonance mode. C_0 and C_m are the piezoelectric and motional capacitances respectively. f_r and f_a are the resonance and antiresonance frequencies respectively. c) Equivalent electric circuit (Mason scheme) of a piezoelectric element. R_0 represents the electrical losses into the piezoelectric ceramic. Elasticity (1/stiffness), mass and damping are represented by a motional capacitance C_m, an inductance L_m, and a resistance R_m respectively.

By neglecting the effect of electrical losses, the admittance of this circuit is:

$$Y = \frac{I}{V} = jC_0\omega + \frac{jC_m\omega}{1 + R_mC_m\omega + j^2L_mC_m\omega^2} \tag{1.9}$$

As with every solid, mechanical resonances occur at particular frequencies. The fundamental resonance f_r[1] and anti-resonance f_a frequencies are the poles and zeros from Eq.1.9, by neglecting the mechanical losses.

$$f_r = \frac{1}{2\pi}\sqrt{\frac{1}{L_mC_m}}$$
$$f_a = \frac{1}{2\pi}\sqrt{\frac{1}{L_mC_m}}\sqrt{1 + \frac{C_m}{C_0}} \tag{1.10}$$

Previous equation leads to the response time t_r[2] of the piezoelectric ceramic when a voltage step is applied to its electrodes:

$$t_r = \frac{1}{2.f_r} \tag{1.11}$$

Thus, high dynamic features of piezoelectric actuator are better understand. Short response time - typically a few μs - makes them suitable for dynamic operation. The next sections attempts to show how to take advantage of these features.

---

[1] One notice that by replacing electrical terms by their mechanical equivalent lead to $f_r = \frac{1}{2\pi}\sqrt{\frac{K}{M}}$ as in a simple harmonic oscillator

[2] In practical situations, the response time of the actuator can be limited by the load time value of the electronics defined as $t_{load} = \frac{C_f.\Delta V}{I_{lim}}$ with ΔV and I_{lim} are the voltage amplitude and the current limitation of the electronic power supply.

1.3.2 2nd conversion - motor: from vibration to motion

As mentioned above, the converse piezoelectric effect leads to deformations whose order of magnitude is a few microns. It is not sufficient for many applications. Amplification is possible up to a certain extent, but remains limited to reach several millimetres of stroke. Stepping principles are a possibility to increase the range of the actuators while maintaining the advantage of a high resolution.

It consists in adding a friction interface. The vibrations generated by the ceramic are used to drive a payload by means of friction. It makes it possible to reach long stroke while maintaining resolution.

Moreover, as the demand for small-sized actuator applications increases, piezoelectric motor technology is likely to gain further on importance. This tendency is explained graphically in Fig.1.11. Piezoelectric motors are virtually insensitive to size in terms of efficiency (Rocon and Pons, 2006). They offer other important advantages including high power/weight ratio (Zupan et al., 2002) and efficiency (Huber et al., 1997), no backlash, no power consumption in steady state (Ouyang et al., 2008), MRI compatibility (Hemsel and Wallaschek, 2000), operation at cryogenic temperature (Blackford et al., 1992) and vacuum compatibility (Yamagata et al., 1990).

Numerous piezo-motors have been developed from the concept of electro-mechanical conversions. The next section proposes to classify the main existing structures.
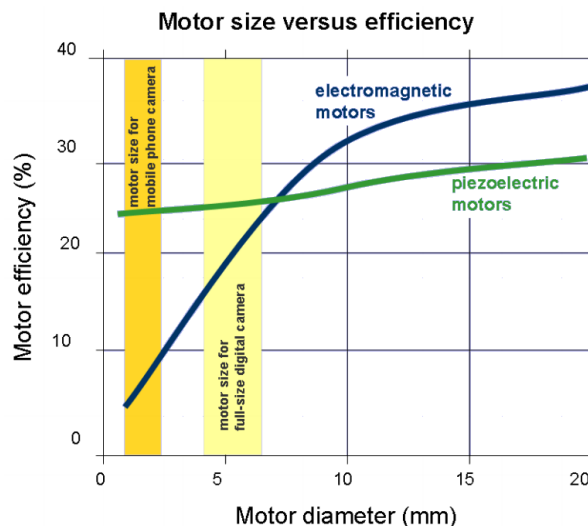
Figure 1.11 – Comparison of piezoelectric and electromagnetic motors based on efficiency *vs.* size. Piezoelectric motors whose efficiency is virtually not affected by size are superior to electromagnetic motors in μ-motor applications (From Henderson, 2005).

1.4   Piezoelectric motor classification

From the concept of piezoelectric motor, literature classically considers that three categories of motors emerged: ultrasonic, inchworm and inertia motors. A classification is proposed in Fig.1.12. It is based on the main features of the 1st and 2nd conversion stages respectively. One should notice that the behaviour of the 1st conversion stage is already optimised with respect to the 2nd stage. Motor classification depends more on the way the friction interface is exploited. While a brief description of each category is given in the following sections, the reader could find further details in Peng et al. (2015); Ouyang et al. (2008); Hemsel and Wallaschek (2000).
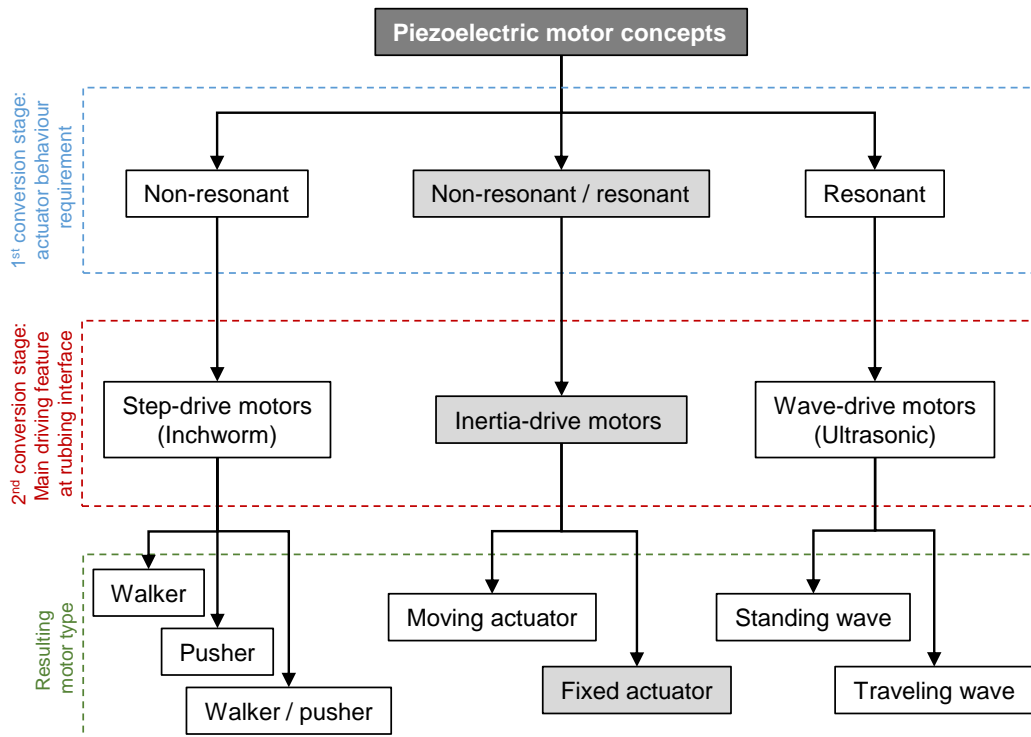
Figure 1.12 – Piezoelectric motors classification flow chart based on their respective operating principle in the different conversions stages (see section 1.3). Gray blocks correspond to the motors studied in this work.

1.4.1 Inchworm motors: strong but bulky

An "inchworm" mechanism is a type of clamping and feeding mechanism which imitates the step-by-step movement of the inchworm in nature. It has been first introduced by Brisbane (1968). It usually consists in three PZT piezoelectric ceramics. The central one is used as a feeding mechanism to produce displacement along the motor shaft, while the other two serve as clamps. One complete cycle is as follows (Fig.1.13.a-c): (i) PZT 3 releases its grip on the shaft; (ii) PZT 2 contracts to move the shaft to the left; (iii) PZT 3 clamps the shaft; (iv) PZT 1 releases its grip of the shaft; (v) PZT 2 expands to feed the shaft to the left again; (vi) PZT 1 clamps the shaft and the cycle begins again.

Piezoelectric inchworm motors presented in the literature can be categorized in three groups. In the first group, called "walker" (Brisbane, 1968; Zhang and Zhu, 1997), the body of the actuation mechanism can move through a fixed guide way (Fig.1.13.a). The "pusher" is the second configuration (Fig.1.13.b). Here, the shaft moves through a fixed actuation mechanism body (Burleigh Instruments website, Last update: 2014; Newton et al., 1998). The third technique can be referred to as the hybrid "walker-pusher" (Fig.1.13.c), which mixes the actuation methods of the two previous groups (Blatter and Hsu, 1966; Locher, 1967).

Compared to other piezoelectric motors, the clamping mechanism of an inchworm motor can generate a higher driving force and a quasi-static operation (Fig.1.13.d). It also reduces wear due to the clamping operation when the shaft is stationary. However, in the meantime, the clamping operation and relatively large volume reduce the PZT driving frequency. An inchworm mechanism needs at least three phases, causing its operation to be complex. In addition, the mechanisms, especially the chucks, seem to be hard to miniaturize.

1

(a) (b) (c)

(d)
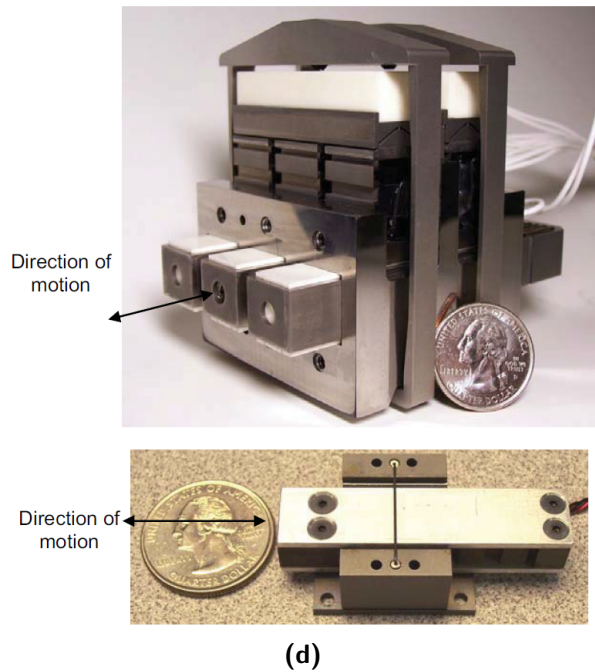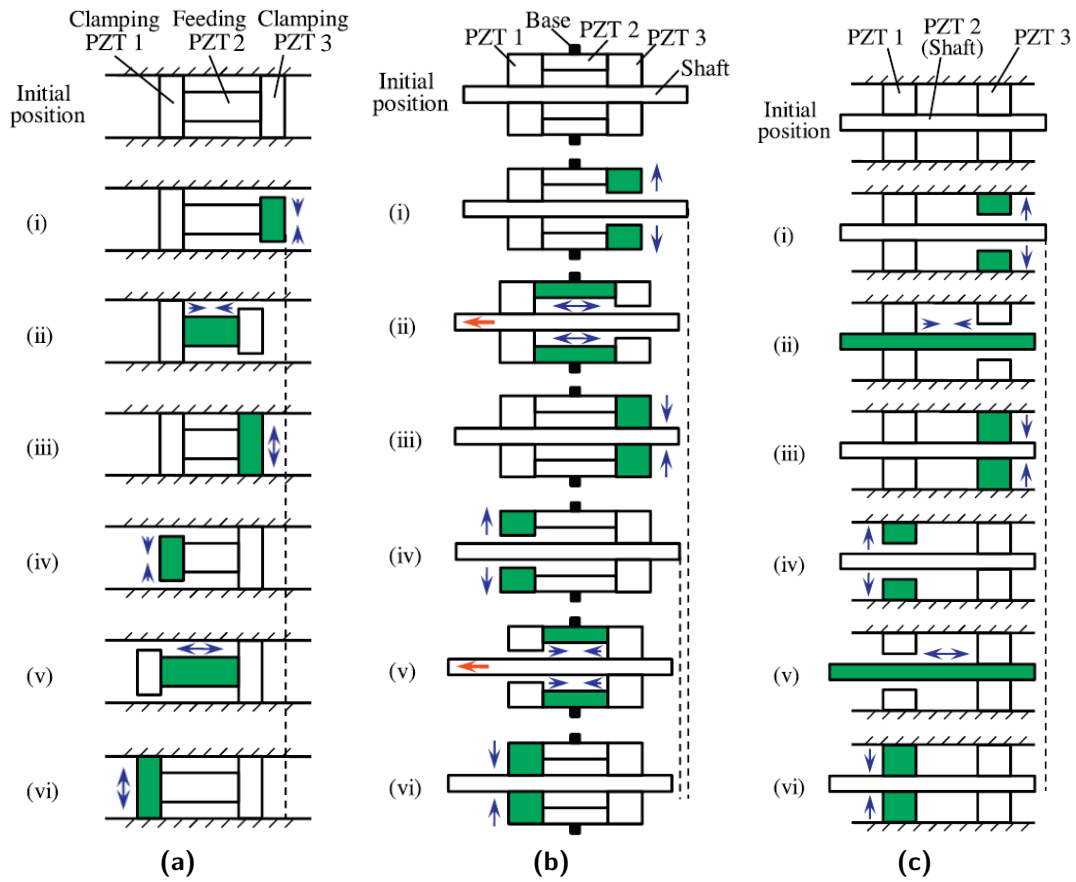
Figure 1.13 – Operating principle and realisations of piezoelectric inchworm motors (From Paine et al., 2008). Operating steps (i)→(vi) are described in the text. (a) Inchworm "walker" motor. (b) Inchworm "pusher" motor. (From Peng et al., 2015). (c) Inchworm hybrid "walker-pusher" motor. (d) Prototype of DSM's 2000 N Impulse Piezomotor™ at the top and DSM's Impulse 30 at the bottom.

1.4.2 Ultrasonic motors: fast but sensitive

An ultrasonic mechanism takes benefit from the high-frequency vibration of a piezo-ceramic excited at resonance. It is the oldest category of piezoelectric motor since it has been first introduced by Williams (1937). Generated vibration follows an elliptical oscillation which drive a slider/rotor by means of the frictional interface (Fig.1.14.a-b).

Piezoelectric ultrasonic motors presented in the literature can be categorized in two groups. In the first group, called "standing wave" (Barth, 1973; Vasiliev et al., 1981), the ceramic is excited in a bending and longitudinal resonance modes (Fig.1.14-a). In the second group, called "traveling wave" (Sashida, 1985), the ceramic is excited in a circumferential bending resonance mode (Fig.1.14-b). Unlike the standing wave motor which utilizes one elliptical motion generated in the stator, every point on the stator face of the travelling wave type motor follows an elliptical trajectory. Therefore, a surface particle of the contact surface of the stator can draw an elliptical locus and cause intermittent movement of the slider/rotor.

Compared to other piezoelectric motors, piezoelectric ultrasonic motors have many merits, including lightweight, compact size, high revolution (rotational types) or speed (linear types), self-braking without power, no noise, and electromagnetic immunity. Therefore, by using piezoelectric ultrasonic motors, micro mechanical systems can be realised for precise positioning over long strokes (Fig.1.14-c,d).

The demerits of ultrasonic motors include necessity for a high frequency power supply, less durability due to frictional drive, drooping torque speed characteristics, and control complexity due to multiple input signals. It is required that the motor should have special frequency, amplitude and phase of driving signals. So, the driving signals should be adjusted continuously to keep a stable output when the operational environments change, such as temperature, humidity and pre-load.
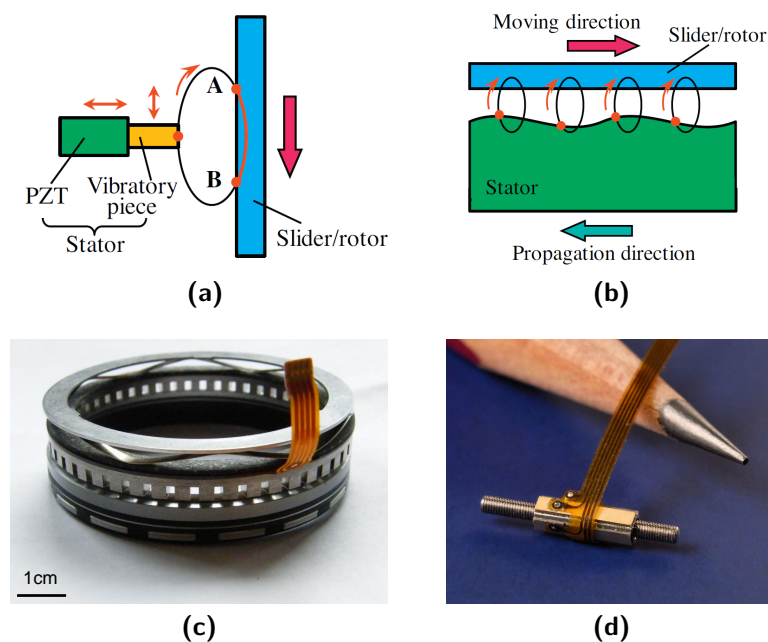
Figure 1.14 – Operating principle and realisations of piezoelectric ultrasonic motors: (a) principle of the standing wave type motor. (b) principle of the travelling wave type motor. (From Peng et al., 2015). (c) Ultrasonic piezoelectric motor used in camera autofocus apparatus. Released in public domain by the copyright holder: Yorkshire Terrier. (d) Squiggle motor (From New Scale website).

1.4.3 Inertia motors: limited performances but a reliable structure

The invention of inertia motor, based on stick-slip, is commonly attributed to Pohl (1987b) or Higuchi et al. (1987). Anders et al. (1987) should be also mentioned. They presented their works in July 1986 on the same conference as Pohl and published a paper almost at the same time as him. But their paper met with far smaller response than Pohl's. In fact, Söderqvist already described devices for fine positioning using electromagnetic and piezoelectric actuators in 1973 in a Swedish patent (Soderqvist, 1973). It is unlikely that Söderqvist's patents were known to the later inertia motor developers.

Inertia motors presented in the literature can be categorized in two groups. In the first group, called "fixed actuator" (Fig.1.15-a), the piezoelectric ceramic remains fixed (by neglecting the generated vibrations) while the payload moves (Howald et al., 1992; Chang and Li, 1999). In the second group, called "moving actuator" (Fig.1.15-b), the piezoelectric ceramic moves with the payload (Buchi et al., 1995; Idogaki et al., 1995; Niedermann and Choffat, 1996). In both groups, the ceramic is actuated in low-frequency, far below its first natural frequency. This makes it possible to be less sensitive to environmental change (*e.g.* due to temperature and humidity) or preload (*e.g.* due to wear) contrary to ultrasonic motor. In addition, inertia motors based on fixed actuator type offers a potential of unlimited stroke (no moving electrical wires to consider). This is why these motors are considered in this work. In both cases, operating principle is based on stick-slip.

1.4.3.1 Stick-slip operating principle

Stick-slip phenomenon (Yoshizawa and Israelachvili, 1993) is often described as a dynamic instability and a source of noise (Asamene and Sundaresan, 2012; Ferrer et al., 2010; Tonazzi et al., 2013; Meziane et al., 2010). In inertia motor, this friction bound phenomenon is no more synonym of energy loss but becomes the source of motion. It consists in an asymmetric vibration of piezoelectric actuator illustrated in Fig.1.15.

- Period 1: piezoelectric ceramic is in a neutral state with no voltage applied.

- Period 2 consists in a slow increase of the voltage order. Piezoelectric ceramic slowly expands, driving the friction element and so the moving body with a low acceleration. An external force is created on the moving body. This force depends on both the mass of the moving body and the acceleration of the friction element. As long as it remains smaller than the static friction force between the friction element and the moving body, they stick and move together. This is the stick phase.

- Period 3 consists in a fast decrease of voltage order until neutral state. Piezoelectric ceramic fast contracts, and pulls the friction element with a high acceleration. An external force, higher than the static friction force, is applied on the moving body. In a perfect situation, the moving body stands still with respect to the ground, by means of its inertia. In reality, a slight backlash occurs and the moving body moves back a little. This is the slip phase.

- Period 4: piezoelectric ceramic is in a neutral state again with no voltage applied.
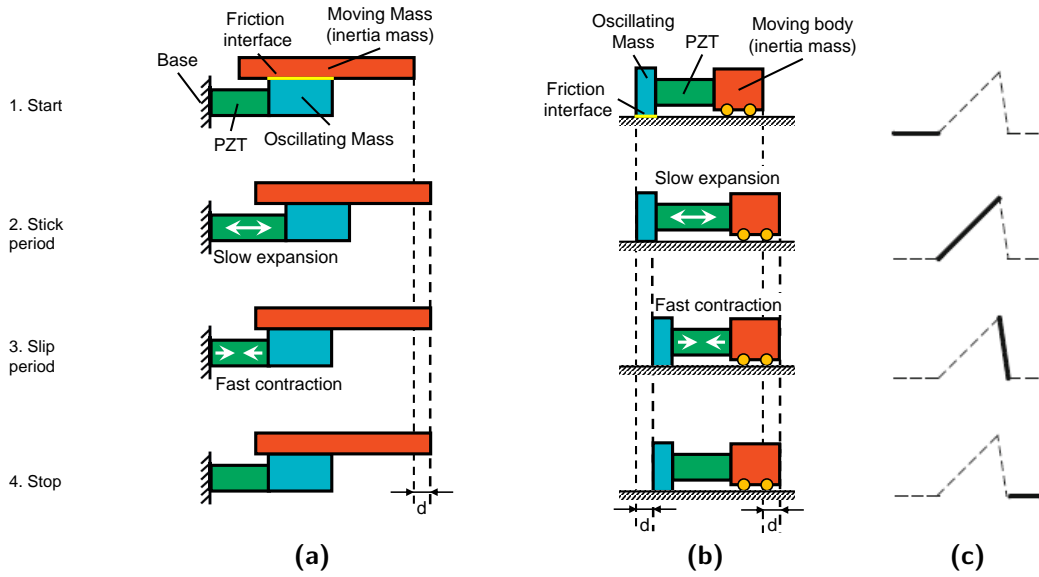
Figure 1.15 – Stick-slip operating principle of inertia motors (adapted from Peng et al., 2015). Actuator type: (a) fixed PZT piezoelectric ceramic; (b) moving PZT. (c) Voltage order scheme: in stick period, input voltage changes slowly; in slip period, input voltage changes quickly enough for triggering a relative displacement between the slider and the actuator.

By continuously alternating periods 2 and 3, step movement appears and moving mass keep moving in a large range stroke. If the shape of the voltage is in a reverse order, the moving mass will travel to the opposite direction. Above description can be summarized in Eq.1.12 (The influence of gravity is not taken into account: horizontal assumption).

$$
F_f\left(t\right) = \begin{cases} m_{MM}\ddot{x}_{MM}\left(t\right) & \text{if } \begin{cases} \dot{x}_{MM}\left(t\right) = \dot{x}_{OM}\left(t\right) \\ \left|m_{MM}\ddot{x}_{MM}\left(t\right)\right| \leq \mu_s\,F_N \end{cases} \\[2em] \mu_d F_N sgn\left(\dot{x}_{MM}\left(t\right) - \dot{x}_{OM}\left(t\right)\right) & \text{if } \begin{cases} \dot{x}_{MM}\left(t\right) \neq \dot{x}_{OM}\left(t\right) \\ \left|m_{MM}\ddot{x}_{MM}\left(t\right)\right| > \mu_s\,F_N \end{cases} \end{cases} \quad (1.12)
$$

where F_f and F_N are the friction force and the normal force respectively; μ_d and μ_s are the dynamic and the static friction factor respectively; m_{OM}/m_{MM}, $\dot{x}_{OM}/\dot{x}_{MM}$ and $\ddot{x}_{OM}/\ddot{x}_{MM}$ are the masses, the velocities and the accelerations of the oscillating/mobile masses (OM/MM) respectively.

A third group, called "slip-slip" (Morita et al., 2012), could be added to the these first two. It consists in exploiting resonance frequencies of the previous mechanical structure by means of a auto-tuned high-frequency asymmetrical signal. In this case, oscillations are fast enough for moving mass remains always in sliding conditions. Step motion remains possible because the time during the "low" change order is longer that the time during the fast change order (Fig.1.15-c). Thus, the moving mass slides longer in a direction than in the other one. Higher speed can be reached with a resonant motor. However, resonance frequency locations are sensitive to boundary conditions and environmental change. Thus, such motors, as ultrasonic motors (see section 1.4.2), require the development of an electronic control board which tunes the actuation signal in real time. Such a development is not addressed here and focus is rather done on non-resonant motors, whose performances are less dependent on environment changes.

1.4.3.2   Interest in inertia motors

Compared to other piezoelectric motors, inertia motor - and more specifically the fixed-actuator category - is a trade-off. It has the main advantage of extreme simplicity, both from mechanical and from a control point of view. Furthermore, it is relatively easy to implement. Even though their performance are classically lower than the other categories, they are just compound of three parts, what offers a great potential of miniaturization and reliability (Fig.1.16). They also includes lightweight, compact size, self-braking without power, and electromagnetic immunity.
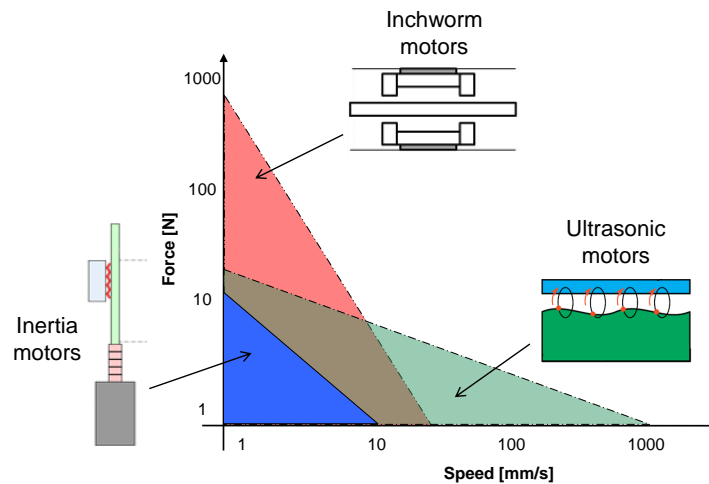
Figure 1.16 – Comparison of performances between inertia, inchworm and ultrasonic motors (Adapted from Spanner and Koc, 2010).

1.5   Inertia motors application fields

In the years following the first publications (see section 1.4.3), several researchers developed inertia motors in a multitude of designs. Practically all of these developments focused on microscopy applications (Lyding et al., 1988; Blackford and Jericho, 1990; Yamagata et al., 1990; Judy et al., 1990; Renner et al., 1990; Matsuda and Kaneko, 1991; Park et al., 1991; Probst et al., 1991), for instance, the scanning tunnelling microscopes and other scanning probe microscopes.

However, the numerous developments were not intended for industrial production, but for use in the developers' own laboratories. Improvements mostly concerned vertical motion (Renner et al., 1990; Agrait, 1992; Libioulle et al., 1993) and the integration of multiple degrees of freedom (Fig.1.17).

Since 1990, the number of publications regarding inertia motors has continuously increased. Positioning applications in laboratory such as microscopy (Niedermann and Choffat, 1996; Meyer et al., 2005; Drevniok et al., 2012), cell manipulation (Kudoh et al., 1998; Bergander and Breguet, 2002; Sievers et al., 2005), and micro/nano handling (Buchi et al., 1995; Woern et al., 2001; Reynolds et al., 2008; Fatikow et al., 2008; Rakotondrabe et al., 2009; Edeler, 2011) still are a main area of application for piezoelectric inertia motors today. Compatibility with harsh environment such as cryogenic (-195°C in Blackford et al., 1992), thermal (60°C in Belly et al., 2011) and magnetic (Belly et al., 2010) make them relevant for these applications. They were also used in robotics by Higuchi and Yamagata (1991); Bacher (2003); Martel et al. (2001) and in imaging applications (Saito and Nagano, 1991).
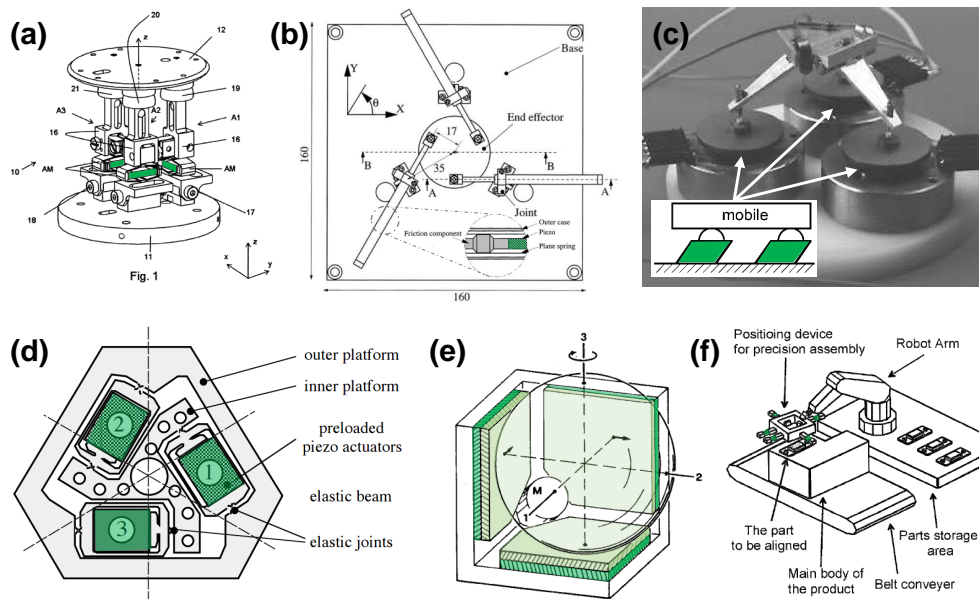
Figure 1.17 – Realisations of multi-DoF inertia motors. Piezoelectric elements are coloured in green. (a) Belly et al., 2014, (b) Morita et al., 2002, (c) Breguet and Clavel, 1998, (d) Zesch et al., 1995, (e) Howald et al., 1992, (f) Yamagata and Higuchi, 1995.

Other applications then appeared in consumer goods such as Braille cells (Velázquez et al., 2012). Thus, inertia motors became popular in zoom and autofocus applications for cameras by providing an anti-blur function (Fig.1.18).

As an anecdotal information, inertia motor with a single fixed actuator can also move multiple objects, ranging from two masses, which can be moved independently by varying the driving signal (Li and Yamamoto, 2016), to large numbers of microscopic particles (Eglin et al., 2006).
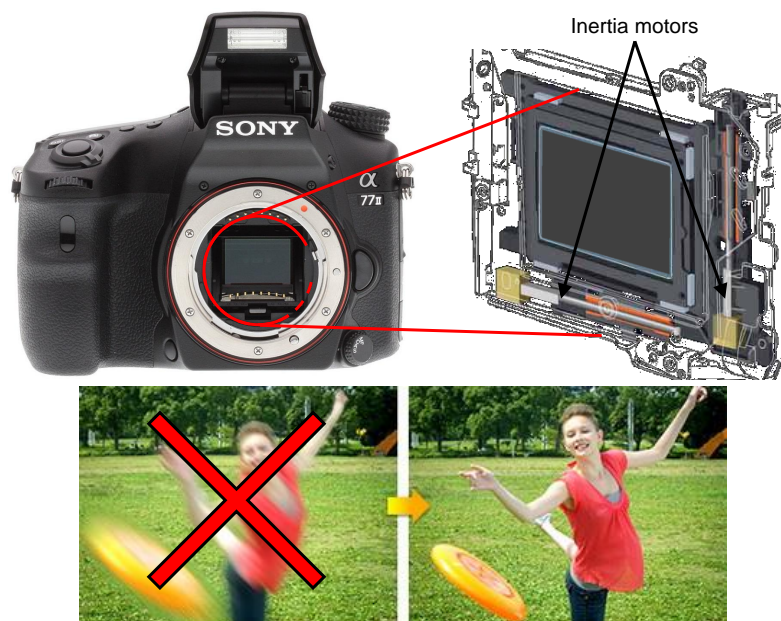
Figure 1.18 – Anti-blur camera system based on two inertia motors (Takano et al., 2005).

2

SPA: inertia motor based on amplified piezo-actuator

As inertia motors belong to the most recent category of piezoelectric motor, they still have a strong innovative potential. The various applications exhibited in the previous chapter also highlight an economic context suitable for new developments. For the last decade, the Stepping Piezoelectric Actuator (SPA) has been one of the developments of inertia motor. It relies on an amplified piezoelectric actuator. By this way, SPA speed is, at low actuation frequency, higher than the common values. Nevertheless, SPA is still a young motor. The limitations identified in previous works must be raised. Overcoming these limitations is the general scope of this PhD research work. In this chapter, first, the different SPA characteristics, which will be used in the rest of the thesis, are introduced. Second, the SPA limitations are highlighted. At last, the addressed framework, in particular (i) wear and lifetime, (ii) noise and (iii) integration issues, is detailed.

2.1 SPA at a glance

Piezoelectric ceramics are able to generate a force higher than thousand Newtons (Eq.1.7 in chapter 1). Nevertheless, inertia motors make steps as soon as the ceramic-induced force exceeds the friction force - typically about 0.1 to 50 Newtons -. Stepping Piezoelectric Actuator (SPA), patented in Claeyssen and Barillot (2008), is an inertia motor which exploit a leverage structure to convert the full potential of the force generated by the ceramic into an increased displacement. It relies on a hinge-diamond shell, so-called Amplified Piezoelectric Actuator (APA®, Fig.2.1-a), patented in Claeyssen et al. (1995). This leads to increase the motor speed at low actuation frequency. Thus, two SPA (Fig.2.1-b,c), developed by Belly (2011), are commercially available since then.

(a) **(b)** **(c)**
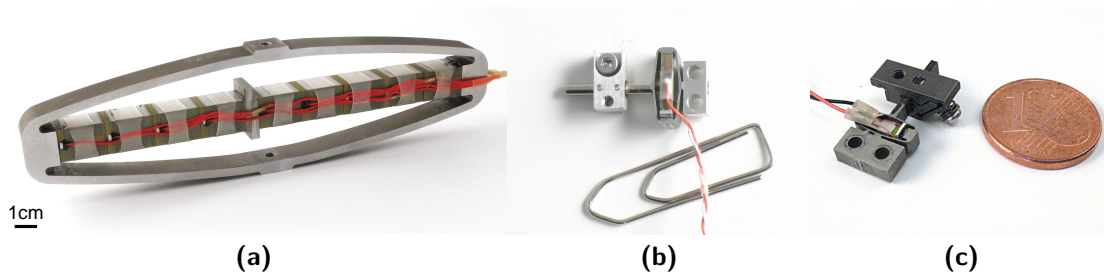
Figure 2.1 – Mechanical structures based on Amplified Piezoelectric Actuator (APA®). (a) APA1000XL: strain of the piezoelectric stacked ceramics is increased from 180μm to 1050μm by means of a diamond shell. (b) LSPA35XS: Linear SPA based on an APA35XS actuator. (c) LSPA30μXS: Linear SPA based on an APA30μXS actuator.

A recent review of inertia motors proposed by Hunstig (2017) confirms that SPA are well positioned in term of speed in comparison with other marketed motors[1] (red circles on Fig.2.2). In addition, the volume of motor remains compact since it is lower than 6cm^3 and lower than 1cm^3 for LSPA35XS (Fig.2.1-b) and LSPA30μXS (Fig.2.1-c) respectively.
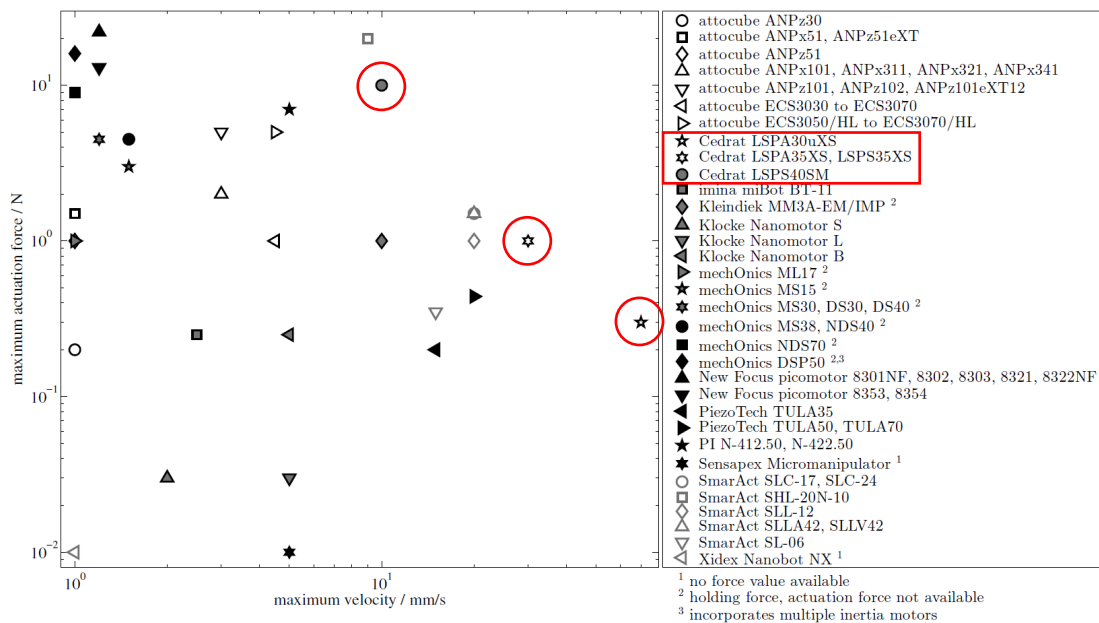
Figure 2.2 – Maximum actuation force and velocity of commercially available linear inertia motors (From Hunstig, 2017). Excepted the imina miBot, every mentioned inertia motor are in fixed actuator category (Fig.1.15). LSPA30μXS and LSPA35XS refer to Linear Stepping Piezo **Actuator**. Their design is similar to previously introduced inertia motor, with a moving mass sliding along an oscillating mass. LSPS35XS and LSPS40SM refer to Linear Stepping Piezo **Stage**[1].

In reference with the Fig.1.15 from chapter 1, notations used in the rest of the manuscript, in particular Oscillating Mass (OM) and Moving Mass (MM) as well as the displacement-time relationship are recalled on Fig.2.3.

---

[1]Linear Stepping Piezo Stage (LSPS), such as LSPS35XS and LSPS40SM, are an additional category of motors. They only differ from LSPA by their additional threaded interfaces, guidance, and integrated displacement sensor and they are not considered in the rest of this work.
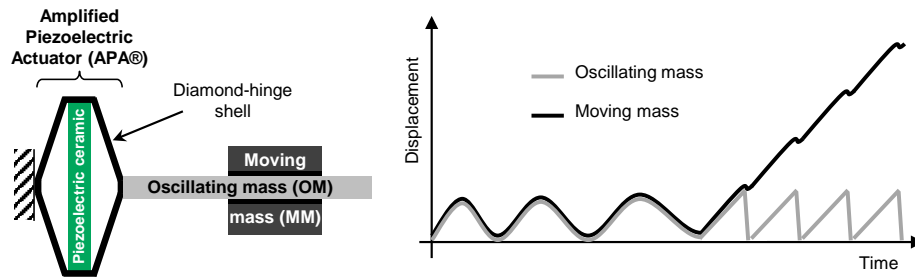
Figure 2.3 – Principle scheme of a SPA type inertia motor using an amplified structure for piezo-electrically actuating the oscillating mass (OM) and so making the moving mass (MM) travelling.

2.2 Characteristics of the motor

The basic characteristics of inertia motors, such as SPA, are easy to consider. The actuator, an Amplified Piezoelectric Actuator here (section 2.2.1), is controlled by a single electrical signal (section 2.2.2) to generate speed (section 2.2.3) and force (section 2.2.4), with a resolution down to a few nanometres (section 2.2.5), by means of a friction interface (section 2.2.6).

2.2.1 Amplified Piezoelectric Actuator (APA®)

Using an APA® instead of a "simple" piezoelectric ceramic makes it possible to address two inherent shortcomings. They are pre-stressed for increasing the range of deformations (section 2.2.1.1). They are amplified for maximising the actuator stroke and so the step size (section 2.2.1.2). In addition, by focusing on practical aspects, a mechanical shell also provides threaded interfaces to overcome potential failures of the ceramic which occur because of the impact generated by the driving signal (section 1.4.3).

2.2.1.1 Benefit of a pre-stressed piezoelectric ceramic

As multi-layer ceramics are laminated and brittle materials, they cannot bear any tensile forces. Beyond the tensile and the compressive stresses, material failure appears (Garbuio, 2006). To exploit greater deformations and stronger constraints, ceramics are stressed to maintain them in compression (Fig.2.4). The pre-stress allows the amplitude of deformation to increase without risking the material failure (Claeyssen et al., 2010).
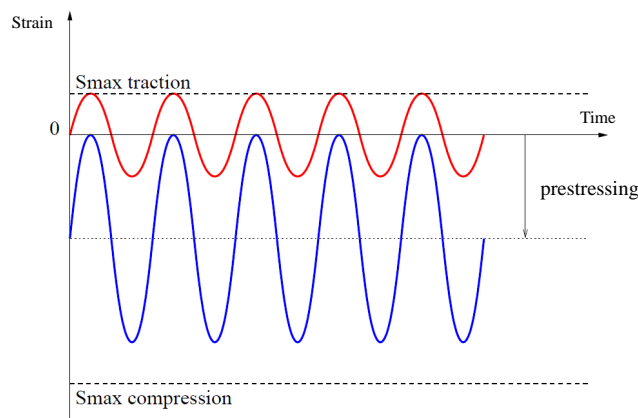
Figure 2.4 – Effect of a pre-stressing on the ceramic performances (From Garbuio, 2006).

2.2.1.2 Benefit and limit of an amplified actuator

Belly and Charon (2012) highlight that the stroke of the actuator is the main parameter for maximising the step size of an inertia motor. Thus, for a same ceramic size, the higher the amplification factor is, the bigger the step size is (Fig.2.5). While piezoelectric ceramic deformations are limited to a few microns or tens of microns, the diamond shell amplifies this stroke up to 20 times.
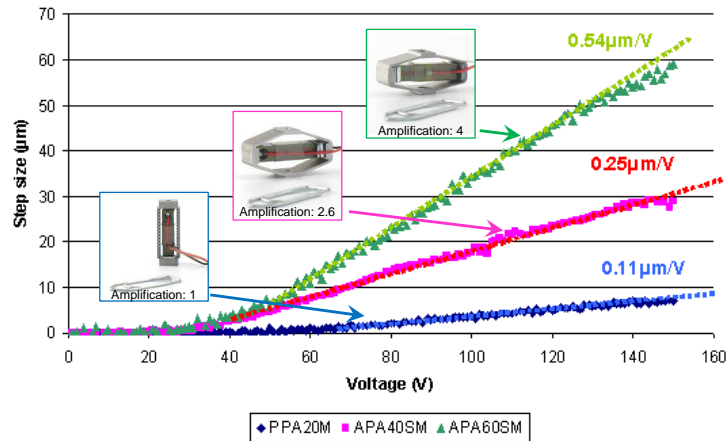
Figure 2.5 – Evolution of step size related to input voltage amplitude ($\propto$ actuator stroke, section 1.3.1.1) with the amplification ratio of three inertia motors (From Belly, 2011). PPA20M is not amplified. APA40SM is amplified with a ratio of 2.6. APA60SM is amplified with a ratio of 4.

Amplification also implies some limits. It imposes stiffness reduction, which is detrimental especially when motor natural frequency and signal frequency are close to each other (see section 1.3.1.2). In case of frequency coupling, the input voltage may lead to overcome the tensile/compressive limits leading to material failure (Fig.2.4). Although amplification makes it possible to increase the step size and so the speed, the generated force has to be confronted to static friction force. If the actuator is not able to make the MM sliding, no step will occur. It imposes to the amplification factor to remain between 2 and 6 (empirically set) for designing a consistent motor based on volume-force-speed considerations (Fig.2.6).
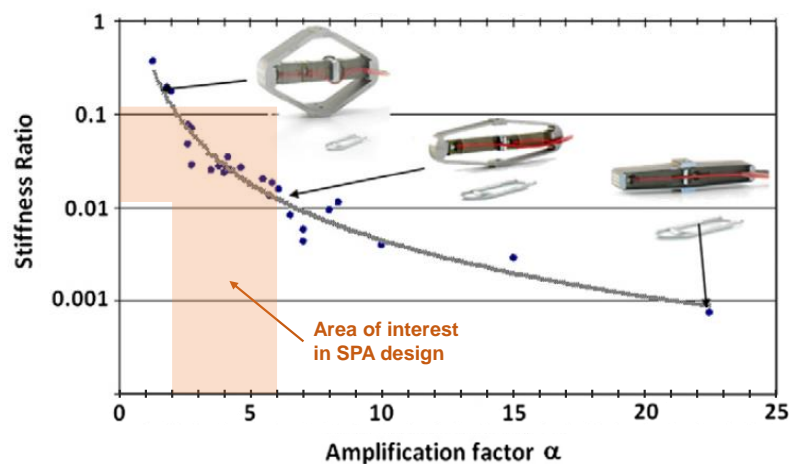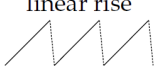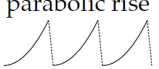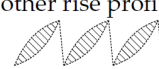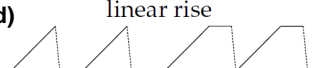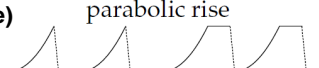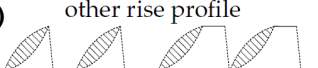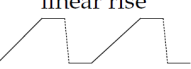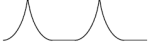
Figure 2.6 – Amplification impact on the stiffness ratio (From Belly and Charon, 2012). Empirical area of interest for SPA actuated at low-frequency is [2; 6] amplification factor.

2.2.2 Driving signals

Inertia motors are classically driven with a periodic sawtooth signal (Pohl, 1987b; Anders et al., 1987) with a linear slow increase and a linear fast decrease of voltage for the stick and the slip phases respectively (and *vice versa* in the reverse direction). Over the years, other driving signals have been implemented, differing mostly by the shape of the slow increase and by the occurrence of a dead time (constant voltage). They have been recently reviewed and synthesized in Table 2.1 by Hunstig (2017).

Table 2.1 – Voltage signals for piezoelectric inertia motors with examples gathered from literature: Compilation by Hunstig (2017) (See the related paper for the reference numbers).

sawtooth without plateau		
(a) linear rise [30,34,36,41,42,55,61,65,76,81,96,97,106,115, 116,154,160,163,166,172,186,192,238–240]	**(b)** parabolic rise [160,241]	**(c)** other rise profile [104,154,160,242–244]
sawtooth with one plateau		
(d) linear rise [47,63,114,157,192,245–247]	**(e)** parabolic rise [52,62,110,155,157,158,247]	**(f)** other rise profile [93,114,153,157,164,166,167,194,242,247]

sawtooth with two plateaus	cycloid	
(g) linear rise [21,26,63,166,173]	**(h)** without plateau [44,49–51,154,166] (with slightly modified shape [127,192])	**(i)** with low plateau [165,248]

Anders et al. (1987) and Pohl (1987b) have initially used a linearly rising voltage for the stick phase (Table 2.1-a). Higuchi and Watanabe (1990) and Yamagata et al. (1990) introduced a signal with a parabolic rise leading to a constant acceleration and thus to a constant inertial force (Table 2.1-b). By this way, inertial force caused by the contraction does not exceed the static friction force and stick phase is fully exploited to generate steps (Fig.2.7). They also explain that the fast contraction of the piezoelectric actuator can be used to generate additional displacement. Other sawtooth-like signal patterns - with different shapes of the voltage increase (Table 2.1-c,f) and with deadtime (Table 2.1-d,e,g) have also been used. In addition, Renner et al. (1990) introduced a cycloid signal to actuate the payload in a vertical motion. He emphasized that the driving signal provides better performances without the occurrence of two opposing acceleration peaks (stick → slip and slip → stick) found in a sawtooth signal patterns (Table 2.1-h,i).

After these signals were introduced, several authors have compared them, but they came to different conclusions. Bordoni et al. (1994) only reach an atomic resolution and reproducible steps with a cycloid signals. In contrast, Silveira and Marohn (2003) observed that a sawtooth signal generates larger and reproducible steps. Smith et al. (1996) find sawtooth excitation to be most efficient but mention that a cycloid signal was more effective with larger moving masses.

From bibliographical considerations, one can not conclude about the most relevant signal to adopt. Thus, experiments were performed for testing some of them onto SPA (Belly, 2011). As a result, the reference start signal used in this PhD research work is the "parabolic rise" (Table 2.1-b), because it gives reproducible results and reliable performances. In addition, results are easy to interpret by actuating with this signal.

Based on Eq.1.12, and under friction assumption of Coulomb (μ=F$_T$/F$_N$), optimal motor behaviour is fast to set depending on preload (F$_N$), voltage order amplitude (V), actuation frequency (fr) and MM mass (M$_{MM}$)[2]: On the one hand, if F$_N$ is too low, or fr or V or M$_{MM}$ are too high: the stick phase is not exploited at its full potential (Fig.2.7-c). On the other hand, if F$_N$ is too high or Fr or V or M$_{MM}$ are too low: backlash occurs in slip phase and global step size decrease (Fig.2.7-d).
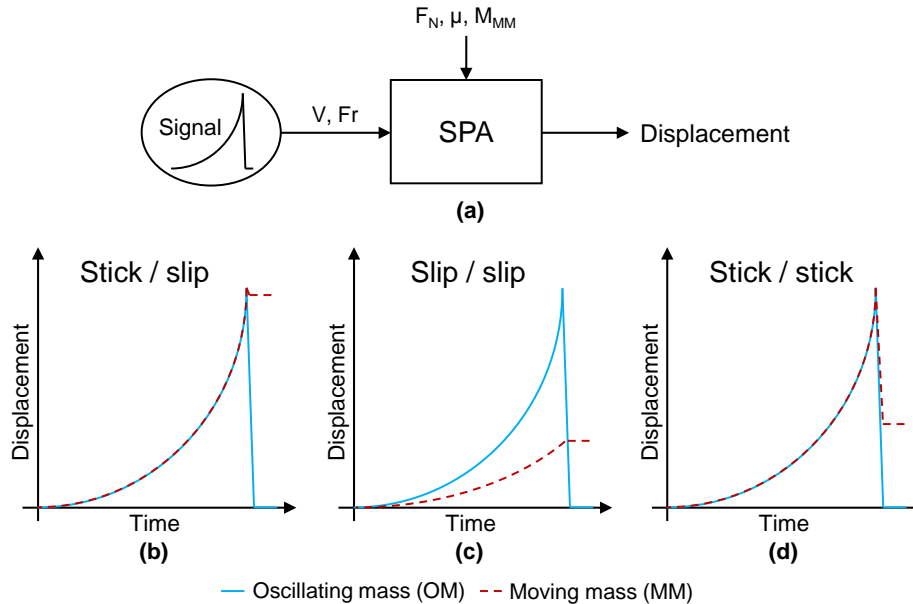
Figure 2.7 – Typical displacement curves of both the actuator (droved with a "parabolic rise" signal) in blue and the payload in red, respectively. (a) Displacement as a function of actuation frequency Fr, voltage amplitude V (proportional to displacement amplitude of the actuator), friction factor μ and preload F_N: (b) nominal reference; (c) partial slip in stick phase; (d) partial stick in slip phase.

2.2.3 Speed

As inertia motors operate with discrete steps, the generated velocity is the product of step size by actuation frequency. This affirmation is quite rough and deserves some additional considerations - such as frequency-dependent optimal speed (section 2.2.3.1), voltage threshold (section 2.2.3.2) and step size asymmetry (section 2.2.3.3) - to be reminded to better approach the notion of speed generated by the motors.

Notice that as the step size is increased by means of the diamond shell (section 2.2.1), the speed is increased in turn as long as there is not dynamic effects.

2.2.3.1 Resonance frequencies

Speed increases with actuation frequency[3] as long as this frequency does not couple with the motor natural frequency (section 2.2.1.2) and does not trigger partial slip in stick-phase (Fig.2.7). This is in agreement with literature (Fig.2.8).

The explanation relies on the stiffness of the system. In general, for a system with one degree of freedom, the frequency of the system imposes a bandwidth which

---

[2]Notice that a change in the motor performances - without changing any of the previous parameters - emphasizes a change in the friction factor.

[3]Other parameters such as friction, voltage or preload are considered constant here.
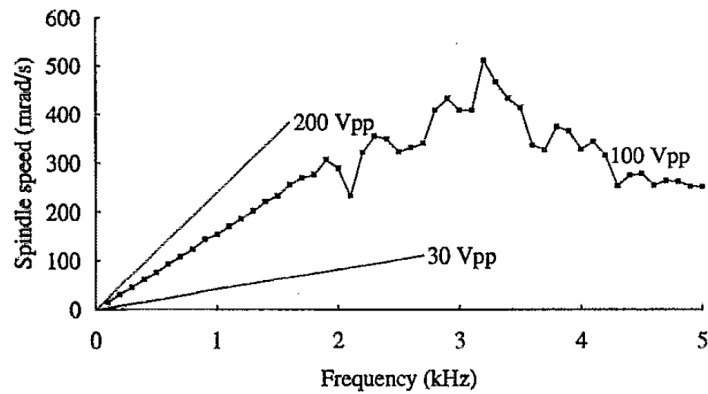
Figure 2.8 – Speed of inertia motor *vs.* sawtooth frequency at 100 V_{pp}. At lower frequencies speed depends linearly on the sawtooth frequency. After a maximum frequency the speed drops due to resonance effects in the construction. The "200 V_{pp}" and "30 V_{pp}" lines, respectively, above and beneath the 100 V_{pp} curve, give indications about the speed dependency with respect to frequency at different voltage amplitude and before that resonance effects occur (From Van der Wulp et al., 1995).

limits the frequency of excitation (Lambert et al., 2003). These frequencies are excited when the voltage order sharply changes from stick to slip phase. It generates free oscillations. Generating a new step at the moment when the mass rebounded in one direction or in the other will have a clear influence on final speed (and on the symmetry of performances). Classical solution, to be independent of the rebound, is to increase the stiffness and decrease masses of the overall system (Breguet, 1998; Zesch, 1997). A trade-off appears. For keeping repeatable the performance of the SPA, the maximum reachable speed is limited by the modal landscape of the motor.

2.2.3.2   Voltage threshold

Now, by considering constant the actuation frequency, a voltage threshold appears. The displacement of the motor is not possible below this threshold (Karrai, 1996, Fig.2.9-a). This would arise because of the too low acceleration provided by the actuator, which does not compensate the tangential stiffness of the friction interface (Fig.2.9-b).

(a)   (b)
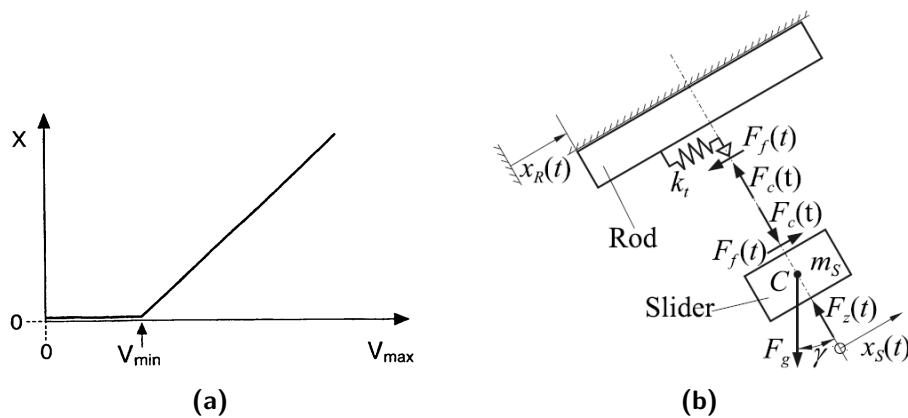
Figure 2.9 – Voltage threshold highlighting. (a) Graph showing step size plotted against input voltage. Until V_{min}, generated force is not sufficient to overcome contact stiffness (From Karrai, 1996); (b) Contact stiffness representation by means of a rigid body model applied to a simple linear inertia motor (From Hunstig, 2017).

2

In case of SPA, the total elasticity from the actuator to the friction contact must be also considered since the use of an amplified shell decrease the stiffness in actuation direction. It also leads to a voltage threshold (Fig.2.5 and below about 30V on Fig.2.10).
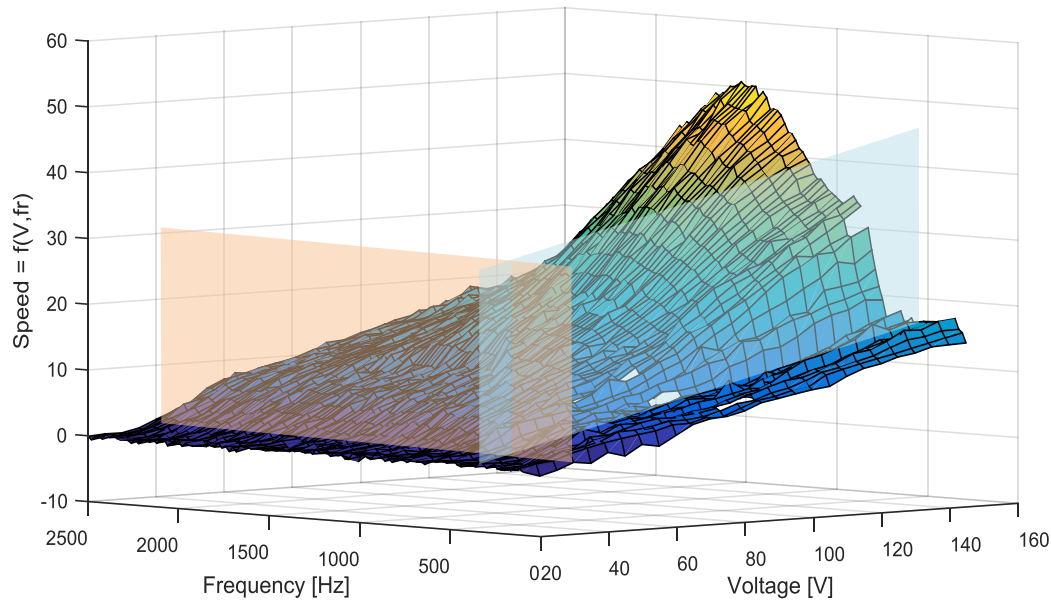
Figure 2.10 – Speed mapping of a SPA35XS actuated with a "parabolic rise" signal. Plot is done in terms of frequency and voltage. Each node of the mesh correspond to a measure from a laser vibrometer. Blue area corresponds to a linear increase of speed with voltage below the first actuation frequency ($\simeq$ 500Hz). Red area corresponds to the voltage threshold ($\simeq$ 30V).

Beyond this threshold steps are generated. Some authors consider a linear evolution (Breguet, 1998; Silveira and Marohn, 2003; Rakotondrabe et al., 2007; Okamoto and Yoshida, 1998). Some others clarify and show a different behaviour near the voltage threshold (Higuchi and Watanabe, 1990; Fung et al., 2008). In agreement with these authors, personal experiment (Fig.2.10) emphasizes an increasing speed as long as the actuation frequency is below the first resonance frequency (from 100Hz to 500Hz). Then, speed drastically increases because of the deformation of the actuator at the resonance frequency[4]. Finally, speed decreases when actuation frequency is too high because partial slip starts to occur in stick phase (Fig.2.7).

2.2.3.3 Step size asymmetry

The motion generated by an inertia motor is theoretically totally reversible. However, literature emphasizes a slight asymmetry in step size and so in speed (Fig.2.11). Thus, Bhatia et al. (2008) and Breguet (1998) observes a difference of performance according to the direction of displacement of around 10% (Fig.2.11-a,b). Breguet (1998) partly attributes this asymmetry to the voltage amplification (its electric response time is 2.3μs in positive direction and 4μs in negative direction).

---

[4]Interesting speed are reached but, as they are dependent on a resonance frequency, one prefers only considering nominal speed as a speed obtained below the resonance frequencies in this work.
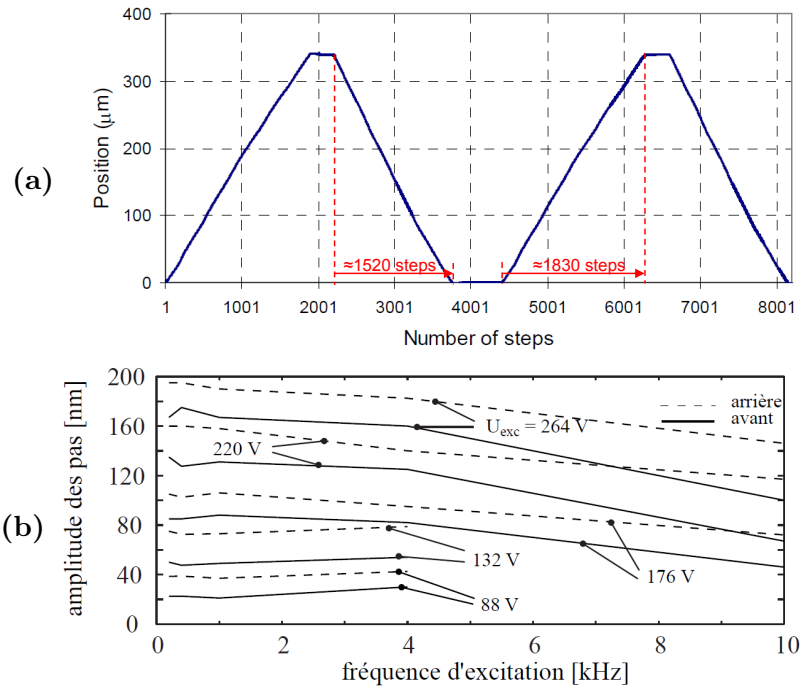
Figure 2.11 – Examples of inertia motor whose speed is asymmetric. (a) Based on Konica Minolta inertia motor (From Bhatia et al., 2008). (b) Based on a linear inertia motor (From Breguet, 1998).

Additional reasons could be attributed to the speed-mobile position dependence (Breguet, 1998), to an asymmetry between tensile and compression forces generated by the actuator itself (Belly, 2011), to the friction interface (or a combination of these reasons).
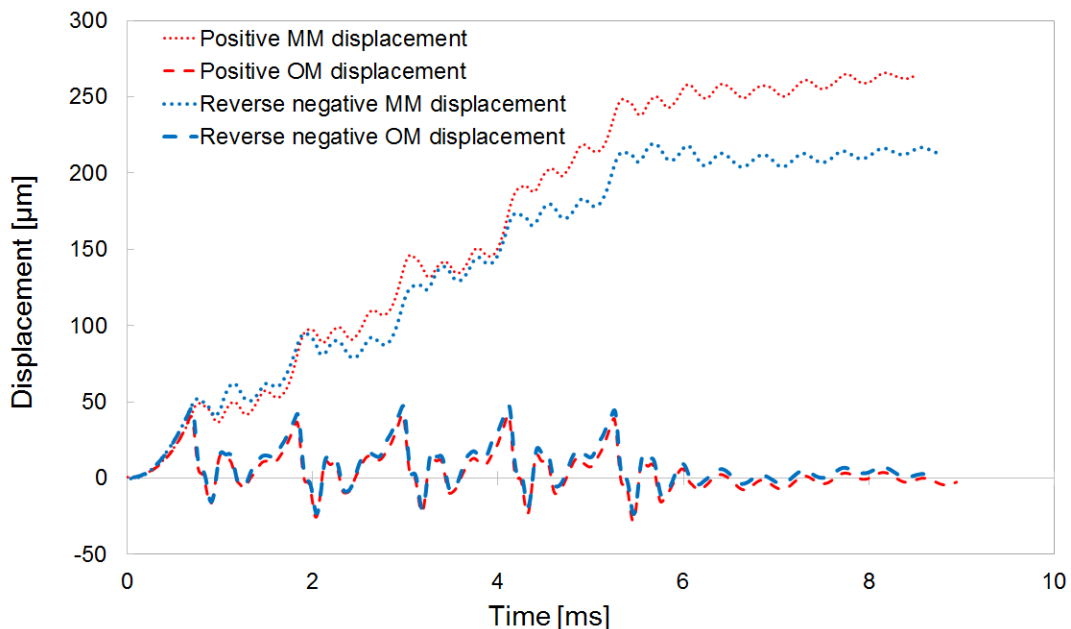
Figure 2.12 – SPA35XS asymmetric displacement curves. Red/blue curves correspond to actuation in positive/negative directions respectively. Blue curves have been reversed (150V→0V⇒0V→150V) to highlight the asymmetry. Dashed/dot lines correspond to the OM/MM displacements respectively. Resulting asymmetry is around 10-15%.

Previous reasons are all the more amplified by the effect of free-oscillations in dead-

time period between two stick-slip patterns. Experiments emphasize a 10-15% displacement asymmetry between back and forth direction even though same deadtime was ordered (Fig.2.12). Thus, such an asymmetry is inherent to the motor vibratory behaviour. It will depends both on conception and manufacturing processes.

To conclude this section about speed, the considerations of resonance frequencies, voltage threshold and step size asymmetry, seems to make inertia motor speed difficult to apprehend. However, as long as one remains in low-frequency range at a nominal level of voltage with consistent level of preload, speed remains easy to consider as a rough product of frequency and step size.

2.2.4 Load capabilities

Load capability refers to the capability of an actuator to generate force. Yamagata and Higuchi (1995) found that a same motor has a different load capability depending on if it pulls a weight or moves against a frictional force. From this observation, Zhang et al. (2012) qualify inertia motors in terms of three functional modes of force generation: (a) *hanging mode*, (b) *carrying mode*, and (c) *kicking mode* (Fig.2.13).

Traditionally, piezoelectric inertia motors are almost exclusively used in carrying mode for positioning applications with little to no force to generate. The indentation device developed by Rabe (2006) is one of the few examples where force is generated by an inertia motor (kicking and hanging modes). As a rule, although the nominal operating purpose of an inertia motor is to carry a load, one can presume that maximising hanging and kicking mode is necessary to make it robust and so reliable. It becomes necessary to measure it systematically. To do so, different methods appears: (i) making the MM to move against a spring - the force is either determined from the deformation of the spring (Rakotondrabe et al., 2009; Cheng and Hung, 2011; Belly and Charon, 2012) or from a load cell connected to the spring (Idogaki et al., 1995; Hunstig et al., 2014) -; (ii) making the MM to move directly against a load cell (Bergander et al., 2003; Kang et al., 2006; Edeler, 2011; Suzuki et al., 2012; Zhang et al., 2012; Yokose et al., 2012); (iii) another option is to make the motor to lift weights (Belly, 2011; Yokozawa and Morita, 2015); (iv) a last possibility consists in estimating it from the transient behaviour of the motor under a step voltage order (Nishimura et al., 2012).

(a) Hanging Mode

(b) Carrying Mode

(c) Kicking Mode
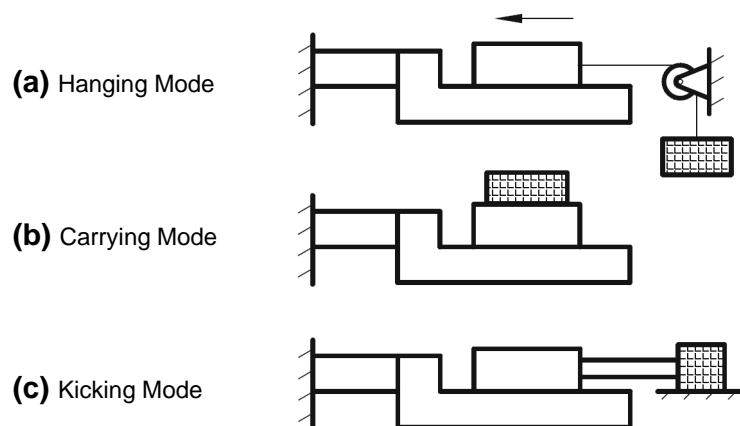
Figure 2.13 – Mass transfer modes of inertia motors (From Zhang et al., 2012). Ceramic is fixed to the ground. Payload is represented by a meshed box. (a) Hanging mode is considered in nano-positioning with a hinge-guidance for instance. (b) Carrying mode is the most common mode in positioning applications. (c) Kicking mode may represent the mechanical losses in using a guidance.

As for driving signal comparison, some authors have qualified the load capability in terms of actuation frequency, input voltage amplitude, preload, but come to different conclusions. Yoshida et al. (1999) highlight that (in hanging mode): (i) load capability decreases with the increasing actuation frequency, (ii) it increases then decreases along with the increasing friction force but with a very small change, and (iii) it increases and then maintains at the same level when voltage increases (Fig.2.14).
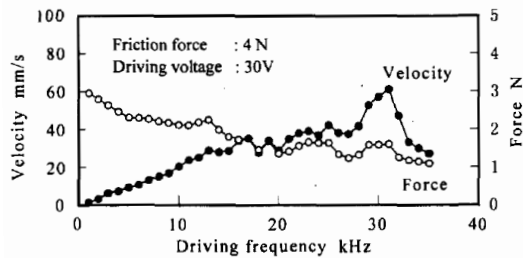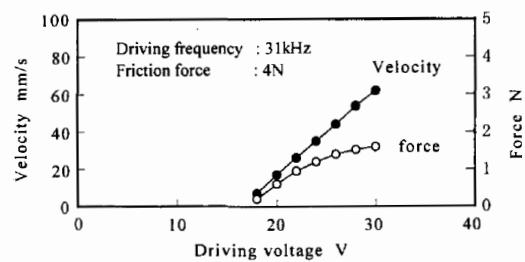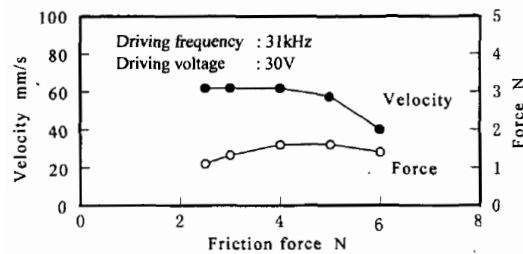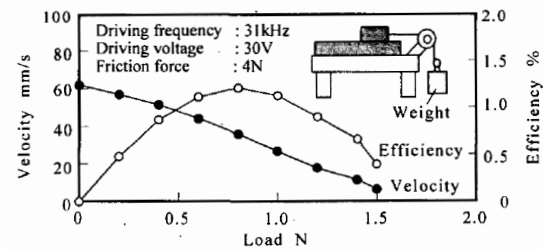
Figure 2.14 – Load capability qualification of inertia motor (From Yoshida et al., 1999). Load capability decreases with the increasing actuation frequency (Fig.13). It increases a few and then decreases with the increasing friction force (Fig.14). It increases and then maintains with increasing voltage (Fig.15). Resulting load curve (Fig.16). No-load speed is 60mm/s, blocked force is 1.5N.

Van der Wulp et al. (1995) found that load capability (torque) linearly increases with the increasing preload. But, contrary to Yoshida's results, they also found that frequency did not cause a big change to load capability. He also highlights that maximal generated force and maximal speed does not appear for a same actuation frequency. Higuchi et al. (1992) found on their side that load capacity increases with friction force. Okamoto and Yoshida (1998) compared Pulse Width Modulation (PWM) and triangle signals and found a modified load capability: PWM signal lead to low force and high speed while triangle signal lead to higher force but lower speed. From these bibliographical considerations, one can not conclude about load capabilities trends. It becomes necessary to qualify the SPA experimentally to get this characteristic.

Qualification test of the kicking mode appears to be few representative of SPA force potential. Related load capability would not be reliable if final application requires dry or lubricated friction for instance. As highlighted by Yamagata and Higuchi (1995), hanging mode capability is lower than kicking mode capability. In addition, it has been recently shown that running the MM against a spring (hanging mode) is a robust method of determining the force generation potential of an inertia motor (Hunstig et al., 2014). It provides results independent of the spring stiffness as long as it is sufficiently low. This method was used to determined the load curve of a SPA35XS (Fig.2.15). Thus, it will be also used to qualify the mechanical performance changes due to vibratory improvements (see Chapter 6).

2
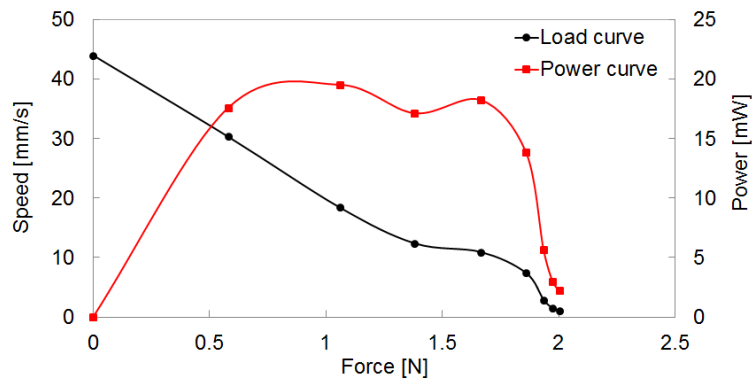
Figure 2.15 – SPA35XS load (in black) and power (in red) curves.

2.2.5 Accuracy and resolution

Inertia motors generate theoretically unlimited displacements by means of successive steps (*stepping mode*), with a positioning accuracy equal to the step size (Fig. 2.16-a). The design of inertia motors allows a second mode of operation so-called *scanning mode* (Lambert et al., 2003; Bergander et al., 2003; Chu and Fan, 2006; Claeyssen et al., 2008). In this mode, voltage order is low - typically a low frequency sine signal -. There is no more stick-slip but only stick. Thus, the moving mass motion depends on the actuator motion. The resolution in this mode is typically below 1 nanometre (Arnold et al., 2008; Minase et al., 2010), limited only by the driving electronics (Fig. 2.16-b). Notice that accuracy is kept as long as effort applied on the moving mass is lower than friction force when power supply is switched off.
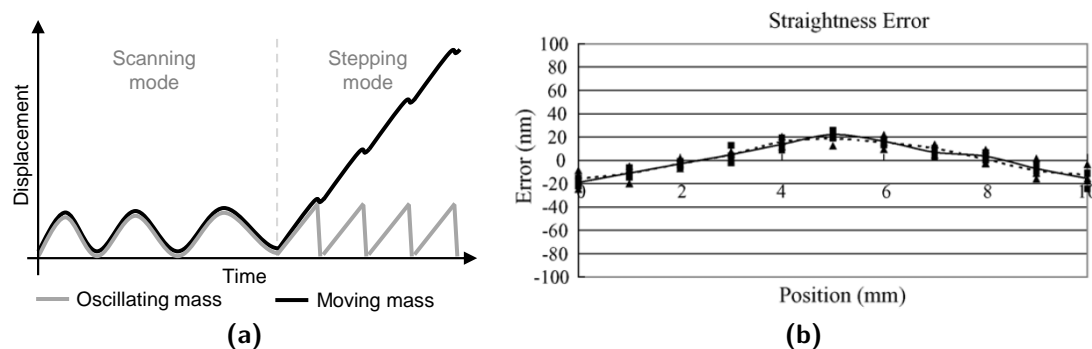
Figure 2.16 – (a) Schematic principle of both stepping and scanning mode available in inertia motors. In stepping mode, the moving mass reaches a long stroke by means of stick-slip. In scanning mode, voltage order is slow - typically a low frequency sine signal -. The moving mass sticks to the oscillating mass what ensure a nanometre accuracy and precision. (b) Measurement of positioning stage straightness error: (■) forward, (—) forward average, (▲) backward and (- - -) backward average (From Chu and Fan, 2006).

2.2.6 Friction material couple

In SPA, medium frequency fretting friction conditions - stick-slip at 1kHz and $50\,\mu$m amplitudes - with superimposed macroscopic sliding - 10 Hz, 1-10 mm stroke length - occur (Rehbein and Wallaschek, 1998). This contact dynamic is essential for the generation of driving force. Related tribological processes not only determine load capability, speed, but also lifetime and repeatable behaviour of these motors. The

appropriate choice of frictional materials at the interface is therefore crucial in the design of SPA. Their further development may be strongly accelerated by detailed investigations about friction and tribological solicitations.

Lubricated contacts — There are few investigations of lubricated inertia motors. It can be attributed to Pohl works. Most of the inertia motors use dry friction contacts. He showed a significant loss of velocity and load capacity as soon as the friction interface is lightly lubricated (Pohl, 1987a). Anantheshwara et al. (2008) results seems to confirm this point. They compare lubricated and dry steel-steel couples, using the same control signal for both cases, what led to step size reduction. On the contrary, experiments by Furutani et al. (1998) with steel couples and different lubrication fluids indicate that lubrication can be beneficial for different reasons. It increases the uniformity of the contact, resulting in less variation of the step size and less movement of the slider perpendicular to the contact. With lubrication, they achieve the same or a slightly higher velocity than without and the lubricant additionally prevents corrosion. However, the influence of lubrication on wear was not investigated. Lubricated contact is not considered in this work because (i) it implies a risk of failure in the lubricant supply, (ii) a lubricant supplying system is not consistent with the miniaturization potential of SPA and (iii) it may lead to fluid projection on lenses or any optical load (prism, mirror...) in optical positioning system.

Dry contacts — There were more investigations about dry contact. Among them, Aluminium oxide predominates (Hack, 1998; Patil et al., 2005; Göken, 1994; Darby and Pellegrino, 1997; Bobji et al., 2006; Chuang and de Lozanne, 2007; Anantheshwara et al., 2008), but quartz (S_iO_2), (Blackford et al., 1992; Hack, 1998; Darby and Pellegrino, 1997), and different glasses (Yamagata et al., 1990; Asenjo et al., 1994; Kang et al., 2006; Ko et al., 2006) are also used. Combinations of one of these hard materials with metals are also found. Mostly, they rubs against steel (Howald et al., 1992; Renner et al., 1990; Smith et al., 1994; Wildöer et al., 1994; Kang et al., 2006; Lambert et al., 2003; Bergander and Breguet, 2002; Woodburn et al., 1993), sometimes also with other metals such as Invar (Iron-Nickel alloy) (Curtis et al., 1993), or titanium (Wang and Lu, 2012). A steel-steel couple is used sometimes (Probst et al., 1991; Libioulle et al., 1993; Higuchi and Watanabe, 1990; Claeyssen et al., 2008; Anantheshwara et al., 2008), while couples of steel with other metals such as brass (Tuncdemir et al., 2011), or with a very soft partner like PTFE (Judy et al., 1990; Furutani et al., 1998) or other plastics (Claeyssen et al., 2008; Morita et al., 1999) are rare. Some of the previous examples are exhibited on Fig.2.17.

Some authors have experimentally compared different friction couples on their own inertia motors, (*e.g.* Niedermann et al., 1988; Erlandsson and Olsson, 1996; Furutani et al., 1998; Ko et al., 2006; Claeyssen et al., 2008; Belly, 2011). Edeler et al. (2010) compare rough and polished steel, aluminium, and bronze surfaces in contact with ruby hemispheres. They observe larger steps with polished surfaces and harder materials. Similarly, Claeyssen et al. (2008) observe larger steps with a steel-steel contact compared to a steel-polymer contact in most setups. They also show a different influence of the moved mass on the motor velocity with different friction couples. Ko et al. (2006) observe that their high-frequency motor requires different friction couples to reach its maximum velocity and its maximum actuation force. Bergander and Breguet (2002) developed a test bench dedicated to inertia motor. They compared sapphire contact with different coated steel, aluminium, and silicone regarding mechanical performances

and wear. The best results have been obtained on sapphire or ruby half spheres samples *vs.* NiP flat antagonist. They also noticed that a 1-μm-TiN deposit did not bear large forces (1.5N) but operated well for small normal loads (300mN). As well, MoS_2 coated steel in contact with sapphire was also beneficial for the repeatability of movements and reduced wear.

These observations confirm the intuitive expectation that tangentially stiff contacts are beneficial to decrease mechanical losses in antagonist deformations. However, the optimum friction couple appears to depend on the motor design, its excitation and its application.
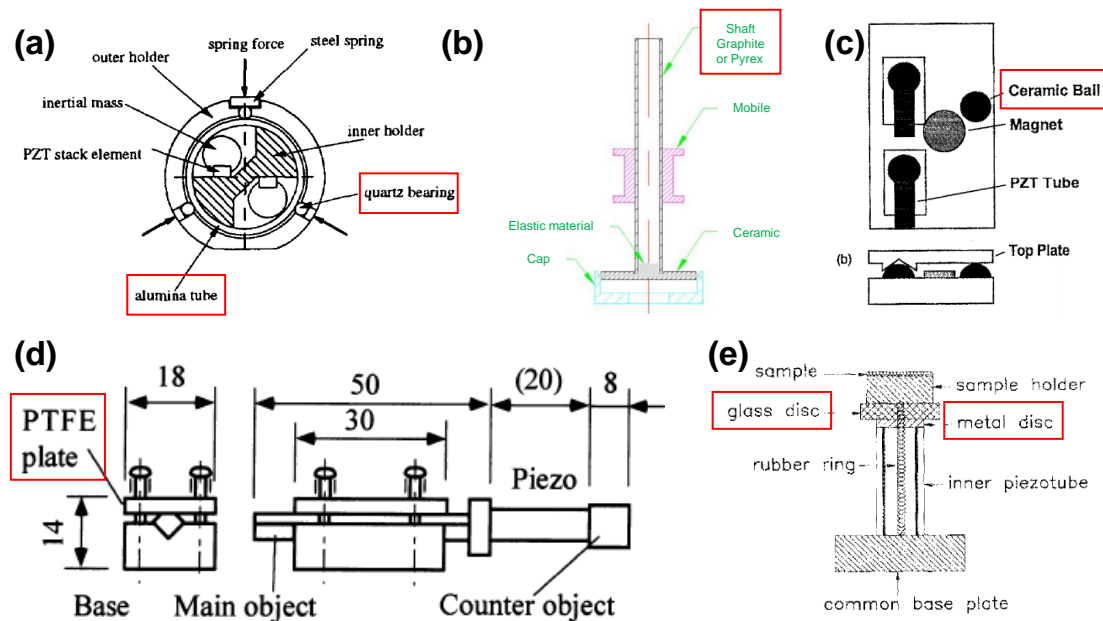
Figure 2.17 – Examples of friction couple used in inertia motors. Red boxes emphasize the employed friction couples. (a) Alumina *vs.* Quartz (From Hack, 1998). (b) Graphite or Pyrex (From Ko et al., 2006). (c) Ceramic *vs.* Ni-hardened metal (From Curtis et al., 1993). (d) Lubricated contact with PTFE *vs.* stainless steel (From Furutani et al., 1998). (e) Glass *vs.* Metal (From Asenjo et al., 1994).

Based on these previous considerations, Belly (2011) carried out lifetime tests with different friction couples, representative of what is found in literature such as ceramic/metal, metal (coated or not) / metal (coated or not), in dry conditions. While "classical" material couples generated wear with unsteady performances, the - fibreglass filled polymer / coated Ti-6Al-4V - couple reached the longer lifetime (10^6 operating cycles / 2km equivalent sliding distance with repeatable performances.

Thus, there is not, today, one material couple which could be considered as a trade-off for both reaching a long lifetime with a minimum of wear and repeatable performances no matter the inertia motor. So, based on the works of Belly on SPA, the - fibreglass filled polymer / coated Ti-6Al-4V - friction couple will be used as a start point for the rest of this work.

2.3 Main limitations of SPA

SPA has the main advantages of a simple structure from both mechanical (section 2.2) and driving (section 2.2.2) points of view. Their dynamics (section 1.3.1.2), accuracy and resolution (section 2.2.5), and compact size (section 2.1) as well as their

compatibility to harsh environments make them suitable for many application fields in optics, robotics or consumer good (section 1.5). Thus, although performances - speed (section 2.2.3) and force (section 2.2.4) - are inherently lower than that of inchworm or ultrasonic motors (Fig.1.16), limitations such as wear generation particles, lifetime (section 2.3.1) and noise (section 2.3.2) deserve to be analysed and raised to disseminate these motors.

2.3.1 Friction: wear and lifetime

Friction is inherent to the operating principle of the motor. Despite numerous aforementioned publications toward inertia motors, a few attention has been paid to this topic (only Bergander works to the author's knowledge (Bergander, 2003)). Most of the works usually deals with driving signal (section 2.2.2), impact of the structure on the performances (sections 2.2.3, 2.2.4 and 2.2.5) or with friction material testing (section 2.2.6). Tribological solicitations[5] must be therefore analysed to understand why the fibreglass filled polymer / coated Ti-6Al-4V - friction couple "works" in SPA. This is necessary before considering any improvements such as an increase of the lifetime while considering the wear particle generation as well as keeping reproducible performances.

2.3.2 Noise: mechanical-acoustic performances

Noise can be a serious limitations in some applications, specifically for consumer goods (section 1.5). It appears in particular for long stroke applications which require a series of repeated steps, resulting in persistent noise. This can be due to the vibrations of the actuator driven by a frequency in the audible spectrum - typically a few kHz (section 2.2.3.1) -. In addition, the operating principle of SPA, relying on stick-slip, suggests a secondary friction-induced noise source. To address this issue, Breguet (1998) suggested to maximise the stiffness of the system to avoid exciting parasitic resonance frequencies. Probst et al. (1991) proposed to include decay phases in the excitation signal to damp free oscillations. Although overview about inertia motor characteristics (section 2.2) emphasizes that performances of the motor (sections 2.2.3, 2.2.4 and 2.2.5) are impacted by the driving signal (section 2.2.2) and the mechanical system (section 2.2.1), no literature has been found dealing with both acoustic and mechanical performances of the motor.

2.4 Motivation of this work

The numerous possible avenues of works raise pragmatical issues. The first one is about the temporal and economical sustainability of the actions to engage for the duration of this PhD work. The second issue concerns the study of the phenomena which currently impact the most the dissemination of the SPA.

Thus, the purpose of this PhD research work is to overcome the main limitations of the current SPA: (i) by increasing lifetime while both decreasing the wear particle generation and keeping mechanical characteristics suitable for industrial applications and (ii) characterizing their vibratory behaviour in order to better predict mechanical performances and to decrease the noise level.

In order to address these two issues:

---

[5] The notion of *tribological solicitations* comes from french "sollicitations tribologiques" (**?**), which has no direct equivalent term in English. Here, this notion encompasses (i) applied displacements, speeds and loads, (ii) environmental conditions and (iii) 3rd body behaviour, through its morphology, particles flows, accommodations sites/modes and wear mechanisms.

2

- First, the tribological behaviour of SPA is considered through the development of a dedicated test bench. Related data and observations have been analysed by means of the Godet's 3rd body formalism (Godet, 1984). It makes it possible to characterize the tribological solicitations and the 3rd body flows with a rigorous framework leading finally to the tribological circuit of SPA.

- Second, the vibratory behaviour of the SPA mechanism is approached by numerical and experimental tools. On the one hand, the current 1-DoF lumped modelling is improved by implementing a FEM-lumped hybrid modelling, taking into account motion in the three directions of space. It makes the current model more representative of the SPA motion. On the other hand,experiments are carried out to identify the noise sources and to propose relevant solutions to reduce the generated noise.

In addition, innovative developments which take benefit from tribological and vibratory analyses are proposed. It leads to achieve efficient conception rules to help the technical teams in both design and integration phases. The performances of the SPA are also considered faced with its integration in complex structures such as multi-DoF mechanisms. As well, hyperstatism - typically introduced by a guidance in redundancy with actuation axis - is addressed. At last, the choice of a friction couple is optimised since it ensures the most of the properties of the motor.

2.5 Outlines

To address the issues related to tribological and vibratory performances, the thesis is split into two technical parts and one synthesis part (Fig.2.18):

- Part II deals with tribological approach. It consists in decrypting what happens at the contact interface through the 3rd body formalism.

  - Chapter 3 introduces the methodological framework as well as the development of the test bench which has been designed to simultaneously set up a tribological instrumentation while being as representative as possible to the SPA;

  - Chapter 4 exploits measures and observations by means of both the 3rd body flows and the tribological circuit concepts to characterize the tribological solicitations into the friction interface of SPA.

- Part III deals with vibratory approach. As both the noise and the working of SPA are due to vibrations, it becomes necessary to get a deeper understanding of the SPA vibratory behaviour.

  - Chapter 5 concerns the improvement of the current lumped model used to predict the mechanical performances of SPA;

  - Chapter 6 is dedicated to noise reduction. Several experiments are introduced to determine the main source of noise. Solutions are proposed to reduce it while maintaining valuable mechanical performances.

- Part IV relies on this research work to converge toward practical considerations and wider perspectives.

- Chapter 7 proposes a synthesis. Indeed, an innovative SPA structure has been introduced during this work. It raised integration limitations and makes both the design and the integration phases easier. Based on this motor, a complete design methodology is presented and relies on innovative industrial developments;

- Chapter 8 ends this thesis with perspectives facing with the next gaps to overcome.
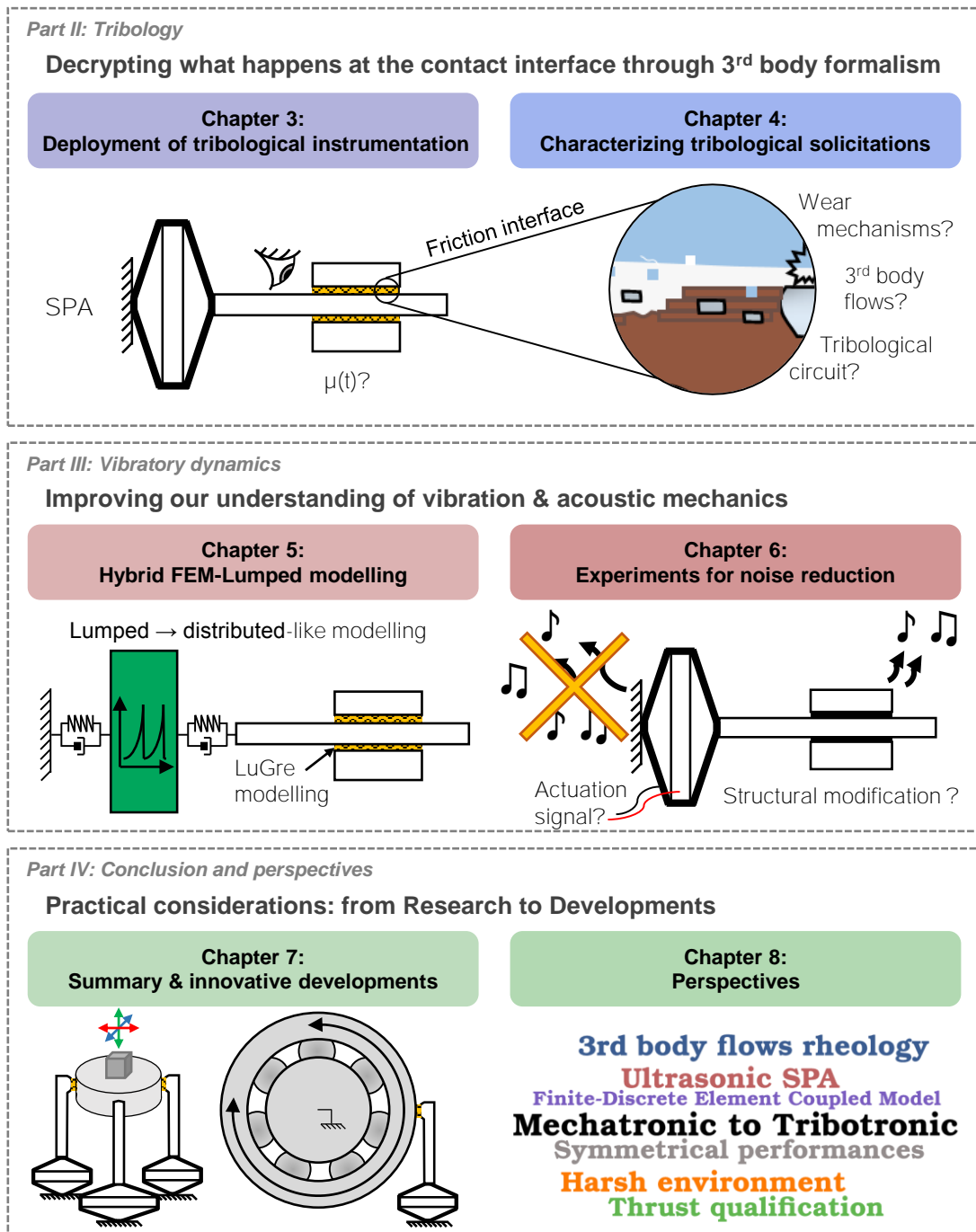
Figure 2.18 – Synoptic of the PhD thesis chapters and related main issues.

Avec le concours des années, l'anneau que nous portons au doigt s'amincit par-dedans, la chute répétée d'une goutte d'eau creuse la pierre, le fer du soc recourbé s'émousse invisiblement dans le sillon, on voit que se sont usées sous les pas de la foule les pierres qui pavent les rues, et les statues d'airain placées à la porte des villes nous montrent des mains usées aussi par le baiser des passants qui les adorent.
Ces objets diminuent donc, nous le voyons, par l'usure. Mais quelles particules s'en retirent à tout instant ? La nature nous en a dérobé le spectacle.

— Lucrèce, 95-55 B.C., De rerum natura

Part II.

Tribological analysis of SPA

If mechanics is the science of movement,
Tribology is science making movement possible.

— M. Godet

Deployment of
a tribological instrumentation

In inertia motors, friction is not synonymous of energy loss but is the source of motion. Their performances are thus prone to wear and friction coefficient variation. These are crucial issues for reaching a long lifetime and performance repeatability. This part aims at improving the understanding of tribological solicitations and to improve tribological performances. This chapter introduces in particular a SPA-dedicated new tribometer aiming at carrying out direct *in-situ* analyses of the friction contact as well as the Godet's 3rd body fundamental notions.

Introduction

As described in the previous part, the technology of inertia motors is based on the relative displacement between two friction materials, by means of stick-slip (Fig.1.15). The performances of these motors such as wear rate and lifetime are consequently inherent to the employed material couple, to the surface conditions, to the environment and to the SPA behaviour. Understanding the tribological solicitations within the SPA is necessary to improve its performances.

Faced with the numerous parameters involved in the design of piezoelectric motors (*e.g.* piezoelectric actuator model, normal load configuration, guidance, actuation frequency (Ru et al., 2016)), and the stick-slip bound tribological solicitations (*e.g.* sliding velocity, contact area, surface energy (Yoshizawa and Israelachvili, 1993)), it is complicated to analyse a given material couple exclusively from bibliographical considerations. Likewise, Discrete Element Modelling (DEM) could be a fruitful approach for getting the dynamic behaviour of a contact interface at a local scale (Kounoudji et al., 2016). However, calculations remain too time-consuming to be considered in this study. It becomes necessary to carry out an experimental approach based on tribometry - throughout the tribological triplet approach (Godet, 1984). It requires beforehand a decryption of the contact life with 3rd body flows to get the tribological circuit (Berthier, 1990, 2005).

Assessing tribological solicitation features of a given material couple may depend on the employed measurement method and contact conditions, as highlighted during

the VAMAS project (Czichos et al., 1987). Bergander et al. (2004) also emphasized that even reciprocating tribometer, closer to the macroscopic motion of SPA, is not close enough to the final application to provide valuable results. Likewise, Blau (1992) highlighted that friction coefficient can change significantly with measurement conditions. Actually, throughout the tribological analysis, contact conditions proper to the mechanism are at least equally important as the material couple itself.

But, taking into account the link between mechanism and contact conditions is not the only point. Another difficulty in studying friction contact is the lack of measurable *in-situ* data without being invasive. To do so, different approaches have been proposed. Some of them were brought by the elastohydrodynamic studies (reviewed in Albahrani et al., 2015) at nano-scale level but they reach limits in dry contacts. Another approach consists in correlating acoustic emission signals and wear mechanisms (Hase et al., 2012). Although this method is the less invasive, this is quite new and does not make it possible to distinguish different wear mechanisms if they occur at the same time. It is also possible to carry out stopped tests with unload/measure/load sequences (Wahl et al., 1998) but 3rd body distribution may change inside the contact (Colas et al., 2013). So, conducting direct *in-situ* tribometry through transparent bodies appears to be a fruitful approach as reflected in the numerous applications (*e.g.* study cases: Play and Godet, 1976; Sliney, 1978; Jullien et al., 1996; Descartes and Berthier, 2002; Singer et al., 2002; Scharf and Singer, 2003; Michler et al., 2005; Dvorak et al., 2007; Chromik et al., 2007; Wahl et al., 2008; Stoyanov et al., 2012; Krick et al., 2012). Although using a transparent material can lead to change in friction behaviour (Fayeulle et al., 1990; Descartes and Berthier, 2002), this makes it possible to observe 3rd body creation and motion inside the contact (Play and Godet, 1976; Sliney, 1978; Descartes and Berthier, 2002; Singer et al., 2002; Scharf and Singer, 2003; Dvorak et al., 2007; Wahl et al., 2008). The evolution of the created 3rd body layer may be then linked to the measured motor performances (Wahl et al., 2008; Scharf and Singer, 2003). Simultaneously, friction materials used in real motors are also tested. All gathered information provides the scenario of the contact life. Both the SPA tribometer and the transparent interfaces presented below are used to achieve this purpose.

To understand the tribological solicitations, one carries out an experimental approach close to the operating conditions of the studied motors with both transparent and real friction interfaces. The objective is to improve tribological performances of SPA - by both increasing the lifetime and decreasing the wear volume while maintaining a stable friction coefficient.

The chapter firstly describes the experimental setup dedicated to SPA from the design to the implemented instrumentation (section 3.1). Then, a point of methodology through the 3rd body formalism focuses on the way the analysis is carried out, by giving a strict framework for the further analyses (section 3.2). The chapter is concluded by the procedure used in the next chapter 4 (section 3.3).

3.1 Experimental setup: SPA tribometer

The main goal in the design of a testing system for material combinations is to be as close as possible to the operating conditions of the final application. In SPA, the influencing parameters of the motion are (i) the piezoelectric actuator, (ii & iii) the inertias of the objects to be displaced (OM and MM), (iv) the guidance and (v) the normal load acting on the contact between OM and MM. The targeted orders of magnitude of both speed and tangential force are based on the studied motors. Setup (Fig.3.1) sizing is detailed in section 3.1.1. Instrumentation aims to simultaneously

measure (vi) friction coefficient, (vii & viii) OM and MM displacements, and (ix) to observe what happens in contact through (x) an observation window. Details of the implemented instrumentation is given in section 3.1.2.

(a)   **(b)**
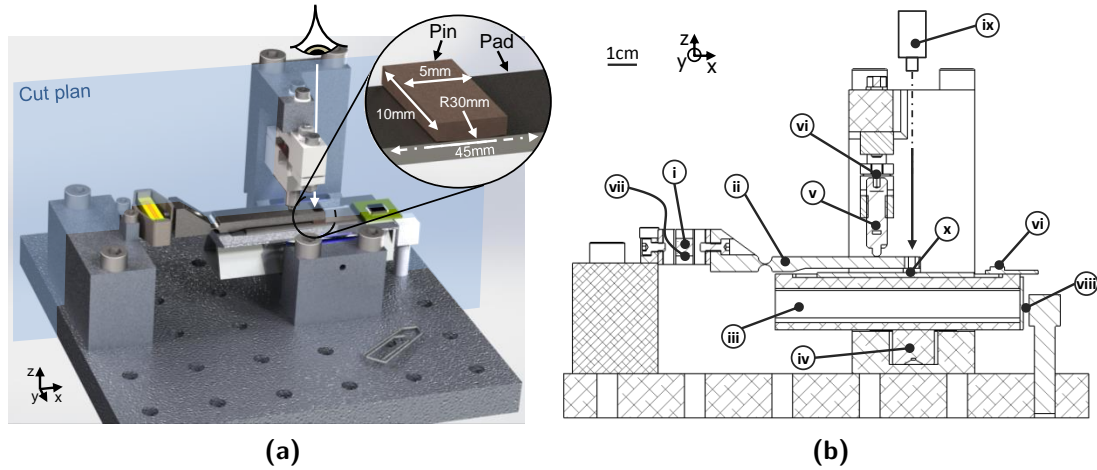
Figure 3.1 – Tribometer setup. (a) illustration and (b) Cut plan. (i) Piezoelectric actuator linked to (ii) the Oscillating Mass (OM) in contact with (iii) the Moving Mass (MM). (iv) Guiding and lift are provided by air bearings. (v) Normal load function is provided by a spring contained in a screw. (vi) Applied normal force is measured by a strain gauge mounted on specific deformable test body. (vii) Strain gauge is mounted on actuator to get the displacement of the actuator and so of the OM. (viii) Eddy current sensor is used to get the displacement of the MM. (ix) Camera or high speed camera. Extra light is provided by LED light to make high speed camera acquisition possible without harming contact. (x) Observation window to see through 1st bodies in contact.

3.1.1 Design

Mechanical design phases are detailed in Fig.3.2.

- **First step** deals with requirements specification (section 3.1.1.1). Speed performances being bound to the inertia of the different parts (*e.g.* OM, MM), it consists in optimising the masses of the system to reach the speed target, representative of SPA. The used tool is a lumped model implemented in Matlab/Simulink by Belly (2011). It makes it possible to size the SPA by linking actuator performances to the other masses of the system with springs and dampers[1].

- **Second step** is a classical structural analysis to ensure the reliability of the tribometer (section 3.1.1.2). It depends on the masses determined above. Finite Element Modelling is used here for both static and dynamic analyses.

- **Third step** is similar to the first one. It is dedicated to the final performance estimation of the tribometer, using lumped model once again (section 3.1.1.3).

At last, after integration, an experimental validation of the tribometer performances is realised by means of (i) an admittance measurement to assess the dynamic behaviour of the mechanism (based on theory introduced in section 1.3.1.2) and (ii) speed performances (section 3.1.1.4).

---

[1]This model will be deeply discussed in chapter 5.

3
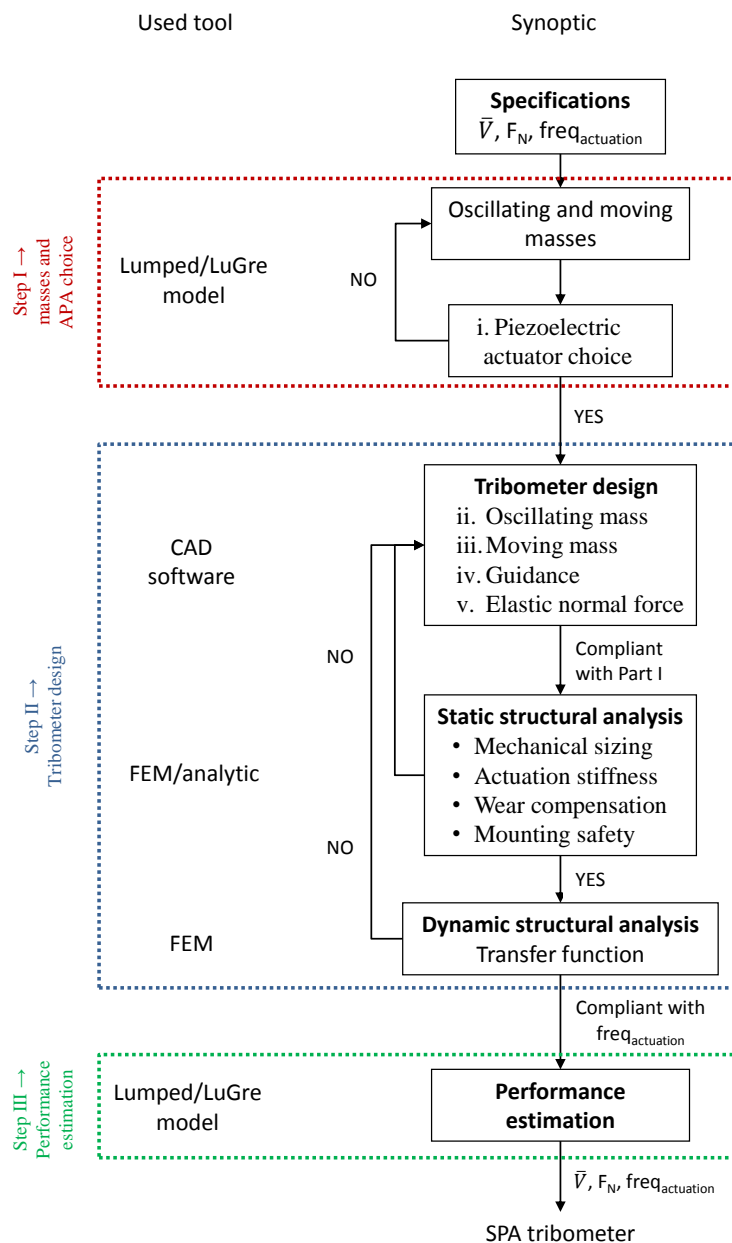
Figure 3.2 – Test bench mechanical design flow chart. Used lumped/LuGre modelling is detailed in (Belly, 2011) and discussed in Chapter 5.

3.1.1.1 Requirements specification

The volume of a SPA is classically lower than 200mm^3, what limits tribological instrumentation. The objective of the tribomter sizing are to assess both the optimal APA® shell and masses to be representative of SPA, while making it possible to observe the contact from the inside, as well as to measure tribological data and to limit impact on the friction behaviour. To do so, actuation frequency, normal force and mean speed have to be in the same order of magnitude - around 1kHz, 5N and 20mm/s (Fig.2.2) respectively - to reproduce the 3rd body behaviour (creation, motion, ejection and recirculation of solid particles into the contact).

i - Piezoelectric actuator — As described in chapter 2, the used piezoelectric actuator takes benefit from an amplified mechanical structure. Classical SPA are based on 2x5x10mm³ or 1.65x1.65x5mm³ piezoelectric ceramic size. In order to remain consistent with this ceramic size while enabling tribological instrumentation, choice is done to pursue with a 5x5x20mm³ size of ceramic. Relative available actuators are APA60S, APA120S, APA40SM and APA60SM (Cedrat Technologies website), whose performances depend on their stiffness and amplification factor (Fig.2.6). By means of lumped modelling, a trade-off appears for an APA60S shell, OM=10gr, MM=40gr, a 1kHz-actuation frequency and 3ms of deadtime to naturally damp free oscillations. Expected $\overline{v}$ is around 15mm/s (Fig.3.3). Notice that actuation frequency and normal force orders of magnitude are prioritised in front of a perfect stick-slip motion in order to get closer to the 3rd body kinematic found in the studied SPA.
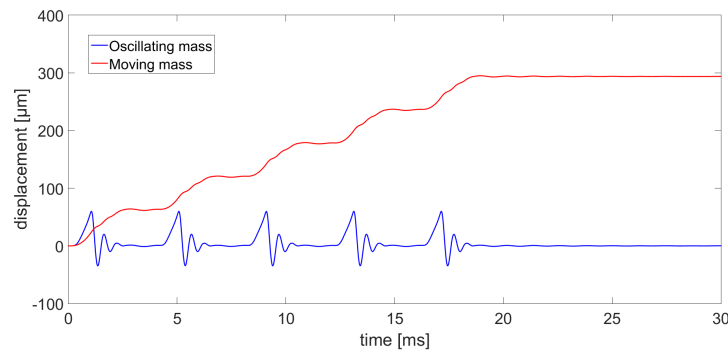
Figure 3.3 – Coarse expected performances from Lumped model. Output data are used as input in mechanical design (Fig.3.2-Step I→Step II). Chosen actuator is APA60S, OM = 10gr, MM = 40gr, actuation frequency is 1kHz, normal force is 5N. Obtained mean speed is 15mm/s.

3.1.1.2 Conception

ii - Oscillating Mass — Two constraints drive the design of the OM. First, to see through one of the friction parts, an observation window must be machined at the location of the contact. Second, in order to prevent the deformation of the actuator shell due to the wear of the proof bodies, a compliant stiffness - by means of a flexure hinge - is anticipated.

In order to see through one of the friction parts, the normal force is not applied at the vertical of the contact. Thus, it let access for an observation window. Length of the OM is set arbitrarily to 60mm for implementing the preload and visualisation functions while limiting its mass.

The design of the flexure hinge is then calculated from Henein (2001). It consists in 1- minimising the stiffness of the hinge in order to limit the impact of wear on normal force variation and 2- maximising the stiffness in actuation direction to limit elastic deformations (Breguet, 1998). Elementary links are favoured since they are easier to manufacture. Circular notch hinge is chosen among blade and wire hinge geometries since it better complies with the above-mentioned restrictions of stiffness (Fig. 3.4).

First element of conception aims to ensure that the variation of the circular notch radius be smooth enough to limit stress concentration (Pomey and Lieurade, 1982). To do so, condition of Eq.3.1 must be respected.

$$\frac{r}{e} > 5 \tag{3.1}$$

where r is the radius of the circular notch and e is the thickness (depicted in Fig.3.4).
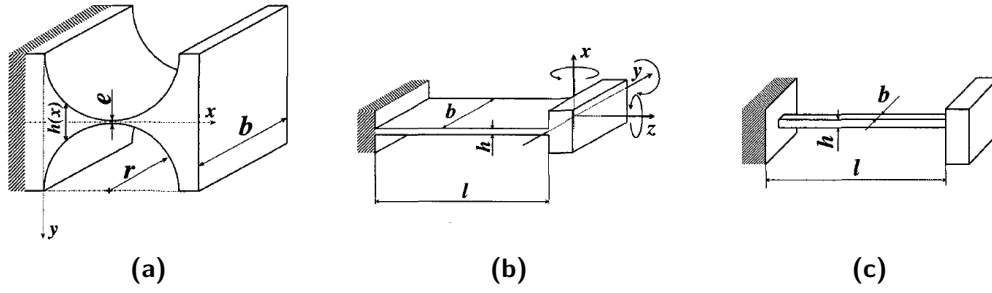
Figure 3.4 – Flexure hinge geometries (From Henein, 2001): (a) neck; (b) blade; (c) wire.

Second element of conception aims to size the allowable stress σ_{lim} [MPa]. Eq.3.2 is used to achieve this purpose. In addition, in order to prevent the rupture, due to simplifying assumptions, a safety coefficient S of 2 is applied.

$$M_{lim} = \frac{be^2 \frac{\sigma_{lim}}{S}}{6} \qquad (3.2)$$

where b [m] and e [m] are the width and the thickness of the notch respectively, σ_{lim} corresponds to the stress limit in fatigue relative to the employed material and the applied limit bending moment M_{lim} [N/m]. Here, material for the OM has been chosen to be Ti-6Al-4V for its high Re0.2 (> to that of steel and aluminium) and for its relatively low density ($d_{Alumina} < d_{Ti-6Al-4V} < d_{steel}$). Stress limit, σ_{lim}<240MPa, is sized based on Ti-6Al-4V Whöler curve.

From the previous equations, purpose is to determine the dimensions of the hinge - e, r, b - from a maximum angle - due to wear of the proof bodies. Length of the OM has been set to 45mm in order to minimise its mass while making it possible to both apply the normal force and let enough space to see through the friction contact. Anticipated maximum wear height is arbitrarily estimated to 100μm. Relative α is 0.13°. Bending stiffness, $K_{\alpha M}$, has been formulated through an analytic approach (Eq.3.3).

$$K_{\alpha M} = \frac{2Ebe^{2.5}}{9\pi\sqrt{r}} \qquad (3.3)$$

Angular stroke, α_{lim}, comes from previous equations (Eq.3.4).

$$\begin{aligned} \alpha_{lim} &= \frac{M_{lim}}{K_{\alpha M}} \\ &= \frac{3\pi\frac{\sigma_{lim}}{S}\sqrt{r}}{4E\sqrt{e}} \\ &\simeq 5.9 \ 10^{-2}\frac{\sqrt{r}}{\sqrt{e}}[°] \end{aligned} \qquad (3.4)$$

By setting r = 10e (compliant with Eq.3.1), α_{lim}=0.19°(compliant with Eq.3.2). So (r,e) ratio is kept thereafter.

Then, stiffness in tension-compression, K_{T-C}, has to be calculated to ensure global stiffness in actuation direction is not too low. This would lead to drastically decrease performances. Eq.3.5 is used to achieve this purpose.

$$\begin{aligned} K_{T-C} &\simeq 0.353\frac{Eb\sqrt{e}}{\sqrt{r}} \\ &\simeq 1.3 \ 10^7 \ [N/m] \end{aligned} \qquad (3.5)$$

With E the Young modulus ($E_{Ti-6Al-4V}$=1.1 10^9 N/m^2), b=10mm (sized below with respect to contact pressure), and r=10e. Obtained stiffness is higher than that of APA60S (1.8 10^6N/m) so equivalent stiffness in actuation direction[2] - 1.5 10^6 N/m - is not decreased too much by adding the hinge.

However, care must be taken about this result since it is calculated with a traction-compression force applied along the centroid axis of the hinge. In the tribometer case, tangential force imposed by the friction contact is not aligned with the APA® thrust axis (Fig.3.1-b). Created momentum results in decreasing stiffness in actuation direction. By means of Finite Element Modelling, corrected stiffness of 3.7 10^6 N/m is assessed (Fig.3.5). This value remains higher than stiffness of APA60S, leading to 1.2 10^6N/m a equivalent stiffness. Notice that this approach is sufficient in a static approach but reach limits in dynamic approach. This point will be considered from a dynamic point of view in chapter 5.
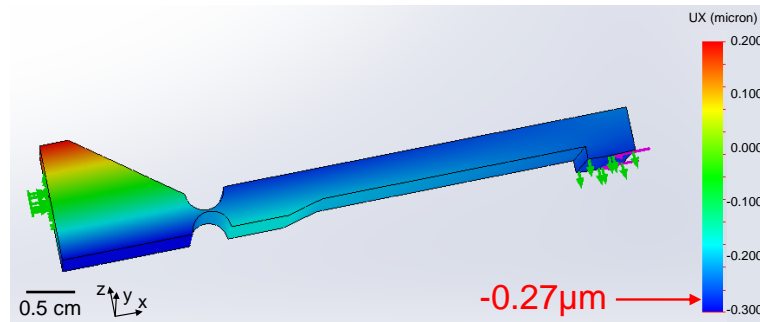
Figure 3.5 – Actuation stiffness of the circular notch hinge determined by means of FEM, taking into account both the traction-compression force and the bending moment due to a 1N-tangential force applied at the location of the friction contact. Resulting corrected stiffness is 3.7 10^6 N/m ($\simeq 1.3\ 10^7$N/m by taking into account only the traction compression force). Boundary conditions are: 1- full boundary conditions where the OM is screwed to the actuator (green arrows on the left hand side), 2-plan contact onto the cylinder friction pin (green arrows on the right hand side).

Finally giving a value for e and r remains. Machining process is planned to be Electro Discharge Machining (EDM). In EDM, the wire can only be guided above and below the workpiece. Thus, the thicker the part is the greater the length of the free wire are. So the forces produced by the process of EDM can deform the wire. Finally e is chosen to be 200μm (so r = 2mm) since it is quite easy to manufacture. Resulting mass is 12gr (OM + friction pin), what remains compliant with requirements specification.

iii & iv - Moving Mass & Guidance — Contrary to the studied SPA, with its sliding shaft-clamp kinematic configuration, the pin-on-pad contact has to be completed with a guidance. An air guidance is used here to decrease losses by parasitic friction (Fig.3.6-a).

The angle of the dovetail - α (Fig.3.7) - is calculated so the MM be vertically balanced (Eq.3.6).

$$\begin{aligned} 2 \times Fcos(\alpha) + F_0 &= F \\ \Rightarrow \alpha &= 65° \end{aligned} \tag{3.6}$$

With F_0 is the force due to the normal force + MM weight and F is the force generated by the air bearings (Fig.3.6-b).

---

[2]Formula for calculating equivalent stiffness of several springs in series is $\frac{1}{k_{eq}} = \sum_i \frac{1}{k_i}$

3
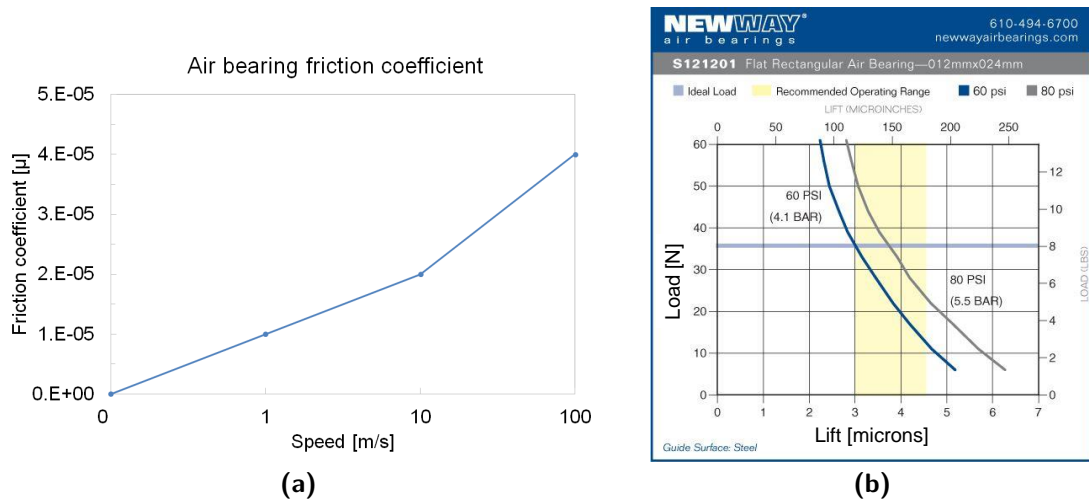
Figure 3.6 – Air bearing characteristics (From NewWay website, Last update: 2012). (a) Coefficient of friction relative to the speed of the guided payload. (b) Load curve.
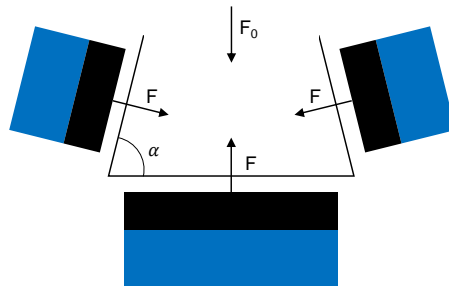
Figure 3.7 – Sizing of the dovetail angle formed by air bearings. F_0 depends of the applied normal force (5N here). F is the thrust force generated by the air bearings (30N here, from Fig.3.6-b).

In addition, to prevent the air flux coming from the air bearing blew the wear particles generated by the friction contact, an edge is designed on the MM. Finally, MM is drilled along the actuation direction to reduce its weight. Final mass is 36gr (MM + friction pad).

Care must be taken about further improvements in term of lifetime. Since there is no contact between air bearings and MM, the wear of the bearing, which would be expected with classical rolling bearing due to Brinelling for instance (Upadhyay et al., 2013), is not considered here.

v - Normal load — As in SPA, normal load is not applied with a deadload but with a spring. Chosen stiffness have to be high enough to compensate the bending of the flexure hinge in case of wear but low enough to drive the normal load function. Vertical stiffness of the oscillating mass at the contact location is 1.0kN/m. To make the integration easy, preload function is ensured by a spring enclosed in a screw. Among the available commercialized parts, chosen stiffness is 2.4kN/m to be compliant with above criteria.

3.1.1.3 Expected performances

Now the design is ended, final expected performances can be obtained with the lumped Model. Fig.3.3 is updated with final parameters. Expected $\overline{v}$ is 20mm/s,

which is consistent with requirements specification (Fig.3.8).
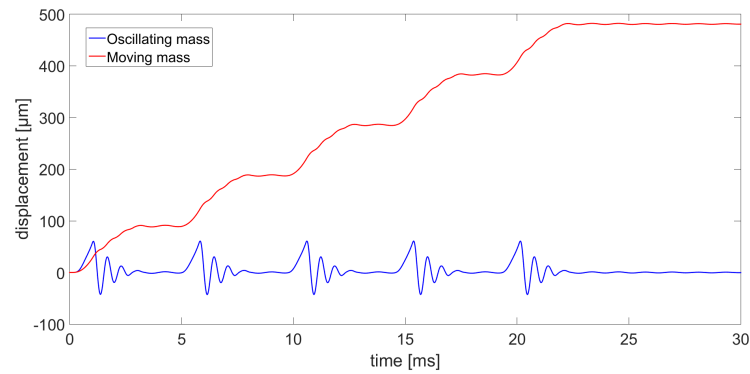
Figure 3.8 – Final expected performances from Lumped model once design is ended (Fig.3.2-Step II→Step III). Chosen actuator is APA60S, OM = 12gr, MM = 36gr, actuation frequency is 1kHz, Normal force is 5N. Obtained mean speed is 20mm/s.

3.1.1.4   Experimental validation of the tribometer sizing

Once the tribometer is integrated, numerical results are finally compared to numerical ones to validate the sizing.

Dynamic behaviour —   Its dynamic behaviour is assessed by means of an admittance measurement[3], considering this piezoelectric system as an equivalent electrical circuit (Eq.1.9). Admittance is measured with an impedance analyser (Fig.3.9).
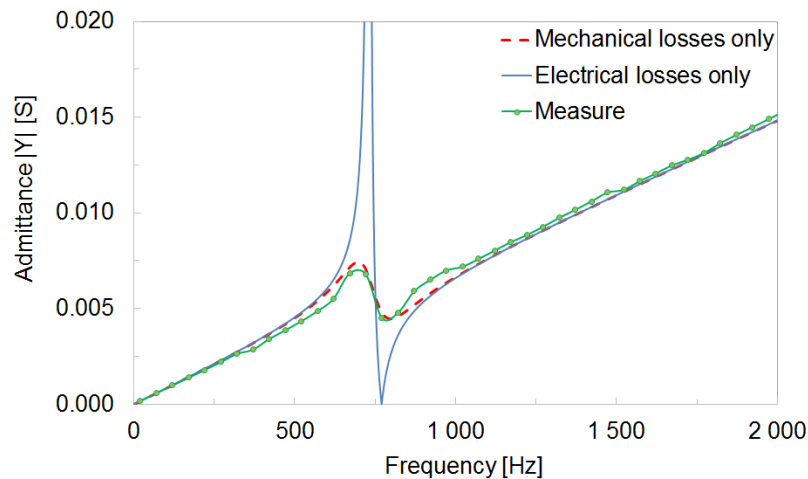
Figure 3.9 – SPA mechanism admittance analysis.

Comparison between this electrical measure and the mechanical values is enabled by the ratio introduced in Table 1.10 (Table 3.1). At low level of excitation, one presumes that no friction occurs and so the L_m value takes into account both the OM and MM mass values, which is in good agreement with measure. In addition with its elasticity in actuation direction, estimations of f_r and f_a exhibit a good correlation with the measure.

---

[3]A sinusoidal voltage with constant amplitude is applied at the terminals of the piezoelectric ceramic. Current response is measured and so admittance is displayed and compared to analytical approach with data stemming from previous sizing.

Table 3.1 – Tribometer dynamic behaviour. Comparison between admittance measurement and mechanical values sized in design phase by means of an electro-mechanical analogy.

		Translation mode	
		modelling	measure
f_r	[Hz]	731	696
f_a	[Hz]	770	771
C_0	[μF]	1.20	
C_m	[μF]	0.13	
L_m	[H]	0.36	

Speed performances — Step size and so speed performances are then measured. This exhibits two differences in front of what was expected with the lumped model predictions (Fig.3.10).

First, an asymmetry, which is more important than that on classical SPA, is observed. The cause of this asymmetry is presumed to be attributed to the distance between the tangential force imposed by the friction contact and the APA® thrust axis. This results in a momentum which would result, as a chalk on a white board, in a different behaviour depending on the friction direction. This assumption has not been investigated any further. But, it is taken into account in the further designs by reducing this distance (Chapter 7). Resulting mean speed is around 21 mm/s, what remains consistent with the previous sizing.

Second, a 370Hz-resonance mode appears during the free oscillation phase. Neither this low-frequency resonance mode appear in the lumped modelling nor in the admittance measure. So this resonance mode is purely mechanical and due to a parasitic vibration in an other direction than that of actuation. This resonance mode is due to the bending of the notch as it will be seen in chapter 5.
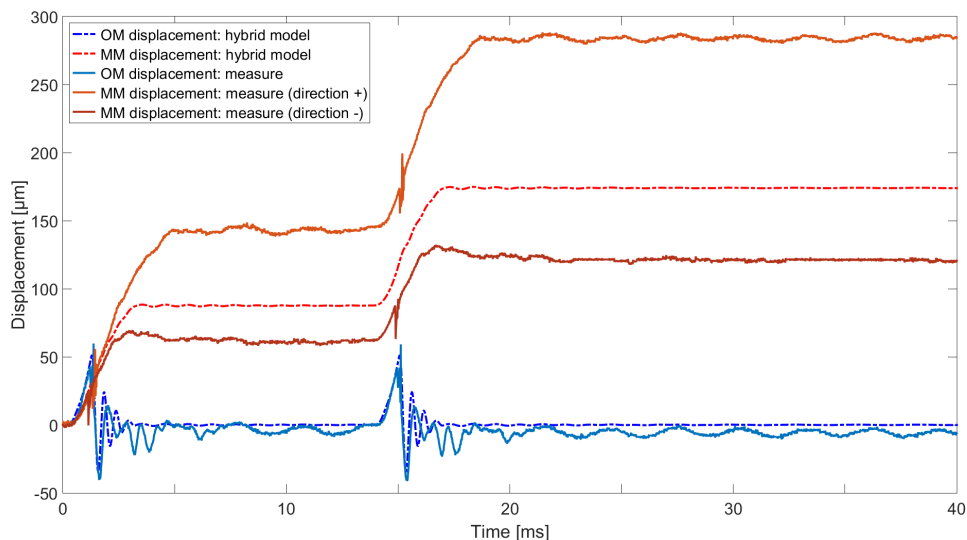
Figure 3.10 – Tribometer displacement performances assessment. Measures of back and forth motion are plotted in absolute value to be compared to lumped analytical modelling before tests.

Mounting conditions — Mounting conditions such as screwing or gluing also may play a role on the experimental validation of the tribometer operation: during assembly, oscillation mass is screwed to the APA®. As a consequence, a torque is applied at the

contact location. To minimize it, pin and pad are glued, to OM and MM respectively, under preload. By this way, glue layer is expected to accommodate the torque.

3.1.2 Instrumentation

After introducing the tribometer design, instrumentation is depicted on Fig.3.11. Details are presented below.
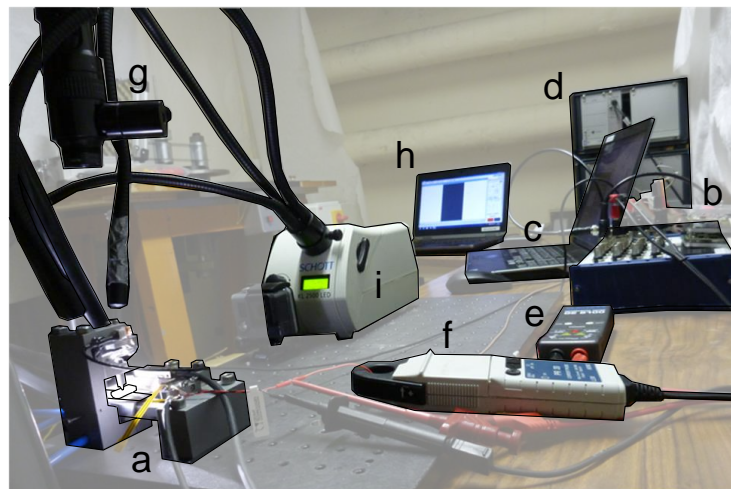
Figure 3.11 – Global SPA-tribometer setup. (a) Tribometer setup. (b) National Instrument NI USB-6259 BNC acquisition and generation board. (c) Labview computer manage signals and post-treatment. (d) LA75C Cedrat Technologies power supply and SG75 strain gauge controller. (e,f) Voltage and current probes to get input electrical energy. (g) High speed camera (V710 Vision Research and Navitar6000 optical zoom) or camera. (h) High speed camera computer. (i) Additional light for high speed camera provided by a Schott KL 2500 LED.

3.1.2.1 Measurements

Measurements as well as actuation signal generation are managed by LabView.

Displacement sensors — In a first approach, tribological tests are considered in no-load conditions to focus on tribological solicitations. Thus, transition between back and forth is ensured by the MM position when it outreaches a programmed stop detected by displacement sensor. In addition, oscillatory motion generated by the piezoelectric actuator is get from a strain gauge.

Friction coefficient — Although a friction coefficient is not inherent to a material couple, as highlighted in section 3, it can be seen as inherent to a given tribological triplet. Thus, it remains a data "easily" measurable which can be linked, with caution, to the contact's life evolution characterized qualitatively. It is classically obtained by dividing the normal force to the tangential force.
Normal force measurement: A 7075 aluminium-proof body has been designed to measure the reaction of normal force applied to the OM. When the normal force is applied, deformation of $700\mu\epsilon$ is expected. For a 7.3N-force[4], this generates a stress of 64MPa in the test body (Fig.3.12-a) and a displacement of 74μm (Fig.3.12-b). The latter stress

---

[4]Due to the necessity of seeing through the contact, a 7.3N normal force is generated to compensate the level arm and to obtain a 5N preload force at the contact location.

value is well below the Wöhler curve of 7075 aluminum (150MPa), thus the lifetime of the test body is theoretically infinite.
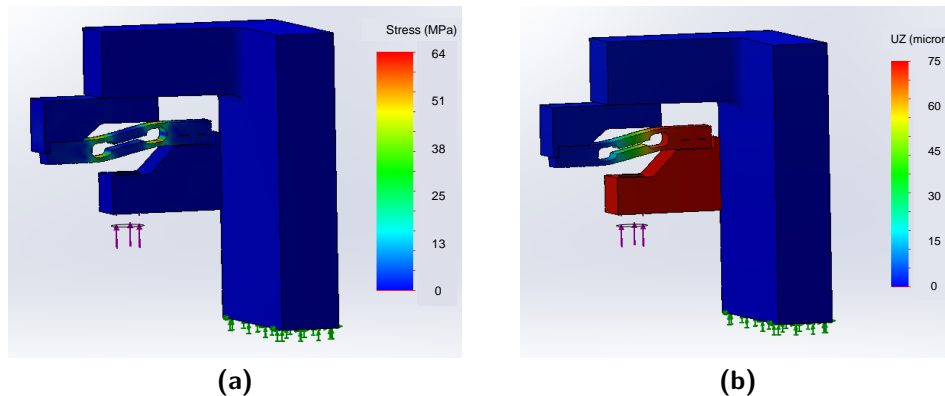
Figure 3.12 – Normal force proof body sizing for measuring the normal force with a strain gauge. Applied normal force is 7.3N to compensate lever arm and impose a 5N-normal force to preload the contact. Resulting (a) stress and (b) displacement are respectively 63MPa, and 74μm. Boundary conditions are 1- full boundary conditions where the support part is screwed onto the casing of the tribometer (on the right hand side), 2- global contact between the different parts bound by screws (on the left hand side).

Tangential force measurement: As highlighted by Hunstig et al. (2013), deriving displacement and speed from position sensor results in a very noise tangential force response. So an accelerometer is implemented to measure directly the acceleration of the moving mass. Tangential force is obtained as soon as a relative displacement occurs in slip phase since friction is the only external force applied (Eq.1.12).

Friction coefficient: Resulting estimation of friction coefficient is obtained in a discrete way[5] (Fig.3.13). Notice that the studied couple of material does not appear in literature so direct comparison about friction coefficient is not possible. However, resulting value - 0.4 at the beginning of the test - is consistent with Qu et al. (2005) results. They measured a value of 0.28 against PTFE, which is known for its low friction coefficient (Jia et al., 2007). In addition, friction coefficient will be considered in front of morphological observations with Scanning Electron Microscopy (SEM) in chapter 4.
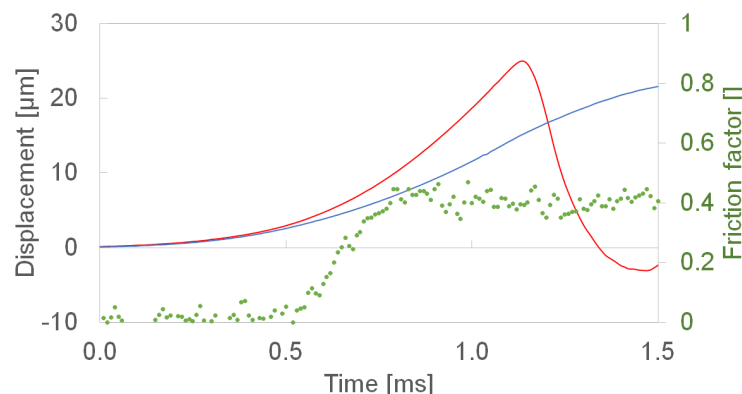
Figure 3.13 – Tangential force measured from the accelerometer on the MM. As soon as relative displacement occurs between OM and MM, acceleration of the MM is considered as constant. Friction coefficient is then obtained by dividing by normal force.

---

[5]Automating the evaluation of friction coefficient - *e.g.* in term of relative velocity - has not been investigated. Post-processing remains necessary to get friction coefficient at a given operating cycle.

3.1.2.2 Direct *in-situ* observations

Direct in-situ observations during operation make it possible to get initiation and evolution of solid particle flows inside the contact. These flows are then (i) linked to measured data and (ii) compared with *post-mortem* observations.

To achieve such a purpose, an observation window has been machined in the OM. Then, intermediate tests with transparent glass pins, filmed with high speed camera or with camera, are proposed. They rubs against coated Ti-6Al-4V or fibreglass filled polymer to assess the flows related to each of these materials.

Impact of this observation window has been assessed by means of an FEM simulation on Abaqus. Cases with and without window are represented on Fig.3.14. When there is no observation window, contact pressure is around 7.5MPa along the contact line. Value is consistent with mean/max Hertz contact pressure: 6.9/8.8MPa (Table.3.2). On the contrary, with the observation window, maximum contact pressure is located on the edges and increases to 9.0MPa. So, as it has not been done here, it would be interesting to carry out test with an OM without observation window.

3
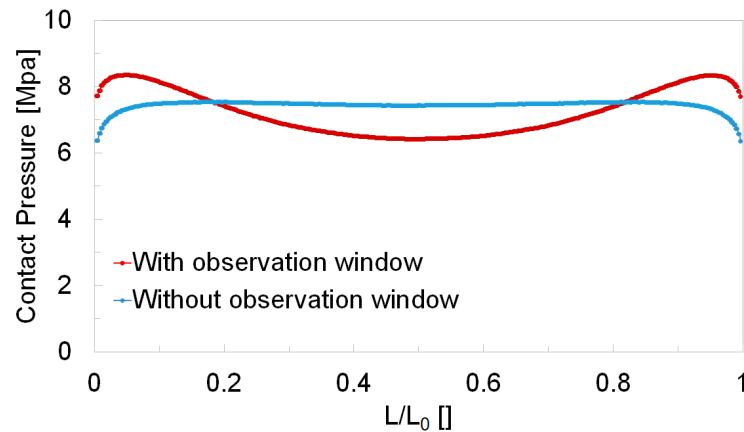
Figure 3.14 – Contact pressure profile: With observation window on red curve. Max contact pressure is concentrated on the edges: 9.0MPa. Without observation window on blue curve. Max contact pressure is constant all along the contact line: 7.5MPa. $L_0 = 10$mm.

Table 3.2 – Material properties and contact conditions.

Materials	Young's modulus [GPa]	Poisson ratio
Fiberglass composite	14	0.39
Ti-6Al-4V	114	0.33
B270 glass	72	0.22
Kinematics	**Stick-slip**	
Actuation period [ms]	1.25	
Delay period [ms]	3.75	
Amplitude [μm]	100 (+/− 40)	
Total stroke [mm]	+/− 45	
Mean speed [mm/s]	18	
Contact conditions		
Geometry [mm x mm]	R30x10-cylinder pin on flat pad	
Contact width [μm]	70	
Mean/Max Hertz pressure [MPa]	6.9/8.8	

3

Tribometer _vs._ SPA: representativity issue — Tribometer kinematic - actu-ator, step size, actuation signal, elastic preload - is finally similar to that of a SPA. Likewise, used materials as well as machining processes are identical. Contact pressure and contact size are also set to be equivalent. This leads to be confident about the representativity potential in comparison with SPA. However, there is no reference for a comparison with existing data in term of tribological solicitations: a tribometer remains representative of itself. Time missed to make the comparison with existing SPA, what constitutes a relevant perspective. Thus, this tribometer will be rather used for future motors design as a sizing tool from a tribological point of view. Indeed, the 3rd body approach introduced in the next section will be identically transposable to any future material or environmental testing[6].

Now that the experimental setup has been presented (synthesis in Table 3.2), a point of methodology is introduced below (section 3.2). The resulting framework leads to the experimental procedure used in the rest of this tribological work (section 3.3). Such a procedure may be used no matter the considered tribological system. The general purpose of this attempt is to get closer to a systematic analysis, less dependent on the observer.

3.2   Analysis framework: 3rd body formalism

Reynolds theory, formulated from fluid mechanic equations makes it possible, for given working conditions, to determine velocity profile and tangential/normal stresses in a thick lubricant film of lubricated contact (Dowson and Higginson, 1977). On the contrary, a general theory of dry friction with solid particles is not available for now because of multidisciplinary involved fields: thermal, mechanic, material science, physicochemical. Godet (1984); Berthier (1990, 2005) developed a phenomenological concept from experimental observations, which makes it possible to describe the be-haviour of dry contact. Concept is based on notions of _tribological triplet_ (section 3.2.1), _velocity accommodation mechanism_ and _tribological circuit_ (section 3.2.2). To get closer to a lubricated contact vocabulary, solid particle motions are treated in terms of flows and linked to mechanism contribution (Fig.3.15-a). It becomes possible to imagine that solid particles are not only destructive but can also be protective, as highlighted in (Singer et al., 2003; Wahl and Singer, 1996). Decrypting them will make it possible to understand why the fibreglass filled polymer / coated Ti-6Al-4V - friction couple "works" in SPA. Then, lessons learned will be used to propose improvements such as an increase of the lifetime while limiting the number of tested friction materials.

3.2.1   Tribological triplet

The elements of the tribological triplet (Fig.3.15) are (i) the mechanism (SPA-tribometer) in which the contact is located (section 3.2.1.1), (ii) the first bodies - mass bordering: cylinder pin and flat pad - (section 3.2.1.2), and (iii) the 3rd body which consists in two screens and a central volume (section 3.2.1.3). The notions of tribological circuits and relative speed accommodation will be then detailed in section 3.2.2.

3.2.1.1   Mechanism

The tribometer mechanism has been described in section 3.1.

---

[6]Notice that air bearing will be changed for rolling bearing to consider vacuum tests.
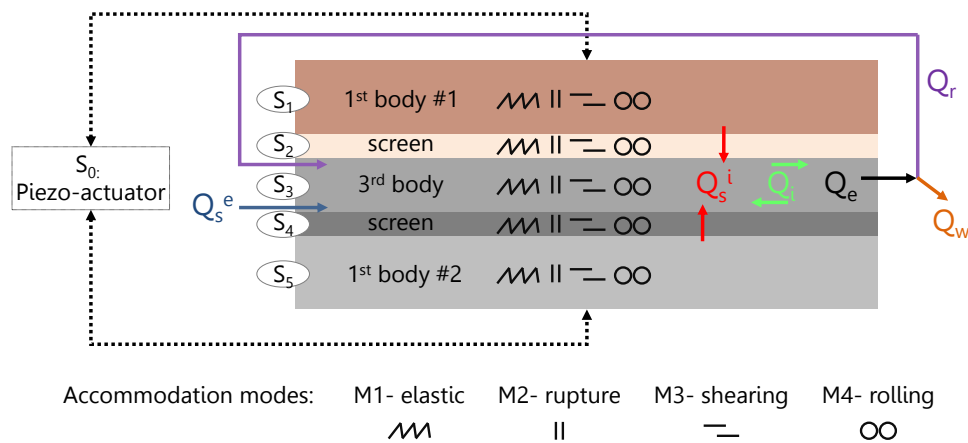
Figure 3.15 – 3rd body formalism. The tribological triplet is composed of a mechanism, its friction parts and the 3rd body particles. The resulting tribological circuit is characterized by (i) solid particle flows: Q_s^i: internal source flow, Q_s^e: external source flow, Q_i: internal flow, Q_e: external flow, Q_r: recirculation flow, Q_w: wear flow and (ii) velocity accommodation mechanisms decomposed in: location sites S_i and accommodation modes M_j.

3.2.1.2 First bodies

As presented in chapter 2, the studied material couple is coated Ti-6Al-4V / non-disclosed fiberglass filled composite. It is inherited from (Six, 2000) for ultrasonic motor and re-used successfully by Belly (Belly, 2011) in SPA.

Coated Ti-6Al-4V — Ti-6Al-4V parts are milled. Then Ti-6Al-4V is coated (Fig.3.16-a). Resulting surface morphology is schematized on Fig.3.16-c from SEM observations (Fig.3.16-b). Ti-6Al-4V is used because of both its biocompatibility properties (Rihova et al., 2012) and MRI compatibility (Belly et al., 2010) making possible to address medical application fields. Due to its cold welding propensity (Merstallinger and Sales, 2011), Ti-6Al-4V substrate is coated (Baumann and Zander, 2005). Coating is obtained by an anodizing process with chemical bath and subsequent thickness is around 5μm. On the high-zoom topography view, a 40-60μm-periodic pattern appears. Actually, coating layer is not homogeneous but composed of clusters whose size is around 4μm. In addition, coating does not cover entirely the substrate, which is confirmed by an EDX analysis. Some cracks due to machining are visible at the substrate surface[7].

fibreglass filled polymer — Composite parts are also milled (Fig.3.17-a). SEM observations (Fig.3.17-b) have highlighted an anisotropic distribution of fibreglass (schematized on Fig.3.17-c). The original length of glass fibres is 250-300 μm and their diameter is between 10 to 12 μm. But, some horizontal fibres appear to be pounded, due to machining process, what reduce their length to a few dozen of μm. The polymer matrix surface aspect is typical of a machining by milling: a periodic pattern appears with some chips[8].

---

[7]Interest in coating Ti-6Al-4V samples is discussed in Appendix B. Resulting speed performances are less stable than with coating. So, coating process is systematically planned in the manufacturing of the Ti-6Al-4V samples.

[8]Notice that EDX analysis is intentionally not disclosed.

3
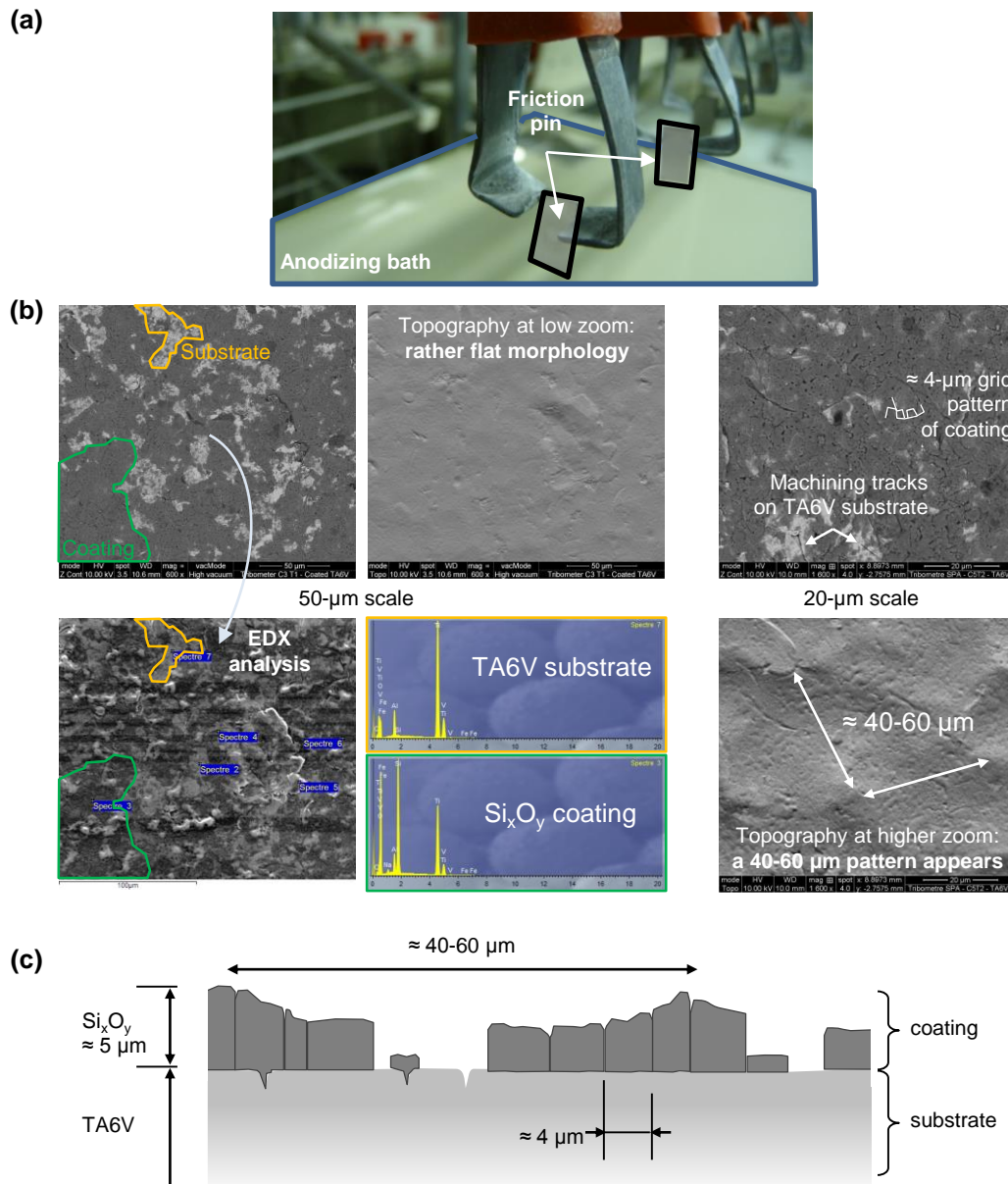
Figure 3.16 – First body #1: Si_xO_y coated Ti-6Al-4V (Baumann and Zander, 2005). (a) Photo of Ti-6Al-4V pins during before coating process (courtesy of the company responsible for the coating). (b) Resulting surface morphology observed by means of Scanning Electron Microscopy and (c) related scheme.
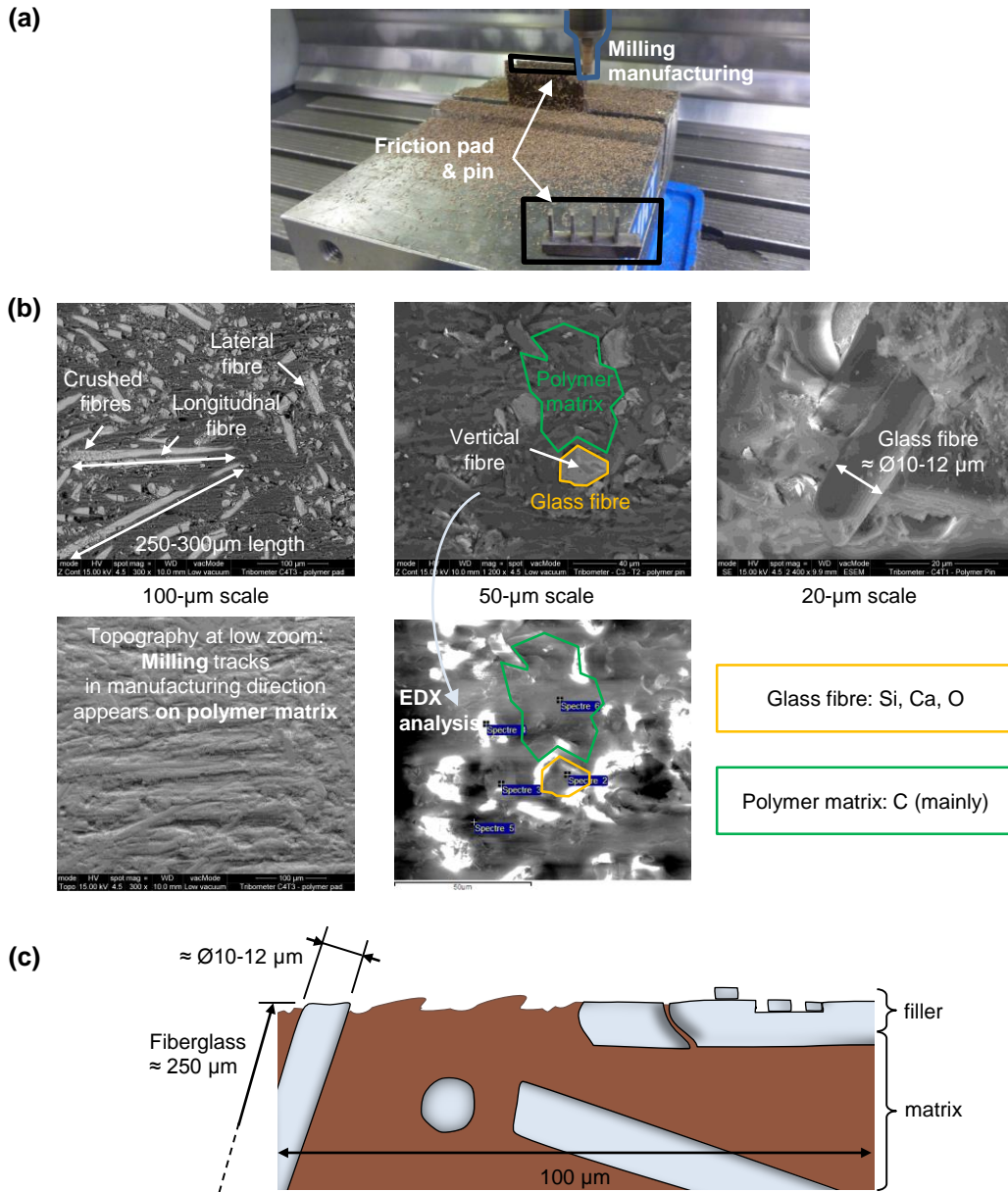
Figure 3.17 – First body #2: Fiberglass filled composite. (a) Parts are machined by milling. (b) Resulting surface morphology observed by means of Scanning Electron Microscopy and (c) related scheme.

If some studies have been led on Ti-6Al-4V tribological properties (Qu et al., 2005; Fouvry et al., 2004; Kloss and Wäsche, 2009), there is not heritage in SPA configuration to the author's knowledge, in particular against this fiberglass filled composite. One could expect that the difference of hardness between both materials would lead to wear of composite (Fig.3.18). So a transfer of composite on metal could be expected either by abrasive, adhesive, fatigue or a combination of these wear mechanisms (Rouchon, 1996). However, due to the presence of glass fibres into the composite, expectations may be reversed. In addition, as few information are available about the coating, it is difficult to foresee how first bodies will wear.
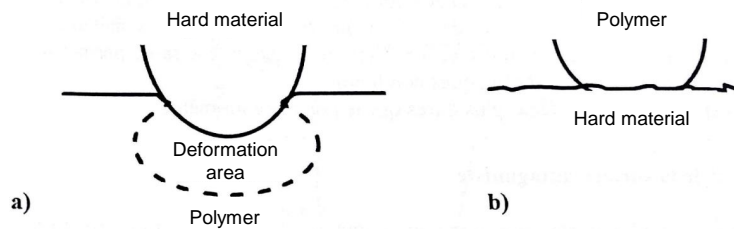
Figure 3.18 – Wear mechanisms of polymer (Translated from Rouchon, 1996).

Contact features — The contact in real motors is a composite-metal cylinder-on-flat geometry (Fig.3.19). So it was retained on the test bench[9]. Cylinder pin dimensions are 5mm x 10mm with a radius of 30mm. Flat pad dimensions are 45mm x 10mm. Roughness are Ra0.2μm and Ra0.5μm for composite and metal counterpart surfaces respectively (Belly, 2011). From the material properties in Table.3.2 and preload value, contact pressure and width are about 8MPa and 70μm respectively (Hertz, 1882), as in real motors.
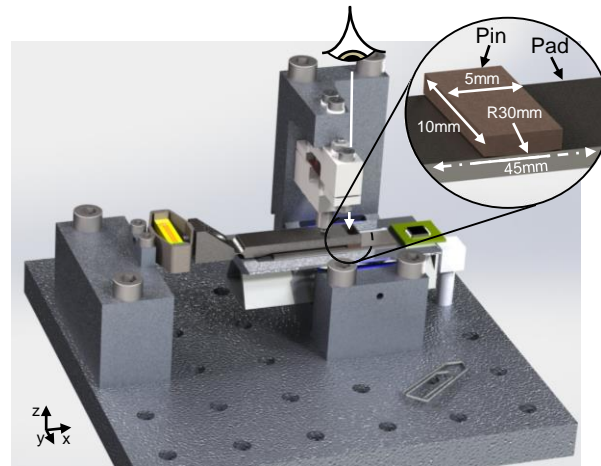
Figure 3.19 – Contact features illustration. Friction pin dimensions are 5x10mm^2 with a 30mm-radius cylinder geometry. Friction pad is flat.

It is easier to manufacture large metal parts with precise tolerance. So, initial pin is in fiberglass filled composite material and pad is in Ti-6Al-4V. However, it seemed interesting here to test both orientations so reciprocal counterparts were manufactured. Mainly composed of silica, as coating on Ti-6Al-4V (Baumann and Zander, 2005) and glass fibres into the composite material, glass material was chosen for being the transparent pins.

---

[9]As the cylinder-on-flat contact is hyperstatic, an additional test with a spherical pin was performed (Appendix A). However, the decrease of transverse stiffness led to unstable and lower performances. Cylinder-on-flat contact geometry turned out to be finally the best trade-off.

3.2.1.3 Flows: first bodies - third body interactions

When relative motion begins, 1st bodies are subjected to velocity gradients. Therefore contacts are subjected to material flows. Wear will be discussed in terms of the 3rd body flows (Fig.3.15-a):

- Q_s^i - internal source flow: characterizes the origin of 3rd body inside the contact. It is obtained by detachment of particles from the degradation of the 1st bodies which are cylinder pin and flat pad;

- Q_s^e - external source flow: is obtained by artificial external supply. Particles constituting this flow can come from different origins: particle detachments from other parts of the mechanism, particles from environment;

- Q_i - internal flow: characterizes the movement of the 3rd body in the contact;

- Q_e - external flow: characterizes particles ejected from the contact. This flow is divided into two subflows: Q_r and Q_w;

- Q_r - recirculation flow: corresponds to the flow of particles reintroduced into the contact after ejection;

- Q_w - wear flow: is composed of particles that will never be reintroduced into the contact after ejection.

All the information gathered during tests and post-mortem analysis of the counterparts make it possible to reconstruct contact life scenario. So, 3rd body flow vocabulary links local wear mechanisms at a contact observation scale to the macroscopic displacements, velocities and loads of the bench. The flow abbreviations (Q_i^j) will be used in the next sections.

3.2.2 Tribological circuit: accommodation mechanisms

In addition with flows, proposed methodology aims at qualifying contact life through accommodation sites and modes (Fig.3.15-b). Once gathered, all these information provide the tribological circuit. Accommodation sites are the locations into the contact where the relative velocity between both 1st bodies is accommodated (Berthier, 1990). Modes, such as rolling (Berthier, 2005, 1988), or shearing (Descartes and Berthier, 2002; Singer et al., 2002; Berthier, 1990, 2005) specify the manner in which the velocity is accommodated. Initially, there is no relative displacement. S_3 site is not yet present. S_2 site is preloaded against S_4 site. Once test starts, tangential forces appear. They induce an additional stress field, superimposed on the one induced by the mechanism. Then damages occur and accumulate, adding new stress fields to previous ones. Each site caters specifically to the stress field by transformations that change more or less mechanical characteristics (e.g. friction coefficient). Schematically, the transformations can either be cracking or surface tribological transformations. They can lead to detachment of particles creating the S_3 site.

Accommodation sites — Six sites S_i make it possible to get a complete decryption of the contact life:

- Site S_0 - the mechanism,

- Sites S_1 and S_5 - bulk of 1st bodies,

- Sites S_2 and S_4 - screens,

- Site S_3 - 3rd body. S_2, S_3, and S_4 sites do not necessarily exist at the same time.

Accommodation modes — In addition with sites, four accommodation modes, noted M_j, help to characterize a contact:

- Mode M_1 - elastic deformation: corresponds to a reversible mechanism. All solids deform elastically and all deformations can account for some velocity accommodation.

- Mode M_2 - normal rupture: is non-reversible. It is not a velocity accommodation mechanism per se as a crack does not accommodate displacement or velocity alone but it allows for much greater deformation through other modes. A cracked block, for instance, will deform elastically very much more than an uncracked block.

- Mode M_3 - shearing: is also non-reversible.

- Mode M_4 - rolling: is also non-reversible. It corresponds to the formation of rolls during friction.

The combination of a site S_i and a mode M_j forms a velocity accommodative mechanism, denoted S_iM_j (Berthier, 1990). For instance, with this notation the hydrodynamic lubrication corresponds to S_3M_3 mechanism, indeed this accommodation takes place in the lubricant layer, site S_3 shear, M_3 mode. When one considers friction with 3rd body, several velocity accommodation mechanisms may occur simultaneously. Identification of S_iM_j makes it possible to link the wear mechanisms to the 3rd body flows and so to the mechanism motor feature. Synthesis is the tribological circuit. The S_iM_j are an expert tool applicable to any contact and generally a transfer tool between simulation and application.

3.3   Experimental procedure

With experience, each S_iM_j may be linked to a particular 3rd body morphology. To describe this morphology in the strictest way, observation protocol is exhibited (Fig.3.20). Thus, each contact is analysed systematically in the same way:

In step #1 (Fig.3.20-S1), before each test, as far as possible, geometry, roughness, surface morphology, and chemical composition - are realised with profilometry, microscopy, Scanning Electronic Microscopy (SEM) and Energy Dispersive X-ray (EDX) (Fig.3.20-S1.1,2). Comparison with post-mortem test provides an estimation of wear flow and framework for analysing the tribological solicitations (Fig.3.20-S3.1,2).

In step #2 (Fig.3.20-S2), measurements and *in-situ* observations make it possible to link macroscopic performance evolution - step size, speed and friction coefficient - to velocity accommodation mechanisms - rolling and shearing for instance - (Fig.3.20-S2.1). Accommodation by plastic flows may require more local post-mortem observations with SEM (Fig.3.20-S2.2). Significant *in-situ* observations- or sensor- events are considered as milestone in a summarized table.
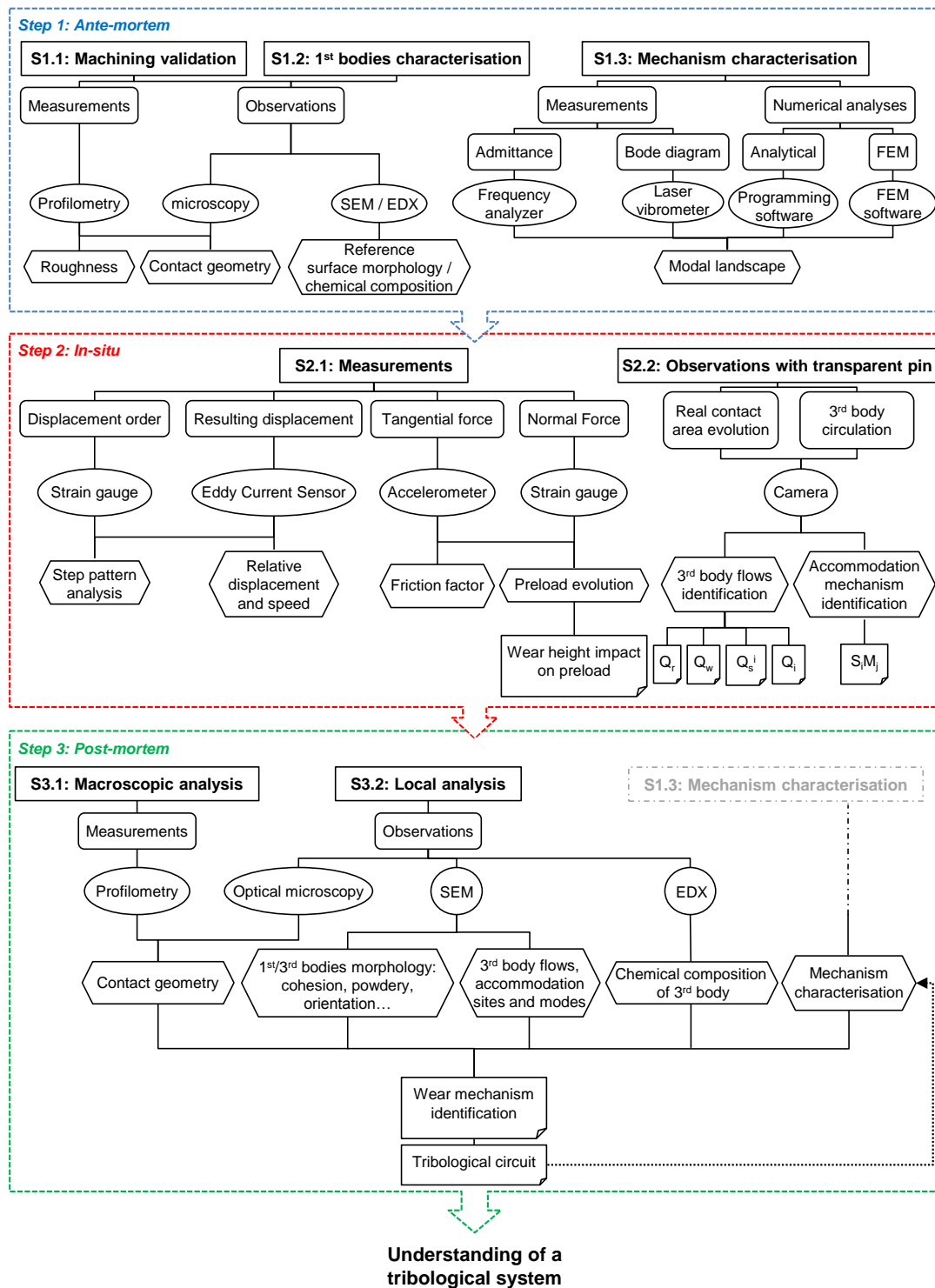
Figure 3.20 – Experimental procedure flow chart. Each step - dashline frame - is structured with substeps - rectangle -, performed in sequences - oblong -, with tools - ellipse -, leading to results - diamond -, and thus to conclusions post-it note.

In step #3 (Fig.3.20-S3), *post-mortem* observations (Fig.3.20-S3) deserve to be detailed:

- First *post-mortem* observations consists in identifying the observation scale, specific to each considered contact (Achanta et al., 2009; Stoyanov et al., 2012). Here, on one hand, step size and contact width are $100\mu m$ order of magnitude. On the other hand, coating height and glass fibre diameter is $10\mu m$ order of magnitude. Each counterpart is so analysed at a *macroscopic* scale, between $100\mu m$ and $500\mu m$. Then, progressive zoom, until $10\mu m$ or $5\mu m$, are performed around significant areas. Reference observations (*i.e. ante-mortem*) at both scales must be retained before test for further comparison (Fig.3.16-c and Fig.3.17-c).

- Second part of the analysis consists in defining what a significant area is. To do so, each contact will be divided in three main areas: mean contact area, frontiers, and out of frontier. In each of these three areas, purpose is to locate and to characterize significant spots.

- Then, spots are described in term of morphology: powdery, ductility, cohesion, compaction, porosity, density, adhesion (SEM), and chemical (EDX[10]) composition. 3rd body volume repartition, punctual presence and preferred orientations, if emerging, are also reported.

- At last, and this is may be the most challenging since it is subjected to interpretations. It consists in deducing where do reported particles come from and so in linking them to the dynamic behaviour of mechanism. 3rd body flows and velocity accommodation mechanism concepts are then used to formalize what occurs during these events and so to reconstruct the contact life in the form of tribological circuits all along the lifetime of the motor.

Material test procedure — Two sequences of material tests are realised:

- The first sequence is carried out with short-term tests to get the surface morphology of counterparts in the first 10^4 operating cycles[11] (20m equivalent sliding distance) in order to see the initiation of 3rd body flows.

- The second sequence is carried out with tests operating at least 10^6 operating cycles (2km equivalent sliding distance) - initial State-of-the-Art lifetime at the beginning of this work[12] - to get the surface morphology of counterparts after their nominal lifetime.

Each sequence is composed of two tests:

- With fibreglass filled polymer pin on coated Ti-6Al-4V pad (section 3.2.1.2);

- With coated Ti-6Al-4V pin on fibreglass filled polymer pad.

Additional tests are carried out with a transparent glass pin, for 10^4 cycles, alternatively on fibreglass filled polymer and coated Ti-6Al-4V pads, in order to see solid particle flows in first cycles (section 3.1.2.2).

Before considering the different test steps, material samples are systematically cleaned with tension active agents and then dried with clean compressed air.

---

[10]Due to technical problems, EDX analyses could not be achieved on each samples.

[11]A operating cycle is defined as a 2-mm back and forth motion.

[12]In Belly (2011), LSPA30μXS reach 10^6 cycles/2km equivalent sliding distance.

All these tests are realised in air at ambient temperature. They are not reproduced because of practical criteria: cost and time. However, as it will be shown in the next chapter, they are consistent with each other, what encourages interpretations but remains a scientific limit of the study and a relevant perspective.

Next chapter is based on the previously introduced setup, methodological framework and procedure. It presents the results of the tribological solicitation analysis of the SPA-tribometer.

3

4

Characterisation of tribological solicitations

The purpose of this chapter is to deal with tribological issues. At the contact scale, it consists in decrypting the tribological solicitations occurring in the SPA-tribometer. At the mechanism scale, it consists in interpreting friction coefficient evolution and wear generation. Both observation scales are bound by the solid particles flows at the contact interface. To characterize such flows, tests with original 1st bodies are completed by tests with transparent parts. In term of methodology, the Godet's 3rd body framework is adopted to ensure an objective and reproducible analysis all along the different tests. Beyond the need of decrypting the wear mechanism occurring in SPA, interest of such a study is to increase their lifetime while decreasing the wear flow Q_w without multiplying tests with numerous friction materials.

4.1 Contact's life decryption

As detailed in the experimental procedure (section 3.3), the first test sequence aims at characterizing the first 10^4 operating cycles, in terms of (i) 3rd body flows - with *in-situ* direct observations -, (ii) friction coefficient evolution - with monitoring - and (iii) accommodation sites/modes - with *post-mortem* SEM/EDX observations. The second test sequence aims at characterizing long-term operations by means of 10^6-cycles test with the help of first test sequence, monitoring and *post-mortem* observations.

4.1.1 1st test sequence: short-term tests with transparent glass pins

4.1.1.1 *In-situ* analyses of short-term tests with transparent glass pins

Tests with transparent pins are recorded by means of a camera. From the generated videos, significant pictures are extracted and compared to monitoring data (Fig.4.1). **S**hort-term **T**est on coated Ti-6Al-4V pad is firstly described [**ST1**] (Fig.4.1-b). Then, **S**hort-term **T**est on fibreglass filled polymer pad is described [**ST2**] (Fig.4.1-c). The next two paragraphs are intentionally descriptive. Indeed, interpretations - leading to wear mechanisms - will be proposed once the *in-situ* analysis is correlated with *post-mortem* observations. Notice that the following observations lead to use notions such
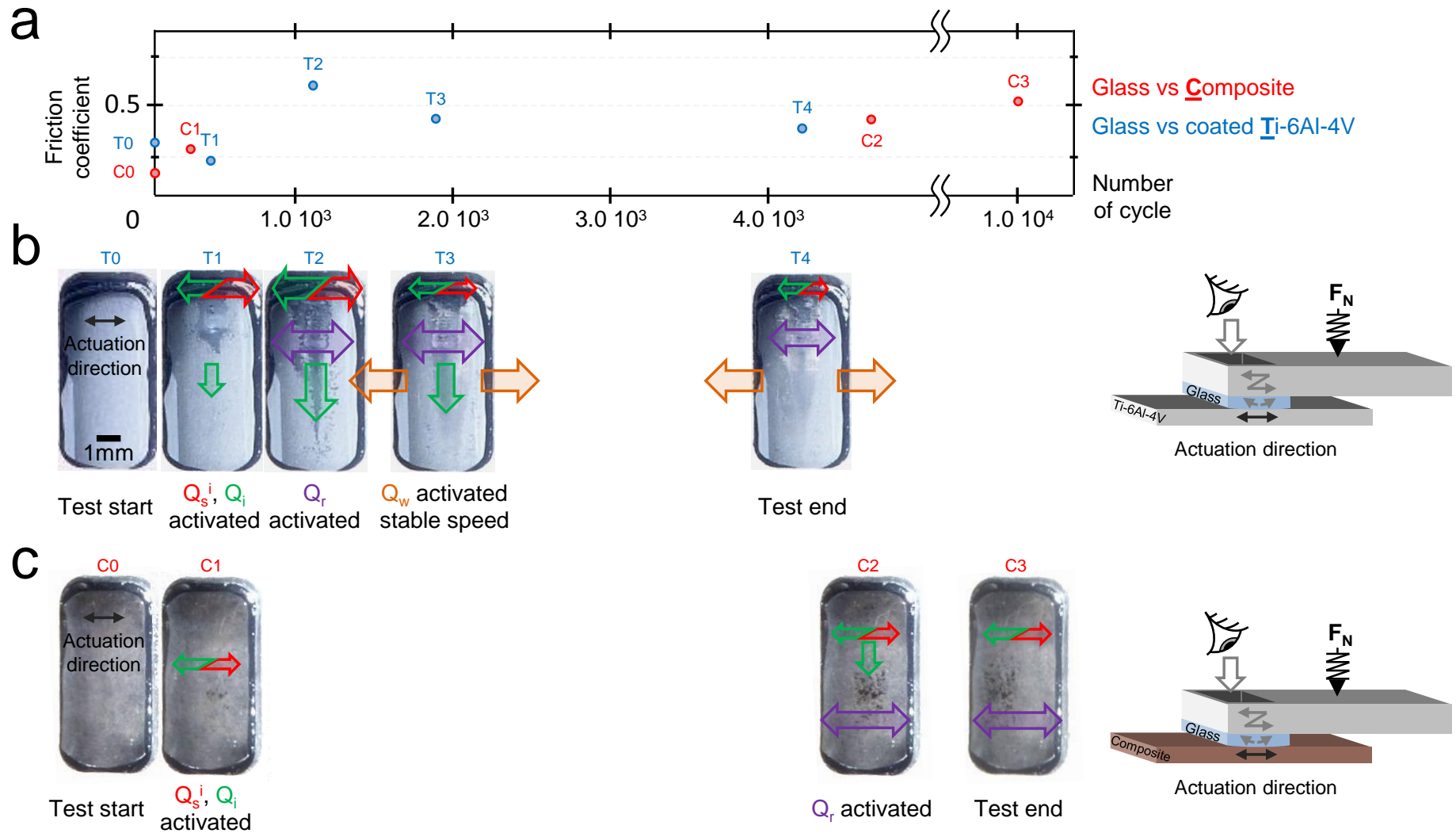
Figure 4.1 – Tribological timeline of the short-term tests with transparent pins. (a) Friction coefficient evolution extracted at significant *in-situ* direct observations. (b) Glass pin / coated Ti-6Al-4V pad contact. (c) Glass pin / fibreglass filled polymer pad contact. (b) and (c) are simultaneously plotted leading to their respective 3rd body flows. Arrow colours are the same as 3rd body flows colour code proposed in Fig.3.15. Size of the arrows represents a rough estimation of the relative 3rd body flow amplitude.

as "powdered". If these terms are used by "feeling", their relevance will be confirmed with SEM observations.

[**ST1: glass pin *vs.* coated Ti-6Al-4V pad**] From T0 to T1 (Fig.4.1-b), contact area materializes by dark particles at the top of observation window: Q_s^i is activated[1]. Until this step, friction coefficient remains quite low - around 0.2/0.3 -. Some particles move with the amplitude of step size ($\sim 100\mu$m) whereas some others move with the amplitude of total stroke (~ 1mm), both in actuation direction: Q_i is activated. Then, they move in a perpendicular direction - toward the less contact pressure area -. From T1 to T2, friction coefficient starts to increase from 0.2 to 0.6. Projections of powdered particles appear: Q_e is activated. These particles remains in the range of the cycle stroke (+/-1mm). So, although they are ejected from the contact, they are quickly re-introduced: Q_r is activated. Between T2 and T3, powdered particles agglomerate into clusters. As soon as cluster size overpasses a threshold, they crack and resulting particles are ejected again. Major part of these ejected particles are projected far away from the contact and are no more re-introduced: Q_w is activated. In the same time, friction coefficient decreases to around 0.4/0.5. Then, white areas appear. They are suspected to be Ti-6Al-4V substrate. From T3 to T4, some dark areas suddenly lighten and move in actuation direction, typical consequence of a shearing mode (Berthier, 1990). White areas are increasingly present. 3rd body flow activity decreases: particles circulate into the contact, are ejected, reintroduced, and ejected definitely. Simultaneously, friction coefficient stabilises around 0.4.

[**ST2: glass pin *vs.* composite pad**] From C0 to C1 (Fig.4.1-c), contact area materializes by shading in the centre of observation window: Q_s^i and Q_i are slowly initiated. Shade area is not homogeneous but seems to superimpose on milling tracks. Until C1, friction coefficient is quite low - around 0.1/0.2 -. From C1 to C2, size of the shaded area grows. The created 3rd body particles move in actuation direction, with the amplitude of the total stroke (~ 1mm): they move rather with the pad than with the pin. Therefore, particles, led by the pad, leave the contact and are re-introduced at each cycle: Q_r is activated. Friction coefficient slightly increases to around 0.3/0.4. From C3 to C4, shade area does not grow a lot but becomes more homogeneous. Friction coefficient continues to increase until 0.5. Globally, contrary to ST1, particle motion in other direction than that of actuation was not detected. Likewise, no Q_w was detected.

Once tests are ended, 1st bodies are separated to be analysed with a SEM. Thus, the disassembly and the transport of the samples have been realised with care and did not seem to have an impact (Fig.4.2). However, it can not be certified.
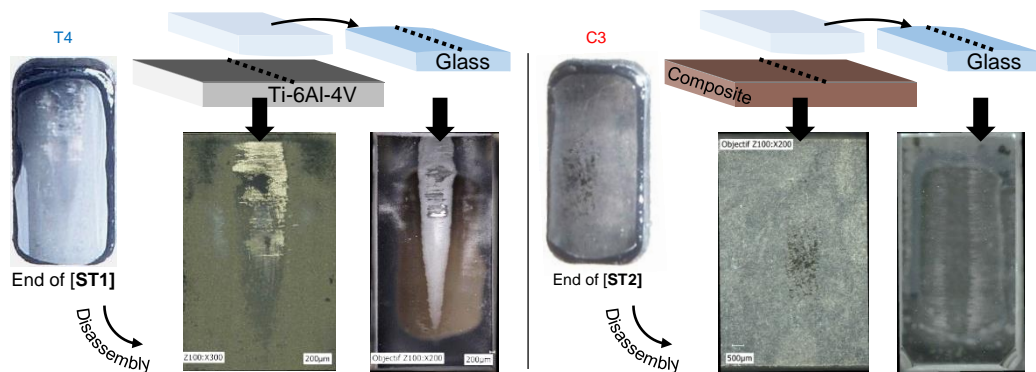
Figure 4.2 – Visual comparison of samples after disassembly and transport.

---

[1]Such an initiation location is consistent with maximum contact pressure depicted on Fig.3.14. It also emphasizes that, instead of the care taken in mounting phase, contact pressure is not symmetrical.

4.1.1.2 *Post-mortem* analyses of short-term tests with transparent pins

1st bodies are separated and analysed in SEM. Significant areas are displayed on Fig.4.3 and located in relation to the macroscopic view introduced in Fig.4.2. Again, short-term test with coated Ti-6Al-4V/glass counterparts is first analysed [**ST1**], and then short-term test with fibreglass filled polymer/glass is analysed [**ST2**].

ST1-A   **ST1-B**   **ST2-A**   **ST2-B**

Short-term test #1: glass pin on coated **T**i-6Al-4V pad (T4)   **Short-term test #2:** glass pin on **C**omposite pad (C3)
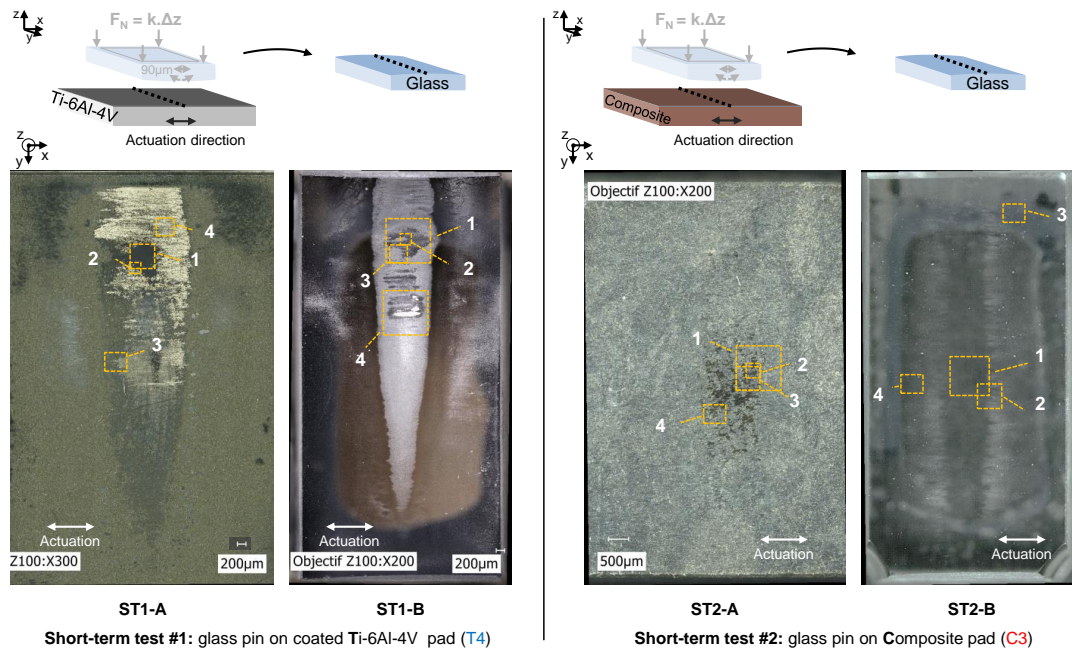
Figure 4.3 – Locations of SEM observations (Figs.4.4,4.6,4.7,4.8) in relation to the macroscopic view of the disassembled samples. Left/right columns corresponds to [ST1]/[ST2] respectively. Resulting observations are analysed in the next paragraph: ST1-A, ST1-B, ST2-A, ST2-B.

ST1-A — First, the coated Ti-6Al-4V pad is considered (Fig.4.4).

[ST1-A.1] stems from *in-situ* visualisation with Q_s^i onset (Fig.4.1-b). In this area, 3rd body layer is mainly oriented along the actuation direction by shearing (S_3M_3). In addition, indent marks appear on layer making it compact and rather cohesive. This morphology suggests an impact - normal separation of the contact - followed by a relative displacement. Occurrence of this impact mode has been measured with a laser vibrometer at the vertical of the pin (Fig.4.5). Impacts happen just after the stick phase. So, it can be supposed that wear mechanisms initiate under effect of shearing and impact - S_1, S_4 - M_2+M_3+impact - and then propagates toward - S_3 - M_3+impact. [ST1-A.2] zooms into [ST1-A.1]. It reveals that, if 3rd body layer is rather cohesive at low zoom, it is very powdered at high zoom. Edges of this powdered particles appear quite sharp, resulting in a rather abrasive 3rd body. Thus, in addition to be accommodated by shearing (S_3M_3), relative displacement can also be partially accommodated by rolling (S_3M_4). Thickness is around $5\mu m$, similar to coating initial thickness. But, because the size of grains is much lower and porosity is higher, this makes the 3rd body layer more spread and homogeneous. [ST1-A.3] confirms this observation. It refers to the frontier of the contact. Contact area is on the right hand side. Indeed, Zcontrast sensor[2,3] exhibits a higher volume of coating particles than

---

[2]The contrast of pictures obtained with a Zcontrast sensor is based on the atomic number. The higher the element atomic number is, the lighter it appears on the picture (From Colas, 2013).

[3]As a reminder, coating is composed of Silica and Oxygen. Thus, their atomic number, 14 and 8 respectively, is lower than that of the Ti-6Al-4V substrate, 22, 13 and 23 respectively.

in non-rubbed area. Finally, Zcontrast sensor in [ST1-A.4] exhibits there is no more coating but Ti-6Al-4V substrate in the area which rubbed the most (S_5M_3). From video observation, Q_w drastically increased from T3 in Fig.4.1 and so the 3rd body layer thickness decrease until exposing a big area of Ti-6Al-4V.
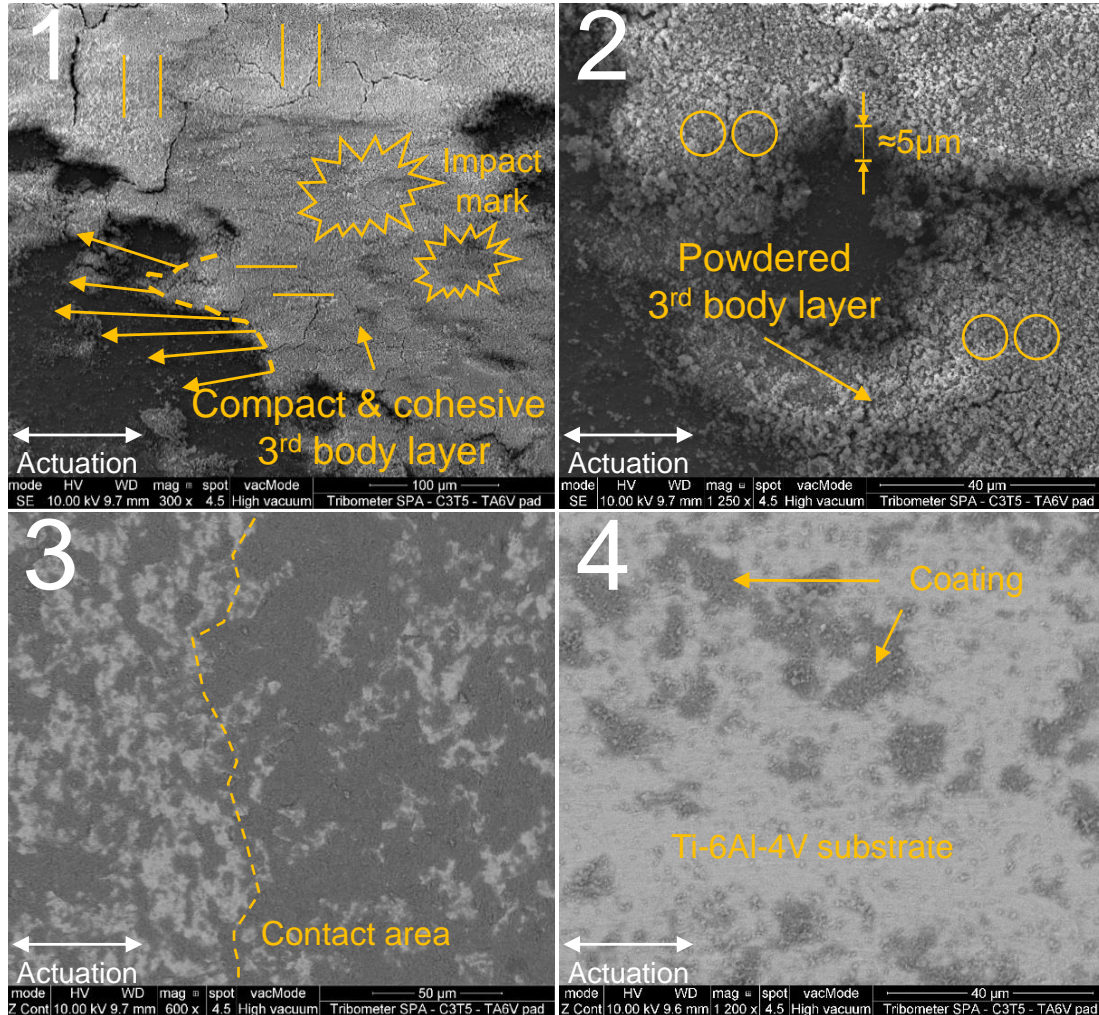
Figure 4.4 – Significant SEM observations of the Ti-6Al-4V pad after the [ST1] (Fig.4.3-ST1-A). Used symbols (=, || and oo for shearing, normal rupture and rolling respectively) refer to accommodation modes introduced in Fig.3.15.
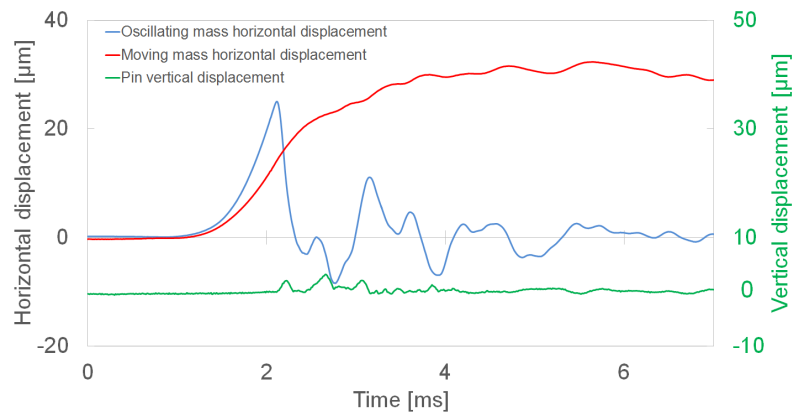
Figure 4.5 – Measure of contact separations (green curve). Impacts occur after stick–slip transition.

ST1-B —   Second, the reciprocal glass pin is considered (Fig.4.6).

[ST1-B.1] is the counterpart area of [ST1-A.1]. A "crater" appears at the centre of the picture, bordered by vertical and horizontal flows of particles. It suggests again the occurrence of the impact and shearing modes (S_1 - impact + M_3). [ST1-B.2] zooms into [ST1-B.1]. On Zcontrast sensor, 3rd body has the same contrast as the glass pin (in dark grey). As glass is mainly composed of Silica, it confirms that the layer is mainly constituted by coating. In addition, Zcontrast sensor reveals the presence of heavy particles: assumed to be Ti-6Al-4V particles coming from the pad once the substrate is reached. Thus, the main accommodation sites are first S_1 -glass pin- and S_4 -coating-, then S_3 -3rd body- and finally S_5 -Ti-6Al-4V substrate-. [ST1-B.3] Highlights the role of the impact mode. Indeed, whereas the glass pin original surface is smooth, the *post-mortem* surface is cracked (S_1 - impact), increasing its roughness. Resulting particle joined the 3rd body layer, increasing its abrasive power. Finally, [ST1-B.4] exhibits that the proportion of 3rd body is much lower on the glass pin than of the Ti-6Al-4V pad. Thus, instead of the increased roughness of the glass, which could trap the 3rd body, it remains rather on the Ti-6Al-4V substrate.

4
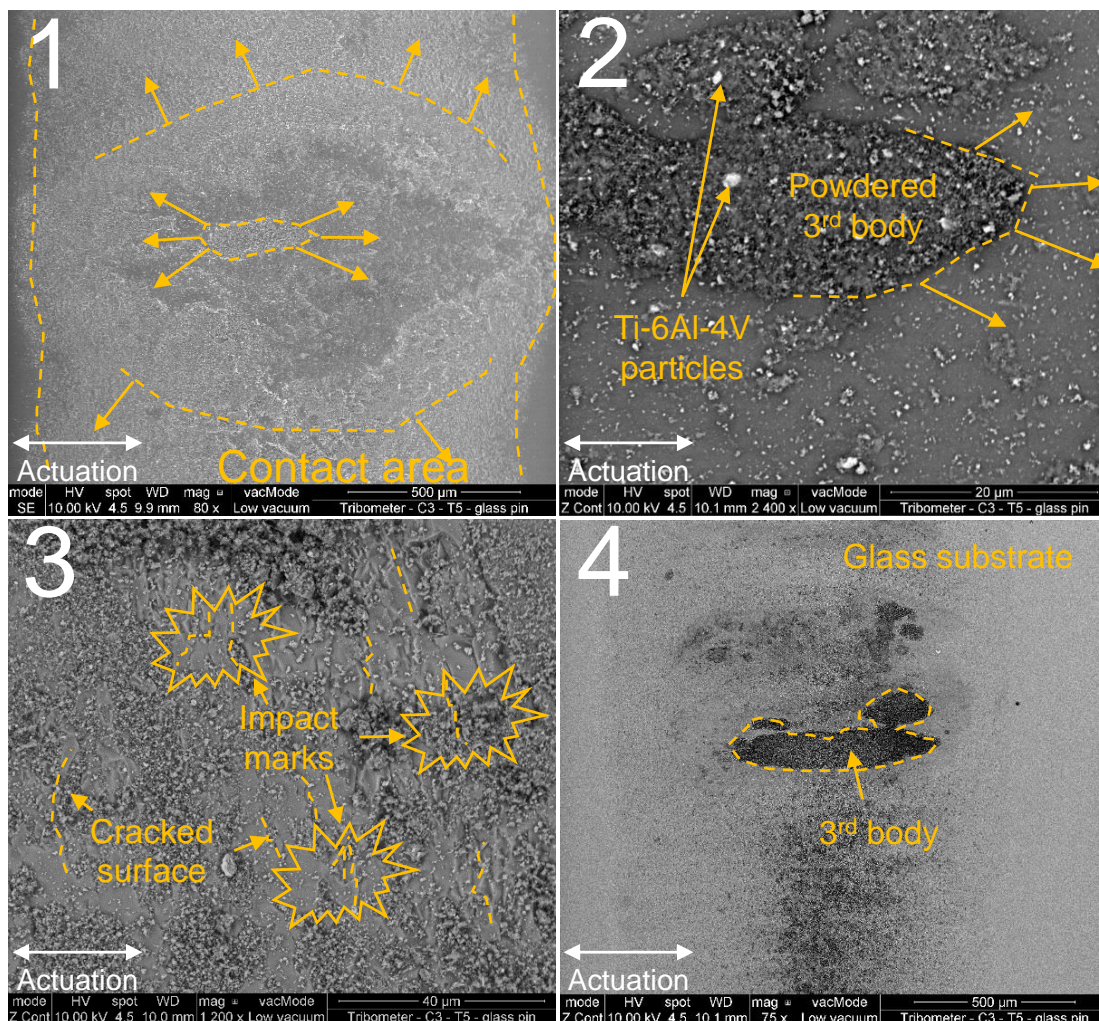
Figure 4.6 – Significant SEM observations of the glass pin after the [ST1] (Fig.4.3-ST1-B).

ST1 - intermediate conclusion — The schematic behaviour of glass pin on coated Ti-6Al-4V pad is proposed in the following tribological circuit (Table 4.1).

At first, 1st bodies, hard and smooth, are in contact. So friction coefficient is low (T0→T1). Then, due to repeated impacts and shearing, coating and glass surface fragments and mixes into an abrasive powdered 3rd body layer (T1→T2). It explains the increase of friction coefficient (Fig.4.1). Thus, accommodation site moves from S_1 and S_4 to S_3 and 3rd body starts to accommodate the impact by compacting (S_3-impact) as well as the relative displacement by shearing (S_3M_3). This powdered layer turns progressively into compact and quite cohesive clusters[4] (T2→T3). In addition, as long as 3rd body is compacting, morphology is powdered and few cohesive. So, rolling mode is expected to accommodate relative displacements (S_3M_4). Simultaneously, friction coefficient decreases to an intermediate level until 3rd body forms a compact layer. Once this layer is too dense, it does not accommodate impacts by compaction anymore, and fragments. It is then definitely ejected by normal rupture and shearing (S_3M_2, S_3M_3). Available material incrementally decreases until Ti-6Al-4V substrate is reached.

Notice that current lifetime of studied SPA is 10^6 cycles, with a low Q_w. In this first short-term test ST1, only a few thousand cycles were reached with an important Q_w. Glass replaced the fibreglass filled polymer. So, assumption about its capacity to retain 3rd body layer formed by powdered coating particles appears. Short-term test with fibreglass filled polymer/glass [**ST2**] is now analysed to address this issue.

4

Table 4.1 – Tribological circuit resulting from short-term test analysis with transparent glass pin on coated Ti-6Al-4V pad. At each step, accommodation sites and modes in bold are the main among those inventoried. Contact-life temporal evolution is deduced from the overlay of contact schemes.

	3rd body flows				Accommodation	Contact scheme
	Q_s^i	Q_i	Q_e		Sites: Modes:	
			Q_r	Q_w	S_i M_j	
T0 Initial state						
T1 (5.0e2 cycles)	++	+			S_1: **Impact**, M_3 S_4: Impact, M_3	
T2 (1.1e3 cycles)	+++	+++	+++		S_1: Impact, M_3 S_3: **Impact**, M_3, M_4 S_4: Impact, M_3	
T3 (1.9e3 cycles)	+	++	+++	+++	S_1: Impact, M_3 S_3: **Impact**, M_2, M_3, M_4	
T4 (4.2e3 cycles)	+	++	++	++	S_1: Impact, M_3 S_3: Impact, M_3 S_5: M_3	

---

[4]Notice that cohesion and powdery are usually opposite notions. However, Fig.4.4-1 and Fig.4.4-2 highlighted both morphologies occurs, depending on the observation scale.

ST2-A — First, the fibreglass filled polymer pad is considered (Fig.4.7).

[ST2-A.1] stems from *in-situ* visualisations (Fig.4.1-c) with Q_s^i onset. It emphasizes that 3rd body appears and propagates along milling tracks. It looks like "chocolate spread": a little adhesive and very ductile. [ST2-A.2] focuses on the border of [ST2-A.1]. Frontiers of 3rd body layer is made of superimposed sheets, highlighting the shearing accommodation mode (S_3M_3) (Berthier, 1990). So, accommodation site quickly moves from S_5 to S_3. In addition, contrary to reference surface morphology (Fig.3.17), glass fibres in the 3rd body layer are shorter - around $40\mu m$ -. It is deduced that impact mode breaks them into smaller ones (S_5 - impact). [ST2-A.3] is a topography view, focusing on the same border as [ST2-A.2]. It shows 3rd body layer is smoother than original surface morphology of fibreglass filled polymer (Fig.3.17). One can deduce that, by shearing, the bumps of the milling tracks has been "spread", filling the hollows and partially recovering the glass fibres which initially overpasses. [ST2-A.4] confirms the relevance of previous assumption. Indeed, it highlights the propagation mechanism of the 3rd body layer. Milling tracks are first "laminated", perpendicularly to actuation direction because of machining orientation. Then, by shearing, layer is spread along the actuation direction. Glass fibres seem to act progressively as rods in armoured cement and so stabilise the 3rd body layer.
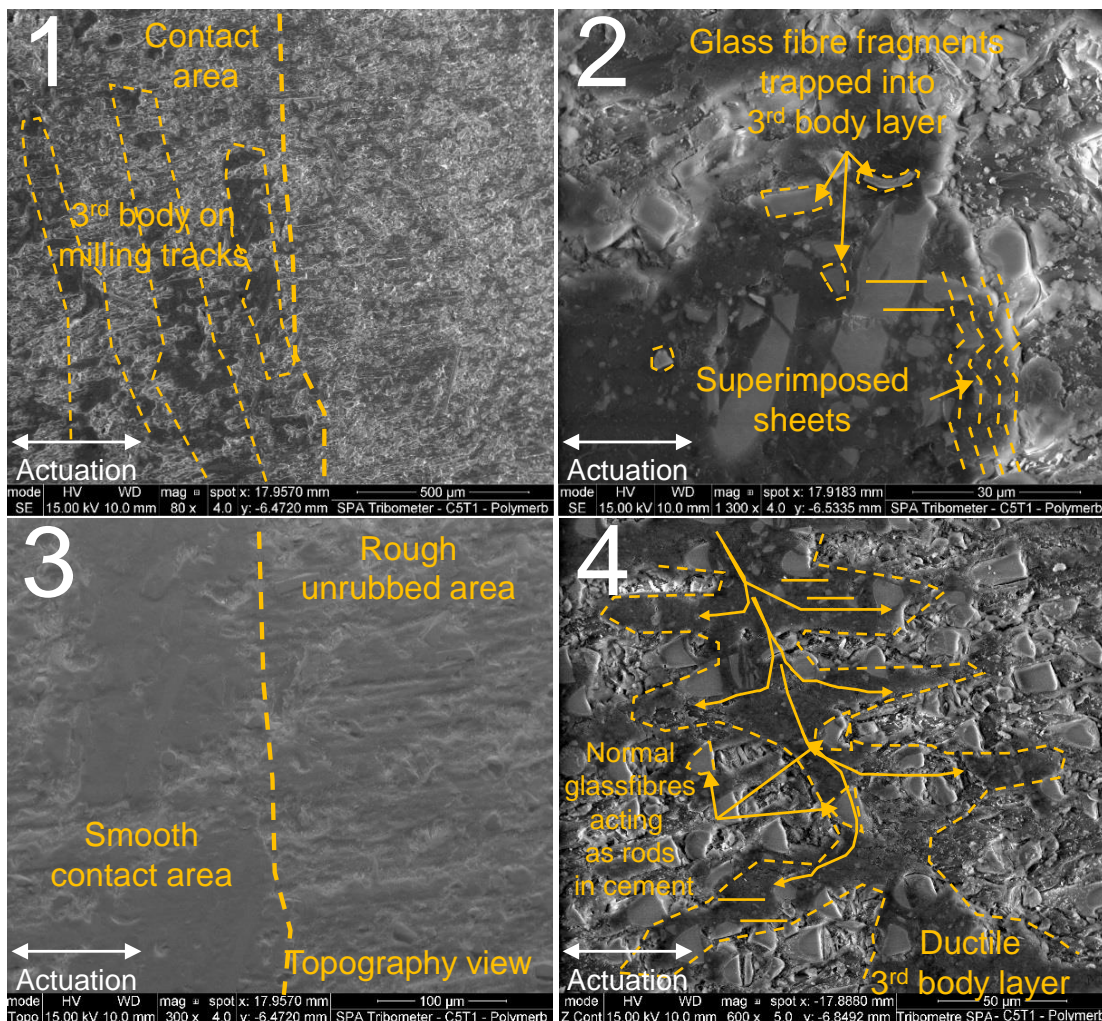
Figure 4.7 – Significant SEM observations of the fibreglass filled polymer pad after the [ST2] (Fig.4.3-ST2-A). Used symbols refer to accommodation modes introduced in Fig.3.15.

ST2-B — Second, the reciprocal glass pin is finally considered (Fig.4.8).

[ST2-B.1] is the counterpart area of [ST2-A.1]. Contact area is pitted. Beyond borders, powdered particles of 3rd body are observed. In comparison with size of particle on the composite counterpart, these particle are much smaller - lower than 1μm -. So they are suspected to be mainly glass particles. [ST2-B.2] focuses on the pitted area. Hole diameter is lower than 15μm. This is consistent with the glass fibre diameter (Fig.3.17). So, they are supposed to be responsible for this pitting (S_1 - impact). [ST2-B.3] refers to the border at the top right hand corner. Zcontrast sensor reveals it is polymer matrix. It can be deduced that shearing of the composite triggers a polymer matrix detachment which are then mixed into the 3rd body layer ($S_1 \rightarrow S_3$ - M_3). Extruded polymer matrix is only visible at the top- and bottom-side. [ST2-B.4] refers to the non-contact area on the left hand side of previously considered [ST2-B.1]. Surface is no more pitted - since not in the contact area. Small glass fragments are visible and contributed to damage glass surface by sanding it. These fragments does not seem to be cohesive and are prone to mix into the 3rd body layer as well as to partially accommodate relative displacement by rolling (S_3M_4).
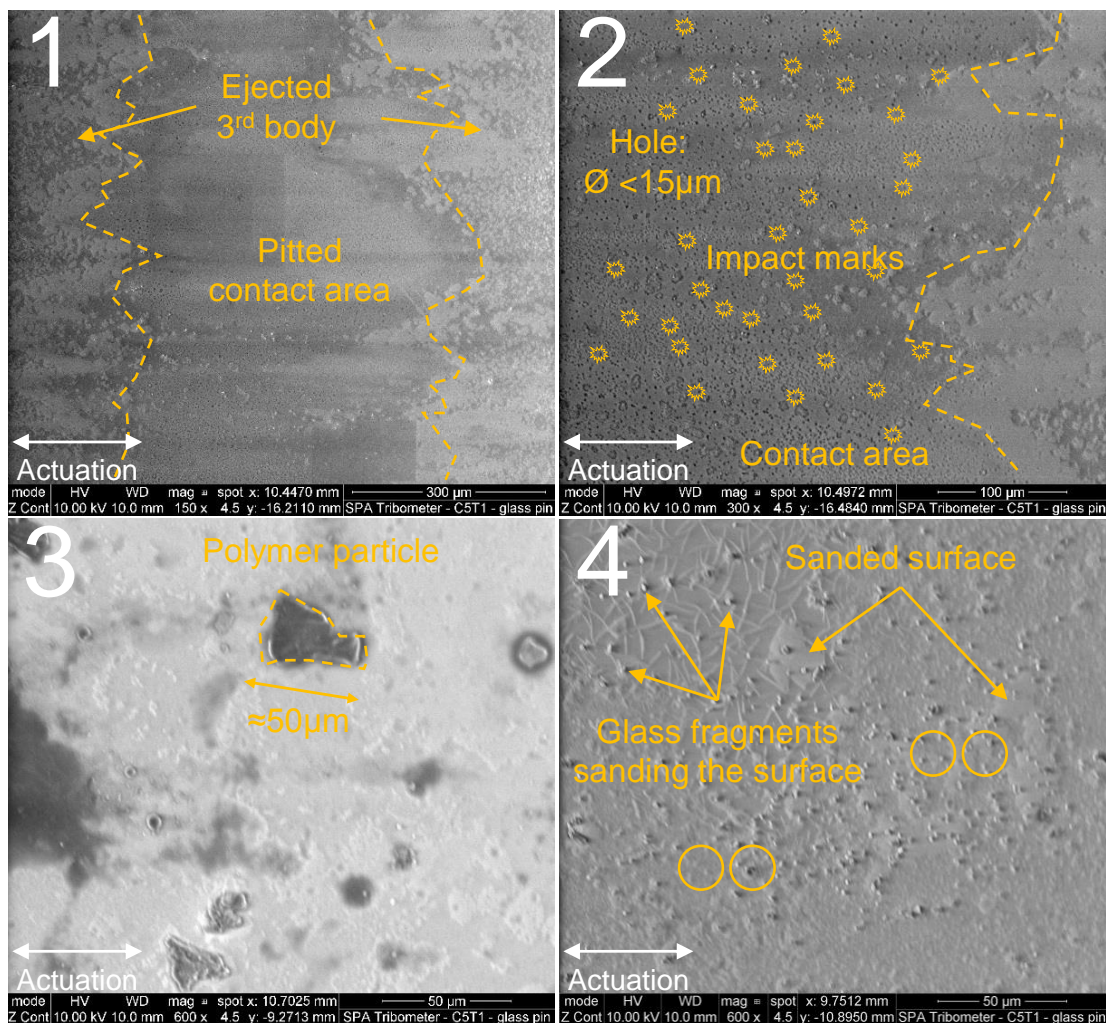

Figure 4.8 – Significant SEM observations of the glass pin after the [ST2] (Fig.4.3-ST2-B). Used symbols refer to accommodation modes introduced in Fig.3.15.

ST2 - intermediate conclusion — The schematic behaviour of the glass pin on fibreglass filled polymer pad is proposed in the following tribological circuit (Table 4.2).

At first, glass pin, harder than the polymer matrix, start to shear the milling tracks of the composite (S_5M_3). Only the smooth glass pin and the polymer are in contact, resulting in a quite low friction coefficient, around 0.1/0.2 (C0). Then, by impact, glass surface is progressively pitted by the glass fibres in the composite (S_1 - impact) (Ballout et al., 1996). In return, glass fibres start to breaks into smaller fibres - around $40\mu m$ length - (S_1 - impact). Simultaneously, 3rd body layer is forming, by mixing the sheared polymer matrix and the glass particles coming from both pin and glass fibres. This results in the transfer of the accommodation sites from the 1st bodies (S_1, S_5) in a ductile and abrasive 3rd body layer (S_3M_3). Throughout this transfer, glass particles are also ejected from the contact. Thus, Q_w is activated but with a much less intensity than in [ST1]. Indeed, the 3rd body layer seems to behave like "chocolate spread": a little adhesive and very ductile. It traps, during the shearing process, the different particles, what results in really slow 3rd body flows. The trapped particle being abrasive, it can also explain the increasing friction coefficient from C1 to C3, around 0.3/0.4.

Notice that, from *in-situ* observations, it has been seen that contact accommodation firstly occurs at the centre of the observation window. One can deduced that, contrary to the Ti-6Al-4V, composite deforms itself under preload action (Fig.3.18). It would results in extrusion of the polymer matrix at the top- and bottom- hand side of the observation window (Fig.4.8.3) and to shearing in the centre. That reveals matrix is extruded by pieces of $50\mu m$ before being compacted into ductile layer by shearing. Previous observations confirms the containment capacity of 3rd body stemming from fibreglass filled polymer.

Table 4.2 – Tribological circuit resulting from short-term test analysis with transparent glass pin on composite pad. At each step, accommodation sites and modes in bold are the main among those inventoried. Contact-life temporal evolution is deduced from the overlay of contact schemes.

	3rd body flows				Accommodation	Contact scheme
	Q_s^i	Q_i	Q_e		Sites: Modes: S_i M_j	
			Q_r	Q_w		
C0 Initial state						
C1 (2.0e2 cycles)	+	+			S_1: **Impact**, M_3 S_5: Impact, **M_3**	
C2 (5.0e3 cycles)	+	+	+	+	S_1: **Impact**, M_3 S_3: Impact, **M_3**, M_4 S_5: M_3	
C3 (1.0e4 cycles)	+	+	+	+	S_1: **Impact**, M_3 S_3: Impact, **M_3**, M_4 S_5: M_3	

4.1.1.3 Short-term tests with transparent pins - intermediate conclusion

Thus, 3rd body flows as well as tribological solicitations are quite different between this two first tests. In [ST1] with a coated Ti-6Al-4V material, 3rd body appears a little cohesive at low zoom but reveals to be very powdered at high zoom. Even compacted by the shearing and impact, 3rd body ends up by leaving the contact, leading to an important Q_w. On the contrary, ductility and adhesion dominate in the 3rd body layer from [ST2] ("Chocolate spread effect").

From previous analyses, keys toward the decryption of the contact's life between the fibreglass filled polymer and the coated Ti-6Al-4V starts to emerge. Coating is expected to be quickly detached from the Ti-6Al-4V substrate and entrapped into the what results in (i) a short running-in phase, (ii) a stable 3rd body layer and so (iii) a stable coefficient of friction.

Impact of using glass can also be estimated. In its initial state, surface of glass pin is smooth and volume is stiff and hard. Resulting 3rd body is very powdered. In comparison, 3rd body produced by fibreglass filled polymer and coated Ti-6Al-4V is more ductile-abrasive and cohesive-powdered, respectively. This could explain that the low intensity of 3rd body flows observed in [ST2] is more consistent with the observations on real SPA than that observed in [ST1].

Analyses of the tests with glass pins are now ended. They will be used in the decryption of the contact life with the original 1st bodies, first with short-term tests (section 4.1.2) and then with long-term tests (section 4.1.3).

4

4.1.2 1st test sequence: short-term tests with original 1st bodies

4.1.2.1   Monitoring analyses of short-term tests with original 1st bodies

Two short-term tests have been achieved with original 1st bodies: composite pin on coated Ti-6Al-4V pad [**ST3**] and conversely [**ST4**]. Relative monitoring data are depicted on Fig.4.9. In [ST3], friction coefficient slightly increases from less than 0.1 to 0.3 (CT points). In [ST4], friction coefficient starts at 0.3 and quickly stabilizes around 0.4/0.5 (TC points). Without any *in-situ* observations, these data will be confronted to *post-mortem* observations to decrypt the tribological circuits.
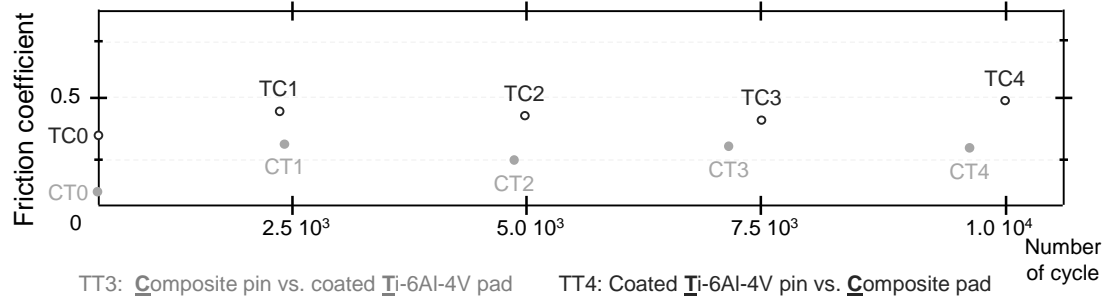
Figure 4.9 – Friction coefficient evolution extracted at regular intervals during short-term tests ST3 - fibreglass filled polymer pin *vs.* coated Ti-6Al-4V pad - and ST4 - coated Ti-6Al-4V pin *vs.* fibreglass filled polymer pad-.

4.1.2.2   *Post-mortem* analyses of short-term tests with original 1st bodies

Then, 1st bodies have been separated and analysed in SEM. [ST3] is first analysed, followed by [ST4], with the same procedure as in section 4.1.1.2. Significant areas are displayed on Fig.4.10.
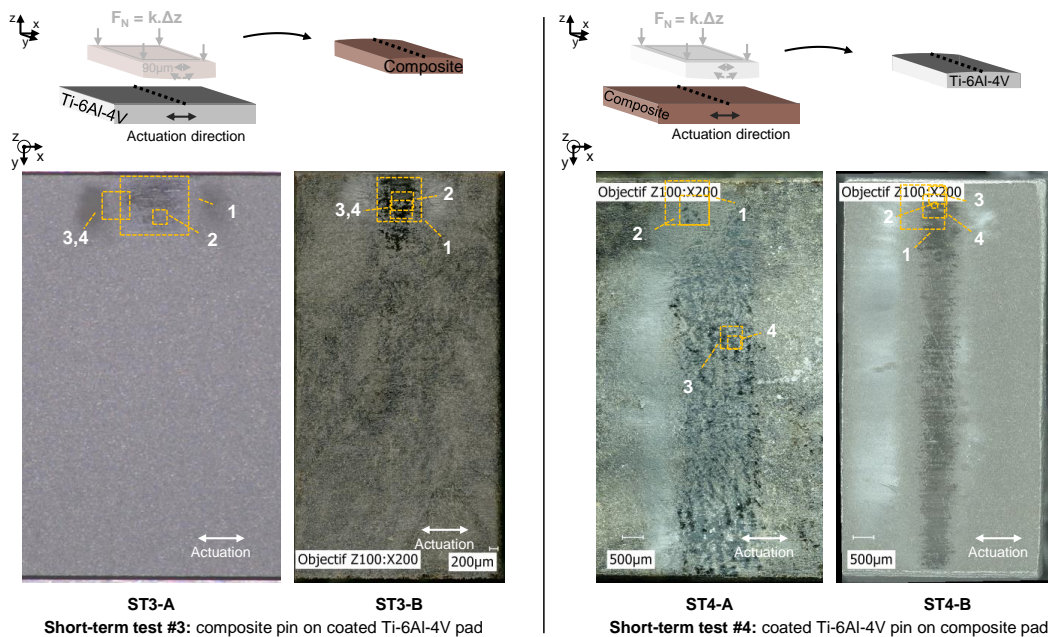
Figure 4.10 – Locations of SEM observations (Figs.4.11,4.12,4.13,4.14) in relation to the macroscopic view of the disassembled samples. Left/right columns corresponds to [ST3]/[ST4] respectively. Resulting observations are analysed in the next paragraph: ST3-A, ST3-B, ST4-A, ST4-B.

ST3-A —— First, the coated Ti-6Al-4V pad is considered (Fig.4.11).

As in [ST1], [ST3-A.1] reveals that accommodation started at the top of the observation window. 3rd body layer materialized by being darker than the non-contact area. Ti-6Al-4V substrate even starts to appear. Out of the frontier, powdered particles have been ejected. [ST3-A.2] zooms in the contact area. Contrary to its initial state (Fig.3.16), the 4-μm clusters are no more more visible but replaced by an homogeneous coating. This could explain why it appears darker. At the centre of the picture, a chips of coating is being to be detached from the substrate by shearing (S_2M_3). Zcontrast sensor also reveals that particles of Ti-6Al-4V substrate and powdered particles of coating. Shearing is not supposed to generate this particles since their morphology differs from the chips. Their occurrence is attributed to the impact (S_1, S_2 - impact). [ST3-A.3] and [ST3-A.4] are the same observation but with two sensors. With Zcontrast sensor ([ST3-A.4]), the closest the contact border is, the more homogeneous is the coating. Conversely, substrate appears where the pad rubbed the most ([ST3-A.4]). Both pictures exhibits that ejected 3rd body particles are mainly composed of coating fine powdered particles.
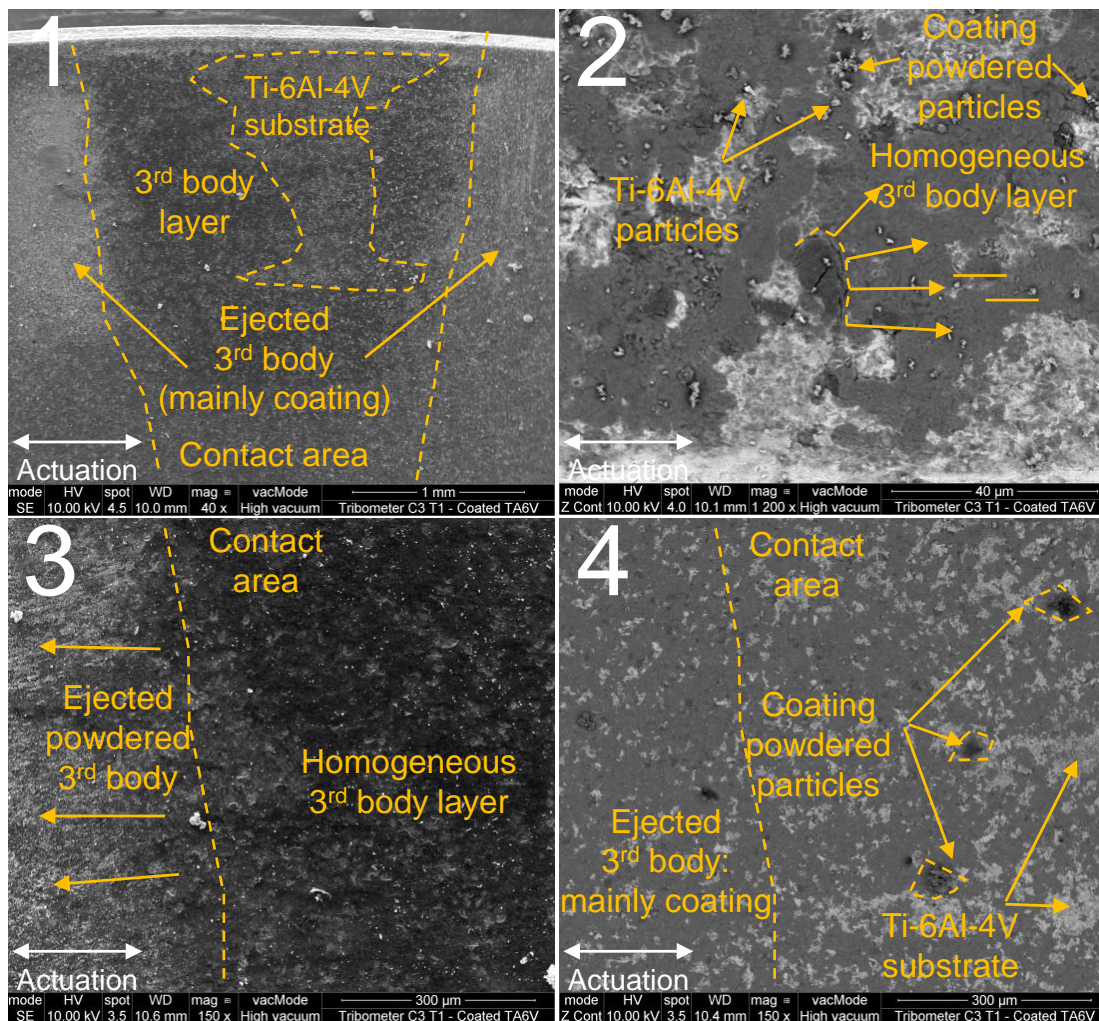
Figure 4.11 – Significant SEM observations of the Ti-6Al-4V pad after the [ST3] (Fig.4.10-ST3-A). Used symbols refer to accommodation modes introduced in Fig.3.15.

ST3-B — Second, the fibreglass filled polymer pin is considered (Fig.4.12).

[ST3-B.1] focuses on the contact area. It materialises by a smooth 3rd body layer, more spread and homogeneous than in ST2 (Fig.4.7). There is also 3rd body ejected far away from the contact. They seems more like cohesive strips than powdered particles, contrary to ST1 (Fig.4.6). [ST3-B.2] zooms into [ST3-B.1]. It is filled by crushed glass fibres, attributed to the repeated impacts (S_5, then S_3 - impact). [ST3-B.3] focus on the 3rd body layer. Aspect of this layer reminds a "chocolate spread" again but it is less ductile but cohesive with the presence of powdered particles: one notices the fissures at the top, leading to a partial accommodation by normal rupture (S_3M_2). Borders of the layer have an aspect of superimposed sheets. So, shearing also accommodates relative displacement on 3rd body once formed (S_3M_3). [ST3-B.4] is an EDX analysis of [ST3-B.3]. It indicates that 3rd body is composed polymer matrix, Silica (glass fibres and coating) and Titanium.

Despite the fact that composite pin was above the coated Ti-6Al-4V pad, there is more particle from the pad than conversely. It tends to confirm the retaining power of 3rd body particles from the composite, leading to a low Q_w.
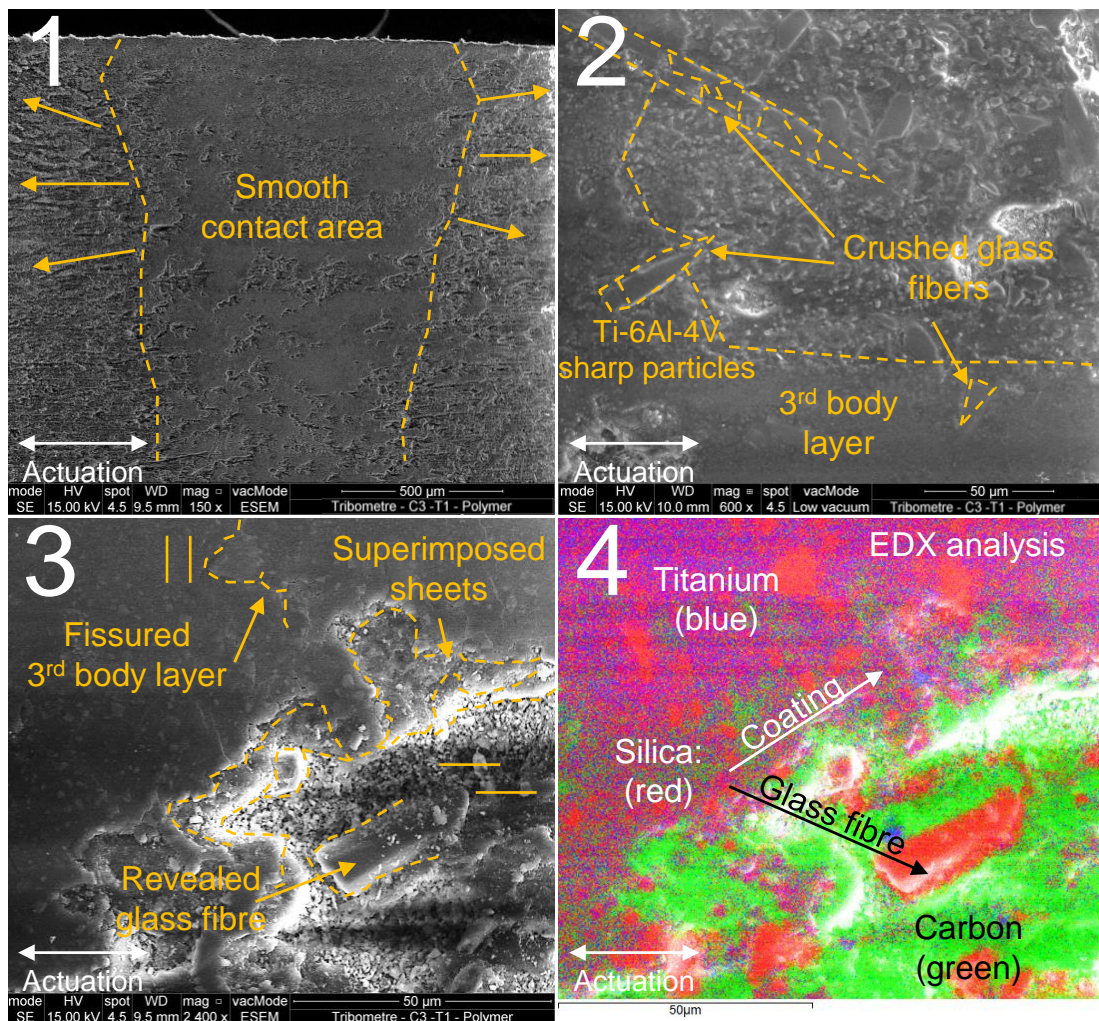
Figure 4.12 – Significant SEM observations of the fibreglass filled polymer pin after the [ST3] (Fig.4.10-ST3-B). Used symbols refer to accommodation modes introduced in Fig.3.15.

ST3 - intermediate conclusion — In comparison with the previous tests, Q_w has a much lower intensity than in ST1 and 3rd body layer with polymer matrix is more homogeneous than in ST2 after the same number of working cycles. In addition, Q_w appears on both composite and coated Ti-6Al-4V surfaces, whereas it did not appear on test with composite. If we already assumed about the retaining power of the 3rd body particles from the composite, it is interesting to see that both coating and Ti-6Al-4V particles seem to decrease the ductility of the 3rd body layer and so to speed up its propagation.

From monitoring data (Fig.4.9), friction coefficient progressively increases and stabilises from less than 0.1 to 0.3 (CT0→CT1). It can be deduced that friction increases as soon as Q_s^i and Q_i are activated, similarly to when glass rubs onto fibreglass filled polymer. Then, forming 3rd body layer becomes compact, mixing polymer matrix, glass fibres, coating particles and Ti-6Al-4V particles. This lead to a slightly decreasing friction coefficient (CT1→CT2), similarly to when glass rubs onto coated Ti-6Al-4V. Then, Q_r and Q_w are activated what stabilise 3rd body flows and so friction coefficient (CT2→CT4). However, their amplitude is much lower.

The resulting schematic behaviour of the fibreglass filled polymer on coated Ti-6Al-4V pad is proposed in the following tribological circuit (Table 4.3).

Table 4.3 – Tribological circuit resulting from short-term test analysis with fibreglass filled polymer pin on coated Ti-6Al-4V pad. Accommodation sites and modes in bold are the main among those inventoried.

	3rd body flows				Accommodation	Contact scheme
	Q_s^i	Q_i	Q_e		Sites: Modes:	
			Q_r	Q_w	S_i M_j	
Initial state						
10^4 cycles	++	++	+	+	S_1: **Impact**, M_3 S_3: Impact, M_2, M_3 S_4: Impact, M_3 S_5: Impact	

The reverse test - coated Ti-6Al-4V pin *vs.* fibreglass filled polymer (ST4) - is now analysed. Switching the 1st body material is not innocuous. It was induced by the issue of sliding distance. Indeed, whereas the pin is always sliding (and wearing), the sliding distance "seen" by the pad depends on the stroke of a cycle (+/-1mm here). Pad will necessarily "see" less sliding distance. Thus, hypothesis was formulated about the benefit of such a reverse configuration for future SPA. The next test will make it possible to address this issue.

ST4-A —— First, the fibreglass filled polymer pad is considered (Fig.4.13).

First, observation can be done on the macroscopic view (Fig.4.10-TT4-A). As in ST2 (Fig.4.7), 3rd body propagates along milling tracks. Thus, 3rd body layer seems to be less homogeneous than that observed in ST3 (Fig.4.12). [ST4-A.1] focuses on the top of the contact area. A smooth contact area appears but is actually not as homogeneous as in ST3 (Fig.4.12). Accommodation mode is nevertheless suspected to be the same: shearing (S_3 - M_3). Likewise, ejected 3rd body does not seem as strips as in ST3[5] (Fig.4.12). It is more powdered here. Based on previous observations (Fig.4.6, Fig.4.11), Zconstrat sensor in [ST4-A.2] enables us to identify powdered particles, as extruded coating due to impact (S_4 - impact). [ST4-A.3] zooms in the contact area. Again, 3rd body morphology looks like "chocolate spread". Volume is less important than in ST3-B. This is consistent with sliding distance "seen" by the pad. [ST4-A.4] zooms inside [ST4-A.2]. It also emphasizes that some powdered coating particles also joined the 3rd body layer, mixing with polymer matrix and crushed fibres ($S_1 \rightarrow S_3$ - impact). Resulting 3rd body appears cohesive - despite the grains of coating - and abrasive, by means of the sheared polymer matrix and the crushed glass fibres.
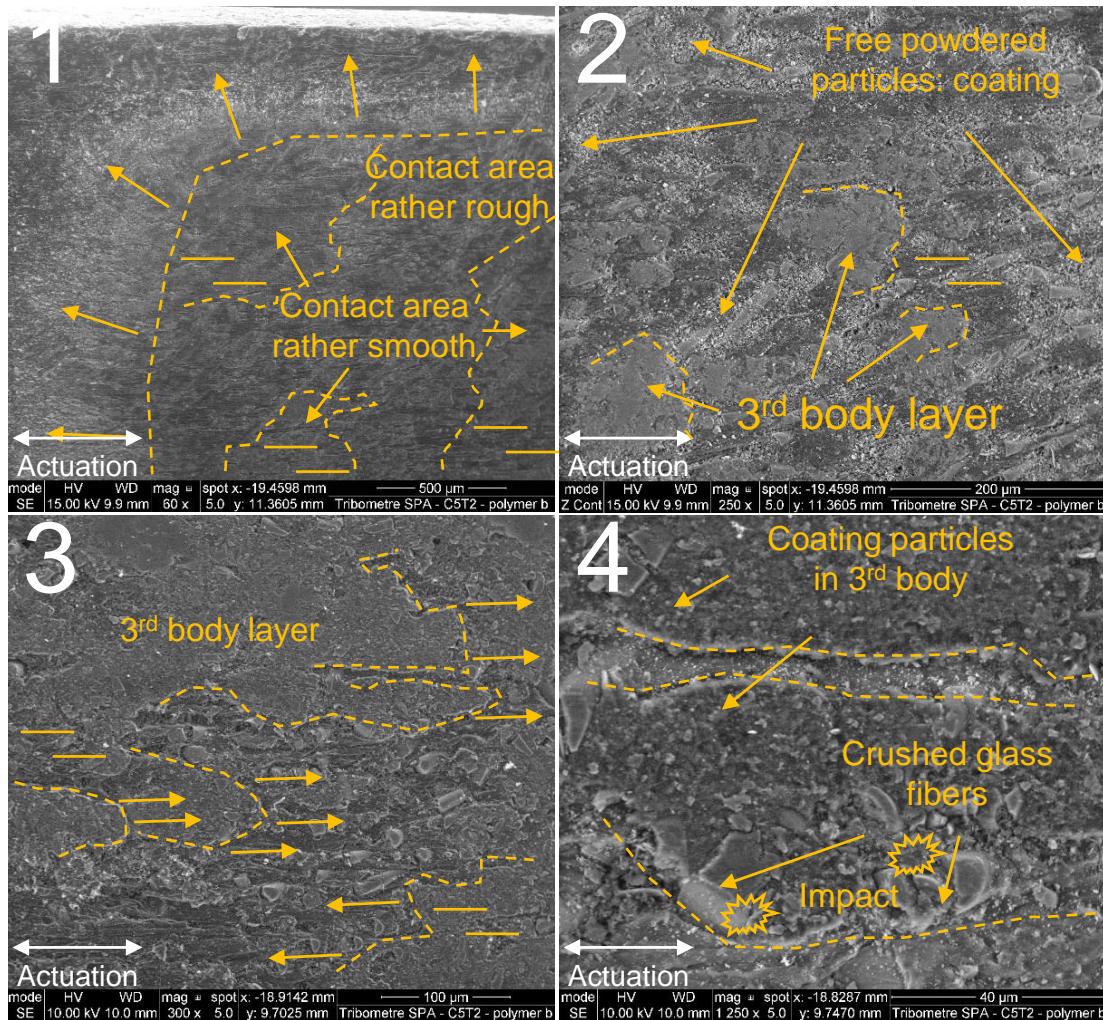
Figure 4.13 – Significant SEM observations of the fibreglass filled polymer pad after the [ST4] (Fig.4.10-ST4-A). Used symbols refer to accommodation modes introduced in Fig.3.15.

---

[5]Notice that a slight misalignment between the pin and the pad led to ejected 3rd body at the top of the contact area and not only on the sides.

ST4-B — Second, the coated Ti-6Al-4V pin is considered (Fig.4.14).

[ST4-B.1] focuses on the contact area. A smooth and cohesive 3rd body layer formed on the coated Ti-6Al-4V[6]. In addition, some ejected 3rd body particles are observed outside the contact area. Based on previous observations, they are identified as polymer matrix (Fig.4.8) and coating particles (Fig.4.6, Fig.4.11). [ST4-B.2] refers to the border of the 3rd body layer. It highlights the smoothness of the contact area in comparison with the original pattern after coating (Fig.3.16). Zcontrast sensor in [ST4-B.3], emphasizes that the 3rd body layer does not recover substrate. Ti-6Al-4V appears in some areas. It is consistent with the un-rubbed surface which was not fully homogeneous (Fig.3.16). [ST4-B.4] focuses on the 3rd body layer. If, the original 4-μm grid pattern is still present (Fig.3.16), it looks like they are merging into a smooth and cohesive layer. Impact and shearing are supposed to be responsible for this surface modification ($S_4 \rightarrow S_3$ - impact, M_3).

It is interesting to notice that no ejected Ti-6Al-4V particles have been detected. This could be attributed to the 3rd body layer formed onto substrate and protecting it.
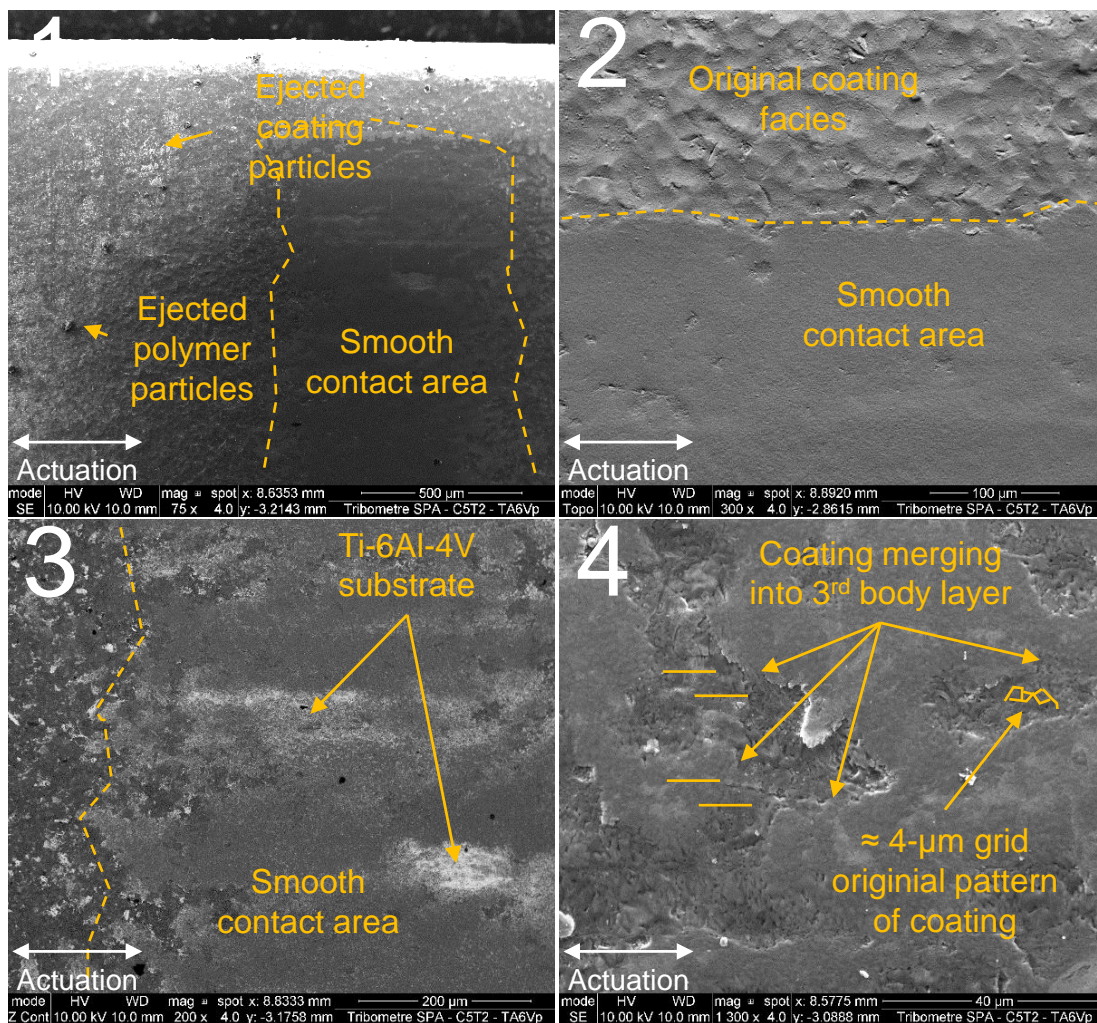
Figure 4.14 – Significant SEM observations of the Ti-6Al-4V pin after the [ST4] (Fig.4.10-ST4-B). Used symbols refer to accommodation modes introduced in Fig.3.15.

---

[6]This smooth layer is observed for the 1st time at the Ti-6Al-4V surface (Fig.4.4, Fig.4.11). This could be attributed to the fact that pin suffers from more repeated impact and shearing than pad at each one working cycle. An interesting perspective would be to check it experimentally or numerically.

ST4 - intermediate conclusion — In comparison with the previous tests, Q_s^i and then Q_i occurred on S_2 -coating on Ti-6Al-4V pin- to form an homogeneous and cohesive 3rd body layer by shearing and impacting coating. Q_s^i, Q_i and Q_r also appeared on S_5 -composite pad- with a lower magnitude since the 3rd body layer is less homogeneous. One also noticed that few mixing appears between the two formed layers. Only a few coating particles appears on the composite pad. So, it is assumed that accommodation remains located on S_2 and S_5. A little Q_w appeared, in particular with coating particles which were not trapped by the 3rd body layer in formation on S_5.

From monitoring data (Fig.4.9), friction coefficient quickly increases from 0.2 to 0.5 (TC0→TC1) and then stabilizes around 0.5 (TC1→TC4). So, behaviour is quite similar as in reverse test ST3. Friction increases as soon as Q_s^i and Q_i are activated: two 3rd body layers mixing polymer matrix, glass fibres and coating particles appears. Then, Q_r and Q_w are activated what stabilises 3rd body flows and so friction coefficient. However, one notices that, as in ST2 when glass rubbed against composite, contact area materializes at the centre of the observation window (Fig.4.3). It can be deduced that, composite deforms itself under preload action (Fig.3.18). By this way, it better complies the antagonist 1st body, what would result in a higher friction coefficient.

The resulting schematic behaviour of the fibreglass filled polymer pin on coated Ti-6Al-4V pad is proposed in the following tribological circuit (Table 4.4).

Table 4.4 – Tribological circuit resulting from short-term analysis with coated Ti-6Al-4V pin on composite pad. Accommodation sites and modes in bold are the main among those inventoried.

	3rd body flows				Accommodation	Contact scheme		
				Q_e	Sites: Modes:			
	Q_s^i	Q_i	Q_r	Q_w	S_i M_j			
Initial state								
10^4 cycles	+++	+++	++	++	S_2: **Impact**, M_3 S_3: Impact, M_3 S_5: Impact, M_3			

4.1.2.3 Short-term tests with original 1st bodies - intermediate conclusion

By means of the different short-term tests -ST1/2 with transparent glass pins and ST3/4 with original 1st bodies-, one learned that abrasion mainly drives wear mechanisms in this SPA-tribometer. In addition, the low wear flow -Q_w- is due to the formation of a ductile 3rd body layer which traps the powdered particles from the coating initially covering the Ti-6Al-4V substrate. These particles make it possible to speed up the formation of the 3rd body layer by normal rupture in decreasing its ductility.

Likewise, one noticed that tribological solicitations were similar between ST3 and ST4 (Table 4.3 and Table 4.4). It was expected because same mechanism (S_0) and 1st bodies are used. However, friction coefficient is higher and more stable in the last case (Fig.4.9). It is attributed to more important flows of 3rd body. Thus, faster flows in first cycles could lead to a shorter tribological running-in phase and maybe to more stable performances. This has now to be checked with long-term tests.

4.1.3 2nd test sequence: long-term test with original 1st bodies

After these two test sequences, **L**ong-term **T**ests have been achieved. Target number of cycle was 10^6 (2km sliding distance). On the one hand, fibreglass filled polymer pin on coated Ti-6Al-4V pad test failed before 10^5 cycles. This test, considered as critical, was duplicated to check its reproducibility. Second time, targeted number of cycle was reached and surface morphologies were similar (Fig.4.15). So, beyond the dispersion on the achieved number of cycles, occurring tribological solicitations are supposed to be the same, leading us to observe the "most worn" test [**LT1**]. On the other hand, coated Ti-6Al-4V pin on fibreglass filled polymer reached the target at the first trial [**LT2**].
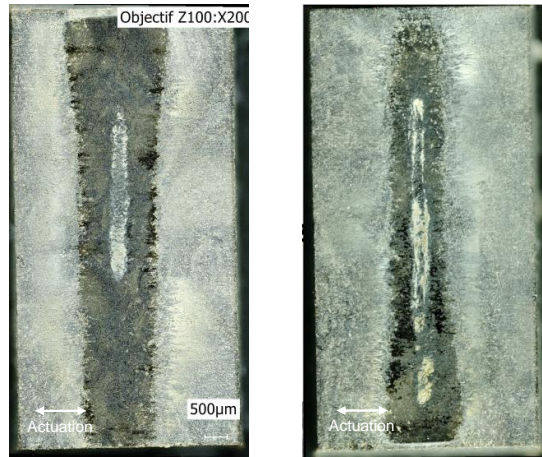
Figure 4.15 – Facies comparison of fibreglass filled polymer pins after Long-term Test [LT1].

4.1.3.1 Monitoring analyses of long-term tests with original 1st bodies

For long-term tests, manual measure of friction coefficient are replaced by an automated measure of mean speed in both actuation directions to speed up data post-treatment and to directly provide mechanical performance evolution.

In [LT1] (Fig.4.16), positive mean speed increased from 15mm/s to 20mm/s in the first $3\ 10^4$ cycles and then progressively decreased to 15mm/s. An important variation of speed appears just before $3\ 10^5$ cycles. After, speed remains stable, around 10mm/s.
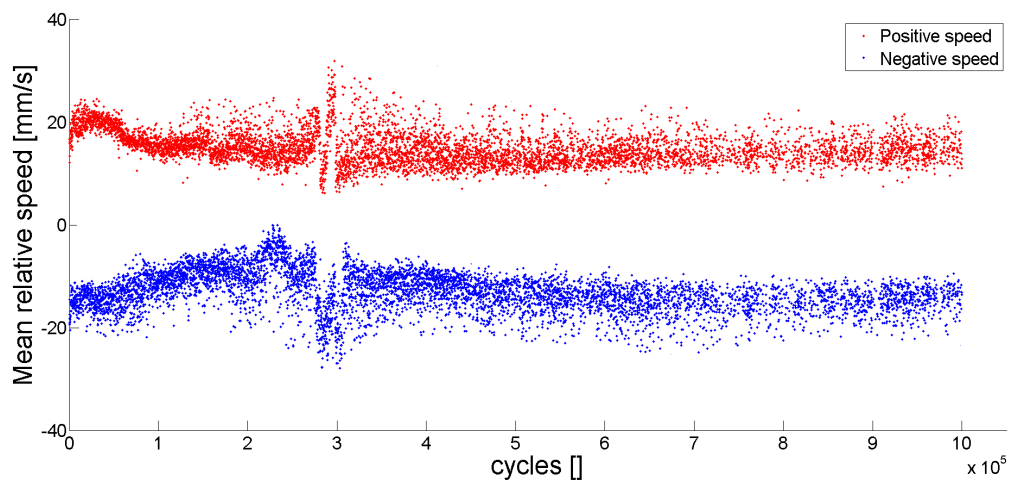
Figure 4.16 – Mean speed in [LT1]: composite pin *vs.* coated Ti-6Al-4V pad for 10^6 cycles.

In [LT2] (Fig.4.17), mean relative speed quickly increases by 25% in the first $5 \cdot 10^5$ cycles. Then, it slightly decreases around 20mm/s until $1.5 \cdot 10^5$ cycles and remains stable until test end (10^6 cycles).
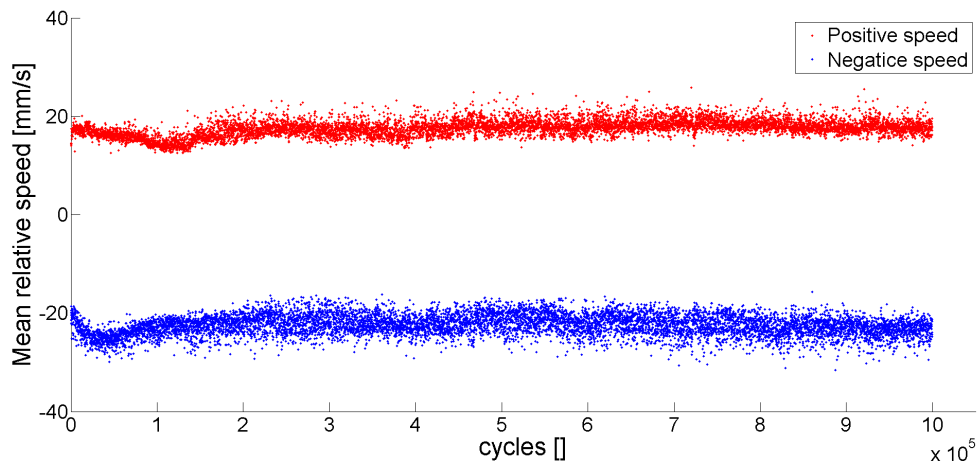
Figure 4.17 – Mean speed in [LT2]: coated Ti-6Al-4V pin *vs.* composite pad for 10^6 cycles.

Again, without any *in-situ* observations, these data will be confronted to *post-mortem* observations in order to decrypt the associated tribological circuits.

4.1.3.2 *Post-mortem* analyses of long-term tests with original 1st bodies

After tests, 1st bodies are separated and analysed in SEM. [LT1] is first analysed, followed by [LT2], with the same procedure as in section 4.1.1.2. Significant areas are depicted on Fig.4.18.
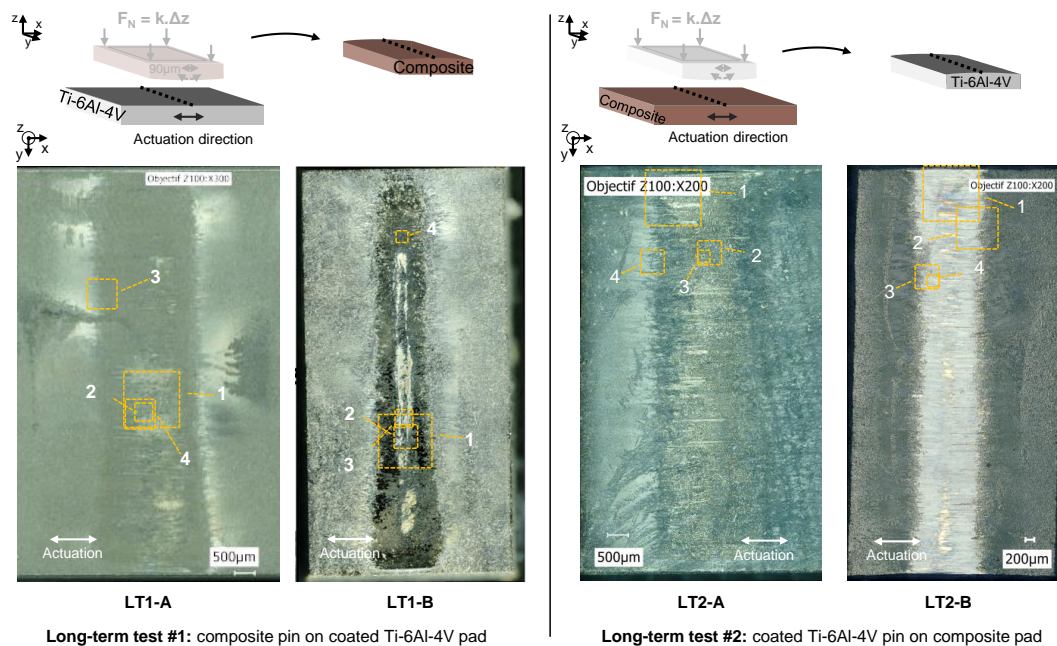
Figure 4.18 – Locations of SEM observations (Figs.4.19,4.20,4.21,4.22) in relation to the macroscopic view of the disassembled samples. Left/right columns corresponds to [LT1]/[LT2] respectively. Resulting observations are analysed in the next paragraph: LT1-A, LT1-B, LT2-A, LT2-B

LT1-A — First, the coated Ti-6Al-4V pad is considered (Fig.4.19).

In comparison with the related short-term test (ST3, Fig.4.11), contact area on [LT1-A.1] is quite similar. It materializes with an homogeneous and smooth 3rd body layer. Powdered particles have been also massively ejected. Ti-6Al-4V substrate areas appears now fully naked, not covered by 3rd body. In addition, plastic grooves appears on 3rd body layer. [LT1-A.2] focuses on the area where Ti-6Al-4V substrate appears. Chips of 3rd body layer is being extruded by shearing (S_3 - M_3). Free particles coming from coating and from Ti-6Al-4V substrate are observed. Their aspect is similar to those in Fig.4.11, so one presumes that they come from the repeated impacts (S_1, S_2 - impact). [LT1-A.3] focuses on out-of-contact area. It emphasizes the massive volume of ejected coating particles, whose aspect is very powdered. [LT1-A.4] focuses on the plastic grooves, whose width is between 30 an 70 μm and length is longer than 500μm. These plastic deformations could be generated by abrasion, due to the glass fibres on the counterface or by rolling. Their occurrence is rather attributed to rolling, based on the mechanism (S_0) behaviour. Indeed, the stick-slip actuation would let shorter marks if glass fibres were responsible for scratching these grooves (step size is around 100μm). In addition, the repeated impacts would rather generate a pitted surface. It remains to find what could generate such grooves by rolling.
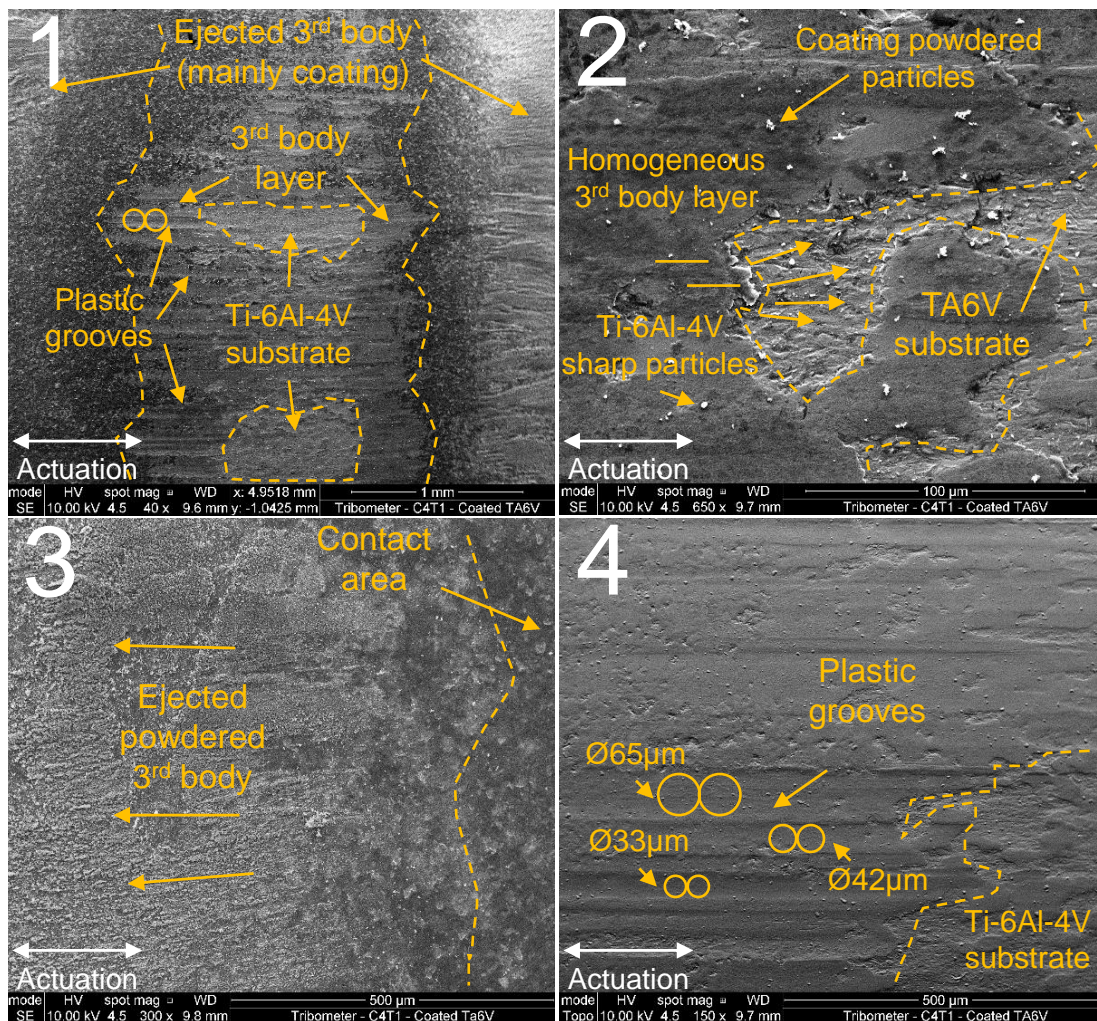
Figure 4.19 – Significant SEM observations of the Ti-6Al-4V pad after the [LT1] (Fig.4.18-LT1-A). Used symbols (= and oo for shearing and rolling respectively) refer to accommodation modes introduced in Fig.3.15.

LT1-B — Second, the fibreglass filled polymer pin is considered (Fig.4.20).

[LT1-B.1] is achieved by topography microscopy to get the shape of pin after test. A triangular "fault" appeared - whose basis is 90μm width and depth is 50μm -. Early end of first test is attributed to this fault. Indeed, as it is perpendicular to the sliding direction, stiffness of the pin in this direction is supposed to drastically decrease. Thus, when it is stressed by actuation, elastic deformation due to this normal rupture occurs and accommodates relative displacement (S_1M_2). Back on macroscopic views (Fig.4.18), areas where fault formed on the composite pin are facing naked Ti-6Al-4V substrate. Thus, fault could be responsible for the massive abrasion of the 3rd body layer and then of the substrate. [LT1-B.2] focuses on the fault. Only vertical glass fibres appears inside. In addition, fault is surrounded by an area without glass fibres. [LT1-B.3] zooms into the fault, focusing on the vertical glass fibres. A 100-μm width composite matrix is being extruded. Based on short-term test (Fig.4.11), one deduces that pin progressively rubs, vertical fibres break into fragments and longitudinal crushed fibres leave the matrix. Thus, after a while, there is no more fibres to cement the matrix. Full of holes, it breaks by shearing and impacts (S_1 - impact, M_3). Fault appears. [LT1-B.4] focuses on contact area with empty glass fibre slots. Longitudinal fibres leaving the matrix, are free to roll (S_3M_4) until being broken into fragments by impact (S_3 - impact). This could explain the "grooves" on counterface.
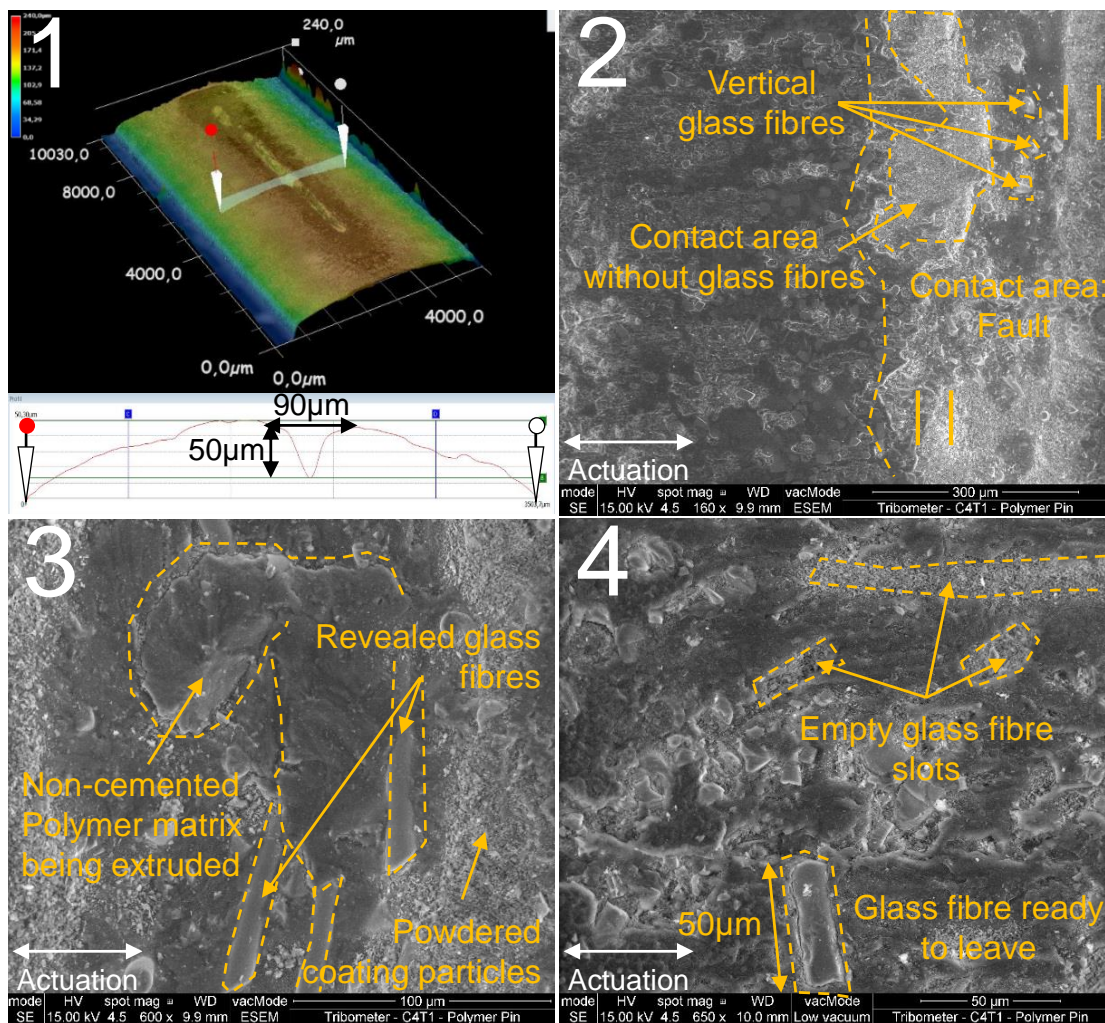
Figure 4.20 – Significant SEM and microscopy observations of the fibreglass filled polymer after the [LT1] (Fig.4.18-LT1-B). Used symbols refer to accommodation modes introduced in Fig.3.15.

Intermediate conclusion — In comparison with short-term test (section 4.1.2), Q_s^i drastically increased, during long-term test, due to the formation of a fault in the composite pin and to the resulting abrasion of counterface. However, the formation of cohesive 3rd body layers on both 1st bodies - mixing coating, glass fibres and polymer matrix - have limited wear flow Q_w. Thus, 3rd body has mainly circulated and re-circulated into the contact (Q_i and Q_r).

Based on monitoring data (Fig.4.9 and Fig.4.16), one deduces that friction coefficient first increases with the formation of a cohesive and abrasive layer: Q_s^i and Q_i are activated. Progressively, layer becomes homogeneous: a balance occurs between the different 3rd body flows. Then, at 3.10^5 cycles, fault would start to appear, increasing roughness and abrading Ti-6Al-4V substrate. Thus, normal rupture starts to partially accommodate relative displacements, leading to a drop of performances (10mm/s) until test end. If, in this case contrary to the first trial, targeted number of cycles - 10^6 cycles - were reached, an upcoming failure due to the fault expanse is expected.

Tribological circuit of the fibreglass filled polymer pin on coated Ti-6Al-4V pad in first cycles (ST3 - Table 4.3) is completed by the previous observations to propose a complete tribological circuit of this contact (Table 4.5).

Table 4.5 – Tribological circuit resulting from long-term test analysis with fibreglass filled polymer pin on coated Ti-6Al-4V pad. Accommodation sites and modes in bold are the main among those inventoried. Contact-life temporal evolution is deduced from the overlay of contact schemes.

	3rd body flows				Accommodation	Contact scheme
	Q_s^i	Q_i	Q_e		Sites: Modes: S_i M_j	
			Q_r	Q_w		
Initial state						
10^4 cycles	++	++	+	+	S_1: **Impact**, M_3 S_3: Impact, M_2, M_3 S_4: Impact, M_3 S_5: Impact	
10^6 cycles	++++	+++	+++	++	S_1: Impact, M_2, M_3 S_3: Impact, M_3, M_4 S_4: Impact, M_3 S_5: Impact, M_3	

This long-term test [LT1] highlighted the impact of 1st bodies orientation. If the composite is a good candidate as pin to get a low wear flow Q_w in short-terms applications, repeated solicitations lead to damage it on a long term. As a result, pursued performances for a long lifetime are not addressed. Thus, it becomes necessary to study the reversion configuration: coated Ti-6Al-4V pin on fibreglass filled polymer pad.

LT2-A —— First, the fibreglass filled polymer pad is considered (Fig.4.21).

Again, first observations can be done on macroscopic view (Fig.4.18-LT2-A). Contrary to related short-term tests (Fig.4.3-ST2-A and Fig.4.10-ST4-A), 3rd body does not propagate along milling tracks anymore. Thus, 3rd body layer is more homogeneous. Topography view in [LT2-A.1] focuses on the top of contact area. In comparison with related short-term test (ST4, Fig.4.13), contact area is quite similar. Topography confirms that an homogeneous smooth 3rd body layer formed onto composite. Based on short-term tests, shearing is considered as the main accommodation mode responsible for the formation of this layer ($S_5 \rightarrow S_3$ - M_3). Likewise, more 3rd body has been ejected than in LT1 (Fig.4.18-LT1). It is consistent in comparison with observations after 10^4 cycles (Fig.4.10-ST4-A). [LT2-A.2] deeply focuses on contact area that appears globally smooth and homogeneous. It emphasizes that, instead it is covered by fragments - resulting from extruded and impacted glass fibres (S_5 - impact) - surface is quite smooth. [LT2-A.3] zooms into [LT2-A.2]. Zcontrast sensors reveals that powdered particles - in silica mainly - fill the space between glass fragments. Resulting 3rd body becomes cohesive, so stable and abrasive. Focusing on contact frontiers ([LT2-A.4]), is mainly powdered but cohesive strips also appears. It can be deduced that the more the 3rd body is sheared and impacted (S_3 - M_3, impact), the more cohesive is the ejected 3rd body.
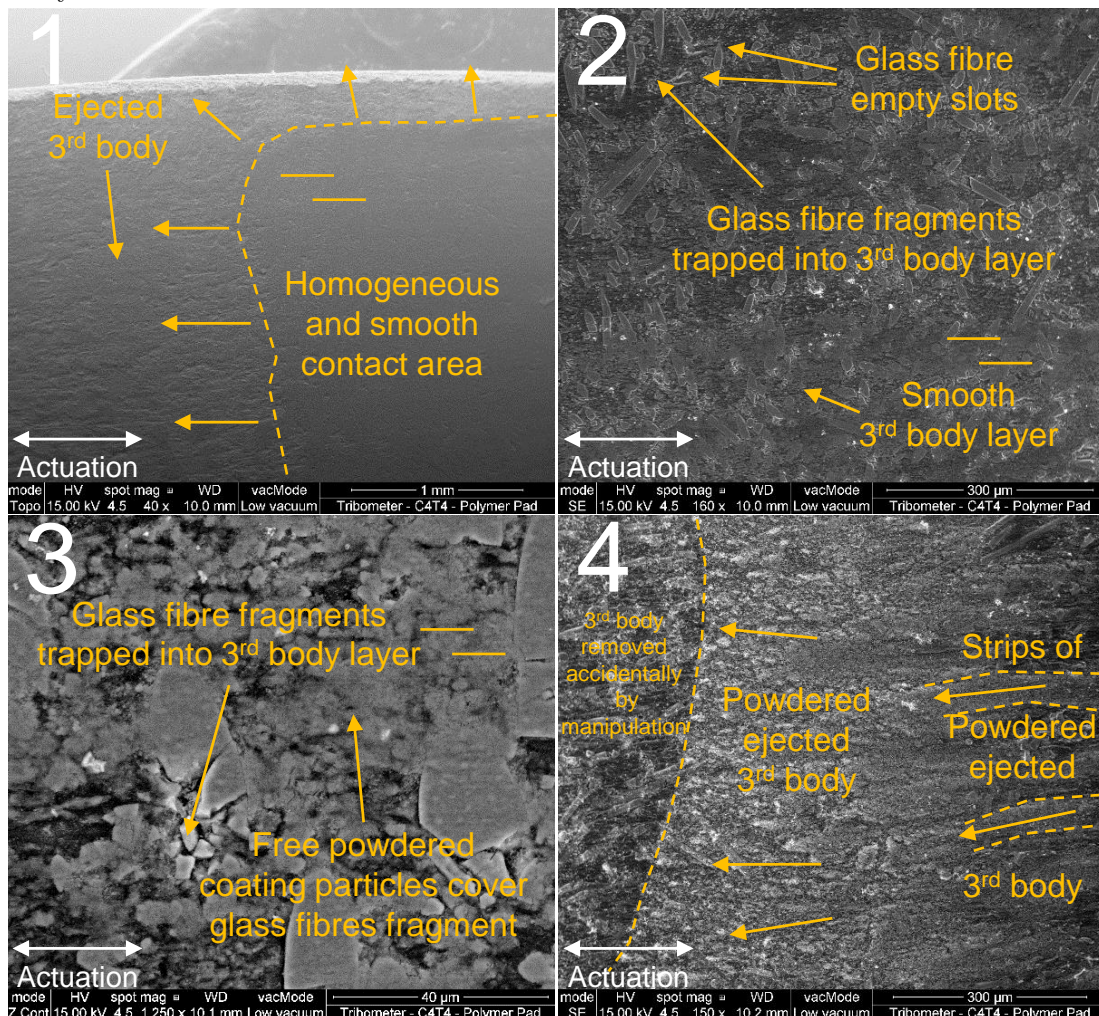
Figure 4.21 – Significant SEM observations of the fibreglass filled polymer pad after the [LT2] (Fig.4.18-LT2-A). Used symbols (= and oo for shearing and rolling respectively) refer to accommodation modes introduced in Fig.3.15.

LT2-B — Second, the coated Ti-6Al-4V pin is considered (Fig.4.22).

In comparison with short-term test (Fig.4.14), 3rd body layer formed onto the coated Ti-6Al-4V pin seems to be similar [LT2-B.1]. Likewise, ejected 3rd body coming from coating and from composite pad (S_2, S_5 - impact, M_3) are also present. However, EDX analysis highlights in [LT2-B.2] that Ti-6Al-4V is becoming naked. So, substrate progressively accommodates relative displacement by shearing (S_1M_3). In [LT2-B.3] as in [LT1-A.4] (Fig.4.19), plastic grooves appears. As glass fibres empty slots have been observed also on the composite side (Fig.4.21), free extruded glass fibres are suspected to leave polymer matrix and then to roll in the contact (S_3M_4) until being broken into fragments and mixed in the 3rd body layer. Finally, Zcontrast sensor in [LT2-B.4] indicates that this abrasive layer led to pit both coating and substrate of the pin side by impact (S_1, S_2 - impact) and to scratch the surface along the actuation direction. One notice that holes let by the pitting are filled by 3rd body, which can be used as tank to progressively providing solid particles, cementing the 3rd body layer on the composite side.
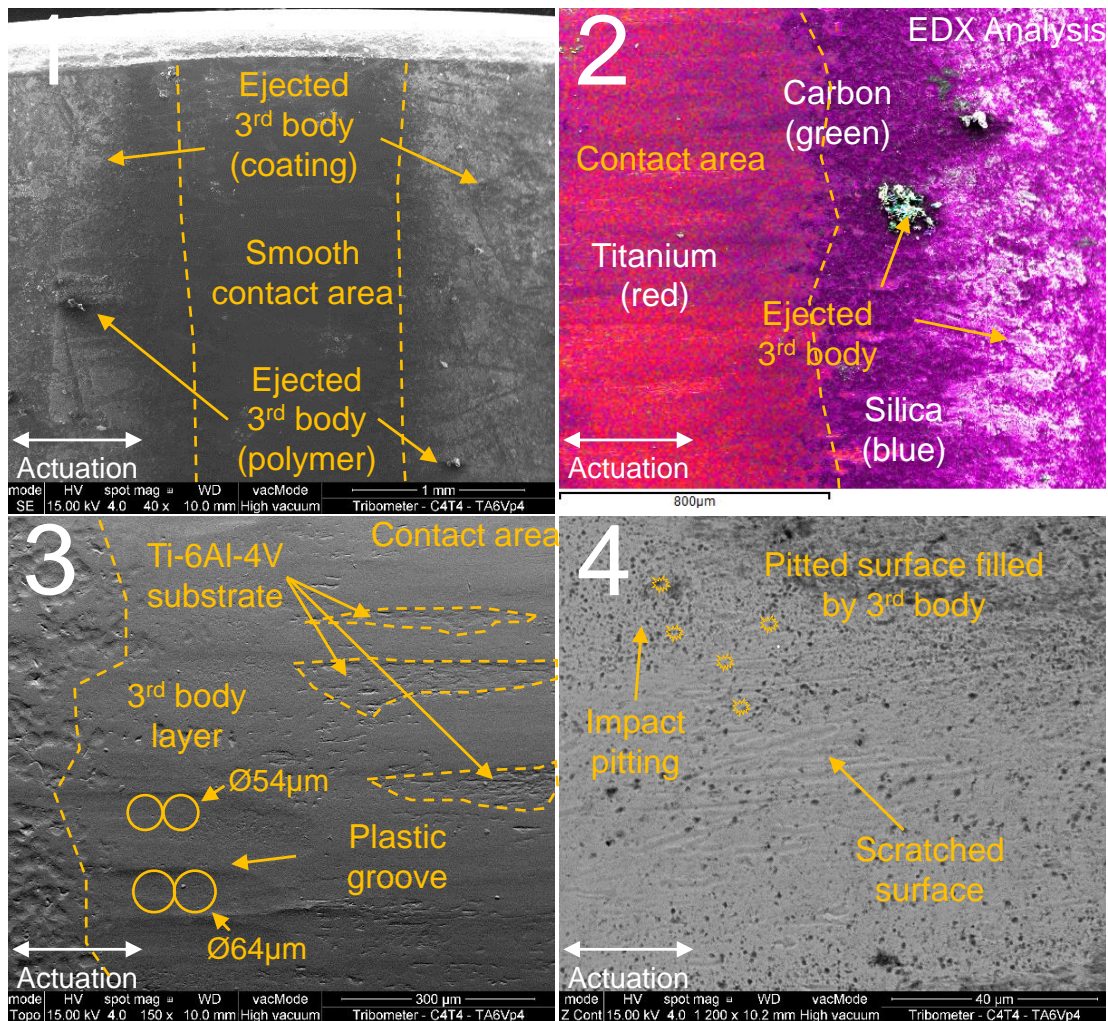
Figure 4.22 – Significant SEM observations of the Ti-6Al-4V pin after the [LT2] (Fig.4.18-LT2-B). Used symbols refer to accommodation modes introduced in Fig.3.15.

Intermediate conclusion — In comparison with short-term test (section 4.1.2), morphologies of both 1st body surfaces are not so different, and so are 3rd body flows. Indeed, lifetime tests last 10^6 cycles against 10^4 in short-term tests. So, volume of mobilized particle are logically more important. However, amplitude of internal source flow Q_s^i and wear flow Q_w did not change. What is interesting with [LT2] is the amount of coating particles which joined and mixed into 3rd body layer on the composite surface to cement the free glass fibres fragment resulting from the repeated impacts. Thus, internal flow Q_i and recirculation flow Q_r may slightly increased.

Based on monitoring data (Fig.4.9 and Fig.4.17), one deduces that friction coefficient behaves similarly to [LT1]. It first increases with the formation of an abrasive layer. Then, progressively, 3rd body layer becomes homogeneous: a balance occurs between the different 3rd body flows and friction coefficient slightly decreases. But, contrary to [LT1], as the 1st body rubbing the most (pin) is in coated Ti-6Al-4V; it does not lead to early failure. In addition, as the 1st body rubbing the less -the composite pad- progressively formed a ductile and cohesive layer from polymer matrix, it leads to trap the different 3rd body particles. This results in a stable and abrasive layer, leading to an important friction coefficient - around 0.5 - stable all along lifetime.

Tribological circuit of the coated Ti-6Al-4V pin on fibreglass filled polymer pad in short-term test (ST4 - Table 4.4) is completed by the previous observations to decrypt the overall contact's life (Table 4.6).

Table 4.6 – Tribological circuit resulting from long-term test analysis with coated Ti-6Al-4V pin on fibreglass filled polymer pad. Accommodation sites and modes in bold are the main among those inventoried. Contact-life temporal evolution is deduced from the overlay of contact schemes.

	3rd body flows				Accommodation	Contact scheme
	Q_s^i	Q_i	Q_e		Sites: Modes:	
			Q_r	Q_w	S_i M_j	
Initial state						
10^4 cycles	+++	+++	++	++	S_2: **Impact**, M_3 S_3: M_3 S_5: Impact, M_3	
10^6 cycles	+++	++++	+++	++	S_1: Impact, M_3 S_2: **Impact**, M_3 S_3: **Impact**, M_3, M_4 S_5: **Impact**, M_3	

4.1.3.3 Long-term tests with original 1st bodies - intermediate conclusion

Long-term tests emphasize that, with fibreglass filled polymer and coated Ti-6Al-4V as 1st bodies, abrasion drives wear mechanisms. When pin is in composite, it results in a quite low wear flow Q_w but in an early test failure due to a normal rupture of the pin. In a reverse configuration, it results in important 3rd body flows leading to a high wear flow Q_w. In this configuration, ductility of the 3rd body layer formed onto the composite surface makes it possible to trap the most of solid particles, leading to quickly stabilize 3rd body flows amplitudes and so the performances in a long lifetime.

4.2 Summary and conclusion

The purpose of this tribological part was to characterize tribological solicitations in SPA. To achieve such a purpose, a tribometer dedicated to SPA has been developed. This tribometer is actuated by an APA® and preloaded with a spring to get closer to the SPA related tribological solicitations. In addition, instrumentation has been implemented to both observe what happens inside the contact by means of a transparent glass pin and monitor friction coefficient evolution. Likewise, an analysis framework - based on Godet's 3rd body approach - have been adopted. This framework enabled to compare - by means of *in-situ* and *post-mortem* observations - different tests with a same methodology to propose systematic analyses, whose conclusions would be less dependent on the observer. This methodology can be summarized in a few points:

- No comparison can be achieved without reference. So, in addition to manufacturing data, when available, first analysis step consists in observing the 1st body morphology before tests. To do so, they have to be previously carefully cleaned.

- Second step has consisted in assessing observation scales. Indeed, they differ with the studied mechanisms. In SPA-tribometer, contact and step sizes were around 100 μm. Stroke was 1mm. So, first observations were realised at 1-mm scale to get the big picture. Then, progressive zooms below the contact size have been achieved to get morphological changes in comparison with reference observations.

- During the different analyses, parts have been systematically oriented along the actuation direction to be comparable. Then, morphology - cohesion, ductility, powdery, abrasion, compaction, porosity - as well as deposit orientations have been assessed. Both have been compared to the SPA-mechanism behaviour to decrypt the different tribological solicitations.

- Finally, the different observations were formalised by solid particles flows and accommodation sites/modes in a summary table: the tribological circuit.

Based on this methodology, two sequences of tests have been achieved:

- *In-situ* observations with glass pin made it possible to observe the chronology of phenomena - such as 3rd body creation and motion - happening during the first operating cycles. These tests made it possible to discover that 3rd body flows coming from coated Ti-6Al-4V were much faster than that coming from fibreglass filled polymer. Thus, powdered coating particles tend to be quickly extruded from the contact, leading to an important wear. On the contrary, composite develop a ductile and cohesive 3rd body layer would looks like "chocolate spread".

- Short- and Long-term tests with original 1st bodies - fibreglass filled polymer and coated Ti-6Al-4V - led us to determine that abrasion mainly drives wear flow Q_w and leads to a high friction coefficient - around 0.5 -.

The *Characterisation of tribological solicitations* stems from above applied methodology: from the first cycles, a 3rd body layer forms on the composite by shearing the carbon matrix. This layer is very ductile and abrasive. It acts as "chocolate spread", traps broken glass fibres and coating particles. Its propagation is all the more accelerated as its ductility is decreased by the entrapped 3rd body particles. Progressively, Ti-6Al-4V substrate is reached. Related ejected particles join the 3rd body layer, leading to a partial Ti-6Al-4V/Ti-6Al-4V contact. The resulting coefficient of friction is quite high ($\sim$0.5) and remains constant, leading to performance repeatability.

4.3 Main outcomes

Two main outcomes result from this work. They stem from previous analyses and aim at being directly exploitable industrially.

4.3.1 A ten time longer lifetime

From the comparison between the orientation of two 1st bodies, a lifetime test with a coated Ti-6Al-4V pin against a fibreglass filled polymer pad has been launched. Targeted number of cycle was ten times higher than before: 10^7 cycles/20km equivalent sliding distance. This test was achieved at first and successfully reproduced (Fig.4.23).

In comparison with shorter tests, sudden decreases/increases of mean speed regularly appear after $5\ 10^6$ cycles and an important cohesive wear is observed (Fig.4.24). We could imagine that, because of its low ductility, the 3rd body layer on composite surface looses its cohesion with repeated stresses. It would lead then to an increase of wear flow Q_w, with ejection of cohesive clusters of particles, in consistence with observations. Some substrate area would be then available to be sheared again (S_5M_3). Thus, a new ductile and cohesive 3rd body layer would form.

If these results constitute a progress, it should be necessary to lead a similar *post-mortem* analysis to confirm the origin of the speed variations.
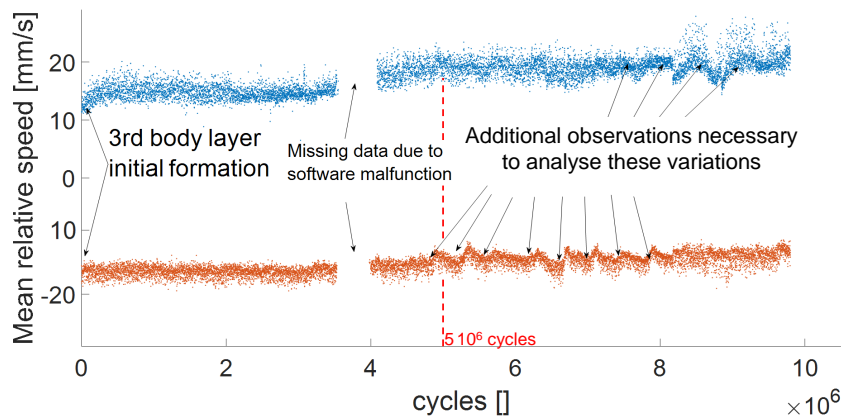

Figure 4.23 – Mean speed in [LT3]: coated Ti-6Al-4V pin *vs.* composite pad after **10^7 cycles**.
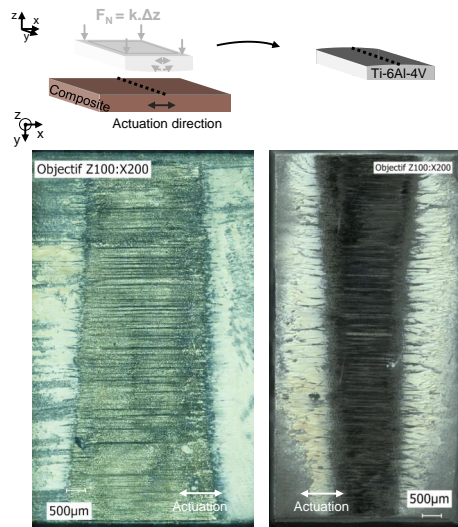

Figure 4.24 – Macroscopic view of the disassembled samples after **10^7 cycles**.

4.3.2 Wear flow reduction: introduction of a new tribological triplet

Although reversing the orientation of 1st bodies led to an increased lifetime and stable performances, resulting wear flow remains too important to address industrial applications such as optical one. One notices that abrasion - due to glass fibres - was responsible for the high wear flow whereas stable performances were rather due to the formation of a cohesive and ductile 3rd body layer from the polymer matrix. In literature, some authors[7] noticed that replacing the fibreglass filled polymer by a carbon fibre filled polymer (same polymer) led to drive wear mechanisms by adhesion rather than by abrasion. This would be all the more interesting since adhesion would favour the retaining power of 3rd body layer and so would additionally limit wear flow.

This second composite has been manufactured and tested in a similar configuration as [LT2] with 10^7 targeted cycles. Test was achieved at first and wear volume is visually lower than with fibreglass filled polymer (Fig.4.25). It might be comparable with that stemming from test at 10^6 cycles (Fig.4.18-LT2). However, tribological running-in phase lasts longer - around 10^6 cycles - before that mean speed stabilizes (Fig.4.26). This seems to be consistent with previous tests. Indeed, in [LT2], abrasion increases Q_s^i amplitude and so the volume of solid particles into the contact. Theses particles mixed into the 3rd body layer, lowering its ductility and speeding up its spreading by shearing. With the carbon fibre filled polymer, adhesion is expected to be in balance with abrasion to drive wear mechanisms, what would result in a longer spreading time for the 3rd body layer.

Thus, without multiplying tests with numerous friction materials, Godet's 3rd body approach made it possible to introduce a new tribological triplet which address both lifetime and wear issues. However, use of fibreglass filled polymer has been validated in vacuum and thermal applications (Belly et al., 2011). So, it is necessary to lead the same previous analysis to characterize tribological solicitations and to test it in similar harsh environments in order to be fully confident in this new triplet.
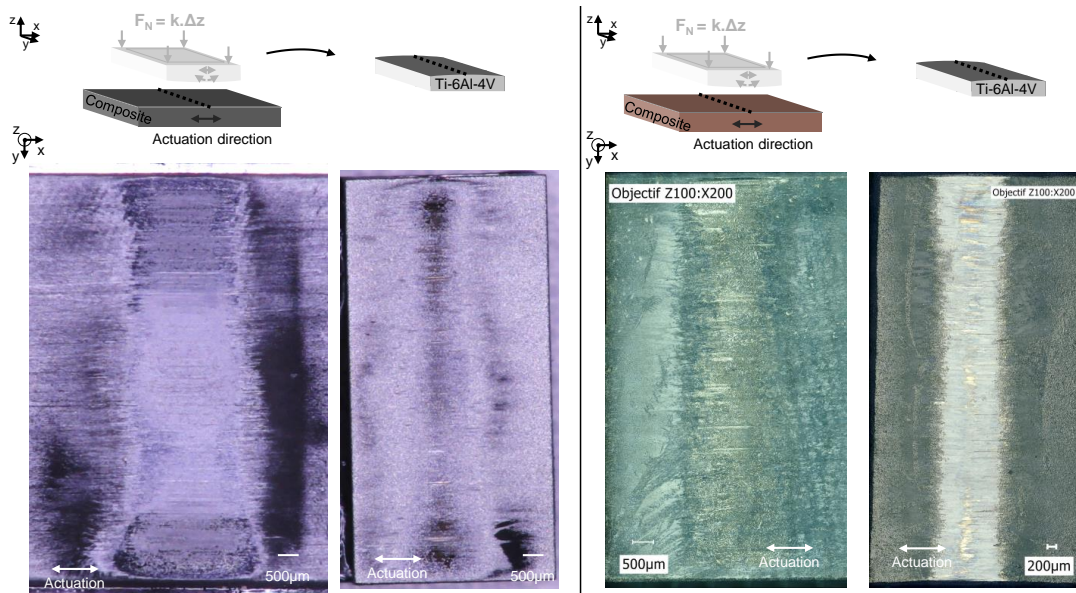
Figure 4.25 – Macroscopic view of the disassembled samples after **10^7 cycles** - **20km** with **carbon fibre filled composite** pad (on the left). Wear volume is lower than 10^6-cycles test with fibreglass filled polymer pad ([LT2] from Fig.4.18 on the right).

---

[7]They are intentionally not disclosed here to protect the composition of the composite.
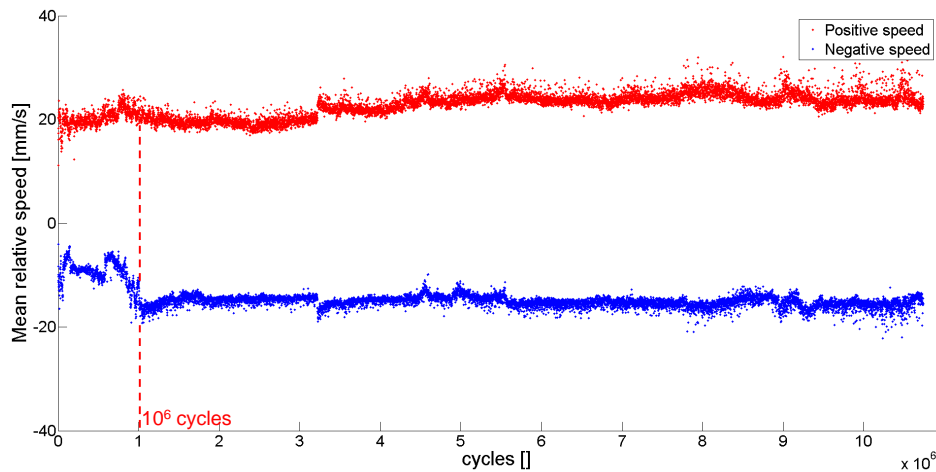
Figure 4.26 – Mean speed in [LT4]: coated Ti-6Al-4V pin *vs.* carbon fibre filled polymer pad for 10^7 cycles. In comparison with [LT3] from Fig.4.23, tribological running-in phase lasts longer -10^6 cycles before speed stabilizes until 10^7 cycles.

4.4 Perspectives

4.4.1 Checking reproducibility

All along this tribological investigation, a consistence occurred between the different tests. However, a first and direct perspective would be reproducing them to ensure the scope of the conclusions. In particular, long-term tests [LT1] and [LT2] are critical since they will drive design choices of future SPA.

4.4.2 Characterizing the tribological solicitations of the new triplet

The introduction of a carbonfibre filled polymer produced a new tribological triplet. This triplet exhibits good performances in term of wear and stable performances in lifetime test. It is now necessary to characterize it with the same methodological framework. Decrypting its tribological circuit will enable to be more confident for its integration on real SPA.

4.4.3 Closing the loop: from tribometer to SPA

Although the introduced tribometer is actuated by an APA® and the contact is preloaded with a spring, some differences with a SPA remains. In particular, with the SPA-tribometer, impact mode, highlighted by SEM observations, helps to form the 3rd body layer and to make the performance repeatable. Maybe impacts also occur in SPA but it has never been demonstrated. So, it would constitute an interesting perspective. Likewise, now the methodological framework has been set up, it could also rely on *post-mortem* observations of SPA to characterize its tribological solicitations.

The tribological part is now ended. The second part of this work will deal with the vibratory behaviour of the SPA mechanism, S_0.

Part III.

Vibratory analysis of SPA

Toward a hybrid FEM-lumped modelling of SPA

Through the analyses of both accommodation sites/modes and 3rd body flows, tribometer made it possible to improve our understanding of tribological solicitations. The purpose is now to better characterize the vibratory behaviour of SPA mechanism, S_0, responsible for step-by-step motion. The existing 1-D lumped model reaches limits when motion has to be considered in three directions of space. To address this issue, a hybrid FEM/lumped model is implemented. It relies on a modal superposition approach, without computational burden. Another interest in this model is to consider every parasitic vibrations impacting the performances of SPA, such as that of tribometer.

Introduction

Until now, the vibratory behaviour of SPA was modelled by means of a 1-D lumped model (Belly, 2011). This model reaches limits when motion in more than one direction has to be considered. For instance, the 370-Hz vibration occurring on the tribometer was not anticipated (section 3.1.1.4). In order to choose a numerical model capable of better reflecting the SPA vibratory behaviour, it becomes necessary to consider the possibility of using another numerical tool or to update the existing one.

The choice of a numerical tool depends on the scale - *macroscopic*, *mesoscopic* or *microscopic* - of the addressed phenomenon (Renouf et al., 2011). However, because a tribological system relies on several scales, no current calculation code is yet capable of modelling the whole tribological triplet (Fig.5.1-a):

- *Macroscopic scale* corresponds to the accommodation site S_0 - the mechanism -. It describes the global motor behaviour by means of the interactions between the piezoelectric actuator, the oscillating mass and the moving mass. This scale is mainly addressed by lumped parameter models (Fig.5.1-b) in piezoelectric motor (Liu et al., 2015). Friction is handled by static (*e.g.* Coulomb, (Coulomb, 1785)) or dynamic (*e.g.* LuGre (De Wit et al., 1995)) models. The main advantage of these models is the low calculation time. But, they are not able to predict local contact conditions and even less 3rd body flows.
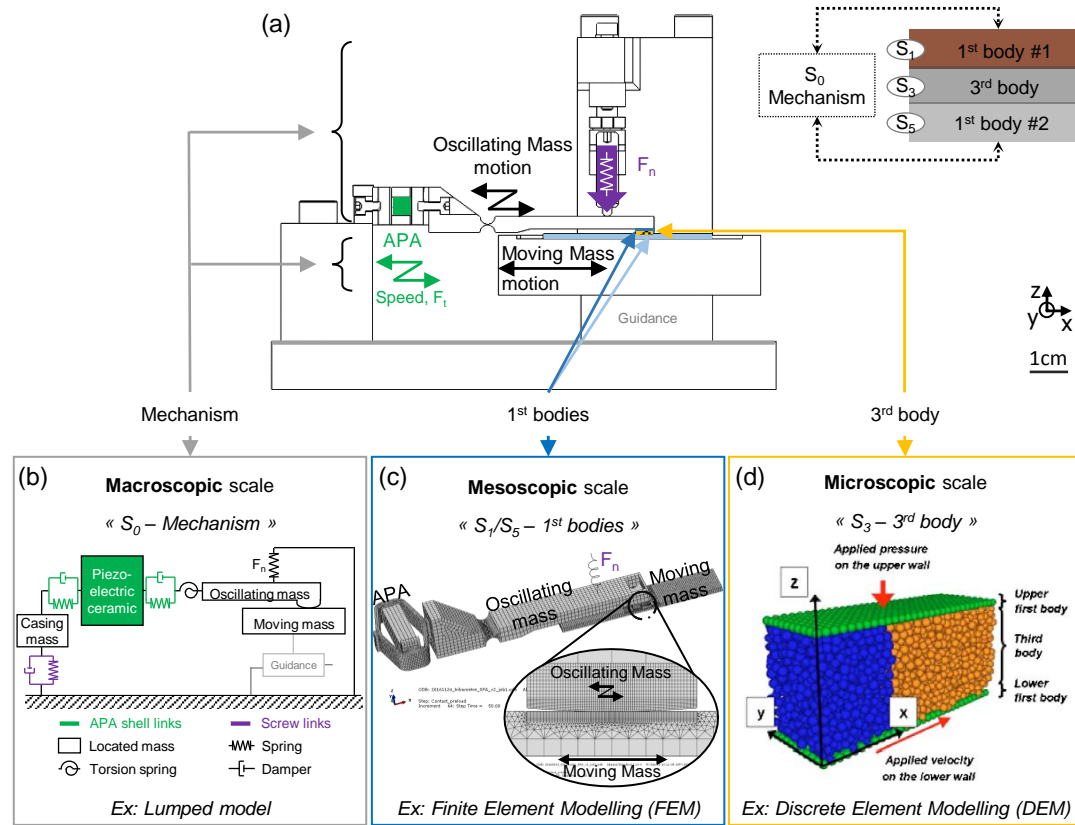
Figure 5.1 – The different modelling scales relying on the tribological triplet approach (Godet, 1984). (a) Overall representation of the SPA tribometer. Green element represents the piezoelectric ceramic.(b) S_0-Mechanism scale modelling. Here, by means of a Lumped model. (c) S_1/S_5-1st bodies scale modelling. Here, by means of Finite Element Modelling (FEM). (d) S_3-3rd body scale modelling. Example of Discrete Element Modelling (DEM) taken from Richard et al. (2007).

- *Mesoscopic scale* corresponds to the accommodation sites S_1/S_5 - the 1st bodies -. It describes local interactions between the oscillating mass and the moving mass. This scale is mainly addressed by quasi-static and dynamic continuous model such as solid mechanics Finite Element Models (Fig.5.1-c). These models give access to the deformations of the 1st bodies and to the local contact dynamics as well as to the global behaviour of the mechanism. So, they help to interpret internal source flow initiation (Q_s^i) and internal flows (Q_i). But, it remains difficult to take into account the 3rd body layer (Linck et al., 2005). In addition, calculation time quickly increases for modelling transient behaviour such as stick-slip in SPA.
- *Microscopic scale* corresponds to the accommodation site S_3 - the 3rd body-. It makes it possible to describe flows of solid particles considered as granular Discrete Elements (Fig.5.1-d). However, although recent models start to take into account the global contact geometry (Kounoudji et al., 2016), calculation time remains too high to consider the whole mechanism and so to get results comparable with previous tribological observations.

Since they do not make it possible to characterize the vibratory behaviour of SPA, Discrete Element Models are set aside in this work. In a first attempt, a dynamic implicit Finite Element Model (FEM) of the whole tribometer has been implemented on Abaqus (Fig.5.1-c). However, the number of elements necessary to capture all the physical phenomena - plasticity, stick-slip, impact - with fidelity, was estimated around 10^6 elements. Resulting calculation time was too high - about three months on a 16-

threads cluster for one stick-slip pattern -. So dynamic analysis by means of FEM was also set aside. Finally, macroscopic modelling remains the most efficient approach for both time and space scales reasonably considered in this study. But, the 1-DoF model does not represents well enough the tribometer whose the notch and the pin-on-pad contact allow motion in other directions than only that of actuation.

A multi-DoF lumped model would be complex to implement and not easily applicable to further potential structural changes. An alternative approach - so-called "hybrid" by Berger (2002) - and combining advantages of both lumped and FEM models is proposed (Fig.5.2). This method consists in getting the vibratory behaviour of a mechanism in every space dimensions with FEM and then projecting it on 1-DoF actuation direction. It can be summarised in three steps: (i) a frequency analysis is led by means of a Finite Element Modelling (FEM). The mechanical structure is then described by its modal amplitudes and spatial modes shapes; (ii) the resonance modes impacting the most the motion in actuation direction are converted into differential equations by means of an electro-mechanical analogy (see section 1.3) and concatenated into a transfer function; (iii) the lumped model is finally replaced by the obtained transfer function. Such a method has already been successfully implemented in acoustic, considering sonar (Johnson, 1990), and in contact mechanics, considering rolling bearings (Mevel, 1992). In addition, the resulting modelling method could be applicable to any SPA configuration.

To achieve such a purpose, first, the lumped model developed for SPA is recalled. Second, the hybrid FEM-lumped model is implemented on a SPA in shaft-clamp configuration. Results are compared to the first model and to measures. Third, the hybrid model is applied to the tribometer and validated experimentally. At last, the model is discussed facing with the formulated hypotheses and its validity domain.

5

Figure 5.2 – Comparison of modelling approaches against key performance criteria: ability to capture relevant problem physics, computational efficiency, and model fidelity (From Berger, 2002).

5.1 Hybrid FEM/lumped model calibration on a known case - SPA35XS

Beyond providing a better understanding of the tribometer vibratory behaviour, purpose of this chapter is to improve the current numerical sizing tool. After a brief reminder about the lumped model (section 5.1.1), the hybrid FEM-lumped method is introduced (section 5.1.2). The purpose of this section is to compare both the current and the new model on a classical SPA to validate the proposed approach.

5.1.1 Reference lumped model

The modelling of a SPA can be decomposed in two aspects: (i) the lumped modelling of the moving parts and (ii) the modelling of the friction contact (Fig.5.3).
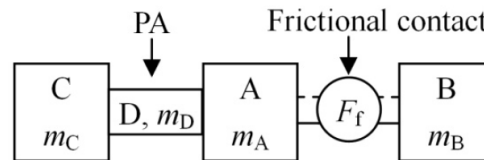
Figure 5.3 – Principle architecture of an inertia motor (From Liu et al., 2015). A: oscillating mass including friction interface #1; B: moving mass including friction interface #2; C: Ground; and D: Piezoelectric Actuator (PA); are the parts of the system. m_A, m_B, m_C and m_D are their respective masses. F_f is the frictional force between parts A and B.

Lumped modelling — Lumped approach is appropriate when the physical object has dimensions that are small relative to the wavelength of vibrations (Smith, 2017). This technique is particularly suitable when the system - mechanical here - consists in components with infinitely rigid masses that can be considered as point. Considering SPA, links between the element masses are then realised by means of springs and dampers. Integration is finally based on Newton's laws resolution.

Friction modelling — the friction contact in SPA, with its small displacements, its high relative velocity and its frequent direction changes, is more difficult to apprehend than the global dynamics and requires an elaborate model choice. Altpeter (1999) compared quasi-static modelling - whose friction force only depends on relative velocity (Fig.5.4-a) - and dynamic LuGre friction modelling (Fig.5.4-b) - which requires more parameters -. He showed that quasi-static models are sufficient for predicting large displacements while more complex model are suitable for motor targeting positioning applications. Works on motors whose step size is in the nanometer range confirms this conclusion (Breguet, 1998; Van Der Wulp, 1997; Edeler, 2011). Since Altpeter's work, numerous modelling techniques emerged. Liu et al. (2015) recently reviewed them and inventory the six models mainly used today: (i) the Coulomb model (Coulomb, 1785), (ii) the Dahl model (Dahl, 1968), (iii) the elastoplastic model (Dupont et al., 2000), (iv) the Leuven model (Ha et al., 2005), (v) the reset-integrator model (Chao et al., 2006), and (vi) the LuGre model (De Wit et al., 1995). Today, there is no general result to conclude about which model is the best suited for describing the stick-slip in SPA. Thus, LuGre model, worked out by Belly (2011), is kept.

(a)   **(b)**
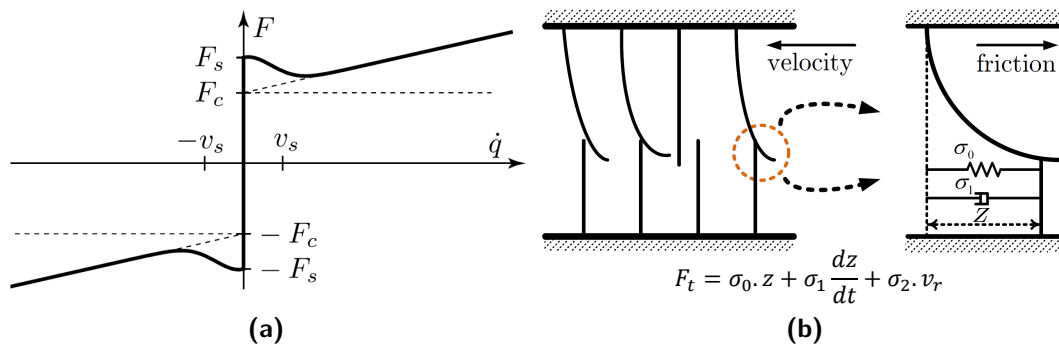
Figure 5.4 – Example of friction models. (a) Quasi-static model (From Altpeter, 1999). Friction force F is depicted depending on relative velocity $\dot{q}$. F_S, F_C and v_S are the static friction force, Coulomb friction force and Stribeck velocity respectively. (b) Dynamic LuGre friction model (Adapted from Asadian et al., 2011). The friction interface between the two antagonists is thought as a contact between bristles. For simplicity, the bristles on the lower part are shown as rigid. Related friction force F_t is obtained by means of both the elastic and damped deflection, z and $\dot{z}$, and the damped relative velocity v_r.

Lumped/friction (LuGre) modelling of SPA — As described in chapter 2, a SPA (Fig.5.5) is composed of four parts: (i) the casing, (ii) the piezoelectric actuator, (iii) the oscillator (so-called shaft in this configuration) and (iv) the moving mass (so-called clamp in this configuration). Actuation signal triggers the oscillating motion of the actuator. This oscillation is converted into displacement by means of the friction interface.
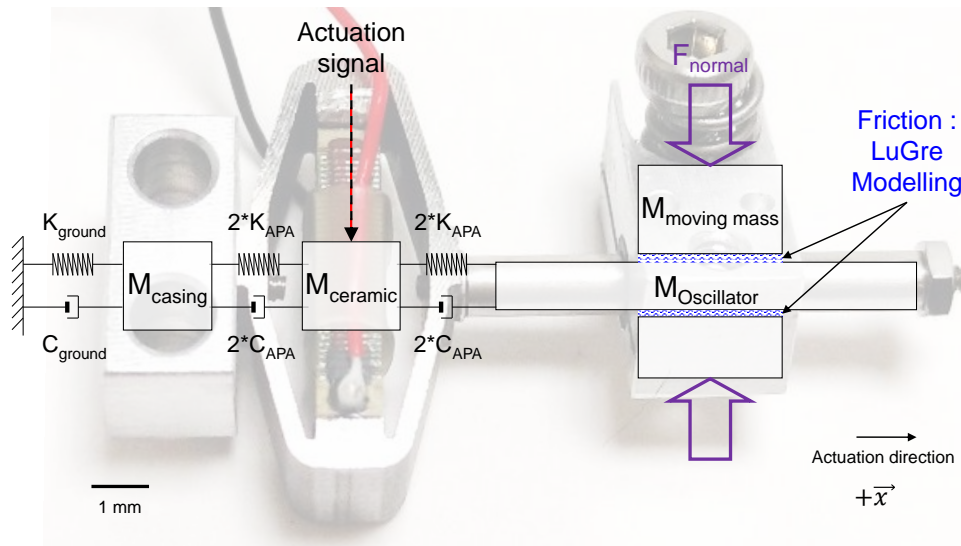
Figure 5.5 – Principle scheme of a lumped/friction model derived from Fig.5.3 applied to SPA35XS in shaft-clamp configuration (Adapted from Belly, 2011).

Related equation systems - Eq.5.1 for the Lumped model and Eq.5.2 for the LuGre friction model - are then implemented in programming software[1].

$$\begin{bmatrix} M \end{bmatrix} \begin{bmatrix} \ddot{U} \end{bmatrix} + \begin{bmatrix} C \end{bmatrix} \begin{bmatrix} \dot{U} \end{bmatrix} + \begin{bmatrix} K \end{bmatrix} \begin{bmatrix} U \end{bmatrix} = \begin{bmatrix} F \end{bmatrix} \tag{5.1}$$

---

[1]Matlab/Simulink is the software used in this work

where $[M]$, $[C]$, $[K]$ and $[F]$ are the mass, damping, stiffness and external force matrices. $\left[\ddot{U}\right]$, $\left[\dot{U}\right]$ and $[U]$ are the acceleration, velocity and displacement matrices.

$$
\begin{aligned}
F_t &= \sigma_0.z + \sigma_1.\frac{dz}{dt} + \sigma_2.v_r \\
\frac{dz}{dt} &= v_r - \frac{\sigma_0}{g(v)}.z.|v_r| \\
g(v_r) &= F_c + (F_s - F_c)e^{-(v_r/v_s)^2}
\end{aligned}
\tag{5.2}
$$

where F_t, F_s and F_c are the friction force, static friction force and Coulomb force respectively (Fig.5.4-a). v_r and v_s are the relative velocity and the Stribeck velocity respectively. Friction force is obtained by means of both the elastic and damped deflection, z and dz/dt respectively, and the damped relative velocity v_r.

Resulting predicted displacements are in agreement with measures (Fig.5.6). Main free-oscillation frequency is around 2400Hz both on measures and simulations. In both cases, parameters of the system are recalled in Table 5.1.
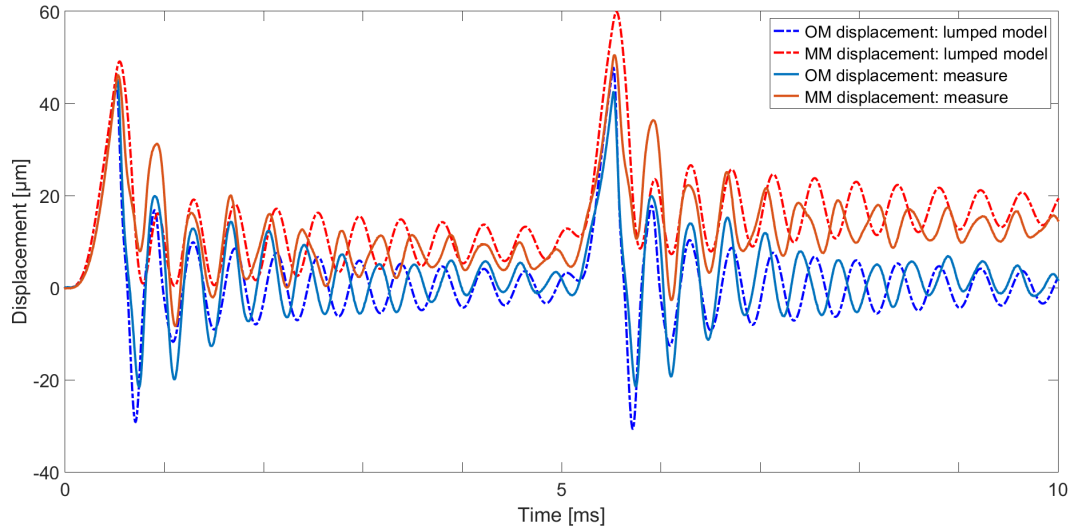
Figure 5.6 – Displacement curves from a SPA35XS with the Lumped/Friction (LuGre) model (full line for the measure and dot line for the simulation). In blue: the displacement of the oscillating mass, in red: the displacement of the moving mass.

Notice that the chosen actuation signal parameters - 2kHz parabolic signal with dead time - have been chosen to observe free oscillations. Resulting speed - 1.4mm/s - is far below what can be reached - 30mm/s -. In addition, as free oscillations are not fully damped, error on the evaluation of the 1st resonance mode results in a slight overestimation of the moving mass displacement.

Table 5.1 – Default values of the Lumped/Friction (LuGre) model parameters in Fig.5.7 and Fig.5.6.

APA	$\mathbf{M}_{casing}$ [gr]	$\mathbf{M}_{OM}$ [gr]	$\mathbf{M}_{MM}$ [gr]	$\mathbf{F}_N$ [N]	μ_s [ ]	μ_d [ ]	$\mathbf{v}_{Stribeck}$ [mm/s]	σ_0 [N/m]	σ_1 [N.s/m]	σ_2 [N.s/m]
35XS	1	0.50	0.72	5	0.40	0.30	0.1	80e6	$10\sigma_2$	2.9

Mechanical characterisation of the SPA mechanism — The vibratory behaviour of a mechanism is characterized by its resonances frequencies and so by its modal landscape. In chapter 3, admittance measure was used to assess the resonance frequencies of the tribometer, "seen" by the piezoelectric ceramic. In addition to these electro-mechanical modes, linearising Eq.5.1 in actuation direction also leads to mechanical resonance modes and so to the complete modal landscape of the mechanism in actuation direction (Fig.5.7). Such a modal landscape can also be obtained experimentally by using a frequency analyser and a laser vibrometer[2]. Results exhibit a quite good correlation between measures and model considering resonance modes in actuation direction - at $\text{fr}_{1-model} = 2400\text{Hz}$ (1.4% error) and $\text{fr}_{2-model} = 5742\text{Hz}$ (4.1% error). These modes correspond to the resonances of the APA® hinges acting like springs. It also emphasizes the occurrence of resonance modes in other directions than that of actuation such as bending modes (at 367Hz, 2817Hz and 4016Hz in the frequency range considered in Fig.5.7). The hybrid approach proposed in the next section consists in taking into the contribution of these other modes onto the actuation direction of the motor.
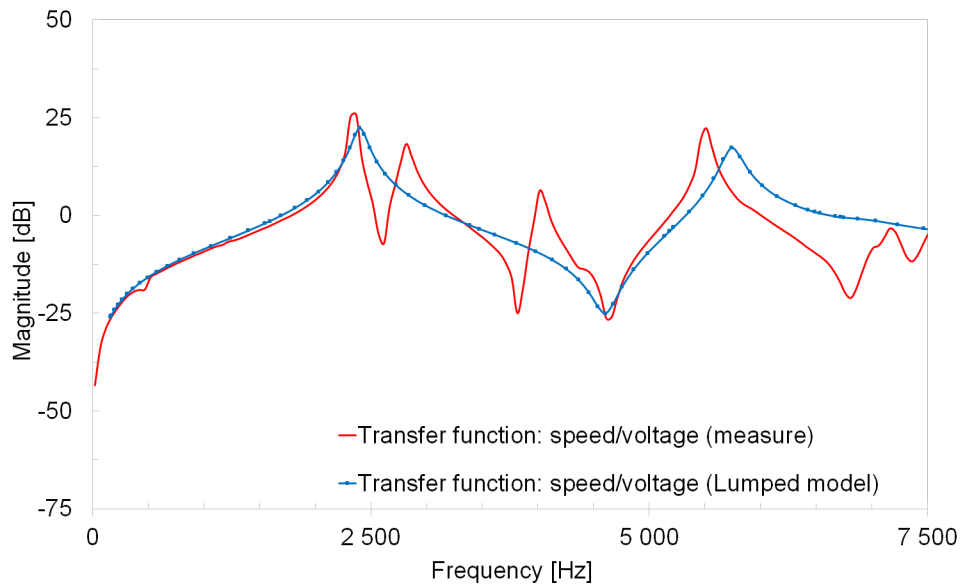
Figure 5.7 – Transfer function of a SPA35XS in term of speed/voltage. In red: laser measures (fr_1 = 2367Hz and fr_2 = 5515Hz). Notice that linearisation considers friction interface as a spring link. In dot-blue: simulation from Lumped/Friction (LuGre) model (fr_1 = 2400Hz and fr_2 = 5742Hz).

5.1.2 Hybrid FEM-Lumped model

Thus, the lumped model of the motor is based on a differential equation system formulated from Newton's laws. If only the actuator is considered, without friction, this system can be linearised. Transfer function is the result of this linearisation, in actuation direction. Purpose of the next section is to use a FEM model instead of a lumped model to generate the transfer function of the actuator, in order to take into account the motion in every space dimensions.

---

[2]The frequency analyser generates a sine order with a constant voltage amplitude and a varying frequency. At the resonance frequencies, SPA's speed of oscillation increases, what is measured by the laser vibrometer and sent back to the analyser. At last, it displays the transfer function: T(fr)=speed/voltage.

Hybrid modelling method consists in three steps (Fig.5.8): (i) a frequency analysis is led on the motor by means of FEM (section 5.1.2.1). Outputs of this analysis are the resonance mode shapes and their contribution to motion in actuation direction by using a Cumulative Effective Mass Participation Factor (CEMPF) (Ahmad et al., 2016). (ii) The most impacting resonance modes are extracted and converted into one transfer function by means of a modal superposition approach (section 5.1.2.2). (iii) The resulting differential equation system is implemented in place of the lumped model in conjunction with the LuGre model to get the global vibratory behaviour of the SPA (section 5.1.2.3).
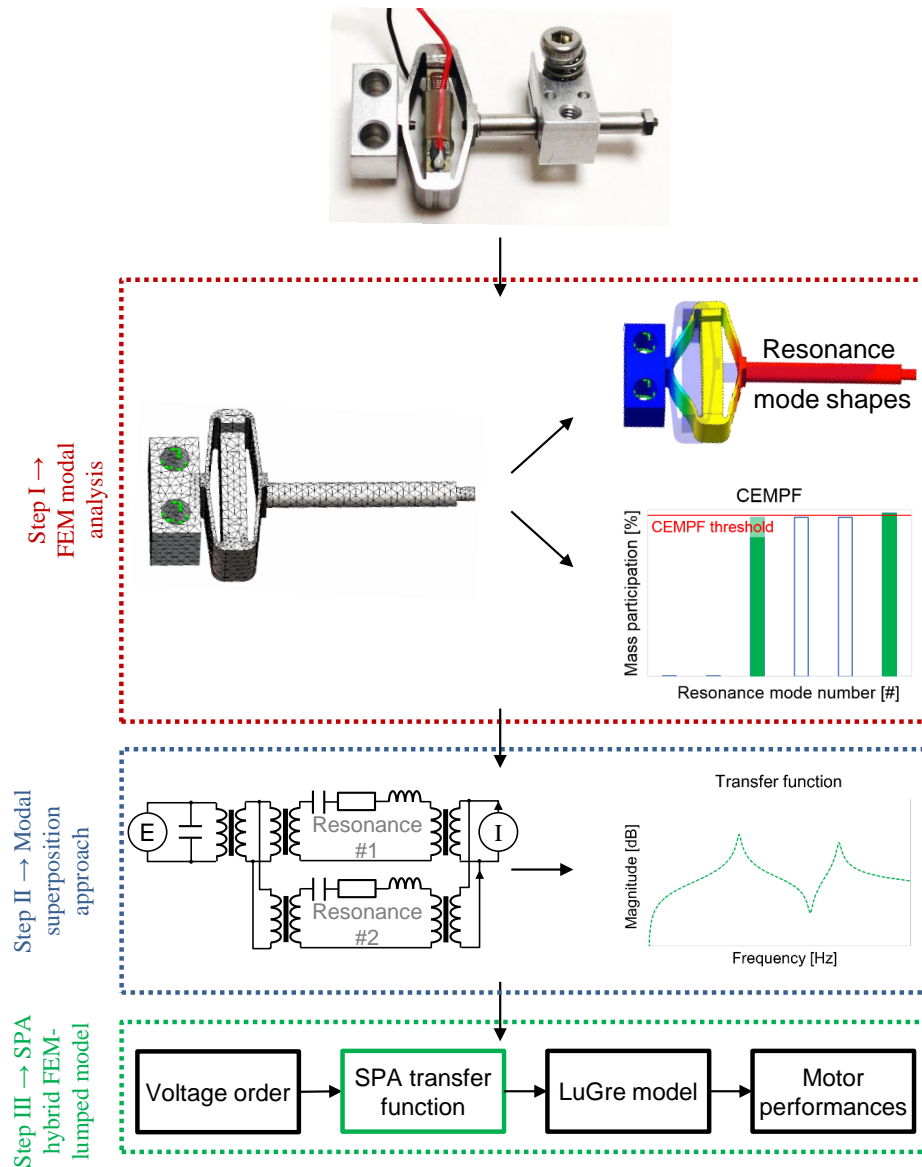
Figure 5.8 – Flow chart of the hybrid FEM-Lumped modelling method implemented for SPA. The presented method is decomposed in three step (color boxes). In step #1 and #2, the numerical tool considered (on the left-hand side) gives outputs (on the right-hand side) which are used for the following step. The resulting transfer function (green box in step #3) is implemented to get the motor performances.

5.1.2.1 Step #1: FEM characterisation of SPA35XS mechanism

FEM characterisation of the mechanism is realised by means of a modal analysis. It consists in solving the equation system 5.1 to determine the natural mode shapes and frequencies. As for any FEM simulation, steps are (i) design, (ii) material properties, (iii) choice of boundary conditions, (iv) mesh and (v) solving. Such a method is classical and already used for designing all the APA®. To be as representative of the motor in operating conditions, full boundary conditions are imposed in screw slots (Fig.5.9). Clamp is considered as a fictive mass to decrease the mesh size.
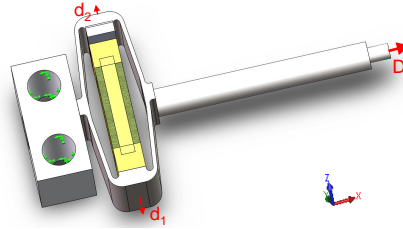
Figure 5.9 – Boundary conditions and nodal notations applied to a SPA35XS for getting its resonance frequencies and its transfer function: D = f(d$_1$ - d$_2$).
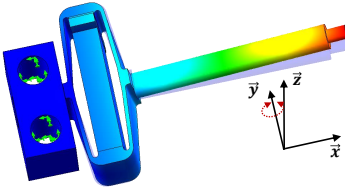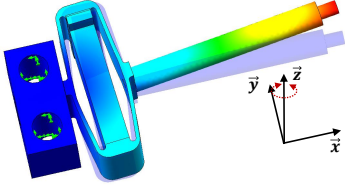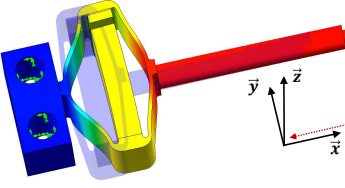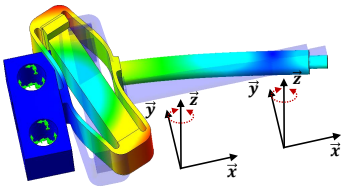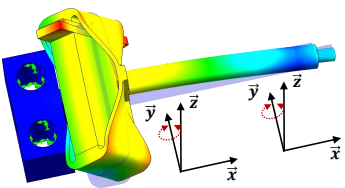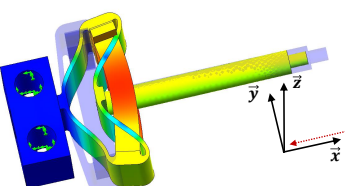
The resulting modes (Table 5.2) can be compared to previous measures (Fig.5.7). Both actuation modes are well identified with 2.8% and 4.4% error respectively, what is consistent with manufacturing dispersion. In addition, one could notice that the resonance modes in other directions than that of actuation (so not taken into account by the lumped model) are well evaluated by FEM.

Focus is now done on the contribution of each mode on actuation direction. Cumulative Effective Mass Participation Factor (CEMPF) is a common indicator to determine it (Ahmad et al., 2016). The mass participation represents the amount of system mass moved by one resonance mode. Therefore, a mode with a large effective mass is a significant contributor to the system's response. There is no admitted value for the cumulative participation threshold. Solidworks website indicates 80% of mass participation while it increases to 95% for spatial requirements (confidential report). For the rest of this work, the highest value is kept. Considering the CEMPF and in accordance with lumped modelling (Fig.5.7), it comes that only actuation mode #1 and #2 are sufficient to characterize the vibratory behaviour of a SPA35XS (Fig.5.10). Only these two contributions will be kept in the following sections.
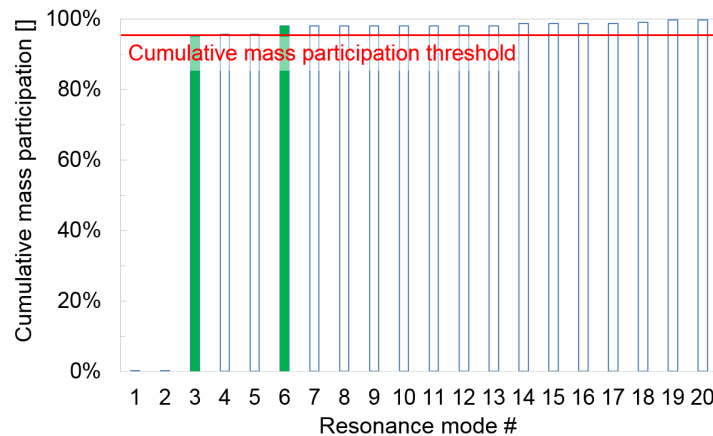
Figure 5.10 – SPA35XS Cumulative Effective Mass Participation Factor (CEMPF). Based on a 95% threshold, only the contribution of both actuation modes (Table 5.2) are kept (green bars).

Table 5.2 – Frequency analysis of a SPA35XS by means of Finite Element Modelling (FEM). Associated spatial mode shapes are also described. Colour scale depicts the displacement scale: blue = no displacement, red = maximal displacement. Initial position of the SPA35XS is depicted in blue shade.

Mode number	Related frequency	Denomination	Mode shape
#1	333Hz	bending mode #1	
#2	386Hz	bending mode #2	
#3	2434Hz	**actuation mode #1**	
#4	3032Hz	dual-node bending mode #1	
#5	4513Hz	dual-node bending mode #2	
#6	5285Hz	**actuation mode #2**	

5.1.2.2 Step #2: Modal superposition: FEM to transfer function

Now that the vibratory behaviour of the SPA35XS is characterized, purpose is to convert the main resonance modes and their respective shapes into differential equations. It is realised by means of a modal superposition approach. Such an approach relies on an electro-mechanical analogy (table 5.3). To do so, Mason scheme (Mason, 1948) is used again as in section 1.3. Assumptions are recalled before the implementation of the transfer function in conjunction with the friction model.

Table 5.3 – Electro-mechanical analogy.

Electrical notations			Mechanical notations			Conversion Ratio
Capacitance	C	[F]	Elasticity	e	[m/N]	$1/N^2$
Inductance	L	[H]	Mass	m	[kg]	N^2
Resistance	R	[Ω]	Damping	C	[kg/s]	N^2
Electrical charge	q	[C]	Displacement	u	[m]	$1/N$
Current	i	[A]	Speed	v	[m/s]	$1/N$
Voltage	V	[V]	Force	F	[N]	N

Assumptions — The use of a modal superposition approach induces restrictive hypotheses which are stated below (Le Letty, 1994)

- Modal deformations are calculated from a finite element model. Resolution of the resulting differential equation system occurs before the resolution of the overall system including the friction model. It is therefore assumed that these modal deformations are not affected by the mechanism of the contact. This hypothesis may seem realistic if we consider that most of the deformation due to the contact is localised at the friction interfaces. A particular attention will be paid to this point since it limits the validity domain for soft actuators.

- Modal superposition approach assumes that the resonance modes are independent from each other. Rigorously, this hypothesis is no longer satisfied when we consider the effect of mechanical losses. These losses will be considered and discussed as modal damping coefficients, which is a classical assumption in dynamic structural analysis (Bathe, 2006).

- The used transient integration scheme assumes a linear variation of the acceleration during the time increment *dt*. This hypothesis may be defeated during an impact for instance. Most digital difficulties can be overcome by choosing a sufficiently small time step or by introducing numerical damping (Zienkiewicz and Taylor, 1977). This point will be also discussed since it limits the consideration of the impact mode observed in previous chapters.

From FEM to transfer function — Based on the CEMPF criteria, only two resonance modes are sufficient to characterize the vibratory behaviour of a SPA35XS. This can be summarised to an equivalent electrical circuit - which links the voltage order (and so the deformation of the ceramic: d_1 - d_2) to the displacement of the oscillating mass D (Fig.5.9) - through two motional branches (Fig.5.11). Mason scheme introduced in section 1.3 is formulated to take into account both the modal deformations and displacement. Only new topology is introduced thereafter, notations such as C_{piezo}, C_i, R_i, L_i, E and I have already been presented. FFEP is the piezoelectric ceramic modal

5

force factor. Under the assumption where hysteresis of the piezoelectric ceramic is not considered, FFEP convert the voltage applied to the ends of the ceramic into the blocked force they can generate. It is a fixed data depending on the used piezoelectric ceramic. FFM_i is the piezoelectric modal force factor at the resonance "i". It corresponds to the conversion of the force generated by the ceramic into deformation (d_{1i} - d_{2i}). D_i is the contribution to the displacement of oscillating mass at this resonance. D_i, d_{1i} and d_{2i} are the output data of the FEM frequency analysis.
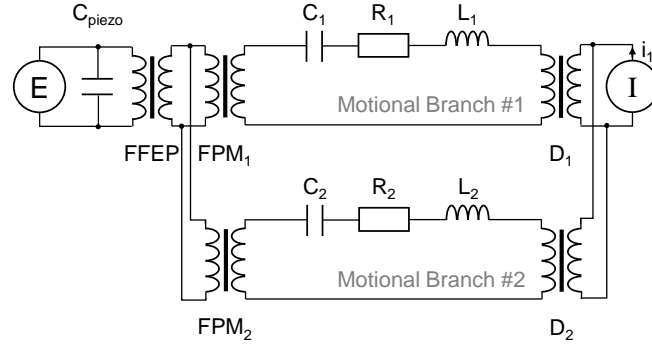
Figure 5.11 – Electro-mechanical analogy of a piezoelectric actuator characterized by two resonance modes (= two motional branches).

Transfer function of one mode "i" can be wrote as:

$$H_i(j\omega) = \frac{FFEP.FFM_i.L_i.C_i.D_i}{1 + R_i.C_i.j\omega + L_i.C_i(j\omega)^2} \tag{5.3}$$

The vibratory behaviour of the actuator is then described by superposing both motional branches.

$$H(j\omega) = \sum_i H_i(j\omega) \tag{5.4}$$

Proof (one notes N_i = FFEP.FFM$_i$):

$$E.N_i.D_i = R_i I_i + L_i \frac{dI_i}{dt} + \frac{1}{C_i} \int I_i dt$$
$$I_i = \frac{du_i}{dt} \tag{5.5}$$

with u_i, output displacement.

$$E.N_i.D_i = \frac{1}{C_i} \left(R_i.C_i \frac{du_i}{dt} + L_i.C_i \frac{d^2 u_i}{dt^2} + u_i \right) \tag{5.6}$$

In complex notations:

$$E.N_i.C_i.D_i = u_i.\left(R_i.C_i.(j\omega) + L_i.C_i(j\omega)^2 + 1 \right) \tag{5.7}$$

As the transfer function which interests us is $H_i(j\omega) = \frac{u_i}{E}$, it comes

$$H_i(j\omega) = \frac{N_i.C_i.D_i}{1 + R_i.C_i.j\omega + L_i.C_i.(j\omega)^2} \tag{5.8}$$

Previous equation is similar to a second order driven harmonic oscillator.

$$H_i(j\omega) = \frac{H_{0,i}}{1 + \frac{1}{Q_i}.j(\frac{\omega}{\omega_{0,i}}) + (j\frac{\omega}{\omega_{0,i}})^2} \tag{5.9}$$

with $H_{0,i} = \dfrac{N_i.C_i.D_i}{\omega_{0,i}^2}$, $w_{0,i} = 2\pi.f_{0,i}$, $f_{0,i}$ is the resonance frequency #i, and Q_i is the associated quality factor (acting as modal damping).

It can be reformulated to exploit FEM output data:

$$H_i(j\omega) = FFEP.\frac{\frac{(d_{1i} - d_{2i}).D_i}{\omega_{0,i}^2}}{1 + \frac{1}{Q_i}.j(\frac{\omega}{\omega_{0,i}}) + (j\frac{\omega}{\omega_{0,i}})^2} \tag{5.10}$$

Transfer function resulting from frequency analysis can then be plot and compared to the previous model and to measures (Fig.5.12).
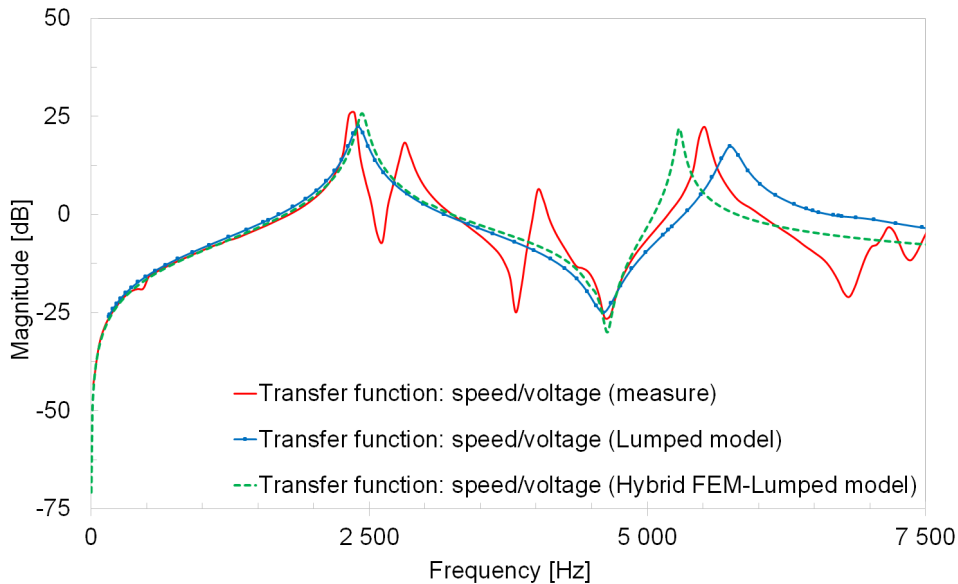
Figure 5.12 – SPA35XS transfer functions resulting from hybrid FEM frequency analysis and modal superposition approach (green dash curve), measure (red curve) and lumped model (blue dot curve). Transfer function from FEM depicts speed instead of displacement in term of voltage to be comparable with previous Fig.5.7.

5.1.2.3 Step #3: Implementation of the hybrid model

Next step is the implementation of both the transfer function and LuGre model to describe the vibratory behaviour of the SPA35XS (Fig.5.13).

Voltage order is first formulated, and sent to a proxy of the electronic linear amplifier (see section 1.3). Resulting amplified voltage order is converted into the acceleration of the oscillating mass by means of previously defined transfer function.

The LuGre model has been described in Belly (2011) and is directly used here. It requires as input the relative speed between the oscillating mass and the moving mass. Output is the friction force.

Friction force transferred to the moving mass is finally integrated twice to get its displacement.
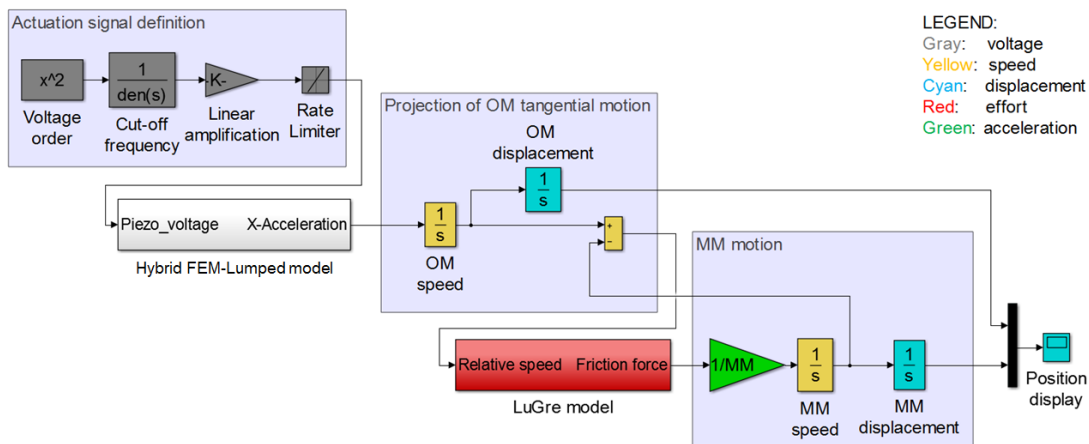
Figure 5.13 – Simulink block diagram of the hybrid FEM-lumped modelling implemented for SPA.

As for lumped modelling, displacements curves are in good agreement -in terms of stepsize amplitude and free oscillation behaviour predictions- with measures (Fig.5.14), what validates the hybrid model for the SPA35XS. Next step is to apply the same method to the SPA-tribometer.
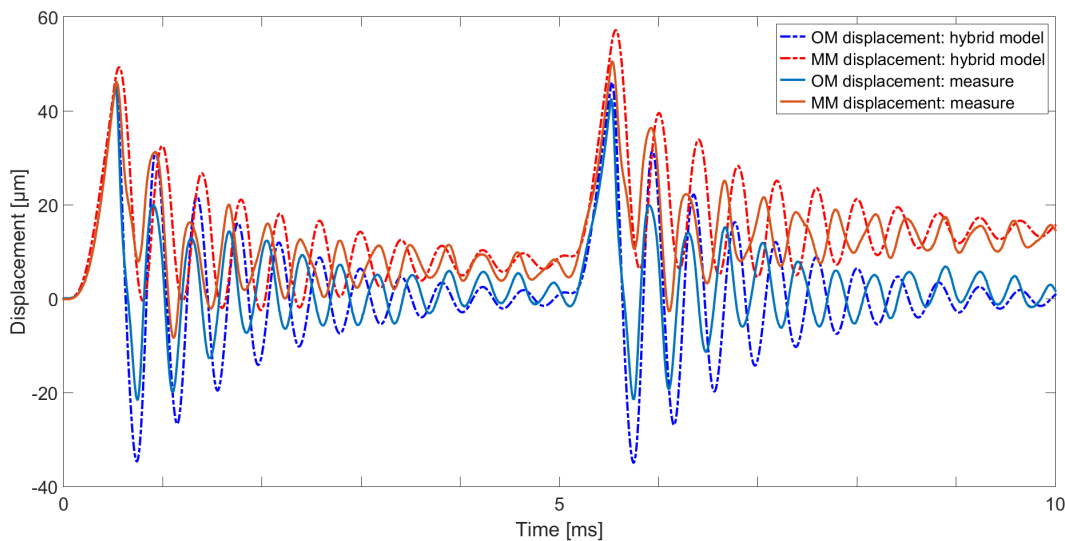
Figure 5.14 – Displacement curves from a SPA35XS with the hybrid FEM/lumped model (full line for the measure and dot line for the hybrid model). In blue: the displacement of the oscillating mass, in red: the displacement of the moving mass. Quality factor have been set (assumption #2) to 10 and 8 for the mode #1 and #2 respectively.

5.2 Model test: application to the SPA-tribometer

Now the hybrid model is validated on a known case, it is applied to the tribometer. To do so, the same method is applied: (i) FEM characterisation of the tribometer by means of a frequency analysis, (ii) formulation of a transfer function composed

by the resonance modes impacting the most the motion in actuation direction (iii) implementation in conjunction with LuGre model.

Step #1: FEM characterisation of the SPA-tribometer — As for the SPA35XS, full boundary conditions are imposed in screw slots (Fig.5.15). Moving mass is considered as a fictive mass to decrease the mesh size. In addition, preload spring is considered as an additional equivalent mass ($m_{eq} = 1/3$ spring mass, Thomson and Dahleh, 1998). Friction pad is also considered to set a slider boundary condition on the flat pad. This point will be discussed.
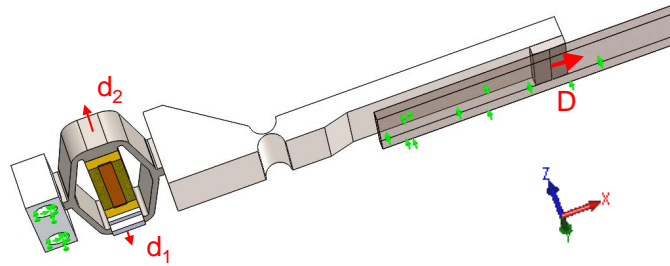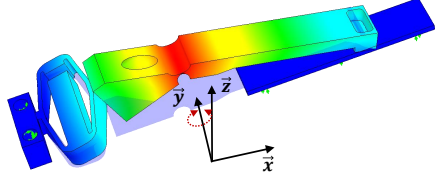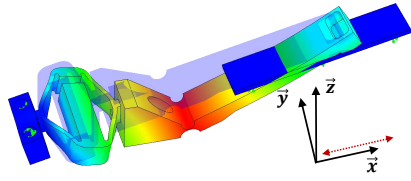
Figure 5.15 – Boundary conditions and nodal notations applied to the SPA-tribometer for getting its resonance frequencies and its transfer function. Full boundary conditions are imposed in screw slot and contact plan boundary condition is imposed on pin.

Resulting CEMPF indicates that resonance modes #6 and #7 are the most significant for actuation motion (Fig.5.16). Notice that the first three resonance modes are rigid body modes of the friction pad in three space dimensions. Modes #4 and #5 are actuator bending modes as in the previous section. The modal identification emphasizes that the mode #6 corresponds to the bending of the oscillator notch at 361Hz (Table 5.4), which is consistent with the frequency of the free oscillations observed on measures in chapter 3. Thus, it becomes necessary to take this mechanical mode into account for predicting the performances of the SPA-tribometer.
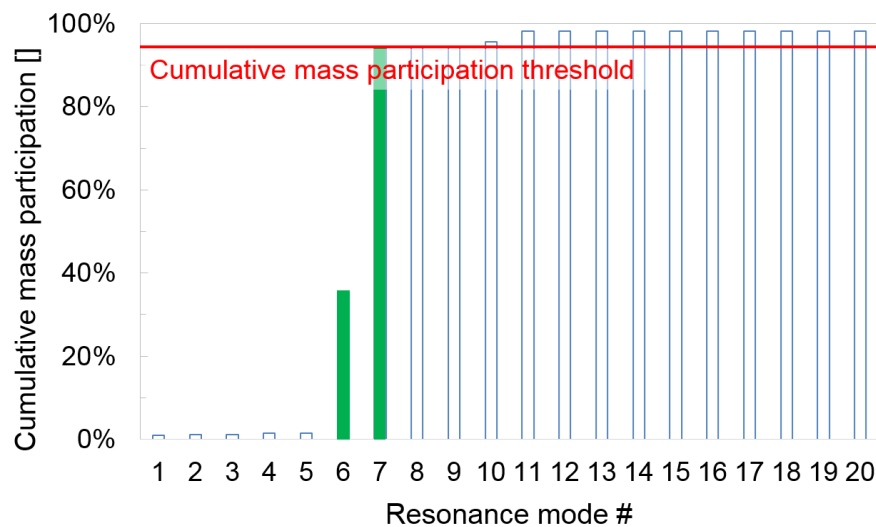
Figure 5.16 – SPA-tribometer CEMPF. Based on a 95% threshold, only the contribution of 1st actuation mode and notch bending mode (Table 5.4) are kept (green bars).

Table 5.4 – Frequency analysis of the SPA-tribometer by means of FEM. Only the modes whose CEMPF indicates that they impact the actuation are presented. Associated spatial mode shapes are also described. Colour scale depicts the displacement scale: blue = no displacement, red = maximal displacement. Initial position of the tribometer is depicted in blue shade.

Mode number	Related frequency	Denomination	Modal deformation
#6	361Hz	notch bending mode	
#7	782Hz	tribometer actuation mode #1	

Step #2: FEM to transfer function — Transfer function resulting from frequency analysis can be plotted and compared to that obtained with the lumped model and to measures (Fig.5.17). For both models, the first actuation mode is well predicted. In addition, the transfer function stemming from FEM also well predicts the bending mode of the notch.
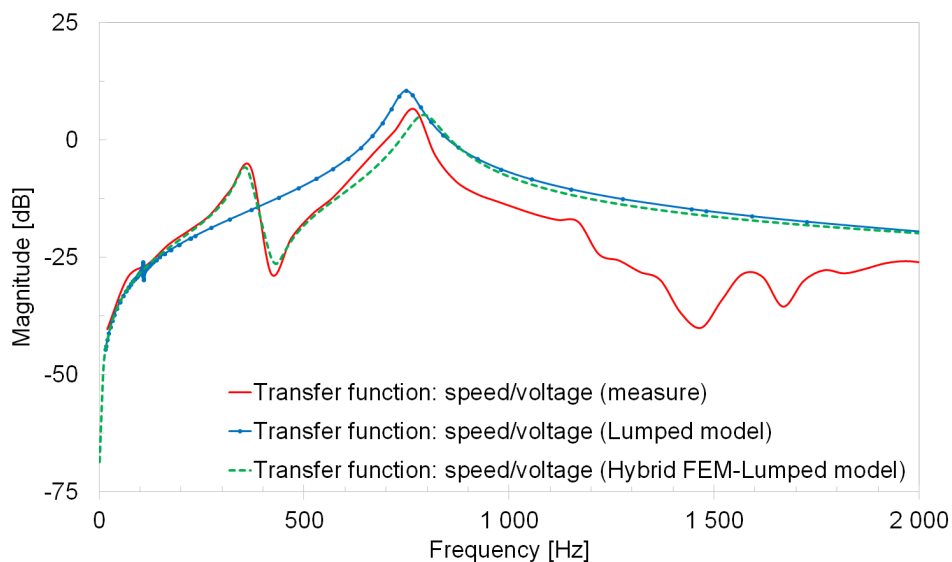
Figure 5.17 – SPA-tribometer transfer functions resulting from FEM frequency analysis and modal superposition approach (green dash curve), measure (red curve) and lumped model (blue dot curve).

Step #3: Hybrid model — The notch bending resonance mode now appears in displacements curves (Fig.5.18). Thus, although the assumption of a linear model does

not make it possible to take into account the asymmetry, simulation results are in better agreement with measures, what validates the hybrid model for the tribometer.
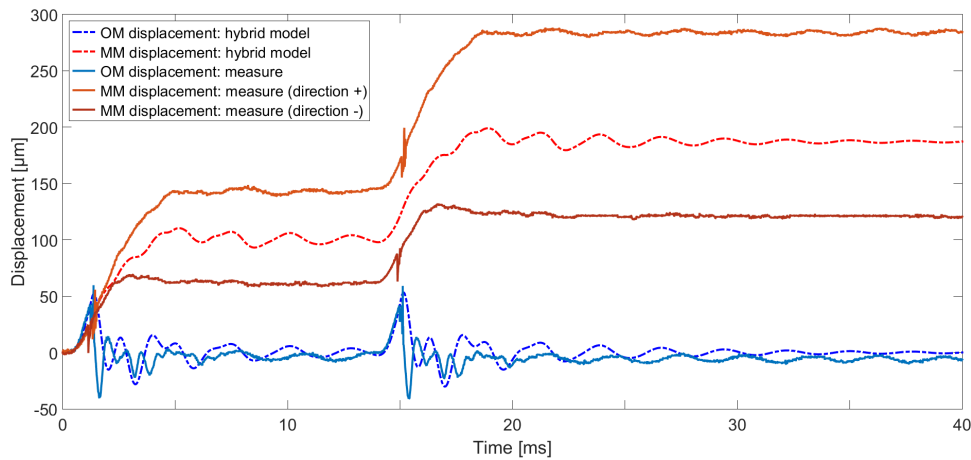
Figure 5.18 – Displacement curves from the SPA-tribometer with both the hybrid model and measures (full line for the measure and dot line for the hybrid model). In blue: the displacement of the oscillating mass, in red: the displacement of the moving mass. Quality factors have been set to 8 and 5 for the modes #1 and #2 respectively.

5.3 Discussion and limits

Hybrid model makes it possible to simulate both a SPA35XS and the SPA-tribometer but it is now necessary to discuss the starting assumptions in order to delimit its validity domain. In particular, first, considering that the modal deformations are not affected by the contact mechanism is a valid hypothesis as long as the actuator stiffness is high enough (section 5.3.1). Second, as in any FEM model, the choice of boundary conditions directly impacts the location of the resonance modes and the associated deformation shapes. The hybrid FEM-lumped model is not an exception (section 5.3.2).

5.3.1 Frontiers of validity domain

Such an introduced model is consistent as long as the contact mechanism and so friction force does not affect the actuator dynamic (assumption #1). In order to test its limits, the model is now applied to a softer motor - SPA30μXS - whose stiffness is 8.0 10^4 N/m [3].
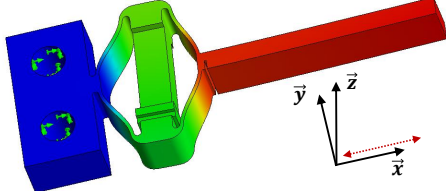
As previously, resonance modes which present the most important contribution are extracted by CEMPF (Fig.5.19), here the #3 only. Related deformation shape (Table 5.5) is converted into transfer function with modal superposition approach (Fig.5.20). However, the resulting displacement curve is not in agreement with measures (Fig.5.21).

---

[3]In comparison with a SPA35XS and the SPA-tribometer whose stiffness are 4.9 10^5N/m and 1.8 10^6N/m respectively.
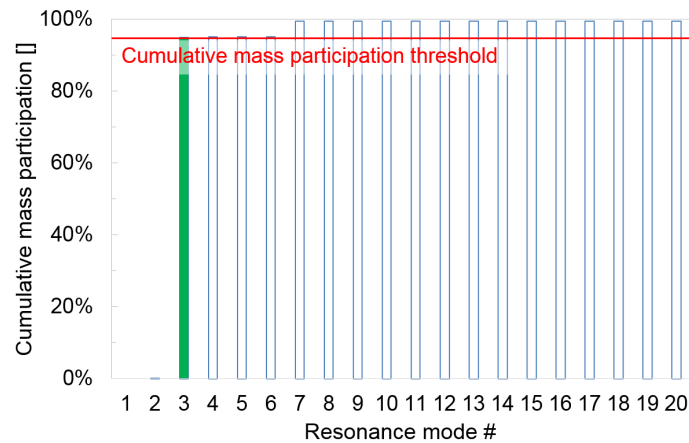
Figure 5.19 – SPA30μXS CEMPF. Based on a 95% threshold, only the contribution of the fisrt actuation mode (#3) (Table 5.5) is kept (green bars).

Table 5.5 – Frequency analysis of a SPA30μXS by means of FEM. Only the mode whose CEMPF indicates that it impact the actuation is presented.

Mode number	Related frequency	Denomination	Modal deformation
#3	2257Hz	Actuation mode #1	
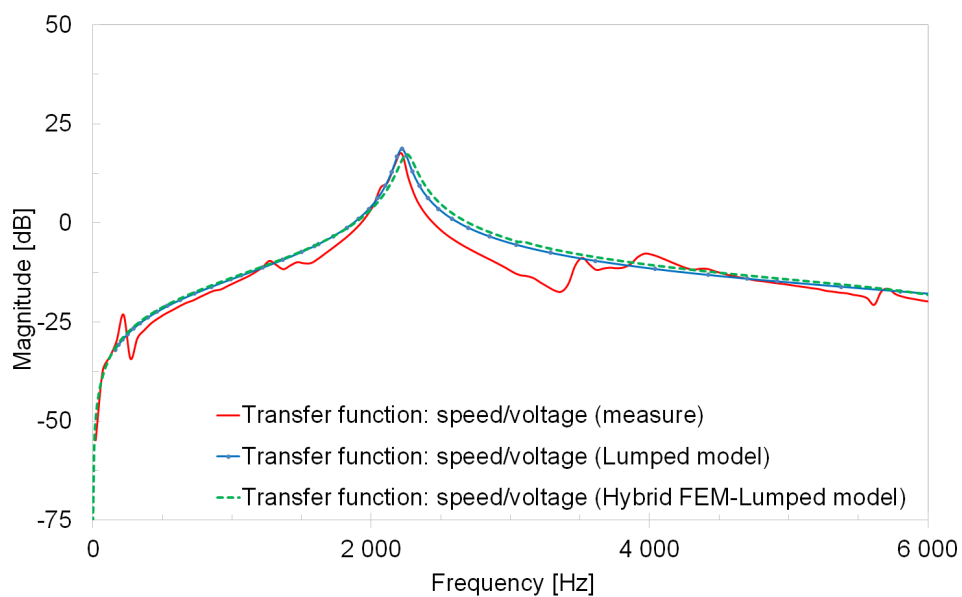
Figure 5.20 – SPA30μXS transfer functions resulting from FEM frequency analysis and modal superposition approach (green dash curve), measure (red curve) and lumped model (blue dot curve). For the FEM curve, damping factor have been set to 15.
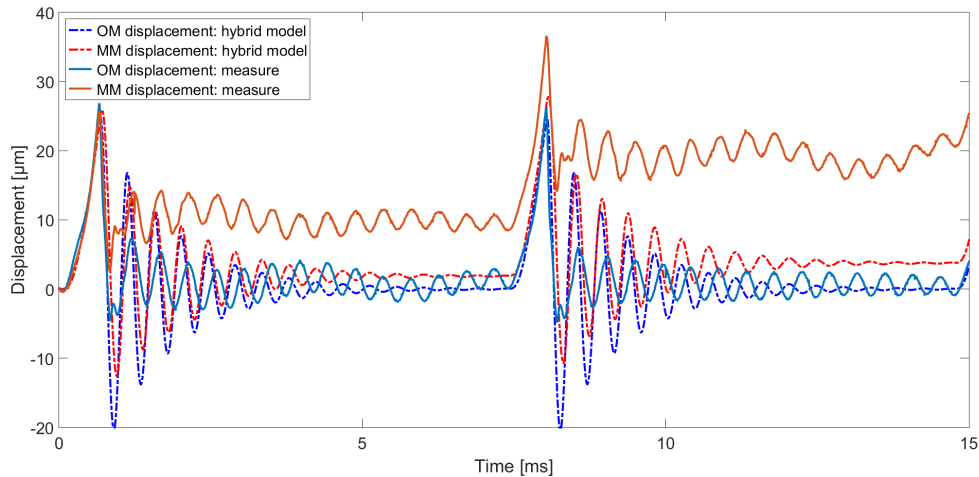
Figure 5.21 – Displacement curves from the SPA30μXS with both the hybrid model and measures (full line for the measure and dot line for the hybrid model). In blue: the displacement of the oscillating mass, in red: the displacement of the moving mass. Quality factor has been set to 10.

To ensure that the problem comes from the effect of the contact mechanism on the modal deformation, the previous transfer function is decomposed in equivalent masses, springs, dampers - as in the original lumped model (Belly, 2011) -. $\omega_{0,i}$, d_i and D_i coming from FEM are kept. Notice that FEM calculation implies a normed matrix mass. So, it is necessary to multiply the resulting differential equation by the equivalent mass of the actuator before being implemented in the lumped model. To get it, Furutani et al. (1998) propose to distribute the mass of the piezoelectric element in half on each of both the oscillating mass and the casing mass. In addition, as for the preload spring of the SPA-tribometer, masses of the elastic flexure hinges of the APA® are considered as additional equivalent masses ($m_{eq} = 1/3$ spring mass, Thomson and Dahleh, 1998). Resulting oscillating mass is evaluated to 0.7gr. Resulting displacement predictions are now in agreement with measures.
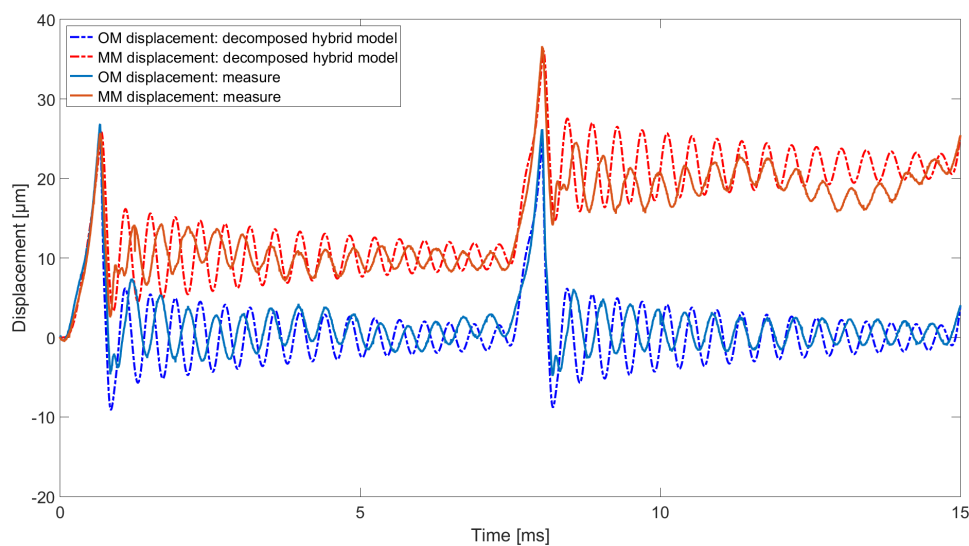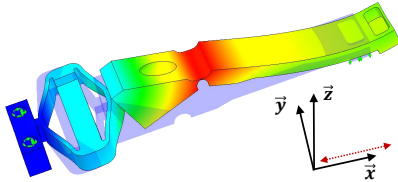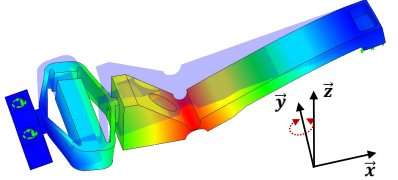
Figure 5.22 – Displacement curves from the SPA30μXS with the hybrid model decomposed in lumped model (full line for the measure and dot line for the hybrid model). In blue: the displacement of the oscillating mass, in red: the displacement of the moving mass. This confirm that contact mechanism can not be underestimated for soft actuators.

Thus, the hybrid model such as implemented above give consistent results as long as the force provided by the actuator is high in front of the friction force. It is nevertheless possible to model softer actuator. Indeed, in the proposed integration scheme (Fig.5.13), the transfer function representing the actuator admit only one input: the actuation signal. By decomposing this transfer function, it becomes possible to take into account more than one external force in system 5.1. However, as soon as two or more resonance modes are necessary for characterizing the actuator, one has to decide how distributing the friction force and so the formulation of the differential equation system would become quite biased. The best remaining option would be the formulation of a lumped model in the significant space directions, but the versatility of the introduced method would be lost.

5.3.2   Effect of FEM boundary conditions

With Finite Element Modelling, it is easy to get results. However, accuracy of the results depends on the choices of the modeller. In frequency analyses, these choices are limited to the definition of material properties, to the mesh quality and to the boundary conditions. This last one is may be the most subjective. Considering the tribometer, one could imagine to impose a slider boundary condition on the cylinder pin contact instead of to the flat pad by supposing a rotation around the cylinder (Table 5.6). However, it results in the inversion of the two main resonance modes identified in Table 5.4. This emphasizes that the proposed numerical tool requires a critical analysis to be used.

Table 5.6 – Frequency analysis of the SPA-tribometer by means of FEM with a slider boundary condition imposed to the cylinder pin instead of to the flat pad. Main resonance modes are inverted in comparison with Table 5.4.

Mode number	Related frequency	Denomination	Modal deformation
#2	658Hz	actuation mode #1	
#3	1019Hz	notch bending mode	

5.4 Conclusion

5.4.1 Summary: a versatile sizing tool

In this chapter, a hybrid FEM-lumped model - including the LuGre friction model developed by Belly (2011) - has been implemented. It consists in modelling the vibratory behaviour of SPA by replacing the 1-DoF lumped model by a transfer function, stemming from both a Finite Element Model and a modal superposition approach. This transfer function is composed of the resonance modes, whatever their space dimensions, which impact the most the SPA motion in actuation direction. This upgraded model is more versatile: it makes it possible to get the performances of SPA no matter their mechanical structure[4]. It can help to determine the potential of future SPA structure which have not been imagined yet.

5.4.2 SPA-tribometer vibratory behaviour: a structure to optimise

The SPA-tribometer was designed by using the 1-DoF lumped model. Nevertheless, a resonance mode, stemming from the notch, was not anticipated. This notch was designed to avoid stress concentration into the APA® shell because of expected wear. But, if tribometer stiffness in actuation direction was good enough in front of other sizing criteria, the resulting low stiffness in other space dimensions highlights that this structure is not optimal in term of vibratory behaviour. In addition, wear considerations indicate that such a notch was not necessary. In addition, the trust direction of the APA® is not coincident with the friction force. This induces a momentum around the contact cylinder. One assume that it is the main cause of the observed asymmetry. Indeed as chalk sliding with an acute or an obtuse angle on a black board, friction behaviour is different for backward and forward motion (Rabinowicz, 1956). Limiting this momentum by both decreasing the distance between the APA® thrust direction and the friction force and increasing the radius of the contact cylinder seems to be valuable leads of improvements for future designs.

5.5 Perspectives

5.5.1 Model test on other SPA

A first and direct perspective of the hybrid model is its dissemination. Indeed, it has been only tested on three motors which is quite few to really assess its potential. It would be interesting to increase the number of modelled motors for (i) refining the domain validity and (ii) considering different mechanical structure, in particular multi-DoF structures. The next chapter 6 addresses the issue of noise generated by the SPA, from an experimental point of view. In this scope, two new motors will be introduced with a different mechanical structures. The hybrid model will be confronted to these two structures.

5.5.2 Improving the friction contact modelling

In this chapter, investigations focused on the vibratory behaviour of the SPA. Friction contact modelling has been set aside since it is already well suited for a macroscopic approach. However, it could become interesting to get closer to the real contact dynamic to get comparison points with previous experimental observations.

---

[4]As long as the force provided by the actuator is high in front of the friction force.

5.5.2.1 Contact geometry

Typically, the contact pressure profile (Fig.3.14), responsible for 3rd body flows initiation is not considered. However, it triggers the wear mechanisms and is responsible for variation of performances due to variation of friction coefficient. To address this contact geometry issue, Teidelt et al. (2012) proposes a new method to describe movements of inertia motors based on the reduction of dimensionality approach. As in lumped model, it consists in deriving motion equations but applied to the contact scale considering Hertz's contact equations and a Coulomb's frictional law. In this case, only the friction contact is considered and it could be interesting to merge both the hybrid model and this contact model. Thus, it would make it possible to compare performances of SPA in terms of the contact geometry.

5.5.2.2 Impact mode: allowing contact separation

Finally, although it was attempted, the impact mode, which was observed in chapter 4, has not been modelled. The considered method was similar to the one which makes it possible to implement the hybrid model. A transfer function was formulated from the vertical displacement of the pin in term of the applied voltage. Purpose was then to compare the generated vertical force against the initial preload by means of an electrical diode modelled by an *if* loop (Fig.5.23-a). The pin was considered as attached to the preload spring but not on the normal contact stiffness (Fig.5.23-b).

Such an approach seemed all the more interesting that it partially explains the asymmetry of speed. Indeed, preload would not be constant anymore but would depend on the signal pattern. However, when contact separation is considered, preload and so g(v) become null what can not occur in initial LuGre formulation (Eq.5.2)[5]. To address this issue, Nakashima et al. (2015) propose an alternative approach by describing the dynamics of collided bodies during the impact as differential equations with respect to an impact formulation. Then, they implement it in an extended LuGre model, considering a state variable as stored energy of the bristle deflection. It could be really interesting to consider it in order to increase the representativity of the hybrid both at macroscopic and mesoscopic scales.
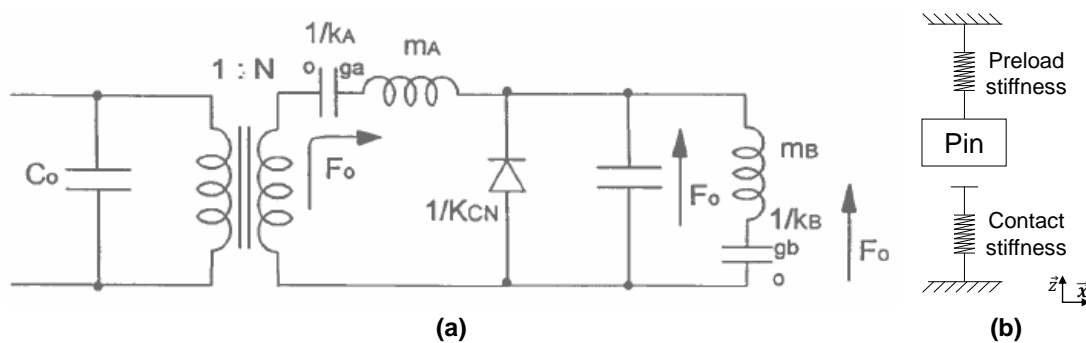
Figure 5.23 – Impact modelling. (a) Equivalent electrical scheme for modelling the impact mode by means of a diode (From Le Letty, 1994). (b) Conceptual mechanical scheme of the contact pin vertical displacement.

Next chapter is dedicated to the vibratory behaviour of SPA from experimental considerations. The purpose is to understand which vibrations are mainly responsible for motor noise and to propose relevant solutions to reduce this noise.

---

[5]Null value was replaced by a low value of preload - 0.1N - to lead the tests.

Optimisation of SPA vibratory behaviour: noise reduction

SPA are noisy. This can be attributed to the vibrations generated by the piezoelectric actuator and by the friction interface. Thus, noise appears to be a touchy issue since any acoustic improvement will impact SPA performances through vibratory and tribological changes. Acoustic modelling is set aside here because it would require to consider also mechatronics and tribological aspects simultaneously. This chapter aims at reducing this noise *experimentally* while maintaining mechanical performances. To do so, insulation, damping, acoustically-optimised actuation signal and structural modification have been tested. This led to a noise reduction of sixteen dBA on classical SPA.

Introduction

In addition to wear issues, another shortcoming of SPA is the generated noise, ranging from 85dBA to 95dBA (measured at 30cm), even in the case of small motors. This amounts to listening traffic noise on major road at 10-m distance. This problem appears in particular for long stroke applications, which require series of repeated steps, resulting in a noise lasting a long time. Noise and related vibrations can be limitations for resolution in micro-positioning applications (Otsuka, 1992; Matsusaka et al., 2007), for response time in robotic applications (Buchi et al., 1995) and for user comfort in consumer goods (Takano et al., 2005). On the contrary, for applications such as in vacuum environment, acoustic waves do not propagate, so only vibrations transmitted solidly would be considered (Yamagata et al., 1990; Furutani et al., 1998). As well, when the addressed function consists in an adjustment of a few steps, noise lasts only a few milliseconds and therefore produces a simple beep sound, what is not annoying.

The previous chapter made it possible to consider the vibratory behaviour of SPA by means of their modal landscape in the frequency domain. Thus, one noticed that the actuation frequency is of a few kHz, in the audible spectrum. Moreover, the working principle of SPA, relying on stick-slip, suggests an additional friction-induced noise source (Meziane et al., 2010; Asamene and Sundaresan, 2012; Ferrer et al., 2010; Di Bartolomeo et al., 2012; Tonazzi et al., 2014) as in many industrial applications such as

disk brake squeal (Ouyang et al., 2005), endoprosthesis vibrations (Weiss et al., 2009), train wheel-rail noise emission (Heckl and Abrahams, 2000).

In a first time, the purpose of this investigation is to identify the noise sources (section 6.1). It consists in itemising each contributor and then eliminating the negligible ones (Cameron et al., 1992). In a second time, noise reduction solutions are proposed (section 6.2), considering:

- (i) insulation;

- (ii) damping (Aglione, 2014);

- (iii) optimisation of actuation signal, firstly approached in (Matsuda and Kaneko, 1991; Blackford et al., 1992; Buchi et al., 1995), by adding a dead-time to damp free oscillations (Wang and Lu, 2012), and by introducing a Quasi-SawTooth (QST) signal - usually used to exploit ultrasonic resonance frequencies (Yokozawa and Morita, 2015) - in kHz order of magnitude;

- (iv) structural modification to operate in ultrasonic range (Morita et al., 2012).

Here, the reader will not find an exhaustive acoustic analysis, but preliminary experiments to determine where efforts must focus.

Noise in SPA appears to be a touchy issue to address. As they are composed of four parts, any changes - to achieve acoustic improvements - impacts SPA performances (Pfeffer et al., 2015). As a consequence acoustic improvements will be systematically discussed with respect to generated speed and force.

6.1 Identification of noise contributors

In SPA, asymmetric vibrations are generated by the piezoelectric ceramic and sent toward the friction interface to produce steps and so macroscopic displacement. Thus, two noise contributors are anticipated: noise due to actuation vibrations and noise due to the friction interface itself. Determining which one is the main contributor consists in evaluating which is the main vibration path (Pavic and Bendridi, 2014).

In order to carry out this investigation, next section is dedicated to describe the acoustic set-up and to remind some essential definitions. These definitions will also drive some of the proposed solutions to decrease the noise level.

6.1.1 Vibration-acoustic framework

Psychoacoustic - human ears — Acoustic studies can *not* be led only from an instrumentation point of view. Here, purpose is also to address human feelings. First notion refers to the definition of acoustic noise. Depending on the frequency of the sound wave, one can distinguish:

- **infrasound waves** - below 20Hz,

- **acoustic waves** - from 20Hz to 20kHz,

- **ultrasound waves** - above 20kHz.

Sound waves in [20Hz - 20kHz] frequency range are called acoustic waves since the human eardrum reacts mainly in this range. For these frequencies, acoustic level, or Sound Intensity Level (SIL), detailed in the next section, is classically displayed in

deciBel (dB) based on a pressure measure. Typical dB values are referred to ambient known noises in Table.6.1.

Table 6.1 – Typical Sound Intensity Level (SIL) values relating to ambient known sources (From Zielinski, 2014).

Source (or character) of sound	P_{rms} [Pa]	SIL [dB]
Threshold of pain	100	134
Hearing damage during short-term effect	20	$\sim$120
Jet engine, 100m distant	6-200	110-140
Hammer drill, 1m distant	2	$\sim$100
Hearing damage from long-term exposure	0.6	85
Traffic noise on major road, 10 m distant	0.2-06	80-90
Moving automobile, 10 m distant	0.02-0.2	60-80
TV set (typical loudness), 1m distant	0.02	$\sim$60
Normal talking, 1m distant	0.002-0.02	40-60
Very calm room	0.0002-0.0006	20-30
Calm human breathing	0.00006	10
Auditory threshold at 2kHz	0.00002	0

(dB ref P_0=20μPa)

In addition, depending on the frequency of the noise, human does not feel same SIL. Literature has shown a psychoacoustic effect varying with frequency. Various filters have been developed to get the mean behaviour of human ears (Fig.6.1). In practice, the dBA filter is widely used as the most representative for human ears (standard IEC, 2013). It highlights human ears are very sensitive to the [1 kHz; 3kHz] range frequency.
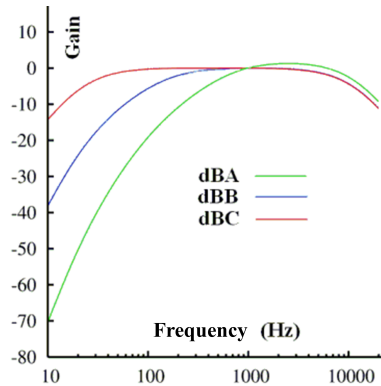
Figure 6.1 – Typical acoustic filters to correlate physical measures to human perception. dBA filter makes it possible to reproduce the behaviour of the average normal ear for a perceived intensity identical to that of 40 dB at 1 kHz. dBC filter have a much more "flat" curve than dBA filter, corresponding to the behaviour of the human ear for higher SIL.

In term of measurements, it means that a noise of 90dBA at a 1-kHz frequency is felt as 60dBA at 50-Hz frequency. Based on these first psycho-acoustic considerations, one notices that actuation frequency of SPA is typically in the most disturbing acoustic range. Thus a first lead of improvement would consist in lowering or increasing the acoustic frequency of generated sounds.

Definitions — SIL is used in the following sections since it is easily measurable in decibels [dB]. It stems from wave equations and is defined by Eq.6.1.

$$\text{SIL}(P)_r = 10 Log_{10} \left(\frac{P}{P_0} \right)_r \tag{6.1}$$

with r and P, source-receiver distance and acoustic pressure respectively. $P_0 = 20\mu$Pa is the threshold from which human ears can hear a noise in the air (standard ISO, 2007).

Two equations emerge from Eq.6.1. First one links pressure variation to dB reduction (Eq.6.2, Fig.6.2). This will makes it possible to lead a quantitative analysis.

$$\text{SIL}\left(\frac{P}{2}\right)_r = 10Log_{10}\left(\frac{P}{2P_0}\right)_r$$
$$= SIL(P)_r - 3dB \tag{6.2}$$

Second one links SIL variation to source-receiver distance, r (Eq.6.3). This imposes to measure the acoustic level always at the same distance, 30cm here to respect plane wave hypothesis and to get comparable results.

$$\text{SIL}(P)_{r\times 2} = \text{SIL}(P)_r - 6dB \tag{6.3}$$
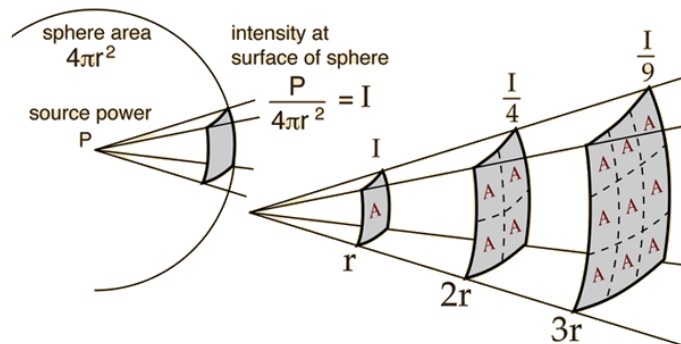
Figure 6.2 – Illustration of wave intensity propagation from an acoustic source (From ?).

Setup description — Measurement setup is depicted on Fig.6.3. Acoustic measures are achieved with a microphone coupled with a Sound Level Meter (SLM). Speed performances are measured with a laser vibrometer. All the setup is stored in a box whose walls are covered by foam to insulate acoustic measurement from ambient noise (Fig.6.3). Inside, mean noise, without actuation, is decreased from 53dBA to 40dBA.
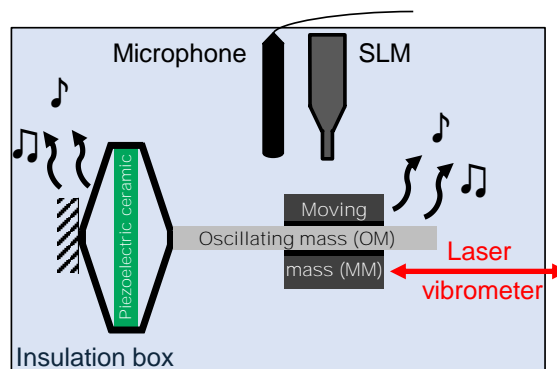
Figure 6.3 – Vibroacoustic setup. Sound Level Meter (SLM) gives access to the mean acoustic level. Microphone makes it possible to see the impact of actuation frequency on the SIL. Laser vibrometer ensures the measure of SPA motion during the tests. Everything is stored in a box whose walls are covered by foam to insulate acoustic measurement from ambient noise.

6.1.2 Noise main contributor: vibrations inherent to actuation

In SPA, two acoustic paths - propagating vibrations from APA® - are suspected. First refers to solid links (screw links for instance). Second refers to friction link (contact interface between the oscillating and the moving masses). Focus is done on each contributor in order to know which one is the main one for the radiated noise. To do so, SPA is first set in fixed-actuator configuration (Fig.6.4-a). In this case, vibration path from the piezoelectric oscillating ceramic to the base is direct. Second, SPA is set in moving actuator configuration (Fig.6.4-b). Generated vibrations must go through friction interface to propagate until the base. Moreover, as additional noise could result from resonant parts (Piriou et al., 2016), measures at achieved on a wide frequency range, centred on [1kHz;1.5kHz] in consistency with classical actuation frequencies.
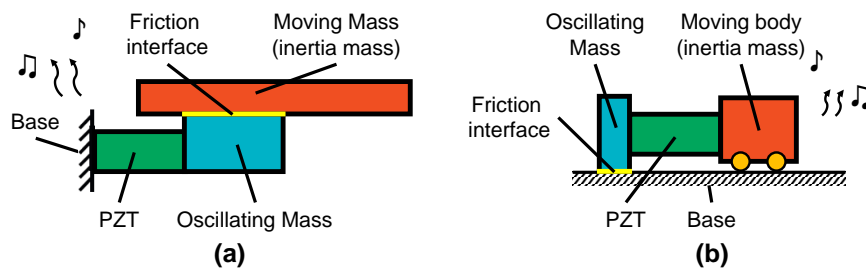
Figure 6.4 – Schematic view of the two tests realised to determine which acoustic path contributes the most to the radiation of noise from vibrations generated by the actuator (From section 1.15). (a) SPA is in fixed-actuator configuration. (b) SPA is in moving-actuator configuration.

Results are depicted on Fig.6.5. In fixed-actuator configuration, mean acoustic level is 92dBA. In moving-actuator configuration, mean acoustic level decreased to 82dBA.
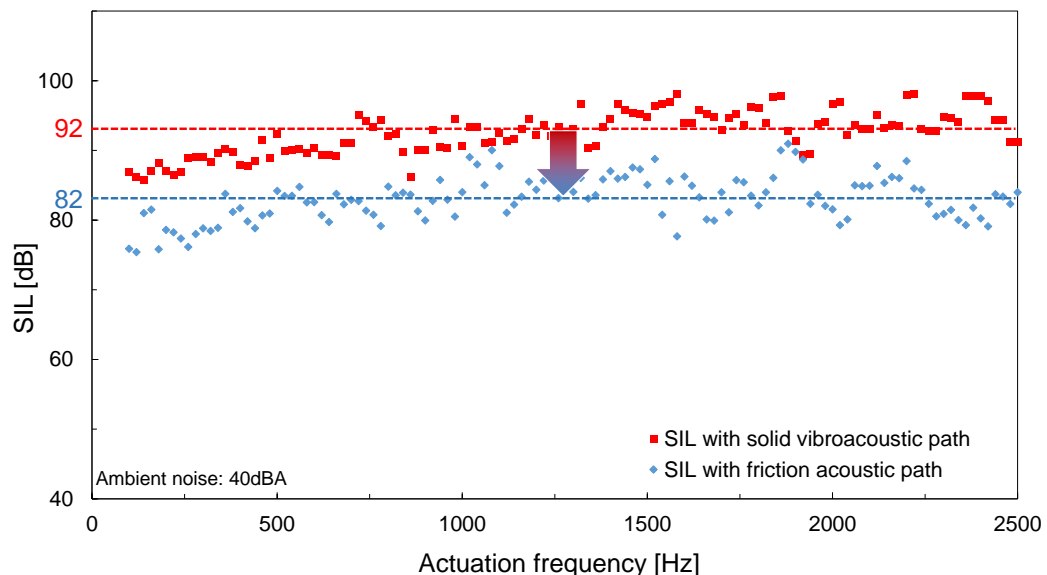
Figure 6.5 – Acoustic measurements with alternatively solid and friction paths to get the main acoustic contributor. Distance between source and receiver was 30cm.

Thus, propagated vibrations through solid links are the main contributor to the noise generated by SPA. Indeed, resulting acoustic pressure is more than six times higher (Eq.6.2). To decrease it, focus is done on actuator part and solid links rather than on the friction interface in the following sections.

6.2 Proposed solutions for reducing noise

After identifying the main contributor, second issue is about possible solutions for reducing the current level of noise. Four possible ways are proposed and will structure the following sections: (i) insulation, (ii) damping, (iii) acoustically optimised actuation signal, and (iv) structural modification.

6.2.1 Insulation

Insulation is maybe the best-known passive way for reducing the perceived noise from an acoustic source. A lot of researchers and companies work to improve acoustic insulation material, like foam, for automobile or building for instance. Thus, insulating both acoustic and tribometer setup with a box whose wall were covered by foam was appreciated by colleagues. However such an insulation requires to know in which system the motor will be installed, to determine how insulating it. This is not always possible. In addition, such a solution is not consistent with the miniaturization potential of SPA. So, insulation has been set aside here.

6.2.2 Elastic damping

Previous measures highlight that vibrations transmitted by solid paths to the base resulted in high levels of noise. Damping these vibrations could represent an alternative to insulation since damper can be implemented directly between the motor and its housing (Aglione, 2014). In addition, dampers such as elastomer pads are less cumbersome than insulation foams. However, such dampers have a much lower stiffness than solid links. From a mechanical point of view, the stiffer the actuation axis is, the better the performances are (Breguet, 1998). It is confirmed by simulating the impact of lowering the stiffness of the link between actuator and base (K_{ground} in Fig.5.5). Resulting mean speed decreases from 17mm/s (Fig.6.6) to 6mm/s (Fig.6.7). So, elastic damping has also been set aside.
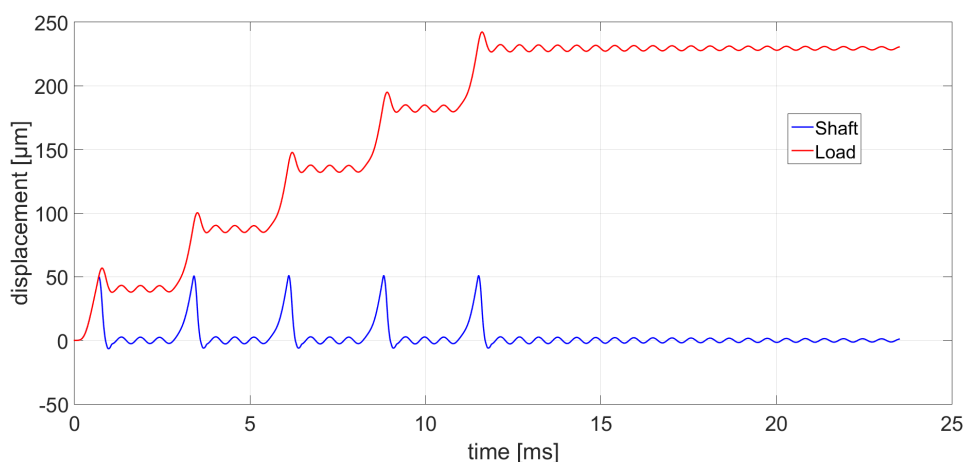
Figure 6.6 – Lumped/friction modelling of a LSPA35XS (Fig.2.1) with a high stiffness - **10^7N/m** - between actuator and base (see Fig.6.4).
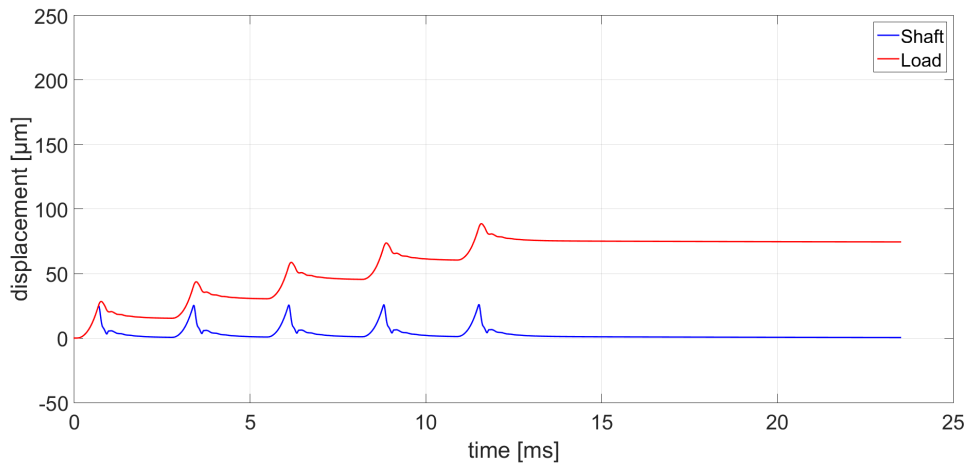
Figure 6.7 – Lumped/friction modelling of a LSPA35XS (Fig.2.1) with a low stiffness - 10^3N/m - between actuator and base (see Fig.6.4).

6.2.3 Actuation signals

Working on actuation signal is the easiest way of improvement so far because it does not imply any mechanical change and obtained results are directly applicable.

Until now, at low frequency, a sharp signal - with acceleration peaks - is used to make stick-slip transitions (section 2.2.2). Acoustically, it is like an hammer blow for each sharp changes of slope (Fig.6.8). Thus, it becomes interesting to check if it is possible to generate steps at low-actuation frequency without sharp stick-to-slip transitions.

(a)   **(b)**
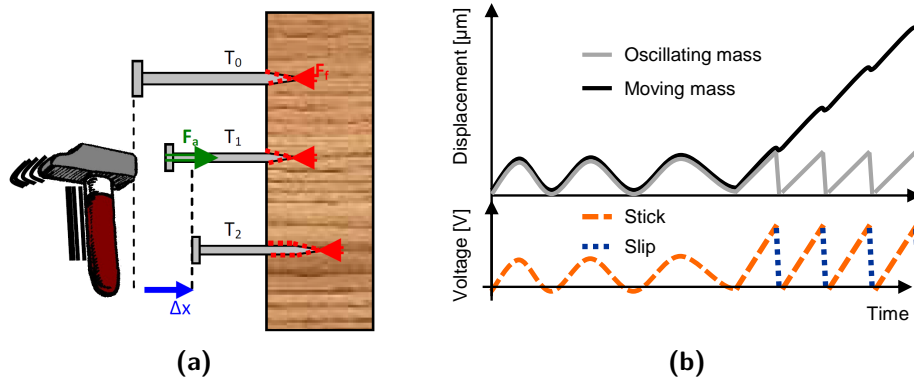
Figure 6.8 – Illustration of SPA acoustic behaviour. (a) from Belly (2011) correlated with (b) sharp signal transitions. Each stick-slip transition behaves like a hammer blow which propagates through the adjacent structure.

From literature, Renner et al. (1990) first emphasized that a cycloid signal (without two opposing acceleration peaks - Table 2.1-h) provides better performances than classical sawtooth signals, in particular for driving a payload vertically. So, actuation signal with less acceleration peaks than classical signals seems to be practicable. In addition, Quasi-SawTooth signals, so-called QST (Eq.6.4), are patterns which look like a sawtooth signal, but without any acceleration peaks. As well as being used for high-frequency motors (Morita et al., 2012), this actuation signal is potentially quieter at low frequency.

$$V_{QST\ signal}(t) = A[sin(\omega t + \varphi) + \frac{1}{3}sin(2(\omega t + \varphi) + \Phi) + B] \qquad (6.4)$$

With ω, signal pulsation, A voltage amplitude of signal (ΔV in Eq.6.5) divided by the norm of sin summation. φ, phase shift to start and end at lower voltage, Φ phase shift between both sine to make appear the quasi-sawtooth pattern, and B [ ], offset to start and end at 0V and to not have parasitic vibrations when electric power is switched on.

Based on these considerations, QST signal is newly introduced for SPA in low-frequency for its noise reduction potential (Fig.6.9-b). It will be systematically compared to a parabolic rise signal, so-called x^2 thereafter (Eq.6.5), introduced as a reference in section 2.2.2 (Fig.6.9-a).

$$V_{x^2 \ signal}(t) = \Delta V[ft - int(ft)]^2 \tag{6.5}$$

With ΔV is the voltage amplitude to the electrical terminals of the piezoelectric ceramic, f is the frequency of the pattern repetition and int() is the integer function.

Likewise, Probst et al. (1991) emphasized that adding a delay makes it possible to damp free oscillations and to not excite high frequencies too much. Moreover, the addition of, for instance, a one-actuation-period delay divides by two the actuation frequency "seen" by adjacent mechanical parts. By this way, it allows separating the actuation frequency from the vibration frequency with a known loss of performance. It becomes possible to determine a trade-off between loss of speed performance - bound to the step repetition frequency (section 2.2.3) - and acoustic performances - bound to dBA filter (Fig.6.1) -. In order to limit the impact of free oscillations on mechanical performances, x^2 and QST signals will be experimentally set aside in front of their equivalent with a delay (Eq.6.6 and Eq.6.7 illustrated on Fig.6.9-c,d). Comparison between both signal will be carried out acoustically first (section 6.2.3.1) and then mechanically (section 6.2.3.2).

$$V_{QST+delay}(t) = \begin{cases} 0, & \text{if } a(N+1) + bN < t < (N+1)(a+b) \\ A[sin(\omega[t - N(a+b)] + \varphi) \\ -\frac{1}{3}sin(2(\omega[t - N(a+b)] + \varphi) + \Phi) + B], & \text{otherwise} \end{cases} \tag{6.6}$$

$$V_{x^2+delay}(t) = \begin{cases} 0, & \text{if } a(N+1) + bN < t < (N+1)(a+b) \\ \Delta V\left[\frac{t-N(a+b)}{a} - int\left(\frac{t-N(a+b)}{a}\right)\right]^2, & \text{otherwise} \end{cases} \tag{6.7}$$

With a, time period of pattern repetition, b, time period of delay and N=int$\left(\frac{t}{a+b}\right)$.

6.2.3.1 Acoustic comparison between x^2 *vs.* QST signal

Similarly to the assessment of main noise contributors (section 6.1), comparison between both x^2 and QST signals are achieved on a [100; 2500Hz] frequency range (Fig.6.10). With x^2 signal + delay, SIL is quite constant - around 77dB - no matter the actuation frequency. Thus, the add of a delay made it possible to decrease SIL. With QST actuation signal, noise is even more decreased - until around 65dB -. However, for some actuation frequencies, SIL with QST signal is higher than SIL with x^2 signal. This is correlated with the modal landscape of the housing on which the SPA is fixed.

Interpretation based on Fourier series — To go deeper in interpretations, all four signals - V_{x^2}, $V_{x^2+delay}$, V_{QST} and $V_{QST+delay}$ - are decomposed in the frequency
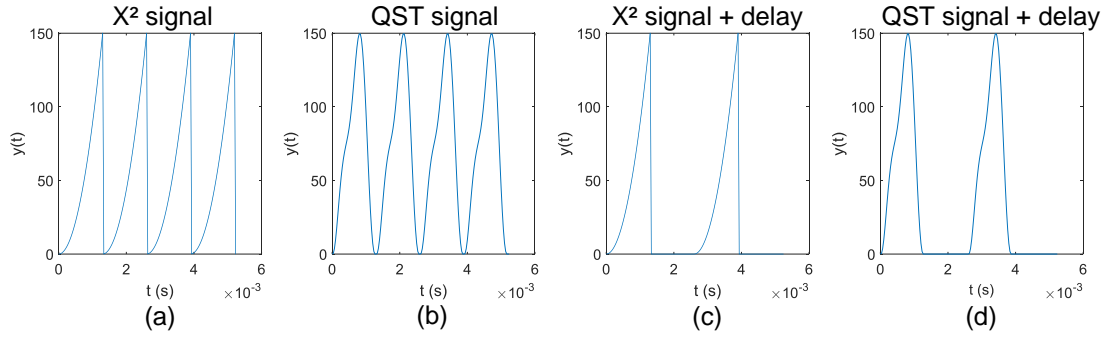
Figure 6.9 – Actuation signals (frequency is set to 800Hz). (a) x^2 signal. (b) Quasi-SawTooth (QST) signal. (c-d) x^2 and QST + delay to damp vibration naturally and to reduce acoustic frequency.
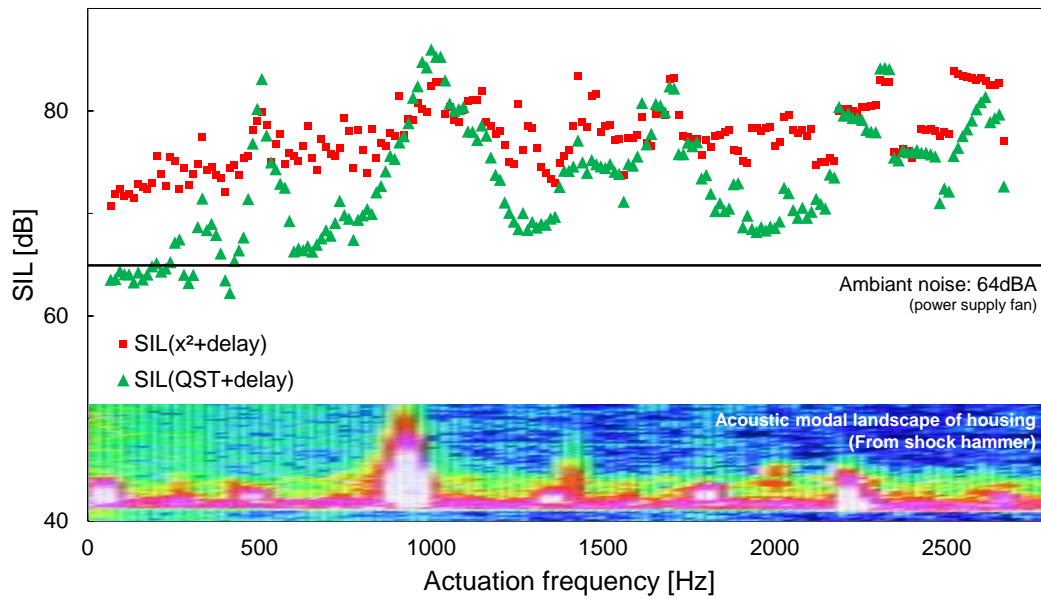
Figure 6.10 – Comparison of QST and x^2 signal acoustic performances. SPA is fixed on a housing whose modal landscape is assessed by a shock hammer (rainbow picture). In comparison with Fig.6.5, the add of a delay already enabled to decrease mean SIL. SIL resulting from QST actuation is lower than that resulting from x^2 actuation except when harmonic of the QST signal are coupled with resonance frequencies of the housing. Distance between source and receiver was 30cm.

space, by means of Fourier series Eq.6.8, into $\widetilde{V}_{x^2}$, $\widetilde{V}_{x^2+delay}$, $\widetilde{V}_{QST}$ and $\widetilde{V}_{QST+delay}$ respectively (Eq.6.10).

$$\widetilde{signal}(t) = a_0 + \sum_{n=1}^{\infty} a_n cos(2\pi n f_0 t) + b_n sin(2\pi n f_0 t) \tag{6.8}$$

With $f_0=1/T_0$, the frequency of the signal, and a_0, a_n, b_n calculated as followed:

$$a_0 = \frac{1}{T} \int_0^{T_0} signal(t)\, dt;$$

$$a_n = \frac{2}{T} \int_0^{T_0} signal(t) \cos\left(\frac{2\pi n t}{T_0}\right)\, dt \text{ for n} > 0; \tag{6.9}$$

$$b_n = \frac{2}{T} \int_0^{T_0} signal(t) \sin\left(\frac{2\pi n t}{T_0}\right)\, dt \text{ for n} > 0.$$

6

$$\widetilde{V}_{x^2\ signal}(t) = \frac{\Delta V}{3} + \sum_{n=1}^{\infty}\left[\frac{\Delta V}{(\pi n)^2}cos(2\pi nft) - \frac{\Delta V}{n}sin(2\pi nft)\right]$$

$$\begin{aligned}\widetilde{V}_{QST\ signal}(t) =\ &AB\\ &+ Acos(\phi)sin(2\pi ft) + Asin(\phi)cos(2\pi ft)\\ &+ \frac{A}{3}cos(2\phi + \Phi)sin(4\pi ft) + \frac{A}{3}sin(2\phi + \Phi)cos(2\pi ft)\end{aligned}$$

$$\begin{aligned}\widetilde{V}_{x^2+delay}(t) =\ &\frac{\Delta V}{6} + \sum_{n=1}^{\infty}\frac{2\Delta V}{(\pi n)^2}(-1)^n cos(\pi nft)\\ &+ \left[\frac{\Delta V}{\pi n}(-1)^{n+1} + \frac{2\Delta V}{(\pi n)^3}((-1)^n - 1)\right]sin(\pi nft)\end{aligned}$$

$$(6.10)$$

$$\begin{aligned}\widetilde{V}_{QST+delay}(t) =\ &\frac{AB}{2}\\ &+ \frac{Asin(\phi)}{2}cos(\omega t) + \frac{Acos(\phi)}{2}sin(\omega t)\\ &+ \frac{Asin(2\phi + \Phi)}{6}cos(2\omega t) + \frac{Acos(2\phi + \Phi)}{6}sin(2\omega t)\\ &+ \sum_{\substack{n=1\\n\neq2,n\neq4}}^{\infty}\frac{A(1 - (-1)^n))}{\pi}\\ &\times\left[\left(\frac{2cos(\phi)}{(2+n)(2-n)} + \frac{4cos(2\phi + \Phi)}{3(4+n)(4-n)}\right)cos\left(\frac{n\omega t}{2}\right)\right.\\ &\left.+ \left(\frac{-nsin(\phi)}{(2+n)(2-n)} - \frac{-nsin(2\phi + \Phi)}{3(4+n)(4-n)} + \frac{B}{n}\right)sin\left(\frac{n\omega t}{2}\right)\right]\end{aligned}$$

6

Resulting Fourier series are depicted on Fig.6.11.

Through $\widetilde{V}_{x^2\ signal}$, one confirms that x^2 signal scatters energy through a large spectrum of frequencies (Fig.6.11-a). Thus, stick-slip motion is generated but a part of the energy (in high frequencies) is used to excite parasitic modes and so generate noise. On the contrary, Fourier series of QST signal focuses energy in fundamental and first harmonic frequency (Fig.6.11-b). Amplitude of fundamental peak is higher than that of x^2. Thus, when actuation frequency couples with resonance frequencies of the housing, it results in a higher SIL than with x^2 signal (Fig.6.10).

The addition of a delay decreases the frequency of the peaks and so the energy available for exciting high-frequency resonances. Indeed, for both signals without delay, fundamental frequency is 800Hz, whereas it is 400Hz with delay, in consistence with their respective temporal representations (Fig.6.9). With QST signal and delay, a tradeoff is reached. Actuation occurs and less energy is dissipated in high frequencies leading to a noise decrease.

Thus, although QST signal made it possible to drastically decrease the SIL, care must be taken about this signal. Modal landscape of the casing where the SPA is fixed is not always an available piece of information so a setting phase must be required. Likewise, it appears the resulting mechanical performances (speed and force) are also impacted. This point is discussed in the next section.
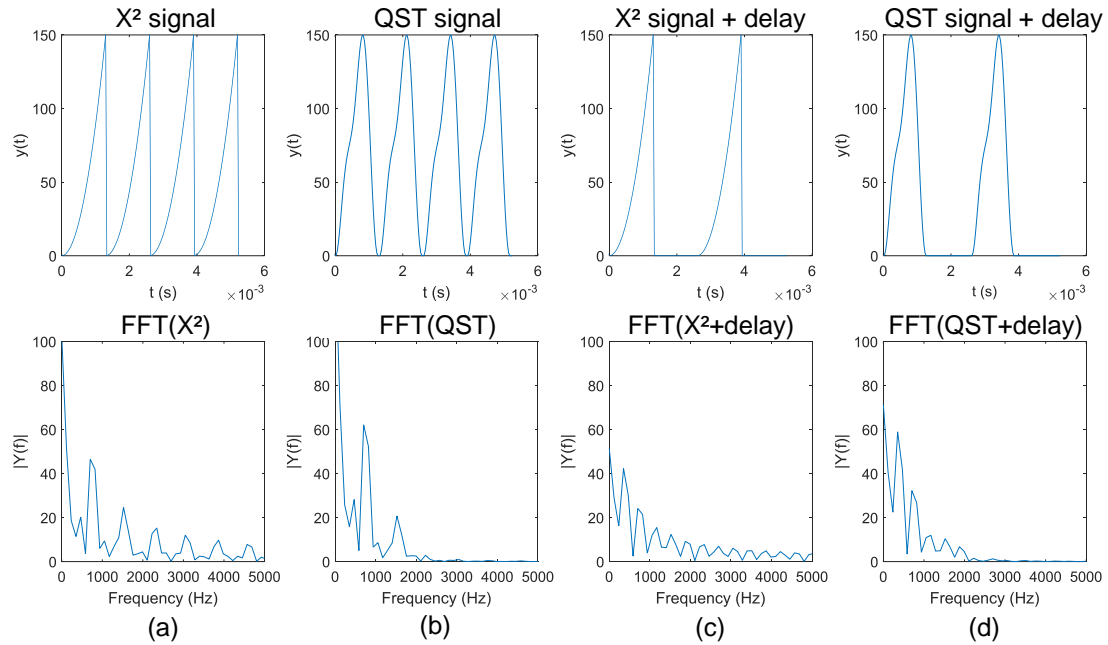
Figure 6.11 – Actuation signals from Fig.6.9 and their related Fast Fourier Transform (FFT). (a) x^2 signal scatters energy through a large spectrum of frequencies. (b) QST signal focuses energy in fundamental and first harmonic frequency. (c-d) Delay divides energy into more frequencies leading to a smaller excitation.

6.2.3.2 Impact of signal modification on mechanical performances

QST signal has shown interesting acoustic performances. It is now approached in term of mechanical performances. Actuation setup (Fig.6.12), introduced in section 2.2.4, is used to compare load curves of a same SPA actuated with x^2 and QST signals. This setup enables the measurement of no-load speed as well as that of maximum force. To do so, the moving mass led by a SPA pushes against a spring in serial with a force sensor. Load curves are assessed in both actuation directions.
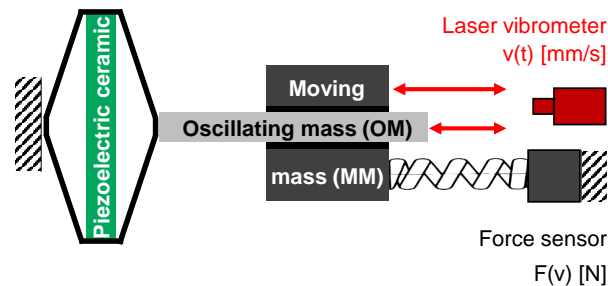
Figure 6.12 – Actuation setup to measure mechanical performances. No load-speed is assessed by means of a position sensor as long as the moving mass is not in contact with spring. Blocked force is reached when actuation force is equal to the compressed spring force.

First, load curve of x^2 signal is measured (Fig.6.13-red square points). SIL, no-load speed and blocked force are around 80dBA (at 30cm), 7.5mm/s and 2N respectively. Second, load curve of QST signal is measured (Fig.6.13-green triangle points). SIL, no-load speed and blocked force are around 61dBA (at 30cm), 1.5mm/s and 0.5N respectively.

Thus, measures highlight that, although noise generated by QST signal is improved,

no-load speed and blocked force are too impacted in comparison with x^2. Investigations on high-frequency actuation signals have shown that generated force increased with the number of harmonics (Hunstig et al., 2014). From these observations, an alternative signal has been attempted. A third frequency is added to the QST-2f signal leading to a so called QST-3f signal. SIL, no-load speed and blocked force are around 64dBA (at 30cm), 7.5mm/s and 1N respectively (Fig.6.13-black points). So, the load curve of this new signal presents quite good mechanical performances without increasing SIL too much.
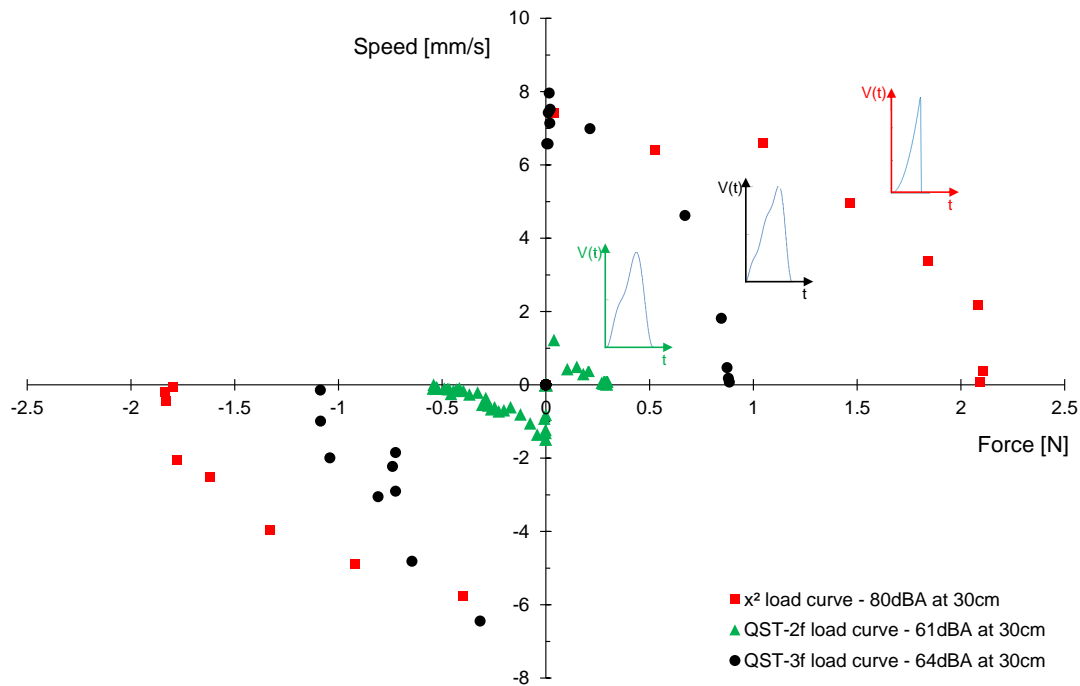
Figure 6.13 – Load curve for SPA with x^2, QST-2f and QST-3f signals. Although acoustic performances of QST-2f signal are good, associated mechanical performances are too low to make reliable SPA. In comparison, QST-3f signal generates a same speed as x^2 signal and a consistent blocked force. It reveals to be a good mechanical-acoustic trade-off.

Proposed interpretation — As seen in section 2.2.2, a signal with a parabolic rise followed by a sudden drop makes it possible to fully exploit both stick and slip phases (Fig.2.7). Indeed, with this kind of signal, the inertia of moving mass exploits acceleration peaks to trigger the stick-to-slip transition and conversely. With a QST-2f signal, these acceleration peaks disappear, inherently to its mathematical definition (Table 6.2). Thus, good mechanical performances of QST-3f signal can be explained by the acceleration ratio between the stick phase and the slip phase: 4, whereas it is 3 for QST-2f. Finally, even if this signal does not generate as much force as x^2_{signal}, it is the best obtained mechanical-acoustic trade-off here.

As a main result, signal optimisation led to a reduction by sixteen dBA (acoustic pressure divided by more than thirty - Eq.6.2). This result is directly applicable to any SPA. To go further, a structural modification is proposed in the next section to operate in ultrasonic range.

Table 6.2 – QST-2f and QST-3f signal illustrations. Acceleration ratio between stick and slip phase is higher for the QST-3f signal, what lead to better mechanical performances.

	QST-2f$_{signal}$	QST-3f$_{signal}$
Normalized displacement		
Resulting acceleration		
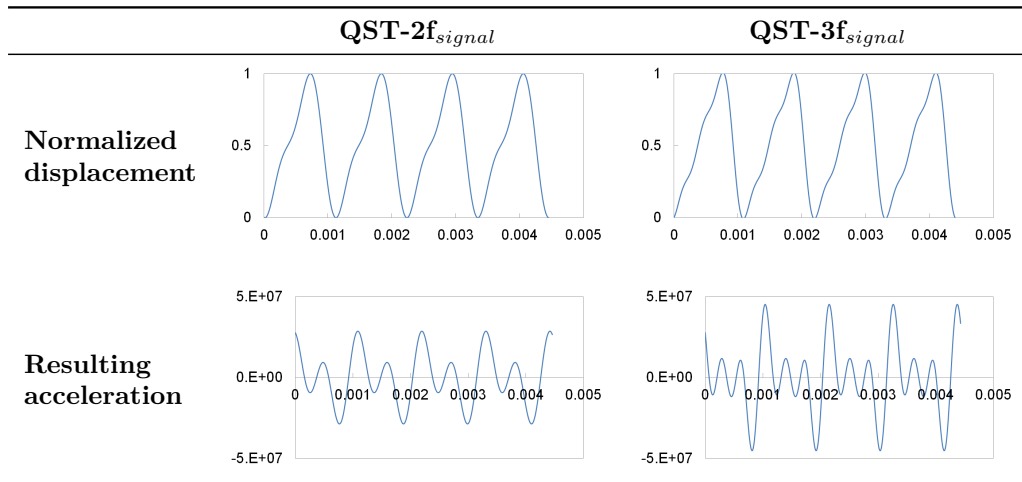
6.2.4 Structural modification: ultrasonic SPA

Structural modification is then considered. It relies on literature about resonant inertia motors (Morita et al., 2012) to developed an amplified ultrasonic SPA.

As seen in Fig.6.1, one way to decrease the SIL perceived by human ears is to decrease acoustic frequency, by means of adding a delay for instance (section 6.2.3). Another way is to increase the acoustic frequency. Indeed, if actuation frequency exceeds 20kHz, sound waves reach ultrasonic domain. They are no more audible by humans (section 6.1.1). Motors seems to be silent.

Ultrasonic motors were already tested in (Six, 2000), in progressive wave configuration (section 1.4.2), making it possible to check the feasibility of ultrasonic motor with amplified actuator APA® . However, cumbersome calibrations have limited industrial expansion.

In literature, ultrasonic Smooth Inertia Drive Motors (SIDM) uses QST signal (section 6.2.3) to exploit both actuation modes of piezoelectric ceramic (Fig.6.14 from Morita et al., 2012). However, used ceramic are not pre-stressed, what make them vulnerable to material failure (section 2.2.1.1). It results in a necessary interface metal part between ceramic and shaft (Fig.6.14). In addition, motion is not amplified mechanically so resulting strain amplitude is around 60nm. Therefore, the overall system is very sensitive to any external perturbations.
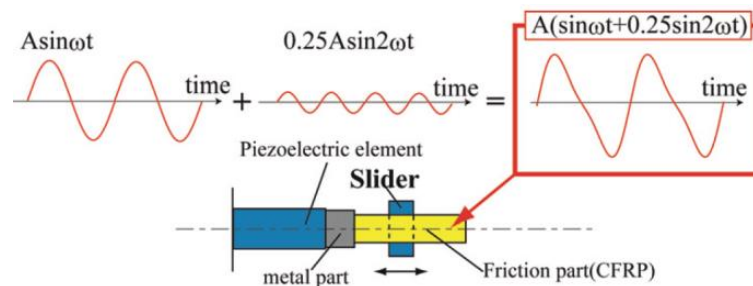
Figure 6.14 – SIDM using Quasi-SawTooth signal at several tens kHz (From Morita et al., 2012).

To address the ultrasonic range of piezoelectric inertia motors, an ultrasonic-SPA (US-SPA) concept is proposed by Cedrat Technologies (Fig.6.15). This concept is based

on an APA® shell to generate larger steps than classical ultrasonic inertia motors. Thus, purpose is to be both silent and few sensitive to external perturbations.

(a)   **(b)**
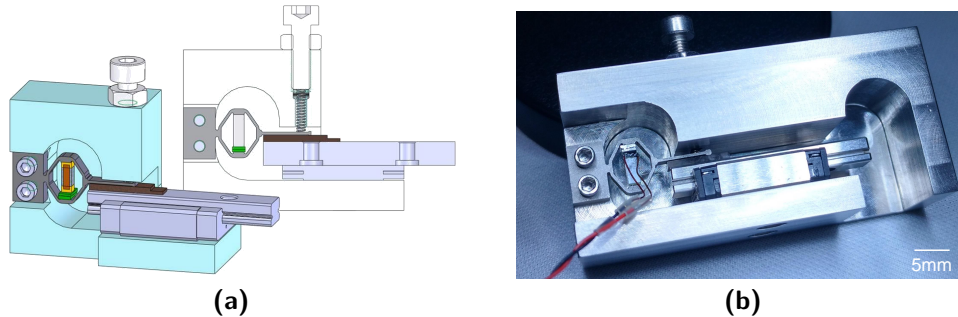
Figure 6.15 – Ultrasonic-SPA. (a) design and (b) development.

Methodology proposed in Nishimura et al. (2012) is applied. Objective is to actuate the US-SPA by an ultrasonic QST, defined by two harmonic frequencies. To reach this objective, both resonance modes of the actuator in actuation direction must correspond to these harmonic frequencies respectively (Fig.6.16). Development of this US-SPA is realised in four steps: (i) FEM design of the actuator, (ii) Hybrid FEM-lumped modelling to assess theoretical speed performances, (iii) manufacturing and integration and (iv) experimental validation of the actuator characteristics and performances.
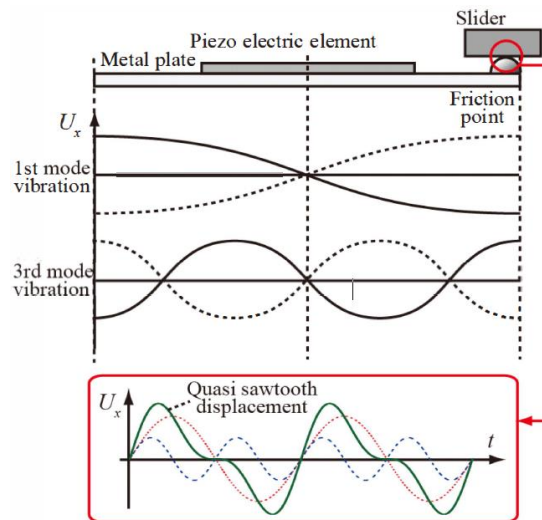
Figure 6.16 – US-SPA design methodology from Yokose et al. (2012).
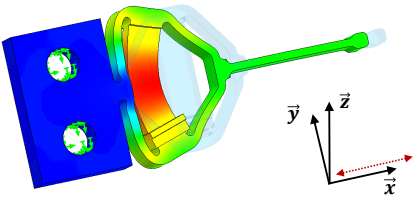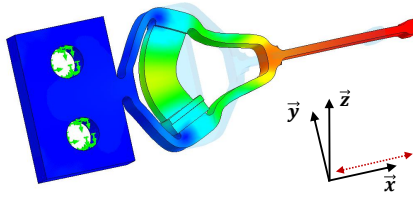
FEM Design — First, US-SPA is design by FEM. The thickness and the length of actuator shaft are adjustable for getting a second resonance mode twice as higher than first one in order to exploit QST signal. Thus, thickness and length are set to 0.32mm (Fig.6.17-a) and 7.10mm (Fig.6.17-b) respectively.
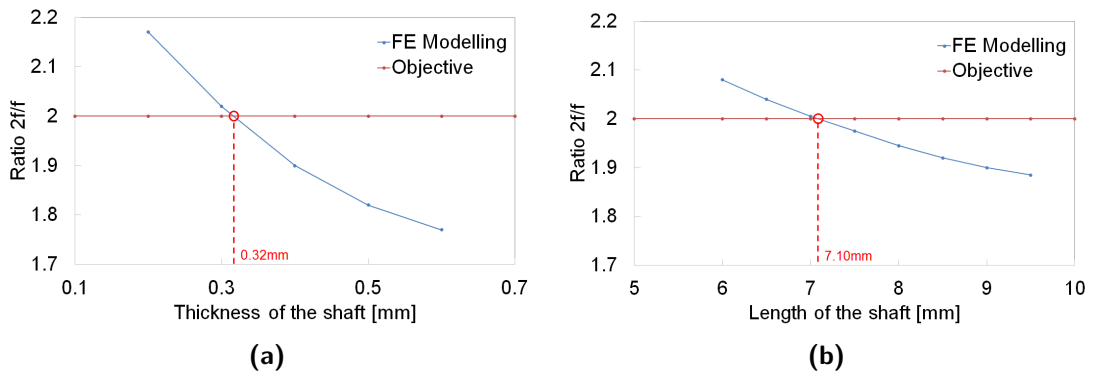
Figure 6.17 – Sizing of shaft dimensions to get a QST working: meaning second actuation mode is twice as bigger than the first one. (a) sizing of shaft thickness. (b) sizing of shaft length.

As a result resonance modes are depicted in Table 6.3. First and second resonance modes are theoretically at 21.9kHz and 42.2kHz respectively. To be perfectly superimposed, second resonance mode should be at 43.8kHz. This leads to an acceptable error of 3.7%. Notice that, based on lessons learned in tribometer design (section 5.4.2), no notch is implemented on US-SPA in order to avoid parasitic vibrations in other directions than that of actuation. Likewise, contrary to chapter 5, there is no boundary conditions imposed to the contact pin. Indeed, no more stick-slip is expected but only slip-slip. So, it is assume that once in resonance, the actuator will not "see" the moving mass. This will be confirmed experimentally.

Table 6.3 – Frequency analysis of the US-SPA by means of FEM.

Denomination	Related frequency	Modal deformation
actuation mode #1	21.9kHz	
actuation mode #2	42.2kHz	

Hybrid FEM-lumped modelling — Once FEM design is achieved, speed performances are assessed by means of the hybrid FEM-lumped modelling introduced in chapter 5. After formulating a transfer function from the previous frequency analysis, speed predictions are depicted on Fig.6.18. Speed becomes nominal as soon as QST pattern becomes effective after resonance were triggered. Resulting expected no-load speed is around 25mm/s.
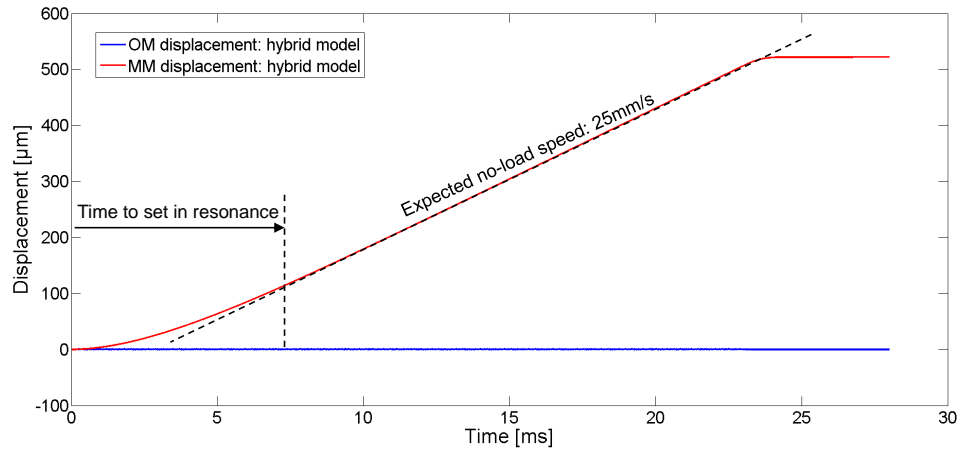
Figure 6.18 – Displacement curves from the US-SPA with the hybrid FEM-lumped modelling. In blue: displacement of the oscillating mass (shaft). In red: displacement of the moving mass.

Integration — Based on previous simulation results, the designed motor have been manufactured. Next paragraph will confirm the frequencies of the resonance modes and detail how the actuation signal has been set to get a QST displacement pattern.

Experimental validation — First step of the experimental validation consists in checking the locations of the resonance peaks. This has been achieved by means of an admittance measurement (Fig.6.19 as in section 3.1.1.4-.

Here, first resonance mode has been well estimated (22.0kHz) but second resonance mode is higher than expected - because of manufacturing dispersion). Hopefully, location of second peak simulated by FEM (42.2kHz) was lower than ideal one (43.8kHz) so error with measure (45.1kHz) remains acceptable: 3.0%.
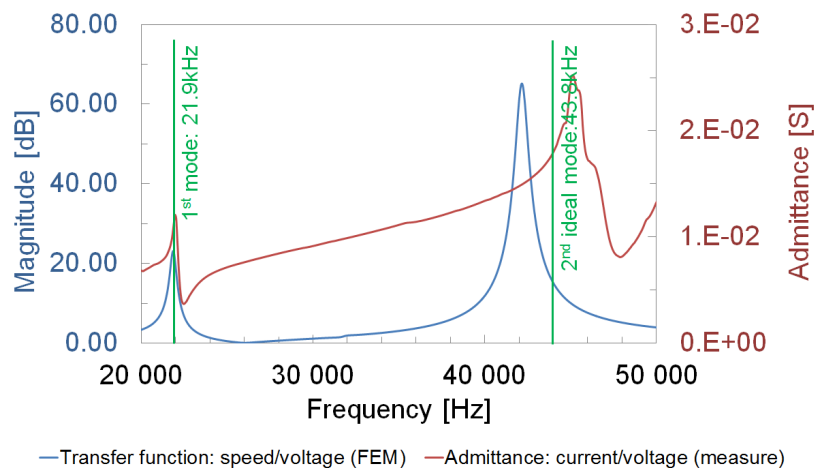
Figure 6.19 – Admittance measurement on SPA-US compared with FEM transfer function.

Second step of the experimental validation consists in setting QST signal. Indeed, objective is to get a QST *displacement* pattern from the coupling between the electrical signal and the amplitude of the resonance peaks. Thus, Eq.6.4 is changed into Eq.6.11, with C and D setting parameters.

$$V_{QSTsignal}(t) = A[\mathbf{C} \times sin(\omega t + \varphi) + \mathbf{D} \times 1/3 sin(2(\omega t + \varphi) + \Phi) + B] \qquad (6.11)$$

Here, C and D coefficients have been measured by means of a laser vibrometer. To do so, a sinusoidal electric signal has been alternatively sent to the motor at both resonance frequencies and full amplitude of voltage.

Simultaneously, thermal observations have been realised to prevent any damage due to electromechanical loss during the deformation of the piezoelectric ceramic. Notice that the Curie temperature of the used ceramic - 190°C (Nec-Tokin website, Last update: 2016) - is not overcame (Fig.6.20).
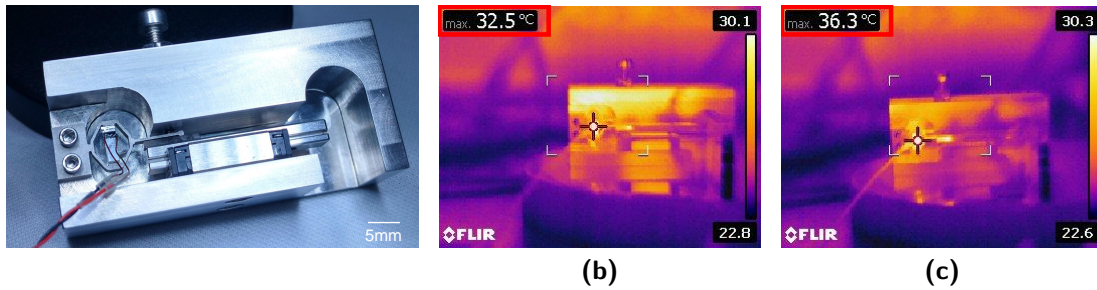
Figure 6.20 – Thermal observations of the piezoelectric ceramic during ultrasonic actuation. Used frequencies are (a) 22.0kHz and (b) 45.1 kHz, does not lead to overcome Curie temperature: 190˚C here. So there is no risk of piezoelectric depolarisation (section 1.2.2.1).

Resulting displacement amplitudes at 22.0kHz and 45.1kHz are respectively 2.78μm and 2.76μm. So C is set to 1 and D is set to 0.34 (Eq.6.11) in order to get a 1/3 ratio between the fundamental and the first harmonic (as Eq.6.4) and reaching a QST displacement pattern. As a result, a back and forth motion has been obtained (Fig.6.21). As previously, an asymmetry occurs. Speed in positive/negative direction are 30/10 mm/s respectively. Notice that asymmetry has not been optimised in this design in front of the ease of manufacturing. Indeed, but speed is not symmetrical. No noise is heard anymore.
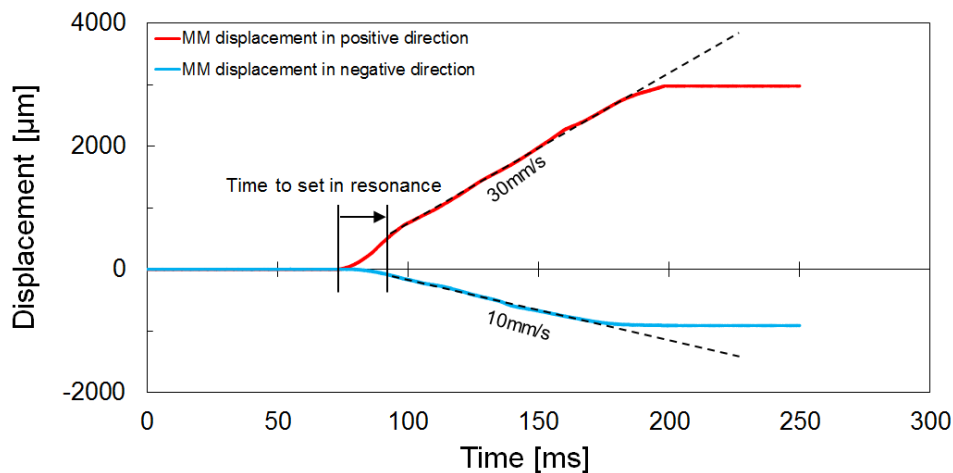
Figure 6.21 – US-SPA displacement curves. Resulting speeds are 10mm/s and 30mm/s.

Discussion and intermediate conclusion — Notice that normal preload has been minimized since purpose was validating US-SPA feasibility. Consequently, generated tangential force is very low (in vertical orientation, the motor is not able to overcome the weight of the MM).

Thus, in this section, a very stiff amplified shell has been successfully coupled with QST signal to work out a silent SPA with a good velocity. However, the lack of actuation force and the time to manually set QST signal constitutes issues to address before making this demonstrator a reliable product. It will be a major perspective of this work.

6.3 Conclusion

In this chapter, experiments have been carried out to identify the main acoustic source among actuation and friction to propose then solutions for noise reduction.

Thus, noise mainly comes from vibrations bound to piezoelectric ceramic actuation and only a few percent comes from friction.

Different solutions have been proposed to improve the SPA in an acoustic approach. (i) Volume required for insulation was not compliant with perspectives of miniaturisation. This solution has been set aside. (ii) Vibration damping appeared to be an interesting way of improvement if and only if a high stiffness in actuation direction is maintained. Therefore, the use of an intermediate damper has also been set aside. (iii) Actuation signal optimisation have been investigated to decrease Sound Intensity Level without any design change, making proposed solutions easily and quickly applicable. Replacing x^2 signal by QST signal, so called QST-3f since it is composed of three-harmonic summation, appears to be a good trade-off in term of acoustic (noise decreased by sixteen dBA), and in term of mechanical performances (speed is slightly decreased and actuation force is divided by two approximately). (iv) Finally, a structural modification has been proposed for actuating at a frequency above 20kHz so that not being audible by human ears. To do so, a very stiff amplified shell has been successfully coupled with QST signal to work out a silent SPA with a good velocity. However, the lack of actuation force and the time to set manually the QST signal are issues to address before making this concept reliable.

6.4 Perspectives

In this chapter, acoustic improvements have been systematically compared with mechanical performances in term of no-load speed and blocked force. However, impact on tribological performances has not been investigated. For instance, one can suppose that QST-3f signal, with less sharp transitions between stick and slip phases, could lead to a decreased volume of ejected particles. So, it has been tested on tribometer. This hypothesis could not be verified because resonance mode of the notch was too excited by this signal. Thus, first step toward this tribo-acoustic perspective would be to make the SPA-tribometer stiffer.

Part IV.

Conclusion & perspectives

If you can't explain it simply,
you don't understand it well enough.

— A. Einstein

Conclusion:
from Research to Development

7.1   General summary

Among the different concepts of piezoelectric motor, Stepping Piezoelectric Actuators (SPA) belong to inertia-drive category. In addition, SPA take benefit from a pre-stressed leverage structure for amplifying the amplitude of vibrations generated by the piezoelectric ceramic, before the conversion into steps by means of friction, through stick-slip. This enables these motors to reach high speed while being easily driven electrically in low frequency range. However, vibrations also generate wear and noise. Thus, the goal of this PhD research work was to consider *SPA, not just as a classical mechatronic, vibratory or tribological system but as a mechatro-tribo-vibratory system.*

To address wear issues, tribological instrumentation has been deployed. On the one hand, instrumentation on a real motor was not possible because of its small size. On the other hand, classical tribometers were not representative enough of SPA dynamic behaviour to provide relevant results. So, a SPA-dedicated tribometer has been developed. In particular, *this tribometer makes it possible to observe solid particle flows into the contact, in operation.* To decrypt the tribological circuit, resulting *in-situ* observations, performed in operation, through a transparent glass interface were compared to *ante-*, *post-mortem* observations and monitoring.

In SPA, friction 1st bodies are coated Ti-6Al-4V and fibreglass filled polymer, so-called composite. Long-term tests have highlighted that *the orientation of 1st bodies impacts tribological performances.* Indeed, when pin, which "sees" more sliding distance than pad, is in composite, it lead to early test end due to material failure. On the contrary, when pin is in Ti-6Al-4V and pad is in composite, the formed 3rd body layer quickly stabilizes solid particle flows and so the performances in a long lifetime.

Deployed instrumentation made is possible to decrypt this good tribological behaviour. From the first operating cycles, 3rd body layer has formed on composite surface by shearing the carbon matrix. This layer acts as "chocolate spread". It traps extruded coating particles as well as glass fibres, crushed by repeated impacts beforehand. Progressively, the Ti-6Al-4V substrate is reached. Related ejected particles mix

into the 3rd body layer, leading to a partial Ti-6Al-4V/Ti-6Al-4V contact. Created layer is mainly ductile and abrasive. Its retaining power stabilizes the different 3rd body flows and so the performances. Resulting friction coefficient is quite high (~ 0.5) and remains constant, leading to good performances in a long lifetime. In keeping 1st bodies in this orientation -coated Ti-6Al-4V pin *vs.* fibreglass filled polymer pad- *lifetime has been increased by ten, reaching at least 10^7 cycles/20km, without failure.*

However, despite a longer lifetime, wear flow Q_w remained too important. In order to lower this flow while maintaining lifetime and performances, a carbon fibre filled polymer has been introduced in place of fibreglass filled polymer. Hypothesis leading to this replacement was to decrease the abrasive power, triggering high wear flow, while increasing adhesive power, to retain even more the 3rd body into the contact. This new tribological triplet also reaches at least 10^7 cycles while leading to a lower wear volume similar to test with fibreglass filled polymer at 10^6 cycles. So, *Godet's 3rd body approach made it possible to introduce a new tribological triplet addressing both lifetime and wear issues, without multiplying tests on friction materials.*

Vibratory issues have been addressed in two times.

First, *a hybrid FEM/lumped model, which considers SPA motion in the three directions of space, has been implemented to better model the actuator vibratory behaviour.* It relies on a modal superposition approach. Such a model highlighted its interest in the case of tribometer by making it possible to identify an unexpected low-frequency resonance mode as that of notch bending. It operates in three steps. After the design of actuator on computer, a frequency analysis is led at first to get the resonance mode shapes and mass contributions to motion in actuation direction. Then, the most impacting resonance modes, selected by a Cumulative Effective Mass Participaton Factor (CEMPF), are converted into a differential equation system by means of a modal superposition approach. At last, this system has been implemented in conjunction with a LuGre friction model to get the global behaviour of the SPA. As a result, this model better reflects the vibratory behaviour of the SPA-tribometer with its notch. In addition, this model is versatile since it makes it possible to get the performances of SPA no matter their mechanical structure as long as the force provided by the actuator is high in front of the friction force.

Second, several experiments have been performed to list the noise sources and to test noise reduction solutions. Indeed, SPA generated noise ranging from 85dBA to 95dBA (measured at 30cm). This amounts to listening traffic noise on major road at 10-m distance. Among the vibrations generated by the actuator and by the friction interface, that from actuator radiate more noise. So focus has been done on it while taking care about mechanical performances. If insulation and damping have been set aside because of their impact on mechanical performances, an acoustically optimised signal has been proposed instead of loud x^2 original signal. So called QST-3f, it looks like a sawtooth signal but without any acceleration peaks leading to acoustic "hammer blows". As a result, *signal optimisation led to a noise reduction by 16dBA*. On the side of performances, speed was maintained but blocked force decreased. So this signal is a trade-off for application whose priority is noise level instead of force generation. To go further, a structural modification has been proposed for actuating at a frequency above 20-kHz audible range. This ultrasonic SPA successfully operates in silence with a good velocity but a big lack of force. It constitutes a major perspective of this work.

Thus, these two avenues of work led to a better understanding of SPA through vibratory and tribological approaches. In addition, the different experiments and simulations led to propose a design methodology for SPA design (section 7.2) and innovative SPA developments (section 7.2), addressing new industrial markets.

7.2   SPA design methodology

The research work presented in this thesis focused on vibratory and tribological understanding of amplified piezoelectric inertia motors SPA. In addition to lessons learned, the different tests and simulations led to develop a SPA design methodology. This methodology is divided in two steps: mechanical design and performance estimation (Fig.7.1).
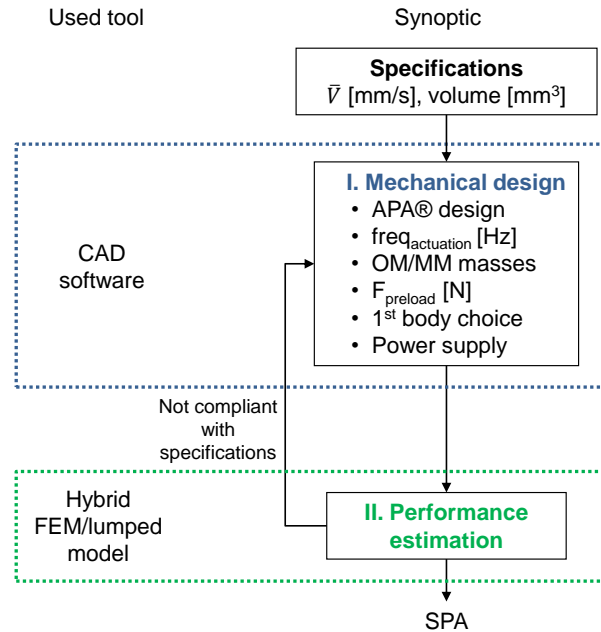
Figure 7.1 – Flow chart for SPA design.

Mechanical design —   Before starting mechanical design on Computer Assisted Design (CAD) software, a few milestones may help to assess consistency of specifications such as *mean speed* and *volume.* They may help then to start driving the final design.

- First, speed directly depends on *APA® design.* Indeed, one can consider that speed is equal to step size times *actuation frequency* (section 2.2.3). Likewise, to be independent on resonance effects, actuation frequency has to be lower than resonance frequencies of the motor.   Thus, both stiffness and stepsize of the actuator give a first piece of information about the final volume of the motor. Notice that, if noise is a priority, QST-3f signal (section 6.2.3) should be used. In comparison with x^2 signal, expected performances will be lower. Moreover, stiffness of the actuator will have to be even more prioritised since energy of the QST-3f signal focuses in frequencies closed to that of actuation.

- Second, focus must be done on energy transfer through the friction interface. It depends on both *oscillating and moving masses* as well as the *preload force* (Eq.1.12). Here, based on tribological monitoring, friction coefficient of 0.5 can be used (Fig.4.9). In order to overcome the friction force and so to trigger the stick-to-slip transition, the force of actuator must be higher than friction force. Notice that necessary preload force will also drive the final *volume* of the motor. Likewise, notice that, to minimize asymmetry of performances, APA® axis must be as close as possible to friction thrust axis.

Beyond mechanical performances, it is also necessary to remind some key points about tribology of *1ˢᵗ bodies design.*

- First, it has been observed that their orientation impact tribological performances. In order to reach a long lifetime with repeatable performances, the coated Ti-6Al-4V part must be that "sees" the most of sliding distance (section 4.2). Notice that, if a low wear is necessary, replacing the fibreglass filled polymer by the carbon fibre filled polymer identified in section 4.3.2, could be considered.

- Second, in this work, contact pressure was calculated by means of Hertz equation in static. About 10MPa was estimated at the beginning of each test (Table 3.2). Such contact pressure drive the geometry of 1st bodies and so the global SPA volume. At last, notice that manufacturing of must be achieved in *dry conditions*, in order to avoid the presence of lubricant inside the contact during operation.

Finally, even if it was not specified at first, previous considerations also drive the choice of piezoelectric ceramic size and, by extension, the *power supply*. Indeed, at voltage full scale, actuation frequency will be limited by both the piezoelectric capacitance and the current limitation of the power supply (Eq.1.4).

Performance estimation — Based on these consideration, if specifications are consistent, design can be achieved. Then, hybrid FEM/lumped modelling may lead to estimate final performances (Chapter 5). First, FEM frequency analysis makes it possible to confirm location of resonance frequencies, depending on the stiffness of actuator, and so the value of actuation frequency. Location and shape of resonance frequencies impacting actuation can be then implemented to quickly determine speed depending on actuation signal. If presizing has been carried out correctly, it should remain just fine adjustments, for instance to get a better stick-slip pattern (Fig.2.7).

In a next future, this SPA design methodology could be automated by means of an optimisation genetic algorithm (Ha et al., 2005), but these few milestones may already help in designing efficiently *SPA*.

7.3   Innovative SPA developments

The tribometer was initially designed to describe the SPA tribological solicitations. In addition, the pin-on-pad contact configuration - instead of the shaft-clamp configuration - makes it possible to co-locate the friction force and the APA® force in an isostatic configuration (Fig.7.2). Thus, this structure of motor, now called Module SPA (M-SPA), offers longer stroke capabilities, in linear or rotary motion - depending on the guidance - and facilitates the design of multi-DoF mechanisms.
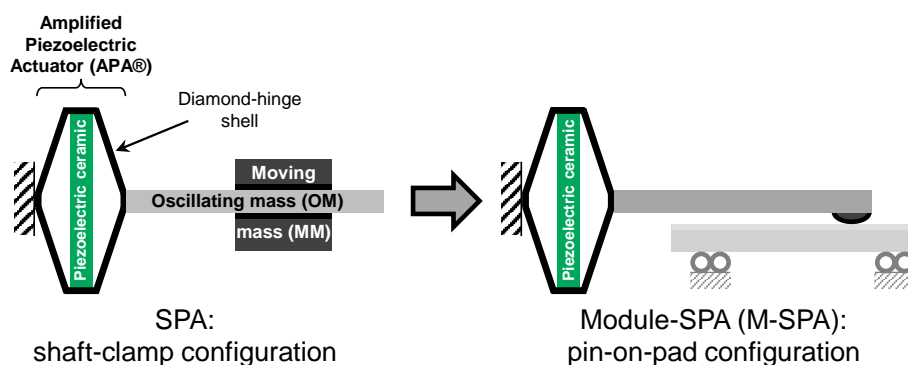
Figure 7.2 – From SPA to M-SPA configuration. M-SPA, in pin-on-pad contact configuration, makes it possible to actuate already guided mechanism, no matter the necessary stroke.

As examples, four motors based on this structure, and developed during this work are introduced below (Fig.7.3). Without detailing them for confidentiality reasons, next sections give an overview of the new SPA potentialities based on M-SPA configuration.
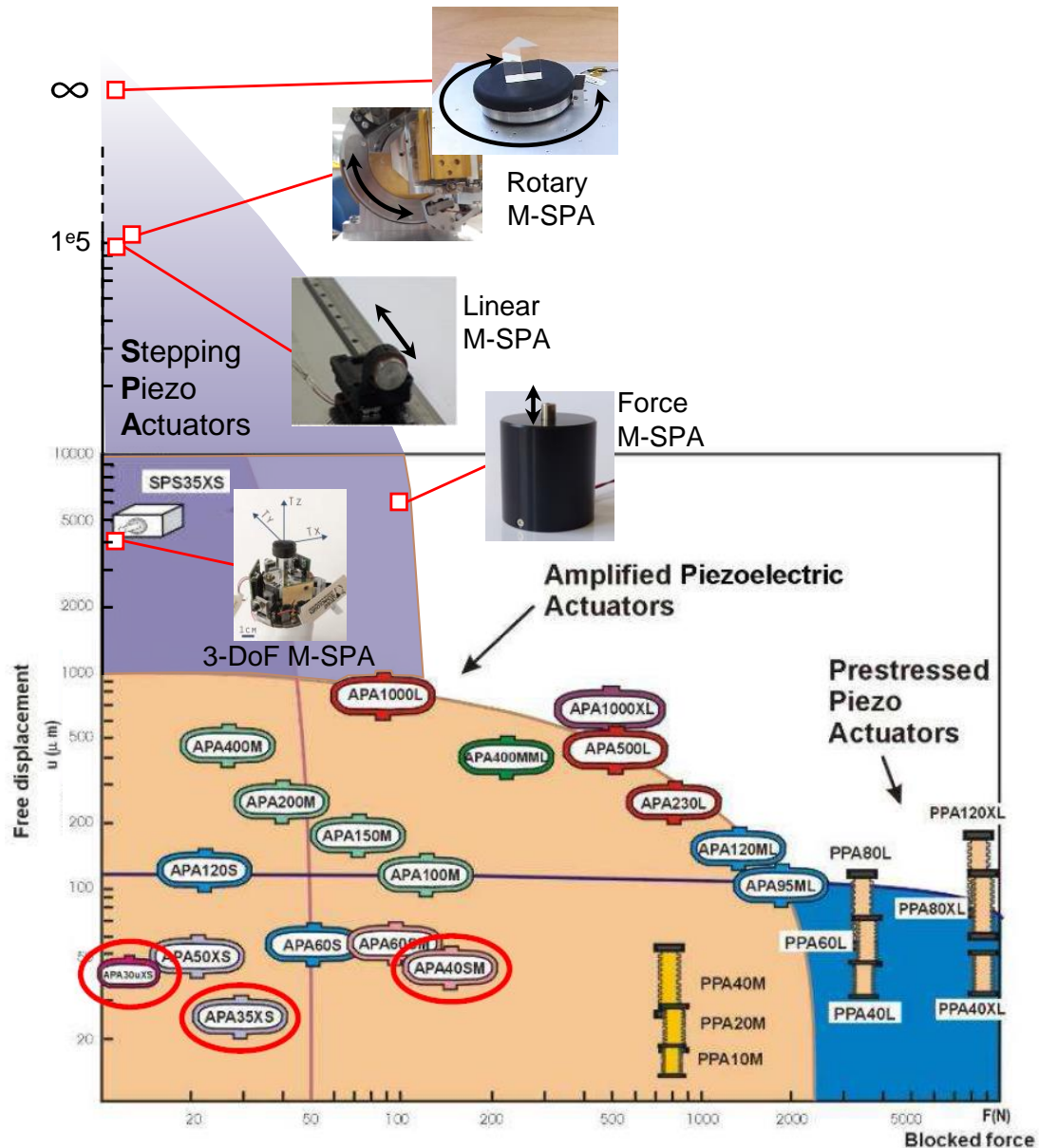
Figure 7.3 – New developments based on MSPA. In comparison with existing Cedrat Technologies product line, M-SPA configuration addresses long stroke applications.

7.3.1 Linear and rotary long stroke M-SPA

By means of a 10-cm long guidance, first development proposes a 10-cm stroke motor (Fig.7.4). It can be typically used to transport optical lenses. In this motor, actuator is moving with the payload so stroke is limited to both the length of the guidance and the electrical wires.
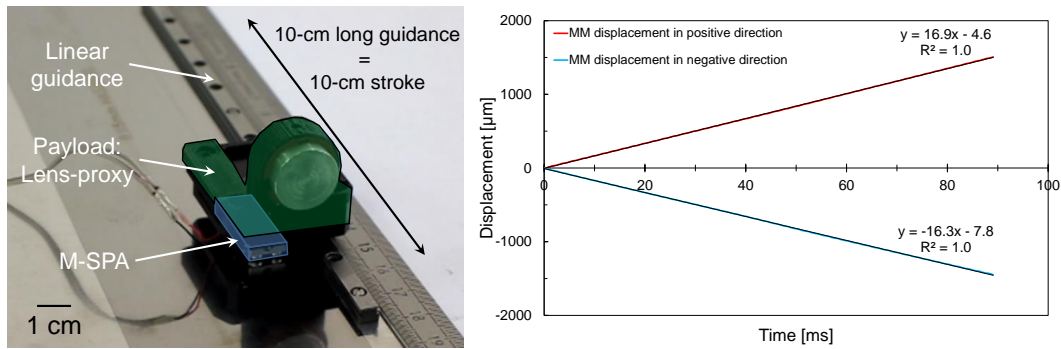
Figure 7.4 – Development of a linear 10-cm stroke M-SPA. Speed in both directions is quite symmetric: 16.9 mm/s in positive direction and 16.3mm/s in negative direction.

Second development is also a 10-cm stroke M-SPA but in a rotary configuration, with a rolling bearing (Fig.7.5). In this motor, payload mass is kg order of magnitude. Resulting speed is 1.8mm/s.
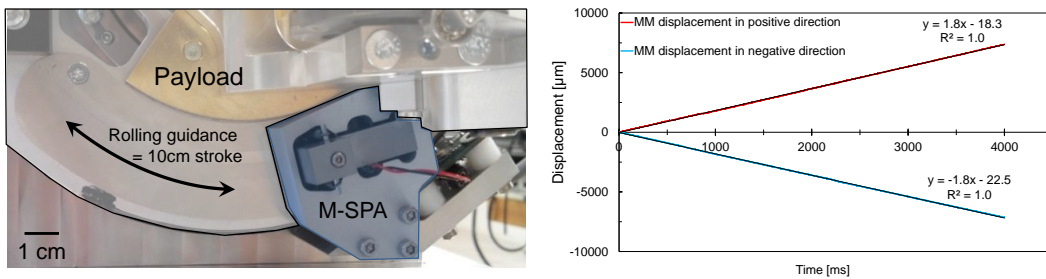
Figure 7.5 – Development of a rotary 10-cm stroke M-SPA. Payload mass is in kg order of magnitude. So mean speed is lower than previous example. They remain symmetric: 1.8mm/s in positive direction and negative direction.

Similarly a second rotary M-SPA has been developed and presented in Actuator 2016 conference (Fig.7.6, Freychet, 2016). Speed monitoring has not been implemented but local measurement by means of a laser vibrometer indicates a 15mm/s speed in both directions.
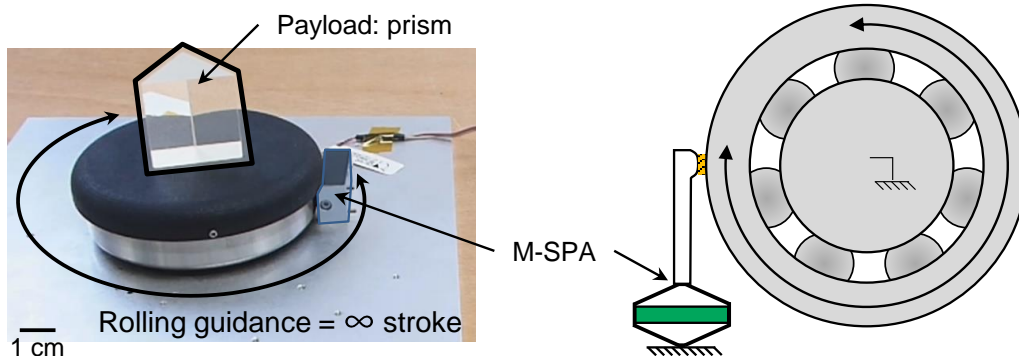
Figure 7.6 – Development of a rotary, infinite stroke M-SPA (Freychet, 2016). Mean speed is around 15mm/s in both actuation directions.

7.3.2 Force M-SPA

By means of a reduction gear, a prototype generating 100N of actuation force, in a vertical axis, has been developed (Fig.7.7). Total stroke, no-load speed, resolution and blocked force at rest are respectively 6mm, 80μm/s, 250nm and 450N.
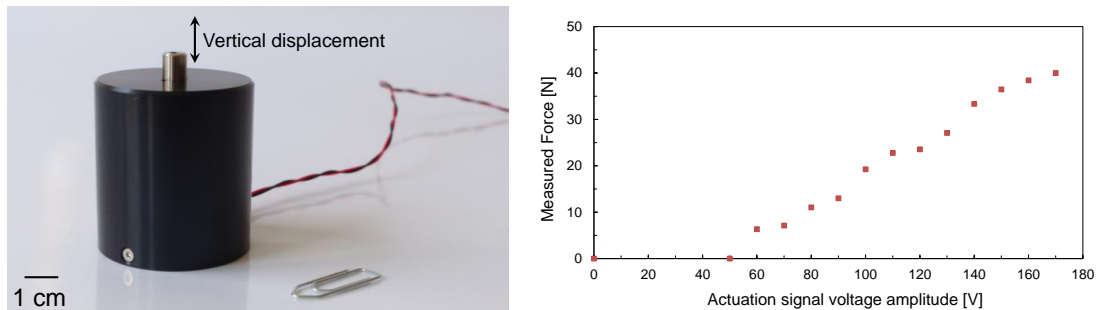
Figure 7.7 – Development of a M-SPA capable of generating 40-N actuation force in vertical direction by means of a reduction gear. Resulting speed is decreased to 80μm/s.

7.3.3 3-DoF M-SPA

A 3-DoF M-SPA has also been developed (Fig.7.8). It relies on 3 M-SPA mounted at 120° around a circle. Thus, they both guide and actuate the payload. Each of three M-SPA actuates in vertical direction making it possible to position a payload in three directions of space with a resolution down to a few μrad.
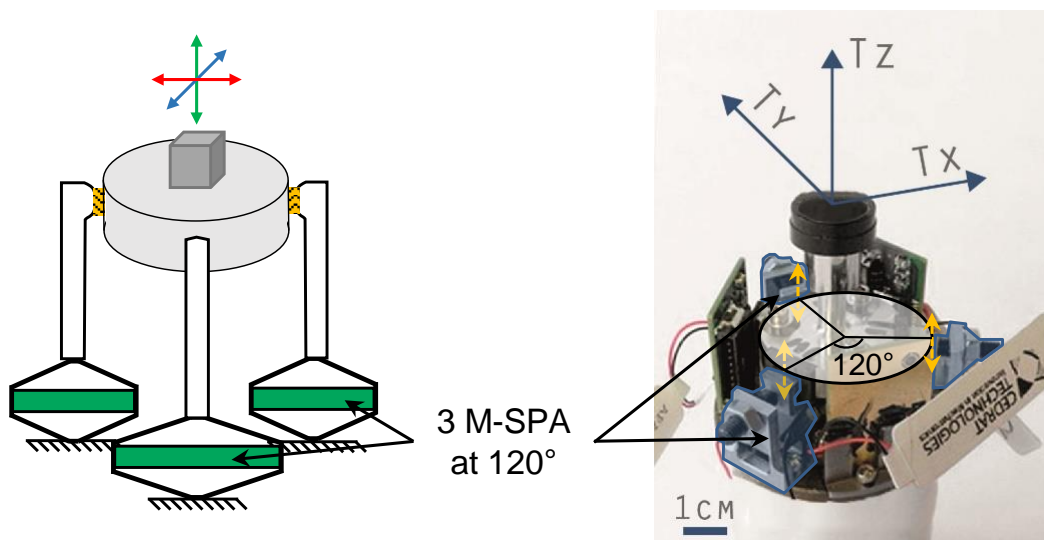
Figure 7.8 – Development of a 3-DoF M-SPA. To do so, 3 M-SPA are mounted at 120° around a circle to guide and actuate a payload in three directions of space.

At last, the versatility of the M-SPA structure has made it possible to quickly develop four applications whose actuation direction and stroke only depend on the guidance. Consequently, they complete the SPA line when mechanisms to drive are already guided. Moreover, the fact that M-SPA inherits from SPA working in harsh environments - such as thermal, vacuum (Belly et al., 2011) and amagnetism (Belly et al., 2010) - enables to address demanding markets such as medical, military and laboratory instrumentation.

8

As for the future, your task is not to foresee it, but to enable it.

— Antoine de St Exupéry

Perspectives

In this research work, initial purposes were to improve tribological and vibratory performances of SPA. To do so, it was first necessary to understand these motor intricacies. Different methodological frameworks were introduced to approach this understanding and led to practical improvements such as lifetime increase and noise reduction. Nevertheless, this work also raised some issues which should be investigated in a next future to go further in the improvements of these motors. Five points deserve, in my opinion, a particular attention. Some of these points are already under investigation by means of the European project Elvisa to bring SPA toward industrialisation.

- First point emerges from our lack of knowledge beside the previously studied tribological solicitations in harsh environment, such as vacuum or thermal. This point is addressed in section 8.1.

- Second point starts from the problem of performance asymmetry. This issue could be addressed experimentally by upgrading the current tribometer to enable thrust assessment in back and forth motion, such as described in section 8.2.

- Third point comes from the analyses of tribological solicitations. Such analyses remain qualitative. To be quantitative, the rheology of 3rd body flows should be investigated as proposed in section 8.3.

- Fourth point is based on acoustic results. Since they are actuated by an electrical signal whose frequency is in an audible range, current SPA definitely make noise. Limits in reducing this noise seems to be reached in this work. To overcome this limit, it could be interesting to trend toward ultrasonic SPA. Section 8.4 details the different steps leading to such an evolution.

- Finally, fifth and last point relies on the "simple" structure of SPA. Indeed, in these motors the way from the actuation toward friction is quite short. Thus, it could be interesting to optimise this tribological system no more passively - with a relevant choice of friction material - but in an active way - by acting in real time on monitored 3rd body flows. Section 8.5 introduces this concept so-called *tribotronic*.

8.1 Operations in harsh environment

As a first step, tribological inverstigation proposed in this work has been achieved in ambient air since this is the main addressed environment for current SPA. In addition, Belly et al. (2011) have tested and validated that SPA ensure operation in cold (until -180°C), hot (+60°C, limited by 1st bodies) and vacuum conditions. He also showed that, although it worked, speed performances were impacted by such environmental changes.

First perspective would consist in reproducing the tribological analysis, in harsh conditions, with the same 1st bodies, to characterize the associated tribological solicitations. Depending on the resulting observations, some improvements could be suggested to either optimise performances in each environment or to find a trade-off working better than the current 1st bodies, no matter the environment (maybe with the carbonfibre filled polymer, introduced in chapter 4).

To reach such a purpose, the methodological framework introduced in chapter 3 and the tribological investigation led in chapter 4 would enable to interpret *post-mortem* observations in a similar way in harsh conditions. Notice that an upgrade of the bench is necessary beforehand to address this perspective, in particular considering bearing. If air bearing was initially implemented to locate friction at the contact interface, it has to be replaced by classical bearing, compatible in vacuum. The development and the use of this bench are in progress (Fig.8.1).
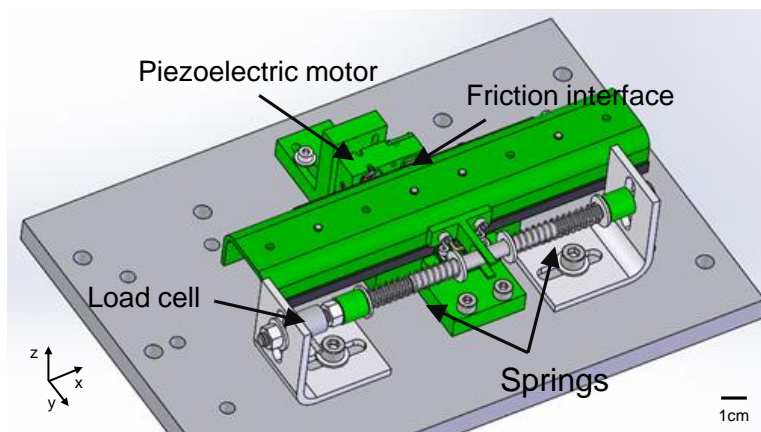
Figure 8.1 – Test bench for tribological investigations in harsh environments. In addition to mean speed monitoring, thrust measure has been automated (in comparison with chapter 6) by means of two springs and a load cell in order to get load capacity in hanging mode (Fig.2.13) all along long-term tests.

8.2 Toward symetrical performances by means of thrust qualification

At the beginning of this work, stroke of SPA was classically lower than centimetre. Thus, speed asymmetry was not a priority since back and forth motion last around one second. The introduction of Module SPA, M-SPA, has enabled to increase the stroke. Increasing stroke exacerbates this asymmetry and it becomes important to deal with this issue.

Second perspective would consist in understanding its origin. If it is partly attributed to electric response time in literature (Breguet, 1998) and to the dynamic

behaviour of actuator (section 2.2.3.3), design of the M-SPA also exacerbates it (section 3.1.1.4). It is attributed to the momentum between the friction contact point and the APA® thrust axis, but without be measured. So, a first step toward the asymmetry origin is automating thrust measure to link it with mean speed variation. Such an automatisation has already been achieved (Freychet, 2016). Preliminary measures emphasize that there is not only an asymmetry on speed (Fig.8.2) but also on thrust force (Fig.8.3). However, such a measure does not enable to determine the origin of asymmetry. Notice that, during this work, an additional long-term test, with a non-disclosed tribological triplet have been achieved under load conditions. Motor was identical with previous test, so an asymmetry was expected. However, resulting mean speed (Fig.8.4) and force (Fig.8.5) were surprisingly symmetrical. Before jumping to conclusions, this preliminary result must be confirmed by repeated tests. However, it emphasises that second step of this perspective would consist in reproducing the 3rd body flows analyses on tests under load conditions in order to characterize asymmetry from a tribological approach.
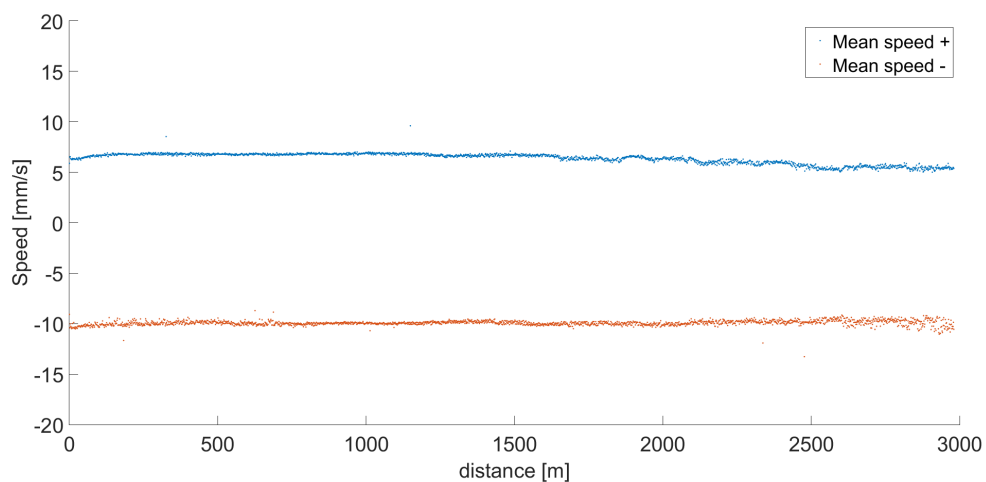
Figure 8.2 – Long-term test under elastic load with original 1st bodies. Positive mean speed is 7mm/s whereas negative means speed is -10mm/s.
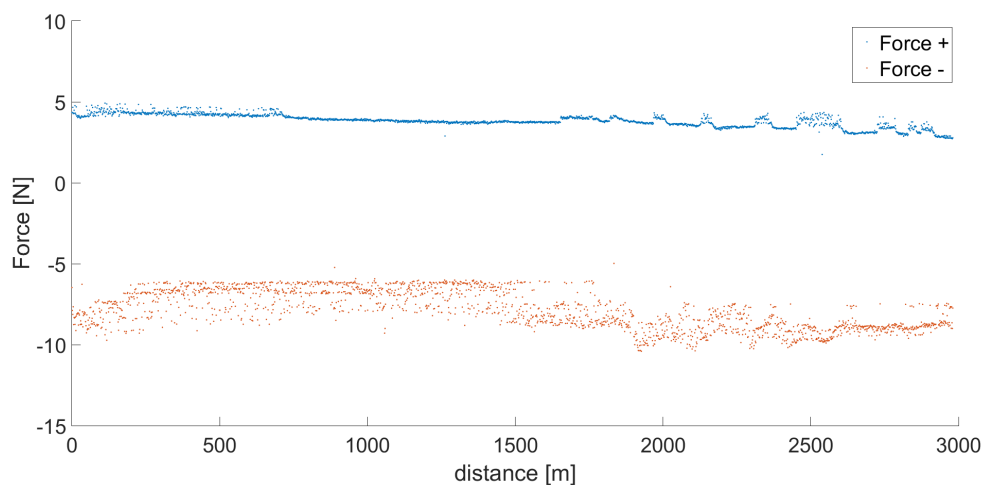
Figure 8.3 – Long-term test under elastic load with original 1st bodies. Positive mean force is 4N whereas negative means force is -7N.
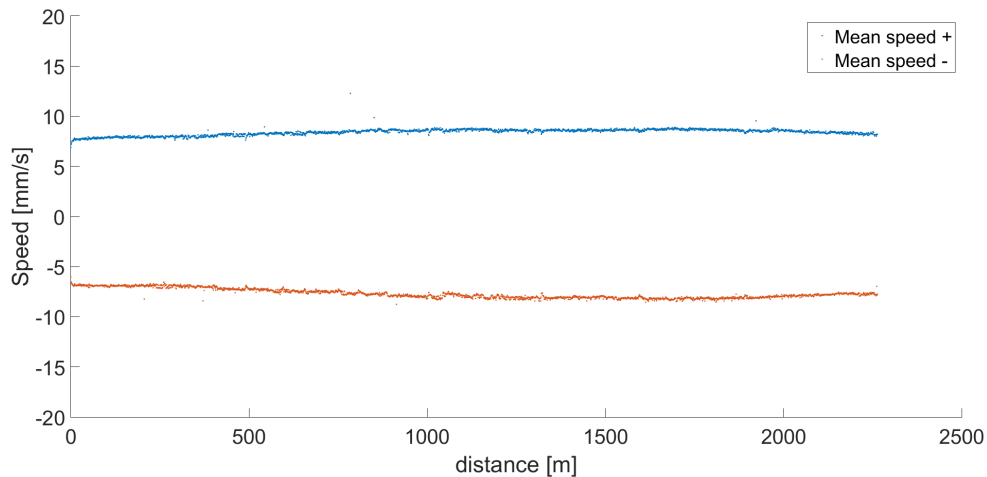
Figure 8.4 – Long-term test under elastic load with non-disclosed 1st bodies. Positive and negative mean speed evolves symetrically between 7 and 9mm/s.
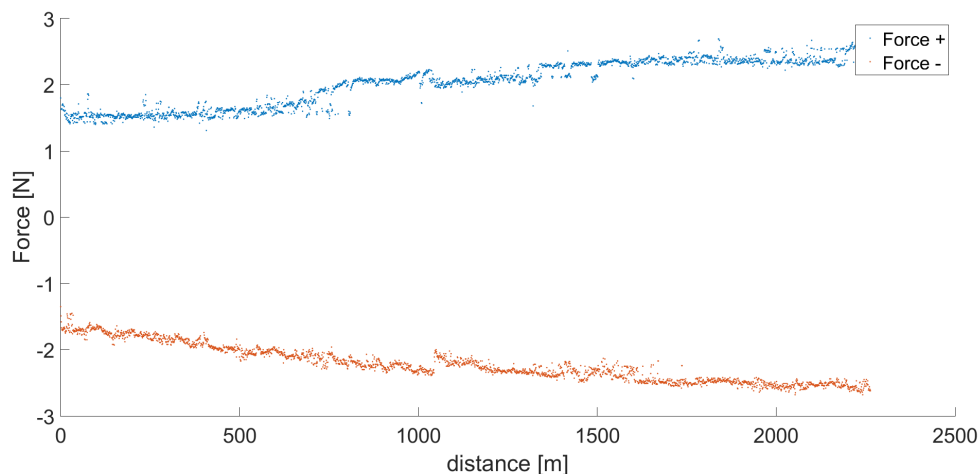
Figure 8.5 – Long-term test under elastic load with non-disclosed 1st bodies. Generated force symmetrically increases from 1.5 to 2.5N.

8.3 Quantifying the wear flow through the rheology of 3rd body

Although the tribological analysis made it possible to anticipate the good behaviour of the carbonfibre filled polymer in a purpose of decreased wear flow, Q_w, (chapter 4), it does not enable to predict such a flow amplitude quantitatively. Indeed, all tribological analyses have been led qualitatively. Properties such as rheology of 1st and 3rd bodies could give access to this assessment but they are not measurable yet. Numerical modelling becomes the most relevant option today.

So, in complement with hybrid modelling implemented in chapter 5, third perspective would consist in modelling the interactions between the three scales of the tribological triplet: S_0-mechanism, $S_{1/5}$-1st bodies and S_3-3rd body (Fig.5.1).

To reach such a purpose, one could imagine using the hybrid FEM-lumped modelling to get the vibratory behaviour of the mechanism. Then, S_0 modelling would send external solicitations to the 1st bodies. Finite Element Modelling could be used to simulate only the 1st bodies and getting the local dynamic interactions in the contact.

Finally, 3rd body layer could be modelled by Discrete Elements to get data such as tangential thrust -in term of preload- and wear flow.

Notice that, in our study as in many others, internal 3rd body comes from 1st bodies. Thus, FEM-DEM coupling model developments are currently in progress (Fig.8.6 from Haddad et al., 2016). Such an approach will certainly be more tangible in a next future.
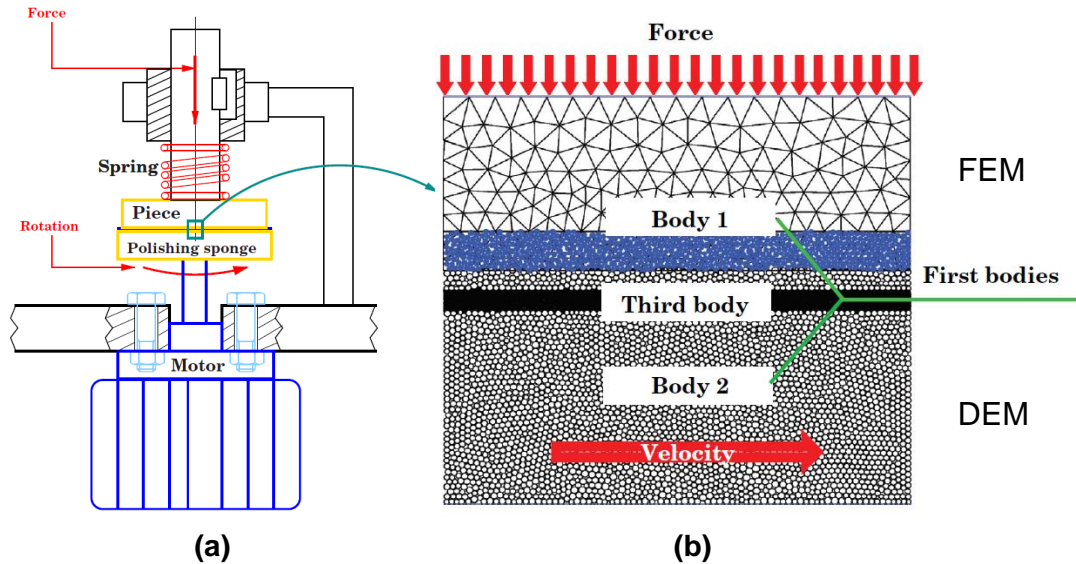
Figure 8.6 – Numerical Finite-Discrete Element coupled Model to study simultaneously the behaviour of both 1st body and 3rd body observations scales (Adapted from Haddad et al., 2016). (a) Polishing machine. (b) Associated tribological circuit. 1st body #1, is modelled by DEM in the area adjacent to the 3rd body while the rest of the structure is modelled by FEM. Other accommodation sites, $S_{3/4/5}$ are modelled by means of DEM.

8.4 A silent SPA: toward ultrasonic motors

As for asymmetry, increasing the stroke of SPA has led to longer period of continuous actuation. This consequently leads to increase the nuisance due to noise. Although noise level has been decreased in chapter 6, it remains annoying for some applications such as consumer goods. However, a limit seems to be reached considering classical SPA. Indeed, actuation being responsible for this noise, it can not be fully deleted without stopping the motor.

So, a fifth and last perspective would be to address this issue by transporting SPA from audible actuation frequency to ultrasonic actuation frequency. Operating principle would remain similar. An asymmetric signal would trigger displacement in back and forth motion. However, in the ultrasonic mode, resonance frequencies have to be used to lower dielectric losses. Thus, a specific actuation signal will be necessarily used to exploit this resonance frequencies and generate a quasi-sawtooth pattern (as in chapter 6). Likewise, since the actuation frequency would be higher than 20kHz, there will be no more stick-slip but only slip-slip (Fig.2.7), leading to tribological solicitations potentially totally different.

Thus, such a perspective requires an important work. First step would consist in optimizing an APA® shell for getting a second resonance frequency equal to twice as much the first one (as in section 6.2.4). Ultrasonic motor are very sensitive to mounting conditions and environment, so second step would consist in tracking resonance

frequency and relative amplitude in real time in order to set the actuation signal efficiently. This require an important electronic development. Last but not least step addresses tribological issue. Although the methodological framework, introduced in chapter 3, could be re-used in the characterisation of tribological solicitations in ultrasonic configuration, the developed tribometer will require an upgrade. Works of Rehbein and Wallaschek (1998) could be used to achieve this upgrade.

8.5 Mechatronic to Tribotronic: toward an electronic closed-loop of 3rd body

Investigation on both tribology and vibratory behaviours led to an interesting synergy. Chapter 3 and 4 made it possible to discover how the SPA mechanism, S_0, interacts with contact's life. Chapter 5 and 6 made it possible to discover how influencing the dynamic behaviour of the mechanism, especially by considering actuation signal.

Thus, a fourth perspective would be to consider the link between actuation and wear from an electronic approach in order to optimise this tribological system no more passively, by a relevant choice of friction material but in an active way. This concept, called *tribotronic*, has been introduced in Glavatskih and Höglund (2008) to transport tribological systems to a dramatically higher level of performance. A first attempt can be found in Tzanakis et al. (2012) through optimisation of a micro-CHP, slipways and recycled plastics. Considering piezoelectric motor, idea is not new since Higuchi already propose to control the velocity of its motors by means of a preload controlled by a piezoelectric ceramic (Higuchi et al., 1992). Drawback of this method is it requires, as in inchowrm motors, a second power supply and an electronic synchronisation. Focusing on SPA, it is assumed that the repeated impacts help to fragment the coating and the glassfibres, what facilitates the rapid installation of a stable and protective 3rd body layer. In very long-term tests, it is assumed that this layer periodically fragments, increasing temporarily Q_w, and reform as long as there is available material, what impact the mean speed (Fig.4.23). So, it would be interesting to space the periods of 3rd body layer fragmentation in order to maximize the lifetime.

To reach such a purpose, a solution would be to modify the excitation signal when necessary. For instance, as introduced in chapter 6, actuation voltage order can be sharp to maximize force transfer or smooth to decrease noise level. Modal landscape of smooth signal is narrower than sharp one, which could make it possible to actuate less strongly. A real progress would be to use a first actuation signal to quickly form the 3rd body layer. Then, switching to a second signal in order to less damage the 3rd body layer. As soon as the performances start to decrease or if Q_w suddenly increases, actuation signals would be switched again to eject the excess of 3rd body and to reform a stable layer and so on. This could be represented by an electronic close-loop for controlling the 3rd body flows (Fig.8.7).
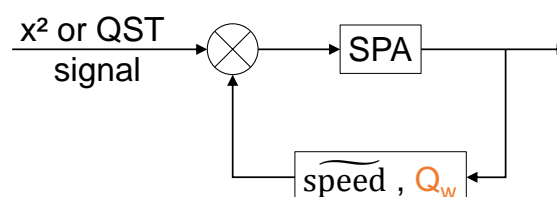
Figure 8.7 – Concept of a 3rd body flow control loop.

Bibliography

Achanta, S., Liskiewicz, T., Drees, D., and Celis, J.-P., 2009. Friction mechanisms at the micro-scale. *Tribology International*, pp. 1792–1799. doi:10.1016/j.triboint.2009.04.018. (Cited on page 66)

Aglione, D.-L., 2014. *Design, Modeling, and Simulation of Battery Pack Suspensions for Off-road Electric Vehicles.* PhD thesis, The Pennsylvania State University. (Cited on pages 128 and 132)

Agrait, N., 1992. Vertical inertial piezoelectric translation device for a scanning tunneling microscope. *Review of scientific instruments*, pp. 263–264. doi:10.1063/1.1142969. (Cited on page 22)

Ahmad, M. S., Jamil, M., Iqbal, J., Khan, M. N., Malik, M. H., and Butt, S. I., 2016. Modal analysis of ship's mast structure using effective mass participation factor. *Indian Journal of Science and Technology.* doi:10.17485/ijst/2016/v9i21/94830. (Cited on pages 110, 111 and xv)

Albahrani, S., Philippon, D., Bluet, J.-M., and Vergne, P., 2015. A review of in situ methodologies for investigating EHD contacts. *Proceedings of the Institution of Mechanical Engineers, Part J: Journal of Engineering Tribology*, pp. 86–110. doi:10.1177/1350650115590428. (Cited on page 46)

Altpeter, F., 1999. *Friction modeling, identification and compensation.* PhD thesis, École Polytechnique Fédérale de Lausanne (EPFL). doi:10.5075/epfl-thesis-1988. (Cited on pages 106 and 107)

American piezo website. https://www.americanpiezo.com/piezo-theory/ceramics.html. (Cited on page 10)

Anantheshwara, K., Murali, N. S., and Bobji, M. S., 2008. Effect of friction on the performance of inertial slider. *Sadhana*, pp. 221–226. doi:10.1007/s12046-008-0015-4. (Cited on page 37)

Anders, M., Thaer, M., and Heiden, C., 1987. Simple micropositioning devices for stm. *Surface Science*, pp. 176–182. doi:10.1016/0039-6028(87)90156-7. (Cited on pages 20 and 29)

Arnold, S., Pertsch, P., and Spanner, K., 2008. Piezoelectric positioning. In *Piezoelectricity*, pp. 279–297. doi:10.1007/978-3-540-68683-5_12. (Cited on page 36)

Asadian, A., Patel, R. V., and Kermani, M. R., 2011. A distributed model for needle-tissue friction in percutaneous interventions. In *International Conference on Robotics and Automation (ICRA)*, pp. 1896–1901. doi:10.1109/ICRA.2011.5979810. (Cited on page 107)

Asamene, K. and Sundaresan, M., 2012. Analysis of experimentally generated friction related acoustic emission signals. *Wear*, pp. 607–618. doi:10.1016/j.wear.2012.07.019. (Cited on pages 20 and 127)

Asenjo, A., Buendía, A., Gómez-Rodríguez, J. M., and Baró, A. M., 1994. Scanning tunneling microscopy/scanning electron microscopy combined instrument. *Journal of Vacuum Science & Technology B: Microelectronics and Nanometer Structures Processing, Measurement, and Phenomena*, pp. 1658–1661. doi:10.1116/1.587256. (Cited on pages 37 and 38)

Bacher, J.-P., 2003. *Conception de robots de très haute précision à articulation flexibles (in French)*. PhD thesis, École Polytechnique Fédérale de Lausanne (EPFL). doi:10.5075/epfl-thesis-2907. (Cited on page 22)

Ballout, Y., Mathis, J., and Talia, J., 1996. Solid particle erosion mechanism in glass. *Wear*, pp. 263–269. doi:10.1016/0043-1648(96)06922-0. (Cited on page 78)

Barth, H., 1973. Ultrasonic driven motor. *IBM technical disclosure bulletin.* (Cited on page 19)

Bathe, K.-J., 2006. *Finite element procedures.* Watertown, MA : Klaus-Jürgen Bathe. (Cited on page 113)

Baumann, A. and Zander, N., 2005. Ti6Al4V with anodization type II: Biological behavior and biomechanical effects. Technical report, DOT America. (Cited on pages 59, 60 and 62)

Belly, C., 2011. *Moteurs piézoélectriques inertiels: conceptions, réalisations, test et applications (in French)*. PhD thesis, Université de Technologie de Belfort-Montbeliard. (Cited on pages 1, 12, 25, 28, 29, 33, 34, 37, 38, 47, 48, 59, 62, 66, 103, 106, 107, 115, 121, 123, 133, v, vii, ix and xiv)

Belly, C. and Charon, W., 2012. Benefits of amplification in an inertial stepping motor. *Mechatronics*, pp. 177–183. doi:10.1016/j.mechatronics.2012.01.006. (Cited on pages 28 and 34)

Belly, C., Mathieu, H., Claeyssen, F., and Letty, R., 2010. MRI-compliant micro-motors for medical and biomedical applications. Technical report. (Cited on pages 22, 59 and 155)

Belly, C., Buttery, M., and Claeyssen, F., 2011. Thermal vacuum behaviour of a stepping piezo actuator. *ESMATS.* (Cited on pages 22, 97, 155 and 158)

Belly, C., Porchez, T., Dubois, F., and Barillot, F., 2014. Long stroke/high resolution tip tilt mechanism. In *In Proceedings of Actuator conference.* (Cited on page 23)

Bergander, A., 2003. *Control, wear testing & integration of stick-slip micropositioning.* PhD thesis, École Polytechnique Fédérale de Lausanne (EPFL), Lausanne. doi:10.5075/epfl-thesis-2843. (Cited on page 39)

Bergander, A. and Breguet, J.-M., 2002. A testing mechanism and testing procedure for materials in inertial drives. pp. 213–218. doi:10.1109/MHS.2002.1058037. (Cited on pages 22, 37 and ix)

Bergander, A., Driesen, W., Varidel, T., and Breguet, J.-M., 2003. Development of miniature manipulators for applications in biology and nanotechnologies. In *Conference on Intelligent Robots and Systems. Proceeding of the Microrobotics for Biomanipulation Workshop*, pp. 11–35. (Cited on pages 34 and 36)

Bergander, A., Breguet, J., and Varidel, T., 2004. Piezoelectric actuator with passive gap for push-pull motion. URL https://www.google.ch/patents/WO2004077584A1?cl=en. WO Patent App. PCT/CH2004/000,099. (Cited on page 46)

Berger, E. J., 2002. Friction modeling for dynamic system simulation. *Applied Mechanics Reviews*, pp. 535–577. doi:10.1115/1.1501080. (Cited on pages 105 and xiv)

Berthier, Y., 1988. *Mécanisme et tribologie (In French)*. PhD thesis, Institut National des Sciences Appliquées de Lyon (INSA). (Cited on page 63)

Berthier, Y., 1990. Experimental evidence for friction and wear modelling. *Wear*, pp. 77–92. doi:10.1016/0043-1648(90)90210-2. (Cited on pages 45, 58, 63, 64, 71 and 76)

Berthier, Y., 2005. Third body reality-consequences and use of the third body concept to solve a friction and wear problems. *Wear, Materials, Mechanisms and Practice*. doi:10.1002/9780470017029.ch12. (Cited on pages 45, 58 and 63)

Bhatia, V., Gregorski, S. J., Pikula, D., Chaparala, S. C., Loeber, D. A. S., Gollier, J., Ozeki, Y., Hata, Y., Shibatani, K., Nagai, F., Yukinobu, N., Naoki, M., and Satoshi, N., 2008. Distinguished paper: Efficient and compact green laser incorporating adaptive optics for wide operating temperature range. In *SID Symposium Digest of Technical Papers*, pp. 962–965. doi:10.1889/1.3069839. (Cited on pages 32 and 33)

Blackford, B. L., Jericho, M. H., and Boudreau, M. G., 1992. A vertical/horizontal two-dimensional piezoelectric driven inertial slider micropositioner for cryogenic applications. *Review of scientific instruments*, pp. 2206–2209. doi:10.1063/1.1143140. (Cited on pages 16, 22, 37 and 128)

Blackford, B. and Jericho, M., 1990. Simple two-dimensional piezoelectric micropositioner for a scanning tunneling microscope. *Review of scientific instruments*, pp. 182–184. doi:10.1063/1.1141870. (Cited on page 22)

Blatter, A. and Hsu, S., 1966. Transducer. URL https://www.google.ch/patents/US3292019. US Patent 3,292,019. (Cited on page 17)

Blau, P. J., 1992. *Scale Effects in Sliding Friction: An Experimental Study*, pp. 523–534. doi:10.1007/978-94-011-2811-7_26. (Cited on page 46)

Bobji, M. S., Ramanujan, C. S., Pethica, J. B., and Inkson, B. J., 2006. A miniaturized tem nanoindenter for studying material deformation in situ. *Measurement Science and Technology*, 17(6):1324. doi:10.1088/0957-0233/17/6/006. (Cited on page 37)

Bordoni, F., De Gasperis, G., Di Battista, S., and Spagnolo, G. S., 1994. A scanning tunnelling microscope with a piezoelectric-driven inertial slider. *Sensors and Actuators A: Physical*, pp. 173–178. doi:10.1016/0924-4247(94)00834-5. (Cited on page 29)

Breguet, J.-M., 1998. *Actionneurs "stick and slip" pour micro-manipulateurs (In French)*. PhD thesis, École Polytechnique Fédérale de Lausanne (EPFL). doi:10.5075/epfl-thesis-1756. (Cited on pages 31, 32, 33, 39, 49, 106, 132 and 158)

Breguet, J. M. and Clavel, R., 1998. Stick and slip actuators: design, control, performances and applications. doi:10.1109/MHS.1998.745756. (Cited on page 23)

Brevier Technical Ceramics website. http://www.keramverband.de/brevier_engl/3/4/2/3_4_2_8.htm. (Cited on page 10)

Brisbane, A. D., 1968. Position control device. URL https://www.google.ch/patents/US3377489. US Patent 3,377,489. (Cited on pages 17 and vi)

Buchi, R., Zesch, W., Codourey, A., and Siegwart, R., 1995. Inertial drives for micro-and nanorobots: analytical study. pp. 89–97. doi:10.1117/12.228639. (Cited on pages 20, 22, 127 and 128)

Burleigh Instruments website, Last update: 2014. http://www.burleigh.com. (Cited on page 17)

Cameron, D. E., Lang, J. H., and Umans, S. D., 1992. The origin and reduction of acoustic noise in doubly salient variable-reluctance motors. *IEEE Transactions on Industry Applications*, pp. 1250–1255. doi:10.1109/28.175275. (Cited on page 128)

Cedrat Technologies website. http://www.cedrat-technologies.com/. (Cited on page 49)

Chang, S. H. and Li, S. S., 1999. A high resolution long travel friction-drive micropositioner with programmable step size. *Review of Scientific Instruments*, pp. 2776–2782. doi:10.1063/1.1149794. (Cited on page 20)

Chao, S.-H., Garbini, J. L., Dougherty, W. M., and Sidles, J. A., 2006. The design and control of a three-dimensional piezoceramic tube scanner with an inertial slider. *Review of scientific instruments*, pp. 1–7. doi:10.1063/1.2210172. (Cited on page 106)

Cheng, C. and Hung, S., 2011. The design and characteristic research of a dual-mode inertia motor (in French). In *Advanced Intelligent Mechatronics*. (Cited on page 34)

Chromik, R.-R., Baker, C.-C., Voevodin, A.-A., and Wahl, K.-J., 2007. In situ tribometry of solid lubricant nanocomposite coatings. *Wear*, pp. 1239–1252. doi:10.1016/j.wear.2007.01.001. (Cited on page 46)

Chu, C.-L. and Fan, S.-H., 2006. A novel long-travel piezoelectric-driven linear nanopositioning stage. *Precision Engineering*, 30(1):85–95. doi:10.1016/j.precisioneng.2005.05.002. (Cited on page 36)

Chuang, T.-M. and de Lozanne, A., 2007. Compact variable-temperature scanning force microscope. *Review of scientific instruments*, pp. 1–7. doi:10.1063/1.2735568. (Cited on page 37)

Claeyssen, F. and Barillot, F., 2008. Fine positioning system using an inertial motor based on a mechanical amplifier. URL https://www.google.com/patents/US8004153. US Patent 8,004,153. (Cited on page 25)

Claeyssen, F., Le Letty, R., and Lhermet, N., 1995. Actionneur piézoactif amplifié à raideur élevée (in French). (Cited on page 25)

Claeyssen, F., Ducamp, A., Barillot, F., Le Letty, R., Porchez, T., Sosnicki, O., and Belly, C., 2008. Stepping piezoelectric actuators based on APAs. In *In Proceedings of Actuator conference*. (Cited on pages 36 and 37)

Claeyssen, F., Belly, C., Le Letty, R., and Bagot, M., 2010. Dynamic strain limits of amplified piezo actuators. In *In Proceedings of Actuator conference*. (Cited on page 27)

Colas, G., Saulot, A., Godeau, C., Michel, Y., and Berthier, Y., 2013. Decrypting third body flows to solve dry lubrication issue - MoS_2 case study under ultrahigh vacuum. *Wear*, pp. 192–204. doi:10.1016/j.wear.2013.06.007. (Cited on page 46)

Colas, G., 2013. *Reasoned use of contaminants to characterise the rheology of both solid 1ˢᵗ and 3ʳᵈ bodies : Application to the tribology in space environments (In French)*. PhD thesis, INSA de Lyon. (Cited on page 72)

Coulomb, C.-A., 1785. *Théorie des machines simples, en ayant égard au frottement de leurs parties et à la roideur des cordages (in French)*. (Cited on pages 103 and 106)

Curie, J. and Curie, P., 1880. Développement, par pression, de l'électricité polaire dans les cristaux hémièdres à faces inclinées (in French). *Journal de Physique Théorique et Appliquée*, pp. 294–295. doi:10.1051/jphystap:018890080014900. (Cited on pages 8 and 10)

Curtis, R., Pearson, C., Gaard, P., and Ganz, E., 1993. A compact micropositioner for use in ultrahigh vacuum. *Review of scientific instruments*, pp. 2687–2690. doi:10.1063/1.1143857. (Cited on pages 37 and 38)

Czichos, H., Becker, S., and Lexow, J., 1987. Multilaboratory tribotesting: Results from the Versailles Advanced Materials and Standards programme on wear test methods. *Wear*, pp. 109–130. doi:10.1016/0043-1648(87)90020-2. (Cited on page 46)

Dahl, P. R., 1968. A solid friction model. Technical report, DTIC Document. (Cited on page 106)

Darby, A. and Pellegrino, S., 1997. Inertial stick-slip actuator for active control of shape and vibration. *Journal of intelligent material systems and structures*, pp. 1001–1011. doi:10.1177/1045389x9700801201. (Cited on page 37)

De Wit, C. C., Olsson, H., Astrom, K. J., and Lischinsky, P., 1995. A new model for control of systems with friction. *IEEE Transactions on Automatic Control*, pp. 419–425. doi:10.1109/9.376053. (Cited on pages 103, 106 and xv)

Descartes, S. and Berthier, Y., 2002. Rheology and flows of solid third bodies: background and application to an $MoS_{1.6}$ coating. *Wear*, pp. 546–556. doi:10.1016/S0043-1648(02)00008-X. (Cited on pages 46 and 63)

Di Bartolomeo, M., Massi, F., Baillet, L., Culla, A., Fregolent, A., and Berthier, Y., 2012. Wave and rupture propagation at frictional bimaterial sliding interfaces: From local to global dynamics, from stick-slip to continuous sliding. *Tribology International*, pp. 117–131. doi:10.1016/j.triboint.2012.03.008. (Cited on page 127)

Dowson, D. and Higginson, G., 1977. *Elasto-hydrodynamic lubrication*. International series on materials science and technology. Pergamon Press. (Cited on pages 58 and ix)

Drevniok, B., Paul, W. M. P., Hairsine, K. R., and McLean, A. B., 2012. Methods and instrumentation for piezoelectric motors. *Review of Scientific Instruments*, pp. 1–6. doi:10.1063/1.3694972. (Cited on page 22)

Dupont, P., Armstrong, B., and Hayward, V., 2000. Elasto-plastic friction model: contact compliance and stiction. In *Proceedings of the American Control Conference*, pp. 1072–1077. (Cited on page 106)

Dvorak, S.-D., Wahl, K.-J., and Singer, I.-L., 2007. In situ analysis of third body contributions to sliding friction of a Pb-Mo-S coating in dry and humid air. *Tribology letters*, pp. 263–274. doi:10.1007/s11249-007-9270-5. (Cited on page 46)

Edeler, C., 2011. Measurements and potential applications of force-control method for stick-slip-driven nanohandling robots. *Key Engineering Materials*, pp. 1556–1561. doi:10.4028/www.scientific.net/kem.467-469.1556. (Cited on pages 22, 34 and 106)

Edeler, C., Meyer, I., and Fatikow, S., 2010. Simulation and measurements of stick-slip-microdrives for nanorobots. In *New Trends in Mechanism Science*, pp. 109–116. Springer. doi:10.1007/978-90-481-9689-0_13. (Cited on page 37)

Eglin, M., Eriksson, M. A., and Carpick, R. W., 2006. Microparticle manipulation using inertial forces. *Applied physics letters*, pp. 1–3. doi:10.1063/1.2172401. (Cited on page 23)

Erlandsson, R. and Olsson, L., 1996. A three-axis micropositioner for ultrahigh vacuum use based on the inertial slider principle. *Review of scientific instruments*, pp. 1472–1474. doi:10.1063/1.1146876. (Cited on page 37)

Fatikow, S., Wich, T., Sievers, T., Jähnisch, M., Eichhorn, V., Mircea, J., Hülsen, H., and Stolle, C., 2008. Automatic nanohandling station inside a scanning electron microscope. *Proceedings of the Institution of Mechanical Engineers, Part B: Journal of Engineering Manufacture*, pp. 117–128. doi:10.1243/09544054JEM836. (Cited on page 22)

Fayeulle, S., Ehni, P., and Singer, I., 1990. *Paper V (ii) Role of transfer films in wear of MoS$_2$ coatings*. Tribology Series. doi:10.1016/S0167-8922(08)70249-9. (Cited on page 46)

Ferrer, C., Salas, F., Pascual, M., and Orozco, J., 2010. Discrete acoustic emission waves during stick-slip friction between steel samples. *Tribology International*, pp. 1–6. doi:10.1016/j.triboint.2009.02.009. (Cited on pages 20 and 127)

Fouvry, S., Duo, P., and Perruchaut, P., 2004. A quantitative approach of ti-6al-4v fretting damage: friction, wear and crack nucleation. *Wear*, pp. 916–929. doi:10.1016/j.wear.2004.05.011. (Cited on page 62)

Freychet, O., 2016. Module SPA (MSPA): critères de conception, création d'un banc de test, essais et conception d'un démonstrateur (In French) (internal report). Master's thesis, Université de technologie Belfort-Montbéliard (UTBM). (Cited on pages 154 and 159)

Fung, R.-F., Han, C.-F., and Ha, J.-L., 2008. Dynamic responses of the impact drive mechanism modeled by the distributed parameter system. *Applied Mathematical Modelling*, pp. 1734 – 1743. doi:10.1016/j.apm.2007.06.006. (Cited on page 32)

Furutani, K., Higuchi, T., Yamagata, Y., and Mohri, M., 1998. Effect of lubrication on impact drive mechanism. *Precision Engineering*, pp. 78 – 86. doi:10.1016/S0141-6359(98)00004-X. (Cited on pages 37, 38, 121 and 127)

Garbuio, L., 2006. *Etude du phénomène de lubrification électroactive à l'aide d'actionneurs piézoélectriques. Application à la réduction des forces de frottement sec dans un moteur à combustion interne (in French)*. PhD thesis, Institut National Polytechnique de Toulouse. (Cited on pages 11 and 27)

Glavatskih, S. and Höglund, E., 2008. Tribotronics - towards active tribology. *Tribology International*, pp. 934 – 939. doi:10.1016/j.triboint.2007.03.001. (Cited on pages 162 and xxiii)

Godet, M., 1984. The third-body approach: A mechanical view of wear. *Wear*, pp. 437–452. doi:10.1016/0043-1648(84)90025-5. (Cited on pages 40, 45, 58, 104, viii, ix and xiv)

Göken, M., 1994. Scanning tunneling microscopy in UHV with an x, y, z micropositioner. *Review of scientific instruments*, pp. 2252–2254. doi:10.1063/1.1144736. (Cited on page 37)

Ha, J.-L., Fung, R.-F., and Yang, C.-S., 2005. Hysteresis identification and dynamic responses of the impact drive mechanism. *Journal of Sound and Vibration*, pp. 943 – 956. doi:http://dx.doi.org/10.1016/j.jsv.2004.05.032. (Cited on pages 106, 152 and xxi)

Hack, T., 1998. Experiments with a new piezoelectric rotary actuator. In *Proceedings of the 1998 IEEE International Frequency Control Symposium*, pp. 724–732. doi:10.1109/FREQ.1998.717980. (Cited on pages 37 and 38)

Haddad, H., Guessasma, M., and Fortin, J., 2016. A dem–fem coupling based approach simulating thermomechanical behaviour of frictional bodies with interface layer. *International Journal of Solids and Structures*. doi:10.1016/j.ijsolstr.2015.11.026. (Cited on page 161)

Hase, A., Mishina, H., and Wada, M., 2012. Correlation between features of acoustic emission signals and mechanical wear mechanisms. *Wear*, pp. 144–150. doi:10.1016/j.wear.2012.05.019. (Cited on page 46)

Heckl, M. A. and Abrahams, I. D., 2000. Curve squeal of train wheels, part 1: Mathematical model for its generation. *Journal of Sound and Vibration*, pp. 669–693. doi:10.1006/jsvi.1999.2510. (Cited on page 128)

Heinzmann, A., Hennig, E., Kolle, B., Kopsch, D., Richter, S., Schwotzer, H., and Wehrsdorfer, E., 2002. Properties of PZT multilayer actuators. In *8th International Conference on New Actuators, Bremen, Germany*. (Cited on page 9)

Hemsel, T. and Wallaschek, J., 2000. Survey of the present state of the art of piezoelectric linear motors. *Ultrasonics*, pp. 37–40. doi:10.1016/S0041-624X(99)00143-2. (Cited on pages 7 and 16)

Henderson, D. A., 2005. Piezo ceramic motors improve phone camera auto focus and zoom. *New Scale Technologies company.* (Cited on page 16)

Henein, S., 2001. *Conception des guidages flexibles (In French).* PhD thesis, École Polytechnique Fédérale de Lausanne (EPFL). (Cited on pages 49 and 50)

Hertz, H., 1882. On the contact of rigid elastic solids and on hardness. (Cited on pages 62 and x)

Higuchi, T. and Watanabe, M., 1990. Apparatus for effecting fine movement by impact force produced by piezoelectric or electrostrictive element. URL http://www.google.ch/patents/US4894579. US Patent 4,894,579. (Cited on pages 29, 32 and 37)

Higuchi, T. and Yamagata, Y., 1991. Micro robot arm utilizing rapid deformations of piezoelectric elements. *Advanced robotics*, pp. 353–360. doi:10.1163/156855392X00150. (Cited on page 22)

Higuchi, T., Hojjat, Y., and Wanatabe, M., 1987. Micro actuators using recoil of an ejected mass. IEEE micro robots and teleoperators workshop. (Cited on page 20)

Higuchi, T., Furutani, K., Yamagata, Y., Kudoh, K. I., and Ogawa, M., 1992. Improvement of velocity of impact drive mechanism by controlling friction in Japanese). *Journal of the Japan Society for Precision Engineering*, pp. 1327–1332. doi:10.2493/jjspe.58.1327. (Cited on pages 35 and 162)

Howald, L., Rudin, H., and Guntherodt, H.-J., 1992. Piezoelectric inertial stepping motor with spherical rotor. *Review of Scientific Instruments*, pp. 3909–3912. doi:10.1063/1.1143290. (Cited on pages 20, 23 and 37)

Huber, J. E., Fleck, N. A., and Ashby, M. F., 1997. The selection of mechanical actuators based on performance indices. In *Proceedings of the Royal Society of London A: Mathematical, Physical and Engineering Sciences*, pp. 2185–2205. doi:10.1098/rspa.1997.011. (Cited on pages 7, 8 and 16)

Hunstig, M., 2017. Piezoelectric inertia motors—a critical review of history, concepts, design, and applications (to be published). *Actuators.* doi:10.3390/act6010007. (Cited on pages 26, 29, 31 and vii)

Hunstig, M., Hemsel, T., and Sextro, W., 2013. Modelling the friction contact in an inertia motor. *Journal of Intelligent Material Systems and Structures.* doi:10.1177/1045389X12474354. (Cited on page 56)

Hunstig, M., Hemsel, T., and Sextro, W., 2014. High-velocity operation of piezoelectric inertia motors: experimental validation. *Archive of Applied Mechanics*, pp. 1–9. doi:10.1007/s00419-014-0940-0. (Cited on pages 34, 35 and 138)

Idogaki, T., Kanayama, H., Ohya, N., Suzuki, H., and Hattori, T., 1995. Characteristics of piezoelectric locomotive mechanism for an in-pipe micro inspection machine. In *Proceedings of the Sixth International Symposium on Micro Machine and Human Science*, pp. 193–198. doi:10.1109/MHS.1995.494237. (Cited on pages 20 and 34)

IEC, 2013. *Electroacoustics - Sound level meters.* reference: 61672-1. (Cited on page 129)

ISO, 2007. *Quantities and units – Part 8: Acoustics.* reference: 80000-8. (Cited on page 130)

Jia, B.-B., Li, T.-J., Liu, X.-J., and Cong, P.-H., 2007. Tribological behaviors of several polymer-polymer sliding combinations under dry friction and oil-lubricated conditions. *Wear*, pp. 1353 – 1359. doi:10.1016/j.wear.2007.01.011. (Cited on page 56)

Johnson, M. P., 1990. Equivalent modal impedance matrix of multiple degree of freedom electroelastic structures. *The Journal of the Acoustical Society of America*, pp. 1–6. doi:10.1121/1.399943. (Cited on page 105)

Judy, J. W., Polla, D. L., and Robbins, W. P., 1990. A linear piezoelectric stepper motor with submicrometer step size and centimeter travel range. *IEEE transactions on ultrasonics, ferroelectrics, and frequency control*, pp. 428–437. doi:10.1109/58.105249. (Cited on pages 22 and 37)

Jullien, A., Meurisse, M., and Berthier, Y., 1996. Determination of tribological history and wear through visualisation in lubricated contacts using a carbon-based composite. *Wear*, pp. 116 – 125. doi:10.1016/0043-1648(95)06813-9. (Cited on page 46)

Kang, C.-Y., Yoo, K.-H., Ko, H.-P., Kim, H.-J., Ko, T.-K., and Yoon, S.-J., 2006. Analysis of driving mechanism for tiny piezoelectric linear motor. *Journal of electroceramics*, pp. 609–612. doi:10.1007/s10832-006-8766-y. (Cited on pages 34 and 37)

Karrai, K., 1996. Positionneur inertiel. URL `https://www.google.com/patents/EP0823738B1?cl=fr`. EP Patent 0,823,738. (Cited on page 31)

Kloss, H. and Wäsche, R., 2009. Analytical approach for wear prediction of metallic and ceramic materials in tribological applications. *Wear*, pp. 476 – 481. doi:10.1016/j.wear.2008.04.034. (Cited on page 62)

Ko, H.-P., Kang, C.-Y., Kim, J.-S., Borodin, S. N., Kim, S., and Yoon, S.-J., 2006. Constructions and characteristics of a tiny piezoelectric linear motor using radial mode vibrations. *Journal of electroceramics*, pp. 603–608. doi:10.1007/s10832-006-8569-1. (Cited on pages 37 and 38)

Kounoudji, K.-A., Renouf, M., Mollon, G., and Berthier, Y., 2016. Role of third body on bolted joints' self-loosening. *Tribology Letters*, pp. 24–31. doi:10.1007/s11249-016-0640-8. (Cited on pages 45, 104 and ix)

Krick, B. A., Vail, J. R., Persson, B. N. J., and Sawyer, W. G., 2012. Optical in situ micro tribometer for analysis of real contact area for contact mechanics, adhesion, and sliding experiments. *Tribology Letters*, pp. 185–194. doi:10.1007/s11249-011-9870-y. (Cited on page 46)

Kudoh, K. I., Tabuchi, S., Higuchi, T., Kakusho, N., and Sato, K., 1998. Development of automatic micromanipulation system for biological cell sorter. *Journal of Mammalian Ova Research*, pp. 167–172. doi:10.1274/jmor.15.167. (Cited on page 22)

Lambert, P., Valentini, A., Lagrange, B., De Lit, P., and Delchambre, A., 2003. Design and performances of a one-degree-of-freedom guided nano-actuator. *Robotics and computer-integrated manufacturing*, pp. 89–98. doi:10.1016/S0736-5845(02)00065-0. (Cited on pages 31, 36 and 37)

Le Letty, R., 1994. *Conception de moteurs piezoactifs à l'aide de la modélisation (in French)*. PhD thesis. (Cited on pages 113, 124 and xv)

Leroy, E., 2013. *Miniature Ultrasonic Piezoelectric Actuators For Compact Spherical Motors*. PhD thesis, École polytechnique, université Paris-Saclay. (Cited on page 9)

Li, X. and Yamamoto, A., 2016. A multi-slider linear actuator using modulated electrostatic attraction and inertia effect. In *2016 11th France-Japan 9th Europe-Asia Congress on Mechatronics /17th International Conference on Research and Education in Mechatronics (REM)*, pp. 296–297. doi:10.1109/MECATRONICS.2016.7547158. (Cited on page 23)

Libioulle, L., Ronda, A., Derycke, I., Vigneron, J., and Gilles, J., 1993. Vertical two-dimensional piezoelectric inertial slider for scanning tunneling microscope. *Review of scientific instruments*, pp. 1489–1494. doi:10.1063/1.1144068. (Cited on pages 22 and 37)

Linck, V., Bayada, G., Baillet, L., Sassi, T., and Sabil, J., 2005. Finite element analysis of a contact with friction between an elastic body and a thin soft layer. *Journal of Tribology*, pp. 461–468. doi:10.1115/1.1866170. (Cited on page 104)

Lippmann, G., 1881. Principe de la conservation de l'électricité, ou second principe de la théorie des phénomènes électriques (in French). *Journal de Physique Théorique et Appliquée*, pp. 381–394. doi:10.1051/jphystap:0188100100038100. (Cited on page 9)

Liu, Y. F., Li, J., Hu, X. H., Zhang, Z. M., Cheng, L., Lin, Y., and Zhang, W. J., 2015. Modeling and control of piezoelectric inertia–friction actuators: review and future research directions. *Mechanical Sciences*, pp. 95–107. doi:10.5194/ms-6-95-2015. (Cited on pages 103 and 106)

Locher, G., 1967. Micrometric linear actuator. URL https://www.google.ch/patents/US3296467. US Patent 3,296,467. (Cited on page 17)

Lyding, J. W., Skala, S., Hubacek, J. S., Brockenbrough, R., and Gammie, G., 1988. Variable-temperature scanning tunneling microscope. *Review of Scientific Instruments*, pp. 1897–1902. doi:10.1063/1.1140047. (Cited on page 22)

Martel, S., Sherwood, M., Helm, C., Garcia de Quevedo, W., Fofonoff, T., Dyer, R., Bevilacqua, J., Kaufman, J., Roushdy, O., and Hunter, I., 2001. Three-legged wireless miniature robots for mass-scale operations at the sub-atomic scale. In *International Conference on Robotics and Automation*, pp. 3423–3428. doi:10.1109/ROBOT.2001.933147. (Cited on page 22)

Mason, W. P., 1948. *Electromechanical transducers and wave filters.* (Cited on pages 14 and 113)

Matsuda, R. and Kaneko, R., 1991. Micro-step xy-stage using piezoelectric tube actuator. In *Proceedings of Micro Electro Mechanical Systems*, pp. 137–142. doi:10.1109/MEMSYS.1991.114784. (Cited on pages 22 and 128)

Matsusaka, K., Ozawa, S., Yoshida, R., Yuasa, T., and Souma, Y., 2007. Ultracompact optical zoom lens for mobile phone. In *Proceedings of Digital Photography III*, pp. 1–10. doi:10.1117/12.702712. (Cited on page 127)

Merstallinger, A. and Sales, M., 2011. Cold welding due to impact and fretting under vacuum. considering scaling for applications in space mechanisms. *Mechanical Properties Of Complex Intermetallics*, pp. 191–248. doi:10.1142/9789814322171_0006. (Cited on page 59)

Mevel, B., 1992. *Comportement dynamique des roulements à billes (in French).* PhD thesis. (Cited on page 105)

Meyer, C., Sqalli, O., Lorenz, H., and Karrai, K., 2005. Slip-stick step-scanner for scanning probe microscopy. *Review of scientific instruments*, pp. 1–6. doi:10.1063/1.1927105. (Cited on page 22)

Meziane, A., Baillet, L., and Laulagnet, B., 2010. Experimental and numerical investigation of friction-induced vibration of a beam-on-beam in contact with friction. *Applied Acoustics*, pp. 843–853. doi:10.1016/j.apacoust.2010.04.012. (Cited on pages 20 and 127)

Michler, J., Rabe, R., Bucaille, J.-L., Moser, B., Schwaller, P., and Breguet, J.-M., 2005. Investigation of wear mechanisms through in situ observation during microscratching inside the scanning electron microscope. *Wear*, pp. 18–26. doi:10.1016/j.wear.2005.02.111. (Cited on page 46)

Minase, J., Lu, T.-F., Cazzolato, B., and Grainger, S., 2010. A review, supported by experimental results, of voltage, charge and capacitor insertion method for driving piezoelectric actuators. *Precision Engineering*, 34(4):692–700. doi:10.1016/j.precisioneng.2010.03.006. (Cited on page 36)

Morita, T., Yoshida, R., Okamoto, Y., Kurosawa, M., and Higuchi, T., 1999. A smooth impact rotation motor using a multi-layered torsional piezoelectric actuator. *IEEE Transactions on Ultrasonics, Ferroelectrics, and Frequency Control*, pp. 1439–1445. doi:10.1109/58.808867. (Cited on page 37)

Morita, T., Yoshida, R., Okamoto, Y., and Higuchi, T., 2002. Three dof parallel link mechanism utilizing smooth impact drive mechanism. *Precision Engineering*, pp. 289–295. doi:10.1016/S0141-6359(02)00111-3. (Cited on page 23)

Morita, T., Nishimura, T., Yoshida, R., and Hosaka, H., 2012. Design for the resonant type sidm (smooth impact drive mechanism) actuator. In *Proceedings of Symposium on Ultrasonic Electronics*, pp. 77–78. (Cited on pages 21, 128, 133, 139, xvii and xviii)

Nakashima, A., Ooka, Y., and Hayakawa, Y., 2015. Contact transition modelling on planar manipulation system with lugre friction model. In *2015 10th International Workshop on Robot Motion and Control*, pp. 300–307. IEEE. doi:10.1109/RoMoCo.2015.7219751. (Cited on page 124)

Nec-Tokin website, Last update: 2016. `http://www.nec-tokin.com/`. (Cited on page 143)

New Scale website. `http://www.newscaletech.com/`. (Cited on page 19)

Newton, D., Garcia, E., and Horner, G. C., 1998. A linear piezoelectric motor. *Smart Materials and Structures*, p. 295. doi:10.1088/0964-1726/7/3/004. (Cited on page 17)

NewWay website, Last update: 2012. `http://www.newwayairbearings.com/`. (Cited on page 52)

Niedermann, P. and Choffat, H., 1996. Actionneur piézoélectrique de très haute précision (in French). URL `https://www.google.com/patents/EP0750356A1?cl=fr`. EP Patent App. EP19,960,401,359. (Cited on pages 20 and 22)

Niedermann, P., Emch, R., and Descouts, P., 1988. Simple piezoelectric translation device. *Review of scientific instruments*, pp. 368–369. doi:10.1063/1.1140206. (Cited on page 37)

Nishimura, T., Hosaka, H., and Morita, T., 2012. Resonant-type Smooth Impact Drive Mechanism (SIDM) actuator using a bolt-clamped Langevin transducer. *Ultrasonics*, pp. 75–80. doi:10.1016/j.ultras.2011.06.013. (Cited on pages 34 and 140)

Okamoto, Y. and Yoshida, R., 1998. Development of linear actuators using piezoelectric elements. *Electronics and Communications in Japan (Part III: Fundamental Electronic Science)*, pp. 11–17. doi:10.1002/(SICI)1520-6440(199811)81:11<11::AID-ECJC2>3.0.CO;2-U. (Cited on pages 32 and 35)

Otsuka, J., 1992. Nanometer level positioning using three kinds of lead screws. *Nanotechnology*, p. 29. doi:10.1088/0957-4484/3/1/006. (Cited on page 127)

Ouyang, H., Nack, W., Yuan, Y., and Chen, F., 2005. Numerical analysis of automotive disc brake squeal: a review. *International Journal of Vehicle Noise and Vibration*, pp. 207–231. doi:10.1504/IJVNV.2005.007524. (Cited on page 128)

Ouyang, P. R., Tjiptoprodjo, R. C., Zhang, W. J., and Yang, G. S., 2008. Micro-motion devices technology: The state of arts review. *The International Journal of Advanced Manufacturing Technology*, pp. 463–478. doi:10.1007/s00170-007-1109-6. (Cited on page 16)

Paine, J. S. N., Johns, M. E., Sesler, J. J., Stefanick, M. T., and Kennedy, J. A., 2008. Linear high-force "step and repeat" piezoelectric motors. In *Proceeding of the 39th Aerospace Mechanisms Symposium.* (Cited on page 18)

Park, C., Park, K.-S., Huh, Y.-S., Jeon, C., and Kim, S., 1991. Scanning tunneling microscope with novel coarse sample positioning technique. *Journal of Vacuum Science & Technology B*, pp. 636–638. doi:10.1116/1.585475. (Cited on page 22)

Patil, S., Matei, G., Dong, H., Hoffmann, P. M., Karaköse, M., and Oral, A., 2005. A highly sensitive atomic force microscope for linear measurements of molecular forces in liquids. *Review of Scientific Instruments*, pp. 1–7. doi:10.1063/1.2083147. (Cited on page 37)

Pavic, G. and Bendridi, A., 2014. Caractérisation d'une petite source de bruit solidien par une approche hybride (in French). *Congrès Français d'Acoustique.* (Cited on page 128)

Peng, Y., Peng, Y., Gu, X., Wang, J., and Yu, H., 2015. A review of long range piezoelectric motors using frequency leveraged method. *Sensors and Actuators A: Physical*, pp. 240–255. doi:10.1016/j.sna.2015.10.015. (Cited on pages 16, 18, 19, 21 and vii)

Pereira, M., Peixoto, A., and Gomes, M., 2001. Effect of Nb doping on the microstructural and electrical properties of the PZT ceramics. *Journal of the European Ceramic Society*, pp. 1353–1356. doi:10.1016/S0955-2219(01)00017-6. (Cited on page 10)

Pfeffer, D., Scholz, C., Belly, C., Wäsche, R., Schlaak, H.-F., and Pott, P.-P., 2015. Influence of the actuation waveform on the performance of piezoelectric stick-slip actuators. In *IKMT 2015*, pp. 1–5. (Cited on page 128)

Piriou, P., Ouenzerfi, G., Migaud, H., Renault, E., Massi, F., and Serrault, M., 2016. A numerical model to reproduce squeaking of ceramic-on-ceramic total hip arthroplasty. influence of design and material. *Revue de Chirurgie Orthopédique et Traumatologique*, pp. 27–32. doi:10.1016/j.otsr.2016.03.005. (Cited on page 131)

Play, D. and Godet, M., 1976. Visualisation of chalk wear. *The Wear of Non-metallic Materials, Mechanical Engineering Publications, London*, pp. 221–229. (Cited on page 46)

Pohl, D. W., 1987a. Dynamic piezoelectric translation devices. *Review of scientific instruments*, pp. 54–57. doi:10.1063/1.1139566. (Cited on page 37)

Pohl, D., 1987b. Sawtooth nanometer slider: A versatile low voltage piezoelectric translation device. *Surface Science*, pp. 174–175. doi:10.1016/0039-6028(87)90155-5. (Cited on pages 20, 29 and vi)

Pomey, G. and Lieurade, H.-P., 1982. Essais de fatigue. Technical report. (Cited on page 49)

Probst, O., Grafström, S., Kowalski, J., Neumann, R., and Wörtge, M., 1991. A tunneling atomic force microscope with inertial tip-to-sensor approach. *Journal of Vacuum Science & Technology B*, pp. 626–630. doi:10.1116/1.585473. (Cited on pages 22, 37, 39 and 134)

Qu, J., Blau, P. J., Watkins, T.-R., Cavin, O.-B., and Kulkarni, N.-S., 2005. Friction and wear of titanium alloys sliding against metal, polymer, and ceramic counterfaces. *Wear*, pp. 1348–1356. doi:10.1016/j.wear.2004.09.062. (Cited on pages 56 and 62)

Rabe, R., 2006. *Compact test platform for in-situ indentation and scratching inside a scanning Ecompact TES.* PhD thesis, École Polytechnique Fédérale de Lausanne (EPFL). (Cited on page 34)

Rabinowicz, E., 1956. Stick and slip. *Scientific American*, pp. 109–118. (Cited on page 123)

Rakotondrabe, M., Haddab, Y., and Lutz, P., 2007. High-stroke motion modelling and voltage/frequency proportional control of a stick-slip microsystem. In *International Conference on Robotics and Automation*, pp. 4490–4496. doi:10.1109/ROBOT.2007.364171. (Cited on page 32)

Rakotondrabe, M., Haddab, Y., and Lutz, P., 2009. Development, modeling, and control of a micro-/nanopositioning 2-dof stick–slip device. *IEEE/ASME Transactions on mechatronics*, pp. 733–745. doi:10.1109/TMECH.2008.2011134. (Cited on pages 22 and 34)

Rehbein, P. and Wallaschek, J., 1998. Friction and wear behaviour of polymer/steel and alumina/alumina under high-frequency fretting conditions. *Wear*, pp. 97–105. doi:10.1016/S0043-1648(97)00163-4. (Cited on pages 36 and 162)

Renner, C., Niedermann, P., and Kent, A., 1990. A vertical piezoelectric inertial slider. *Review of scientific instruments*, pp. 965–967. doi:10.1063/1.1141450. (Cited on pages 22, 29, 37 and 133)

Renouf, M., Massi, F., Fillot, N., and Saulot, A., 2011. Numerical tribology of a dry contact. *Tribology International*, pp. 834–844. doi:10.1016/j.triboint.2011.02.008. (Cited on page 103)

Reynolds, K., Komulainen, J., Kivijakola, J., Lovera, P., Iacopino, D., Pudas, M., Vähäkangas, J., Röning, J., and Redmond, G., 2008. Probe based manipulation and assembly of nanowires into organized mesostructures. *Nanotechnology*, pp. 1–10. doi:10.1088/0957-4484/19/48/485301. (Cited on page 22)

Richard, D., Iordanoff, I., Berthier, Y., Renouf, M., and Fillot, N., 2007. Friction coefficient as a macroscopic view of local dissipation. *Journal of Tribology*, pp. 829–835. doi:10.1115/1.2768083. (Cited on page 104)

Rihova, Z., Stary, V., and Bacakova, L., 2012. A study of the structure and surface properties of nanostructured biocompatible coatings on Ti alloys. *Vacuum*, pp. 630 – 633. doi:10.1016/j.vacuum.2011.07.007. (Cited on page 59)

Rocon, E. and Pons, J. L., 2006. Scaling of piezoelectric actuators: a comparison with traditional and other new technologies. *Boletín de la Sociedad Española de Cerámica y Vidrio*, pp. 132–138. (Cited on page 16)

Rouchon, J.-F., 1996. *Approche tribologique du fonctionnement des moteurs à ultrasons à onde progressive (In French)*. PhD thesis, Ecole Centrale de Lyon. (Cited on page 62)

Ru, C., Liu, X., and Sun, Y., 2016. *Nanopositioning Technologies: Fundamentals and Applications*. Springer International Publishing. doi:10.1007/978-3-319-23853-1. (Cited on page 45)

Saito, S. and Nagano, M., 1991. Driving device. URL https://www.google.ch/patents/US5225941. US Patent 5,225,941. (Cited on page 22)

Sashida, T., 1985. Motor device utilizing ultrasonic oscillation. URL https://www.google.tl/patents/US4562374. US Patent App. US4562374 A. (Cited on page 19)

Scharf, T.-W. and Singer, I.-L., 2003. Quantification of the thickness of carbon transfer films using raman tribometry. *Tribology Letters*, pp. 137–145. doi:10.1023/A:1021942822261. (Cited on page 46)

Shifeng, H., Jun, C., Futian, L., Lingchao, L., Zhengmao, Y., and Xin, C., 2004. Poling process and piezoelectric properties of lead zirconate titanate/sulphoaluminate cement composites. *Journal of Materials Science*, pp. 6975–6979. doi:10.1023/B:JMSC.0000047540.71855.3a. (Cited on page 10)

Sievers, T., Garnica, S., Tautz, S., Trüper, T., and Fatikow, S., 2005. Microrobot station for automatic cell handling. In *Proceedings of the First ICGST International Conference Automation, Robotics and Autonomous Systems ARAS*, pp. 7–12. (Cited on page 22)

Silveira, W. R. and Marohn, J. A., 2003. A vertical inertial coarse approach for variable temperature scanned probe microscopy. *Review of scientific instruments*, pp. 267–269. doi:10.1063/1.1524712. (Cited on pages 29 and 32)

Singer, I.-L., Dvorak, S.-D., Wahl, K.-J., and Scharf, T.-W., 2002. Third body processes and friction of solid lubricants studied by in situ optical and raman tribometry. *Tribology Series*, pp. 327–336. doi:10.1016/S0167-8922(02)80036-0. (Cited on pages 46 and 63)

Singer, I. L., Dvorak, S. D., Wahl, K. J., and Scharf, T. W., 2003. Role of third bodies in friction and wear of protective coatings. *Journal of Vacuum Science & Technology A*, pp. 232–240. doi:10.1116/1.1599869. (Cited on page 58)

Six, M.-F., 2000. *Moteur piezoelectrique pour application spatiale (in French)*. PhD thesis, Institut National des Sciences Appliquées de Lyon (INSA). (Cited on pages 59 and 139)

Sliney, H. E., 1978. Dynamics of solid lubrication as observed by optical microscopy. *ASLE Transactions*, pp. 109–117. doi:10.1080/05698197808982866. (Cited on page 46)

Smith, A. R., Gwo, S., and Shih, C. K., 1994. A new high-resolution two-dimensional micropositioning device for scanning probe microscopy applications. *Review of scientific instruments*, pp. 3216–3219. doi:10.1063/1.1144552. (Cited on page 37)

Smith, J. O., 2017. *Physical Audio Signal Processing*. https://ccrma.stanford.edu/~jos/pasp/. online book, 2010 edition. (Cited on page 106)

Smith, W. F., Abraham, M. C., Sloan, J. M., and Switkes, M., 1996. Simple retrofittable long-range x–y translation system for scanned probe microscopes. *Review of scientific instruments*, pp. 3599–3604. doi:10.1063/1.1147065. (Cited on page 29)

Soderqvist, A., 1973. Method and device for displacement of a workpiece. URL http://www.google.ch/patents/US3957162. US Patent 3,957,162. (Cited on pages 20 and vi)

Spanner, K. and Koc, B., 2010. An overview of piezoelectric motors. In *Actuator conference.* (Cited on pages 22 and vi)

Stoyanov, P., Strauss, H. W., and Chromik, R. R., 2012. Scaling effects between micro- and macro-tribology for a ti-mos$_2$ coating. *Wear*, pp. 149 – 161. doi:10.1016/j.wear.2011.08.021. (Cited on pages 46 and 66)

Suzuki, M., Hosaka, H., and Morita, T., 2012. Resonant-type smooth impact drive mechanism actuator with two langevin transducers. *Advanced Robotics*, pp. 277–290. doi:10.1163/156855311X614563. (Cited on page 34)

Szufnarowski, F., 2013. *Dynamic modeling and bioinspired control of a walking piezoelectric motor*. PhD thesis, University of Bielefeld, Faculty of Technology. (Cited on pages 9 and vi)

Takano, M., Tanaka, Y., Nakamura, K., and Kaihotsu, W., 2005. The anti-shake, camera shake compensation technology of the α -7 digital (in Japanese). Technical report, Sony. (Cited on pages 23 and 127)

Teidelt, E., Willert, E., Filippov, A. E., and Popov, V. L., 2012. Modeling of the dynamic contact in stick-slip microdrives using the method of reduction of dimensionality. *Physical Mesomechanics*, pp. 287–292. doi:10.1134/s1029959912030071. (Cited on page 124)

Thomson, W. T. and Dahleh, M. D., 1998. *Theory of vibration with applications*. (Cited on pages 117 and 121)

Tonazzi, D., Massi, F., Culla, A., Baillet, L., Fregolent, A., and Berthier, Y., 2013. Instability scenarios between elastic media under frictional contact. *Mechanical Systems and Signal Processing*, pp. 754–766. doi:10.1016/j.ymssp.2013.05.022. (Cited on page 20)

Tonazzi, D., Massi, F., Baillet, L., Culla, A., Di Bartolomeo, M., and Berthier, Y., 2014. Experimental and numerical analysis of frictional contact scenarios: from macro stick-slip to continuous sliding. *Meccanica*, pp. 649–664. doi:10.1007/s11012-014-0010-2. (Cited on page 127)

Trainer, M., 2003. Kelvin and piezoelectricity. *European journal of physics*, p. 535. doi:10.1088/0143-0807/24/5/310. (Cited on page 8)

Tuncdemir, S., Ural, S. O., Koc, B., and Uchino, K., 2011. Design of translation rotary ultrasonic motor with slanted piezoelectric ceramics. *Japanese Journal of Applied Physics*, pp. 1–8. doi:10.1143/JJAP.50.027301. (Cited on page 37)

Tzanakis, I., Hadfield, M., Thomas, B., Noya, S. M., Henshaw, I., and Austen, S., 2012. Future perspectives on sustainable tribology. *Renewable and Sustainable Energy Reviews*. doi:10.1016/j.rser.2012.02.064. (Cited on page 162)

Uchino, K., 1990. Recent topics in ceramic actuators-to improve reliability and durability. In *IEEE 7th International Symposium on Applications of Ferroelectrics*, pp. 153–158. doi:10.1109/ISAF.1990.200215. (Cited on page 11)

Uchino, K., 1996. *Piezoelectric actuators and ultrasonic motors.* Springer Science & Business Media. (Cited on page 7)

Uchino, K., 1998. Piezoelectric ultrasonic motors: overview. *Smart materials and structures*, pp. 273–285. doi:10.1088/0964-1726/7/3/002. (Cited on page 7)

Upadhyay, R., Kumaraswamidhas, L., and Azam, M. S., jan 2013. Rolling element bearing failure analysis: A case study. *Case Studies in Engineering Failure Analysis*, 1(1):15–17. doi:10.1016/j.csefa.2012.11.003. (Cited on page 52)

Van Der Wulp, H., 1997. *Piezo-driven stages for nanopositioning with extreme stability: theoretical acpects and practical design considerations.* PhD thesis, Delft University of Technology. (Cited on page 106)

Van der Wulp, H., De With, E., Pistecky, P. V., and Spronck, J. W., 1995. Compact, piezo-driven, vacuum compatible rotation device. *Review of scientific instruments*, pp. 5339–5342. doi:10.1063/1.1146109. (Cited on pages 31 and 35)

Vanel, L., 1996. *Le contact stator-rotor dans un moteur piézoélectrique: modélisation mécanique et étude du frottement métal-polymère en vue de l'optimisation du choix de la couche de frottement (in French).* PhD thesis, École Nationale Supérieure des Mines de Paris. (Cited on pages 12 and v)

Vasiliev, P. E., Klimavichjus, P. A. R., Kondratiev, A. V., Matsjukyavichjus, J. J., Beksha, G. V. L., and Kaminskas, V. A., 1981. Drive means and force control for piezoelectric vibration motor. URL https://www.google.fr/patents/US4249100. US Patent 4,249,100. (Cited on page 19)

Velázquez, R., Hernández, H., and Preza, E., 2012. A portable piezoelectric tactile terminal for braille readers. *Applied Bionics and Biomechanics*, pp. 45–60. doi:10.3233/ABB-2012-0055. (Cited on page 23)

Wahl, K.-J. and Singer, I.-L., 1996. Role of the third body in life enhancement of MoS$_2$. *Tribology Series*, pp. 407–413. doi:10.1016/S0167-8922(08)70802-2. (Cited on page 58)

Wahl, K. J., Chromik, R.-R., and Lee, G.-Y., 2008. Quantitative in situ measurement of transfer film thickness by a newton's rings method. *Wear*, pp. 731–736. doi:10.1016/j.wear.2007.04.009. (Cited on page 46)

Wahl, K., Belin, M., and Singer, I., 1998. A triboscopic investigation of the wear and friction of MoS_2 in a reciprocating sliding contact. *Wear*, pp. 212 – 220. doi:10.1016/S0043-1648(97)00246-9. (Cited on page 46)

Wang, J. and Lu, Q., 2012. How are the behaviors of piezoelectric inertial sliders interpreted? *Review of Scientific Instruments.* doi:10.1063/1.4748275. (Cited on pages 37 and 128)

Weiss, C., Hothan, A., Morlock, M., and Hoffmann, N., 2009. Friction-induced vibration of artificial hip joints. *GAMM-Mitteilungen*, pp. 193–204. doi:10.1002/gamm.200910016. (Cited on page 128)

Wildöer, J. W. G., Van Roy, A. J. A., Van Kempen, H., and Harmans, C. J. P. M., 1994. Low-temperature scanning tunneling microscope for use on artificially fabricated nanostructures. *Review of scientific instruments*, pp. 2849–2852. doi:10.1063/1.1144626. (Cited on page 37)

Williams, A. L. W., 1937. Piezoelectric motor and generator device. URL `http://www.google.ch/patents/US2081862`. US Patent 2,081,862. (Cited on pages 11, 19, v and vi)

Woern, H., Schmoeckel, F., Buerkle, A., Samitier, J., Puig-Vidal, M., Johansson, S. A. I., Simu, U., Meyer, J.-U., and Biehl, M., 2001. From decimeter- to centimeter-sized mobile microrobots: the development of the miniman system. *Proceedings of Microrobotics and Microassembly III*, pp. 175–186. doi:10.1117/12.444124. (Cited on page 22)

Woodburn, C. N., McKinnon, A. W., Roberts, D. A., Taylor, M. E., and Welland, M. E., 1993. A one-dimensional piezoelectric-driven inertial micropositioner with vertical capabilities. *Measurement Science and Technology*, pp. 535–537. doi:10.1088/0957-0233/4/4/016. (Cited on page 37)

Yamagata, Y. and Higuchi, T., 1995. A micropositioning device for precision automatic assembly using impact force of piezoelectric elements. In *International Conference on Robotics and Automation*, pp. 666–671. doi:10.1109/ROBOT.1995.525360. (Cited on pages 23, 34 and 35)

Yamagata, Y., Higuchi, T., Saeki, H., and Ishimaru, H., 1990. Ultrahigh vacuum precise positioning device utilizing rapid deformations of piezoelectric elements. *Journal of Vacuum Science & Technology A*, pp. 4098–4100. doi:10.1116/1.576446. (Cited on pages 16, 22, 29, 37 and 127)

Yokose, T., Hosaka, H., and Morita, T., Oct 2012. Improvement of miniaturized resonant type sidm actuator. In *2012 IEEE International Ultrasonics Symposium*, pp. 1–4. doi:10.1109/ULTSYM.2012.0454. (Cited on pages 34 and 140)

Yokozawa, H. and Morita, T., 2015. Wireguide driving actuator using resonant-type smooth impact drive mechanism. *Sensors and Actuators A: Physical*, pp. 40–44. doi:10.1016/j.sna.2015.04.012. (Cited on pages 34 and 128)

Yoshida, R., Okamoto, Y., Higuohi, T., and Hamamatsu, A., 1999. Development of smooth impact drive mechanism (SIDM)-proposal of driving mechanism and basic performance (In Japanese). *Journal of Japan society for precision engineering*, pp. 111–115. doi:10.2493/jjspe.65.111. (Cited on page 35)

Yoshizawa, H. and Israelachvili, J., 1993. Fundamental mechanisms of interfacial friction. 2. stick-slip friction of spherical and chain molecules. *Journal of Physical Chemistry*, pp. 11300–11313. doi:10.1021/j100145a031. (Cited on pages 20 and 45)

Zesch, W., 1997. *Multi-degree-of-freedom micropositioning using stepping principles.* PhD thesis, Swiss Federal Institute of Technology (ETH). doi:10.3929/ethz-a-001855164. (Cited on page 31)

Zesch, W., Buechi, R., Codourey, A., and Siegwart, R. Y., 1995. Inertial drives for micro-and nanorobots: two novel mechanisms. In *Photonics East'95*, pp. 80–88. International Society for Optics and Photonics. doi:10.1117/12.228638. (Cited on page 23)

Zhang, B. and Zhu, Z., 1997. Developing a linear piezomotor with nanometer resolution and high stiffness. *IEEE/ASME Transactions on Mechatronics*, pp. 22–29. doi:10.1109/3516.558855. (Cited on page 17)

Zhang, Z.-M., An, Q., Li, J.-W., and Zhang, W.-J., 2012. Piezoelectric friction-inertia actuator - a critical review and future perspective. *The International Journal of Advanced Manufacturing Technology*, pp. 669–685. doi:10.1007/s00170-011-3827-z. (Cited on page 34)

Zielinski, T. G., 2014. Fundamental of acoustics. *IPPT PAN institute lecture.* URL `http://bluebox.ippt.pan.pl/~tzielins/index.php?im=0&id=home.html`. (Cited on page 129)

Zienkiewicz, O. C. and Taylor, R. L., 1977. *The finite element method.* McGraw-hill London. (Cited on page 113)

Zimmerman, D., 2002. Paul langevin and the discovery of active sonar or Asdic. In *Northern mariner*, pp. 39–52. (Cited on page 9)

Zupan, M., Ashby, M. F., and Fleck, N. A., 2002. Actuator classification and selection—the development of a database. *Advanced Engineering Materials*, pp. 933–940. doi:10.1002/adem.200290009. (Cited on pages 7, 8 and 16)

Appendices

Some additional tests have been carried out during the tribological investigations. These tests aimed at approaching (i) the impact of contact geometry and (ii) the interest in coated Ti-6Al-4V on mechanical performances.

A   Impact of contact geometry

From a mechanical point of view, the tribometer structure is hyperstatic since the contact geometry is cylinder-plane. This lead to repeatability issues due to mounting. Besides, it has been observed that wear mechanisms initiate either at the top or at the bottom of the observation window. In order to make the structure isostatic, a spheric pin has been designed. Its dimensions - 300-mm radius - are sized to keep a similar theoretical contact pressure: around 10MPa while being not too expansive to manufacture.

A lifetime test (10^6 cycles) has been realised (Fig.A). If the targeted lifetime is reached, mean speed is chaotic. In addition, it remains relatively low in comparison with a cylinder-on-pad contact configuration (Fig.4.17). One can assume that, as the impact mode has been highlighted (Fig.4.5), parasitic motions lead to mechanical losses. Indeed, transverse contact stiffness is drastically decreased by adding the degree of freedom provided by a spherical pin.

To conclude this issue, as the abrasive power of both fibreglass filled polymer and coated Ti-6Al-4V is high, contact conformity appears quite quickly. *Cylinder-on-flat contact geometry turned out to be finally the best trade-off*.
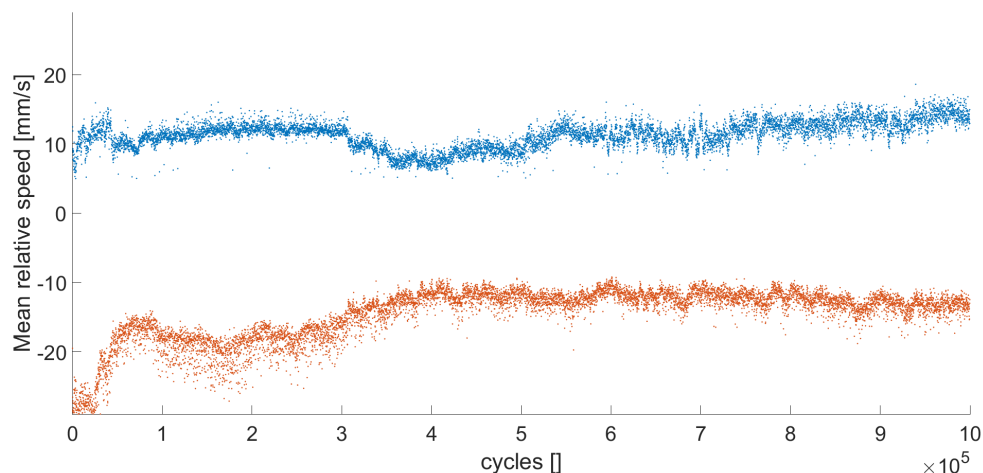
Figure A − 10^6-cycles lifetime test with a **spherical pin**. Performances are chaotic and slower than with a cylindrical pin.

B   Discussing the interest in coating Ti-6Al-4V samples

From the tribological investigations, coating is quickly extruded from Ti-6Al-4V. Then, it is either ejected from the contact or mixes into the 3rd body layer, decreasing its ductility and speeding up its propagation. However, its role in making the performances stable was unclear. In order to address this issue, a cylinder pin in Ti-6Al-4V has not been coated but directly tested against a fibreglass filled polymer pad.

A lifetime test (10^6 cycles) has been realised (Fig.B). Again, the targeted lifetime is reached. Performances are nevertheless a bit lower than with a coated pin (Fig.4.17), what is consistent since coating particle, once mixed into the 3rd body layer, seems to increase its abrasive power. Likewise, performances are less stable than with a coated pin, similarly to 10^7-cycles lifetime test (Fig.4.23). We could imagine that the 3rd body layer looses its cohesion with repeated stresses, leading to accommodate friction by normal rupture (S_3M_2) temporarily until the layer forms again by shearing the composite surface (S_5M_3).

To conclude this issue, coating Ti-6Al-4V leads to better and more stable performances. So, *coating process should be systematically planned in the manufacturing of the samples.*
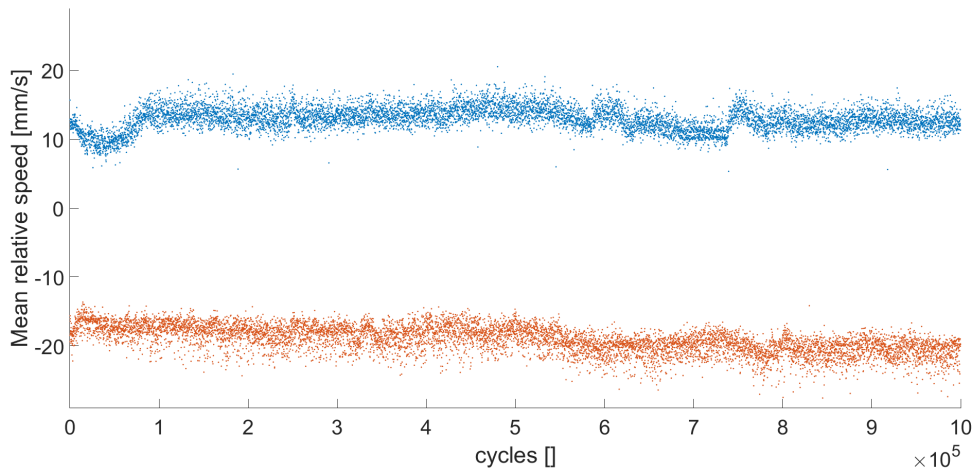
Figure B – Mean speed in 10^6-cycles lifetime test **without** coating covering the Ti-6Al-4V pin. Performances are a bit lower and less stable than with a coated Ti-6Al-4V pin.

Résumé étendu

Ces travaux de thèse CIFRE sont nés d'une collaboration entre l'entreprise Cedrat Technologies, leader français des actionneurs piézoélectriques, et l'équipe Tribologie et Mécanique des Interfaces (TMI) du laboratoire LaMCoS, spécialiste dans les domaines liés à la tribologie et, par extension, à tout ce qui a trait aux problématiques de frottement et d'usure. Ils se proposent d'aborder *le comportement tribologique et vibratoire des moteurs piézoélectriques inertiels*, en particulier ceux basés sur un actionnement amplifié. Ils font suite aux travaux de Christian Belly (2011), qui ont menés aux premiers prototypes de ces moteurs. Ils s'inscrivent également dans un contexte international, ayant été partiellement financés par deux projets européens. Le premier projet, Nepia, s'est concentré sur les aspects tribologiques. Le second projet, μ-Fast, s'est concentré sur les aspects vibratoires. Finalement, ils sont à l'origine et se poursuivent actuellement sous la forme d'un troisième projet européen, Elvisa, qui se concentre sur les aspects d'industrialisation, à partir des développements innovants réalisés en synergie de ces travaux.

Les moteurs piézoélectriques inertiels amplifiés, SPA

Le concept de moteur piézoélectrique a été introduit par Williams (1937). Il repose sur la combinaison de deux étages de conversions d'énergie (Fig.1). Le premier étage convertit un signal électrique en déformation mécanique au moyen d'une céramique piézoélectrique. Cet étage seul sera nommé *actionneur piézoélectrique*. Le second étage convertit la déformation piézoélectrique précédemment générée en déplacement mécanique, linéaire ou rotatif, par l'intermédiaire d'une interface de frottement. On parlera de *moteur piézoélectrique* une fois ces deux étages réunis.
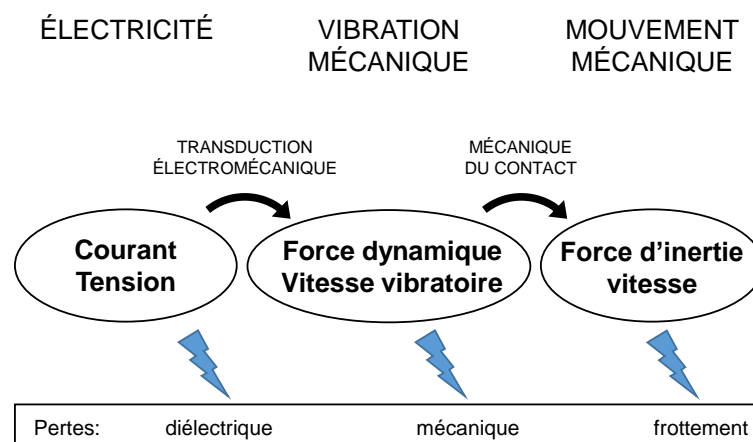
Figure 1 – Schéma de principe de la double conversion d'énergie décrivant les moteurs piézoélectriques (figure original dans Vanel, 1996).

Les actionneurs piézoélectriques — Les matériaux piézoélectriques ont la propriété de convertir une énergie électrique en énergie mécanique (effet direct, Fig.2-a) et inversement (effet inverse, Fig.2-b). Le principal avantage des actionneurs piézoélectriques actuels est qu'ils peuvent générer un mouvement à une résolution sub-nanométrique avec un temps de réponse extrêmement court, de l'ordre de la μ-seconde. Cependant, leur déformation, typiquement 1‰, limite leur course à quelques dizaines de microns et ainsi le nombre d'applications potentielles. Deux solutions ont dès lors été envisagées pour augmenter cette course. La première solution propose d'amplifier mécaniquement la déformation de la céramique jusqu'à 1% mais des courses supérieures à 1mm reste difficile à atteindre, d'autant plus dans un volume compact (il faut un actionneur de 10cm de long pour produire 1mm de course.). Une seconde solution est le moteur piézoélectrique.
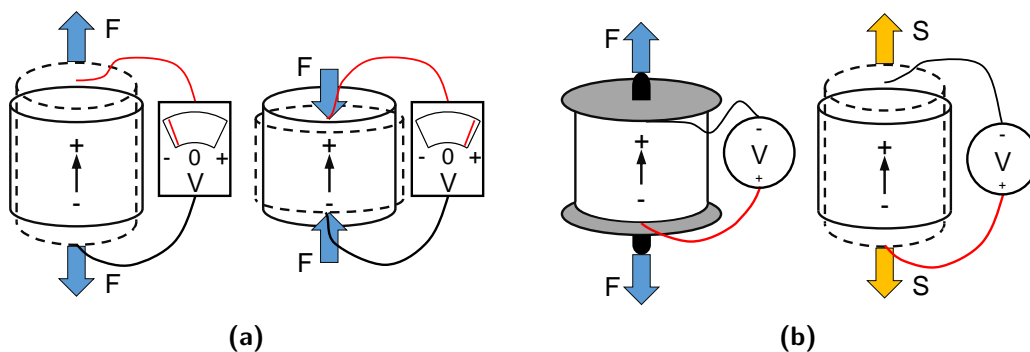
Figure 2 – Schéma introduisant la réversibilité d'un matériau piézoélectrique (figure originale dans Szufnarowski, 2013). (a) Effet direct. Quand un effort de traction ou de compression F est appliqué, une tension est générée. (b) Effet inverse. Sous l'effet d'une tension, le matériau génère de l'effort s'il est encastré, ou se déforme dans le cas contraire.

Les moteurs piézoélectriques — A partir du concept de moteur piézoélectrique (Fig.1), trois catégories sont classiquement présentes dans la littérature: les moteurs "inchworm" (Brisbane, 1968), ultrasonore (Williams, 1937) et inertiels (Soderqvist, 1973; Pohl, 1987b). Ces trois catégories diffèrent par leur design (typiquement le nombre de céramiques piézoélectrique nécessaire) et par leur actionnement (fréquence du signal et direction de polarisation de la céramique) (Spanner and Koc, 2010). Par exemple, le mécanisme d'actionnement à basse fréquence des moteurs "inchworm" leur permet de générer des efforts importants (>100N), avec peu d'usure au dépend d'un encombrement important et d'une vitesse faible. A l'inverse, les moteurs ultrasonores génèrent des vitesses importantes (>100mm/s) tout en étant silencieux et compact. Cependant, leur fonctionnement dépend de fréquences de résonances, ce qui les rend sensibles aux variations de températures. Ainsi, dans ces travaux, on s'intéresse en particulier aux moteurs inertiels qui apparaissent comme un compromis pertinent. En effet, ils sont seulement composés de trois pièces et sont pilotables à relativement basse fréquence. Ils ont ainsi un fort potentiel de miniaturisation tout en étant peu sensibles aux conditions extérieurs telle que la température.

Les moteurs inertiels amplifiés — Les moteurs inertiels sont des moteurs pas à pas. Ces pas sont générés par une alternance d'adhérence-glissement dont l'origine est l'actionneur piézoélectrique (Fig.3). Les vitesses générées sont de l'ordre de 10mm/s.

Afin d'améliorer les performances des moteurs inertiels classiques, Belly (2011) a remplacé l'actionneur piézoélectrique par un Actionneur Piézoélectrique Amplifié (APA®). Ainsi, la céramique n'est plus directement reliée à la masse oscillante mais logée dans une coque métallique en forme de losange, servant à augmenter l'amplitude vibratoire avant conversion en pas: on parle alors de SPA (Stepping Piezoelectric Actuators). Les efforts et vitesses générés sont ainsi plus élevés tout en restant dans un volume compact, de l'ordre du cm^3 (Fig.4).
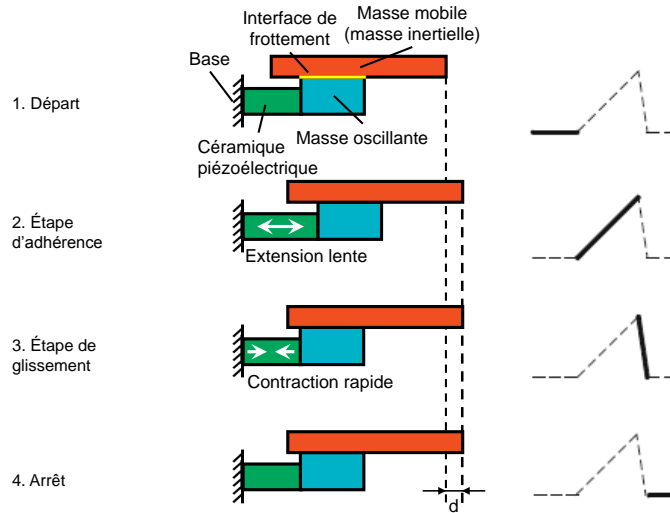
Figure 3 – Principe d'adhérence-glissement à l'origine des pas générés par les moteurs inertiels (figure originale dans Peng et al., 2015). Quand la tension aux bornes de l'actionneur varie lentement, les masses oscillantes et mobiles se déplacent ensemble. Quand la tension varie trop vite, un glissement apparait, générant un déplacement relatif. Par accumulation de ces deux étapes, des pas sont générés et la course du moteur devient théoriquement illimitée.
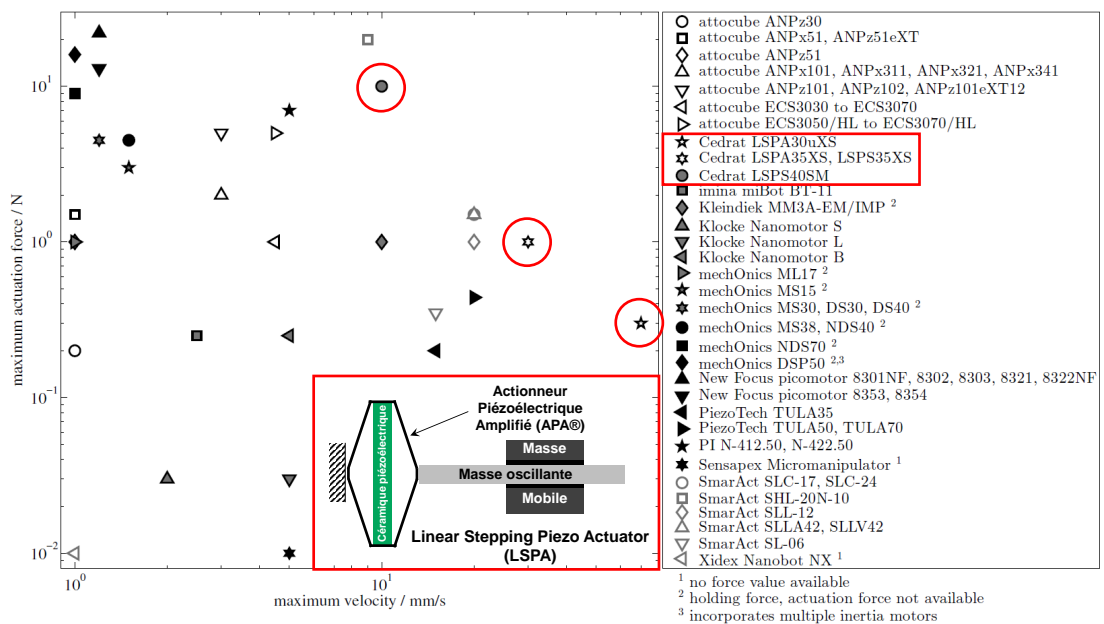
Figure 4 – Classification des différents moteurs inertiels commercialisés selon leurs force et vitesse (figure originale dans Hunstig, 2017). Les moteurs SPA, à base d'actionnement amplifiés, (cercles rouges) atteignent des vitesses et des efforts parmi les plus importants.

vii

Limites des SPA

Le frottement est ainsi inhérent au fonctionnement de ces moteurs. Ce frottement est aussi à l'origine d'usure et impacte directement leur durée de vie. Malgré de nombreuses publications autour des moteurs inertiels, peu d'attention a été portée autour des sollicitations tribologiques. De même, ces moteurs génèrent beaucoup de bruit. Ce bruit trouve son origine dans leur comportement vibratoire. Pour répondre aux deux problématiques, ces travaux adressent *les comportements tribologique et vibratoire de ces moteurs piézoélectriques inertiels amplifiés.* L'objectif est de comprendre les limites énoncées précédemment afin de (i) augmenter leur durée de vie tout en diminuant l'usure générée et (ii) caractériser leur comportement vibratoire afin de mieux prédire leurs performances mécaniques et réduire leur niveau de bruit.

Plan

Pour y parvenir, le manuscrit est décomposé en deux parties qui font suite à une partie I, d'état de l'art.

- La partie II traite de l'approche tribologique. Elle se propose de décrypter ce qui se passe dans l'interface de contact à travers le déploiement d'une instrumentation tribologique et la mise en place d'un cadre de travail lié à la méthode d'analyse des écoulements de 3$^{\grave{e}me}$ corps proposée par Godet (1984). Les mesures et observations qui en résultent permettent de remonter aux sollicitations tribologiques des SPA et d'établir leur circuit tribologique.

- La partie III traite du comportement vibratoire du mécanisme SPA. Cette question est d'abord traitée numériquement afin de mieux prédire les performances des SPA. Pour ce faire, le modèle à constantes localisées 1-D existant est remplacé par un modèle hybride FEM-constantes localisées afin de prendre en compte les mouvements du moteurs dans les trois directions de l'espace. Elle est ensuite traitée expérimentalement afin de déterminer le principal contributeur acoustique et de proposer des solutions pour réduire le bruit que ces moteurs génèrent.

L'ensemble est conclut par une partie IV, proposant (i) un résumé général, (ii) une méthodologie de design des SPA, née des différentes expériences, simulations et développements innovants proposés au cours de ces travaux, ainsi que par (iii) des perspectives.

Axe tribologique

Déploiement d'une instrumentation tribologique

Dans les SPA étudiés, le couple de matériaux frottants est constitué d'un composite polymère renforcé en fibres de verre[1] et d'un Ti-6Al-4V revêtu par bain chimique d'une couche majoritairement composée de silice.

Avant de proposer des solutions pour accroitre la durée de vie et diminuer l'usure des SPA, il était d'abord nécessaire de caractériser les sollicitations tribologiques dans l'interface existante. Pour y parvenir, trois approches ont été envisagées au préalable: (i) une étude bibliographique, (ii) une approche numérique et (iii) une approche expérimentale:

---

[1]Sa composition n'est pas révélée par souci de confidentialité.

- De nombreux tests de matériaux frottants ont été effectués sur des moteurs inertiels dans la littérature, au dépend d'une réelle analyse tribologique. S'il apparait que des interfaces très rigides tangentiellement permettent de maximiser les performances (Bergander and Breguet, 2002), Belly (2011) a montré qu'elles n'étaient pas forcément appropriées pour une longue durée de vie et une faible génération d'usure, dans le cas des SPA, contrairement au couple: composite / Ti-6Al-4V revêtu.

- Une approche numérique par éléments discrets (DEM) devient de plus en plus pertinente pour comprendre le comportement dynamique locale d'une interface de contact. En effet, les modélisation récentes permettent de prendre en compte les écoulements de particules solides ainsi que la géométrie des interfaces au contact (Kounoudji et al., 2016). Cependant, les temps de calcul restent encore trop long pour que la DEM soit envisagée dans ces travaux.

- Ainsi l'approche expérimentale a été privilégiée. Pour ce faire, un tribomètre actionné par un SPA et préchargé par un ressort à été développé afin d'être au plus proche du comportement vibratoire du vrai moteur (Fig.5). De plus, la verticale du contact a été ajourée afin de permettre l'observation des écoulements de 3$^{\text{ème}}$ corps pendant les premiers cycles de fonctionnement. Une fois développé, le banc de test a été instrumenté afin de mesurer le coefficient de frottement, les vitesses et déplacements des masses oscillantes et mobiles et la précharge.

(a) **(b)**
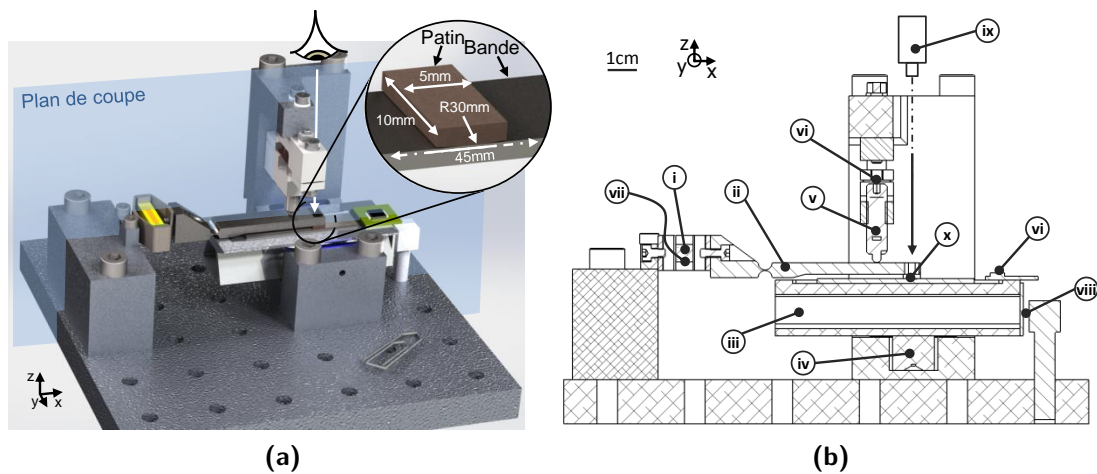
Figure 5 – Tribomètre SPA. (a) illustration et (b) plan de coupe. (i) L'actionneur piézoélectrique est lié rigidement à (ii) la masse oscillante en contact avec (iii) la masse mobile. (iv) Le guidage et (v) la précharge sont assurés par des paliers à air et un ressort contenu dans une vis respectivement. (vi) La force de précharge est mesurée par une jauge de déformation. (vii) Une seconde jauge de déformation est montée sur l'actionneur afin de mesurer l'amplitude vibratoire. (viii) Une sonde à courant de Foucault est utilisée pour mesurer le déplacement de la masse mobile. (ix) Une caméra rapide ou un appareil photo sont utilisés pour (x) observer le contact de l'intérieur quand des patins en verre sont utilisés.

Cadre de travail: les écoulements de 3$^{\text{ème}}$ corps

Les contacts frottants analysés dans ces travaux sont des contacts secs, sans lubrifiant. Si la théorie de Reynolds, formulée à partir des équations de la mécanique des fluides, permet de déterminer les profils de vitesses et de contraintes au sein des films épais de lubrifiants (Dowson and Higginson, 1977), il n'existe pas d'équivalent à cette théorie pour les contacts secs. Ainsi, Godet (1984) a proposé un concept phénoménologique

ix

basé sur des observations expérimentales pour y remédier. Ce concept repose sur les notions de *triplet tribologique*, *mécanisme d'accommodation de vitesse* et de *circuit tribologique* (Fig.6), pour se rapprocher du vocabulaire utilisé dans l'étude des contacts lubrifiés.

Modes d'accommodation: M1- elastique   M2- rupture   M3- cisaillement   M4- roulement
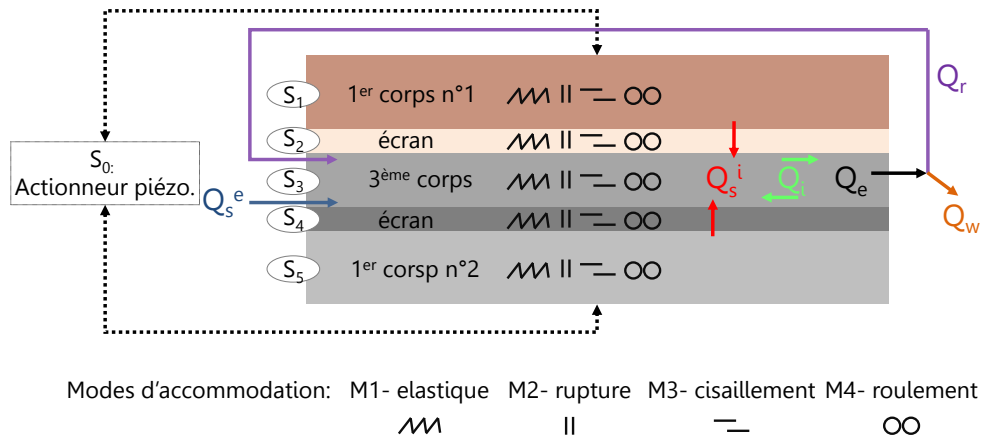
Figure 6 – Formalisme $3^{\text{ème}}$ corps. Le triplet tribologique est composé du mécanisme, des interfaces de frottement, et des particules de $3^{\text{ème}}$ corps. Le circuit tribologique résultant est caractérisé par (i) des écoulements de particules solides: Q_s^i: débit source interne, Q_s^e: débit source externe, Q_i: débit interne, Q_e: débit externe, Q_r: débit de recirculation, Q_w: débit d'usure et (ii) les mécanismes d'accommodation de vitesse relative décomposée en sites S_i et modes M_j.

Ainsi, il devient plus facile d'imaginer que les particules solides à l'intérieur d'un contact peuvent aussi bien être destructrices que protectrices des 1er corps. Caractériser les sollicitations tribologiques revient alors comprendre l'origine et la propagation de ces écoulements ainsi que caractériser les sites/modes d'accommodation.

L'autre intérêt de cette méthode est qu'elle permet d'analyser un contact de manière systématique, en suivant un protocole d'analyse définit à l'avance:

- La première étape de ce protocole consiste à identifier l'échelle d'observation caractéristique du contact étudié. Ici, la largeur de contact calculée par les équations de Hertz (1882) ainsi que la taille d'un pas sont environ 100μm. De même, l'épaisseur de revêtement et le diamètre des fibres de verre sont de l'ordre de 10μm. Donc, chaque contact est observé d'abord à une échelle "macroscopique" de 500μm puis des zooms progressifs jusqu'à une échelle plus "locale" de 5-10μm sont effectués.

- La seconde étape consiste à repérer les zones d'intérêt. Pour y parvenir, chaque contact est divisé au préalable en trois zones: (i) la zone de contact, (ii) la zone qui n'a pas frotté et (iii) la frontière entre ces deux zones. Ensuite chaque zone est décrite par sa morphologie: pulvérulence, cohésion, compactage, porosité, densité, adhésion (avec un Microscope Électronique à Balayage, MEB) et par sa composition chimique (avec une sonde Energy Dispersive X-ray, EDX). La répartition des volumes de $3^{\text{ème}}$ corps ainsi que les orientations des écoulements sont également répertoriées.

- Finalement, l'étape la plus complexe est l'interprétation. Elle consiste à faire le lien entre le comportement vibratoire du mécanisme et les morphologies observées pour remonter aux circuits tribologiques.

En se basant sur cette méthode d'analyse, différentes séries de test ont été effectuées. La première série est menée sur un faible nombre de cycles, 10^4 aller-retours de 1mm

afin d'observer l'initiation des écoulements de $3^{\text{ème}}$ corps. Cette série de tests est effectuée à la fois avec les vrais interfaces et avec les patins en verre. L'analyse *in-situ* en fonctionnement est ensuite complétée par des observations *post-mortem*. La seconde série de test est menée sur un nombre de cycles plus important, 10^6 aller-retours. Ce nombre de cycles est basé sur la durée de vie nominale des actionneurs SPA actuels. Tous les tests ont été réalisés à l'air ambiant.

Mesures et observations

A l'issue des tests, les interfaces sont séparées, ce qui permet de les analyser par microscopie topographique, microscopie à balayage et analyse chimique (Fig.7). Ainsi, en complétant les analyses *post-mortem* avec les données capteurs et les observations à travers les patins transparents (Fig.8), il a été possible de déduire les circuits tribologiques associés (Table 1).
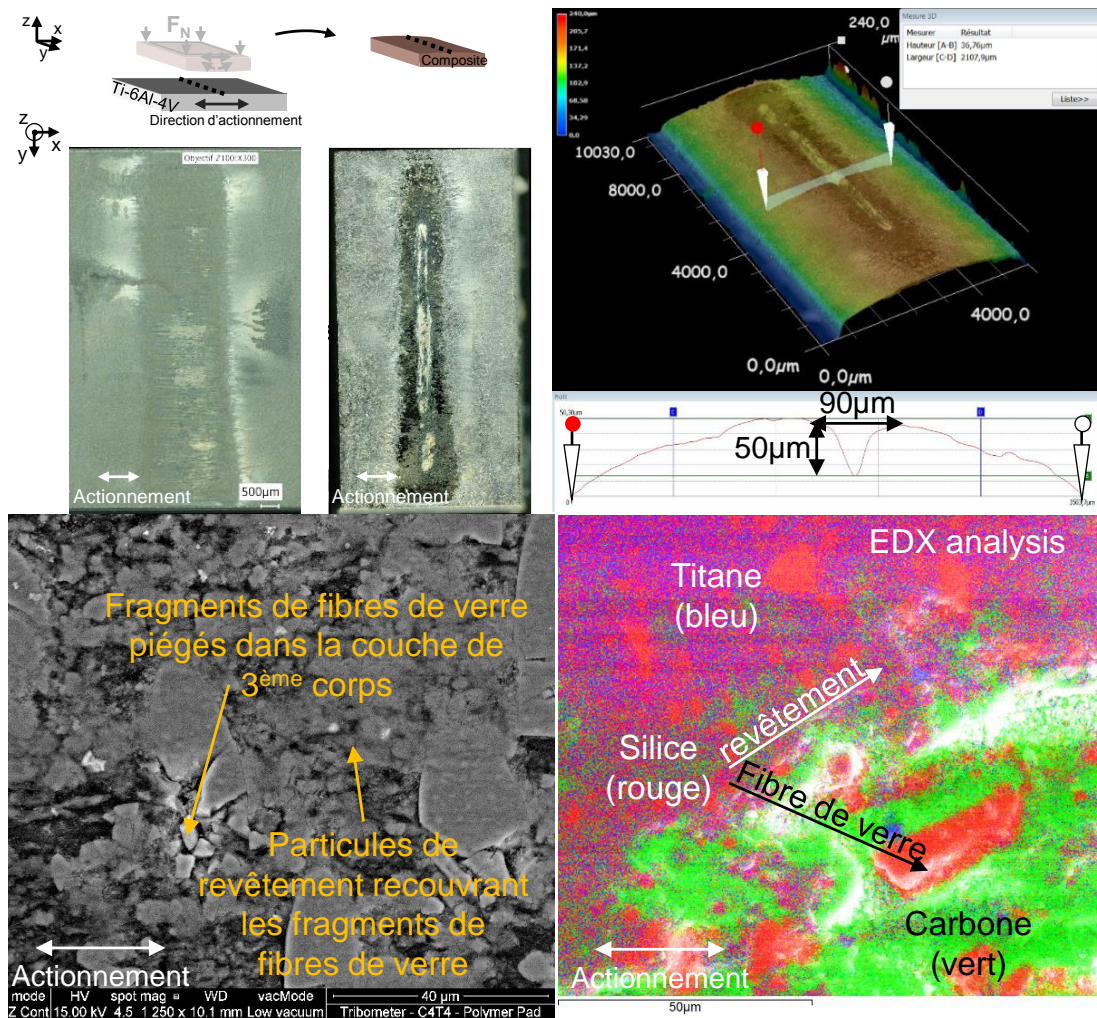
Figure 7 – Exemple d'observations menées en microscopie et microscopie électronique à balayage avec sonde chimique. La première image permet d'avoir une vue complète des corps d'épreuve afin de repositionner les observations plus locales. La seconde image, en microscopie topographique permet d'obtenir une vue en trois dimensions de la surface des corps d'épreuve avec une résolution sur l'axe verticale de l'ordre du micromètre. La troisième image, réalisée au MEB, permet d'observer localement les corps d'épreuve. Finalement, la quatrième image, obtenue avec une sonde chimique, permet d'obtenir la composition chimique en surface, afin d'identifier l'origine des particules de $3^{\text{ème}}$ corps visualisée.
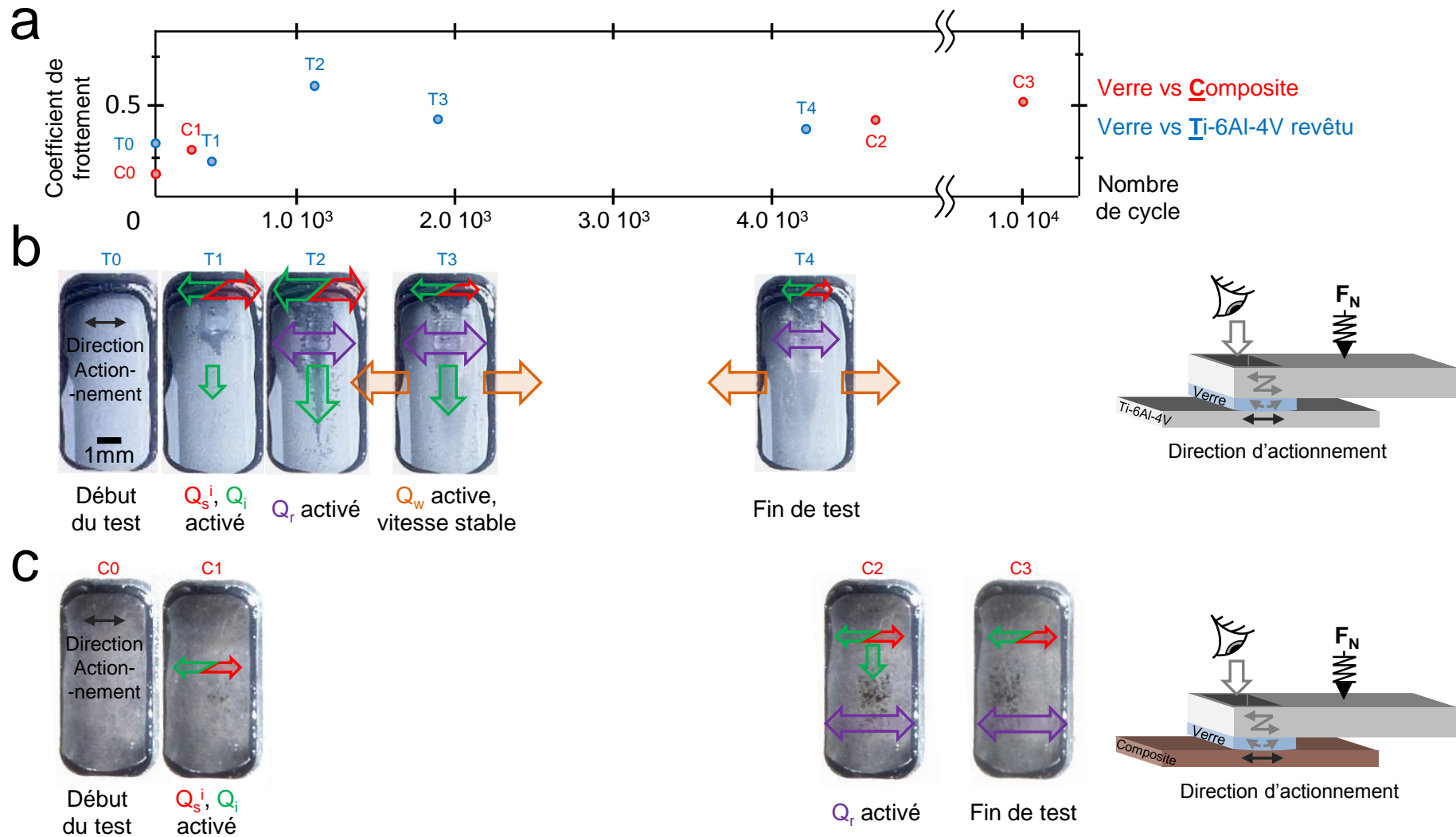
Figure 8 – Ligne de temps tribologique pendant un test court avec des patins transparents. (a) Évolution du coefficient de frottement en vis-à-vis d'observations *in-situ* significatives. (b) Contact patin en verre / bande en Ti-6Al-4V revêtu. (c) Contact patin verre / polymère renforcé en fibre de verre. (b) et (c) sont affichés simultanément pour observer les progressions respectives des écoulements de 3ème corps. Les couleurs des flèches renvoient au code couleur proposé Fig.6. Leur taille représente une estimation des amplitudes des écoulements observés.

Table 1 – Circuits tribologiques résultant des tests avec le patin en Ti-6Al-4V revêtu frottant sur la bande de polymère renforcée en fibre de verre. Les sites et modes d'accommodation en gras représentent les sites et modes prépondérant en comparaison de tout ceux inventoriés.

	Débits de 3ème corps				Accommodation	Schéma du contact
	Q_s^i	Q_i	Q_e		Sites: Modes:	
			Q_r	Q_w	S_i M_j	
État initial						
10^4 cycles	+++	+++	++	++	S_2: **Impact**, M_3 S_3: M_3 S_5: Impact, M_3	
10^6 cycles	+++	++++	+++	++	S_1: Impact, M_3 S_2: **Impact**, M_3 S_3: **Impact**, M_3, M_4 S_5: **Impact**, M_3	

Principaux résultats

La caractérisation des sollicitations tribologiques découle de la méthodologie appliquée ci-dessus: dès les premiers cycles, une couche de 3$^{\text{ème}}$ corps se forme sur le composite par cisaillement de la matrice carbone. Cette couche ressemble à de la pâte à tartiner par sa ductilité. Elle piège les fibres de verre préalablement concassées et les particules de revêtement du Ti-6Al-4V. Sa propagation est d'autant plus accélérée que sa ductilité diminue avec l'augmentation du nombre de particules de revêtement piégées. La couche créée est très cohésive et abrasive. De plus, progressivement, le substrat Ti-6Al-4V est atteint, ce qui conduit à un contact partiel Ti-6Al-4V / Ti-6Al-4V. Le coefficient de friction qui en résulte est assez élevé (environ 0,5) et reste constant, ce qui conduit à une bonne répétabilité des performances.

Il a également été intéressant d'observer que le contact Ti-6Al-4V/composite était différent du contact composite/Ti-6Al-4V. En effet, la distance de glissement "vue" par chacune des interfaces n'est pas la même: le patin est toujours en contact alors que des portions de la bande ne frottent pas toujours. Ainsi, quand le patin est en composite, il finit par se fissurer perpendiculairement au contact, ce qui mène à une accommodation partielle de la vitesse relative par déformation élastique du patin et donc une baisse drastique des performances. Au contraire, quand les interfaces sont interverties (patin en Ti-6Al-4V revêtu et bande en composite), les performances sont rapidement stables et constantes tout au long des tests.

Suite à cette analyse, un test plus long, de 10^7 cycles, faisant frotter un patin en Ti-6Al-4V revêtu et une bande en composite, a été réalisé et dupliqué avec succès. *La durée de vie des moteurs a ainsi été multipliée par 10.* Cependant, le débit d'usure reste trop important pour adresser certaines applications, notamment celles liés au positionnement d'optiques. Pour y remédier, le renfort en fibre de verre du composite a été remplacé par un renfort en fibre de carbone. L'objectif était de diminuer le pouvoir abrasif de la couche de 3$^{\text{ème}}$ corps et d'augmenter son pouvoir adhésif, ce qui

diminuerait d'autant plus le débit d'usure Q_w. *Ce nouveau triplet tribologique a été testé sur 10^7 cycles avec succès, multipliant aussi la durée de vie par 10, et le volume d'usure a été réduit.* Il est comparable au volume observé avec le couple Ti-6Al-4V revêtu / composite après 10^6 cycles. Il restera néanmoins à analyser les interfaces en microscopie afin de vérifier que les sollicitations tribologiques soient cohérents avec ceux attendus.

Ainsi, sans avoir multiplié les tests de matériaux frottants, tel que trouvé dans la littérature, l'approche $3^{\text{ème}}$ corps proposé par Godet (1984), a permis d'introduire un nouveau triplet tribologique permettant à la fois d'adresser les objectifs de durée de vie et d'usure.

Une perspective logique à cette étude sera de reboucler avec les SPA, en répétant des tests longs et des analyses *post-mortem*.

Axe vibratoire

Modélisation hybride

Le premier chapitre traitant du comportement vibratoire des SPA vise à mieux prédire numériquement leurs performances.

Jusqu'à présent, le comportement vibratoire du SPA était simulé par un modèle à constantes localisées 1-D (Fig.9, Belly, 2011). Ce modèle atteint ses limites quand des mouvements dans d'autres directions que celle de l'actionnement doivent être pris en compte. Par exemple, une vibration à une fréquence de 370Hz est apparue sur les mesures du tribomètre. Une telle vibration n'avait pas été anticipée.
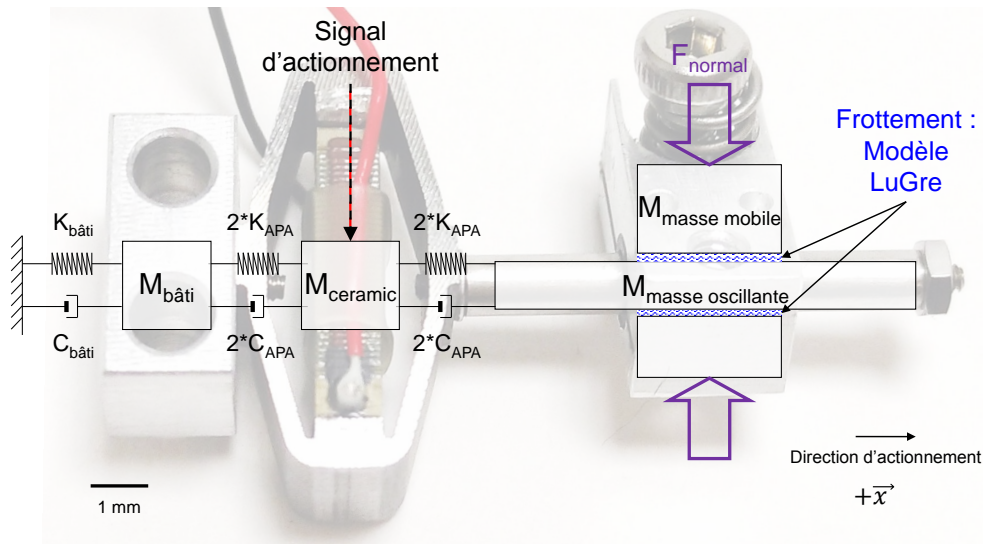
Figure 9 – Schéma de principe d'un modèle à constantes localisées 1-D appliqué à un SPA.

Pour tenir compte de ces mouvements, un modèle à constantes localisées à plusieurs degrés de liberté aurait pu être envisagé. Cependant, un tel modèle aurait été très complexe à implémenter et peu souple pour envisager d'éventuelles modifications dans les futurs design de SPA. A la place, un modèle alternatif, Eléments Finis (FEM)/constantes localisées, appelé *hybride* par Berger (2002), a été implémenté. L'utilisation de la FEM permet d'être plus représentatif du comportement vibratoire du moteur. Coupler cette modélisation à une approche de superposition modale, en constantes localisées, permet

xiv

de prédire les performances des SPA sans augmenter les temps de calcul par rapport au modèle de départ.

La mise en place de ce modèle se résume en trois étapes (Fig.10). Premièrement, une analyse fréquentielle de l'actionneur, dessiné au préalable sur ordinateur, est menée par FEM. La structure mécanique est ainsi décrite par ses modes de résonances. Ensuite, un critère, appelé facteur de participation massique efficace cumulée (CEMPF, Ahmad et al., 2016), permet de déterminer quelles résonances impactent le plus le mouvement de l'actionneur dans l'axe d'actionnement. Ces résonances sont alors conservées et implémentées dans une fonction de transfert à partir d'une analogie électro-mécanique et d'une approche par superposition modale (Le Letty, 1994). Finalement, la fonction de transfert précédemment formulée vient remplacer le modèle à constantes localisées en série de la modélisation de l'interface de frottement (avec un modèle de LuGre, De Wit et al., 1995) afin d'obtenir les performances du moteur.
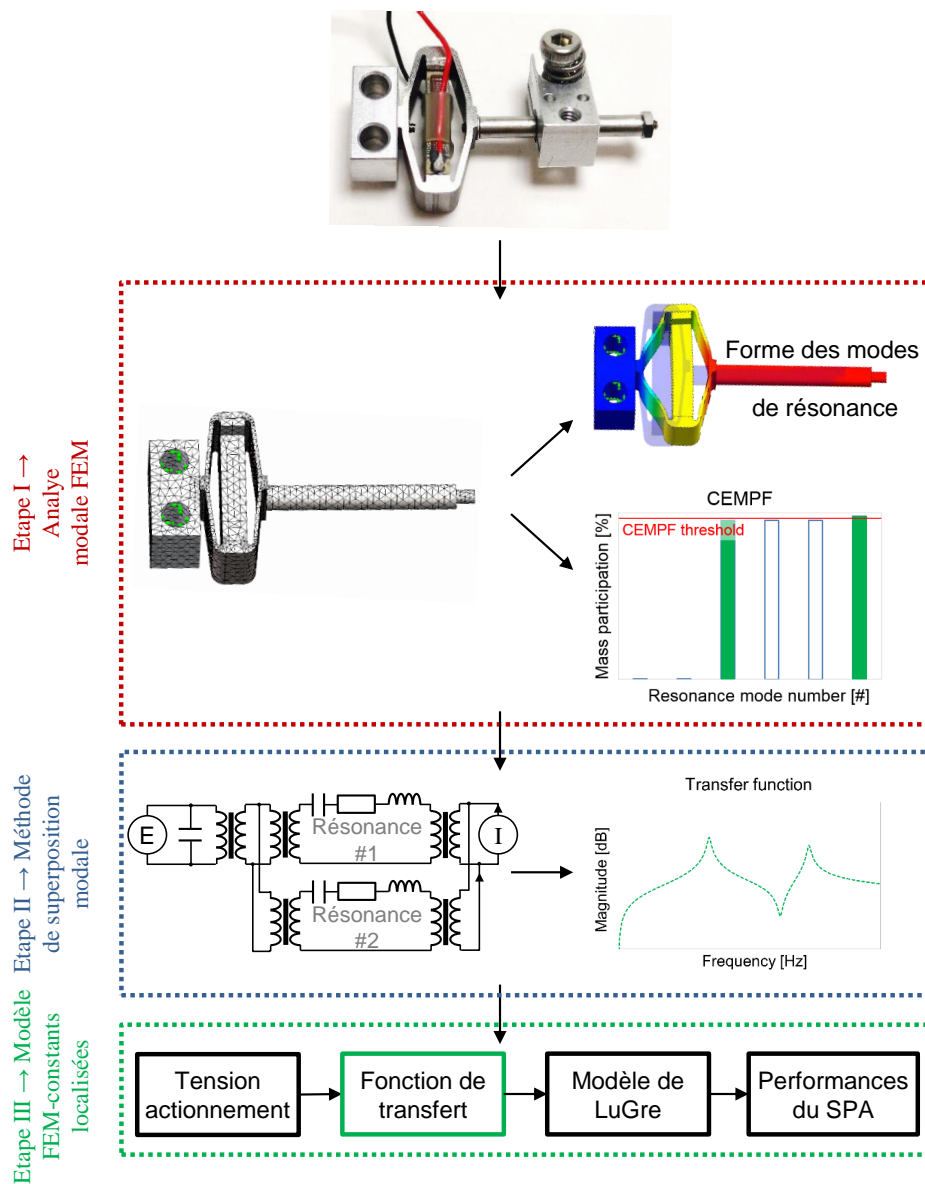
Figure 10 – Organigramme de l'implémentation du modèle hybride FEM-constantes localisées pour le SPA.

Une fois implémenté, ce modèle hybride a permis d'identifier la vibration de 370Hz (Fig.11) comme étant due à la torsion du col de la masse oscillante (Fig.5). Ainsi, ce modèle peut estimer les performances de n'importe quel SPA, quelque soit sa structure. Une limite a également été identifiée. En effet, à cause du schéma d'intégration, la fonction de transfert n'admet qu'une entrée: le signal d'excitation. Ainsi, le modèle hybride n'est pas capable de prédire correctement les performances des SPA quand les efforts de frottement ne sont pas négligeables devant les efforts générés par l'actionneur, typiquement pour des actionneurs souples tels que le LSPA30μXS.
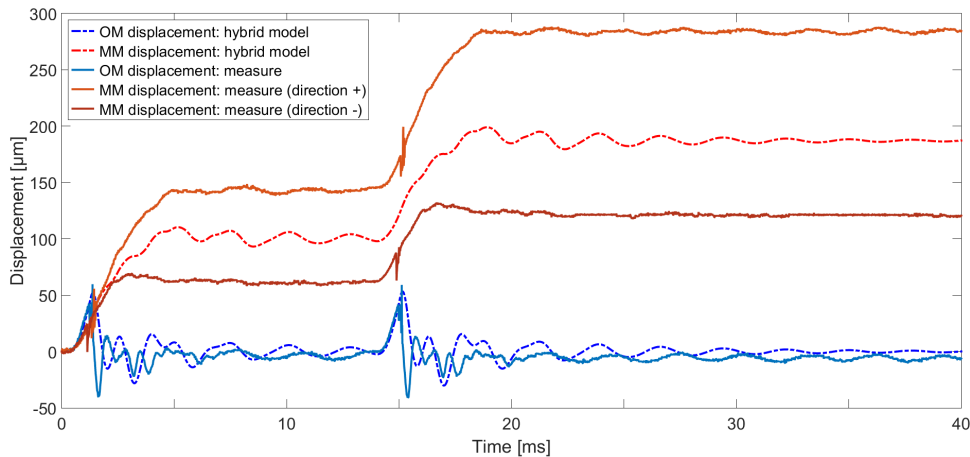
Figure 11 – Courbes de déplacement des masses oscillante (bleu) et mobile (rouge) du tribomètre SPA. En traits pleins les déplacements mesurés. En traits pointillés, les déplacements simulés.

Réduction expérimentale du bruit

Les SPA sont bruyants. Ils génèrent entre 85dBA et 95dBA à 30cm. Cela équivaut à écouter le trafic autoroutier à une distance de 10m. Ce problème est du à la fréquence du signal d'actionnement. En effet, l'oreille humaine perçoit tous les sons dont la fréquence est comprise entre 20Hz et 20kHz. Elle est d'ailleurs particulièrement sensible aux sons dont la fréquence est comprise entre 2kHz et 4kHz. Or, l'ordre de grandeur de la fréquence d'actionnement des SPA est classiquement le kHz. De plus, les signaux d'actionnement utilisés engendrent des pics d'accélérations afin de faciliter la transition adhérence-glissement et ainsi maximiser les performances. Cependant, acoustiquement, on pourrait traduire cela par une succession de coups de marteaux à haute fréquence (Fig.12).
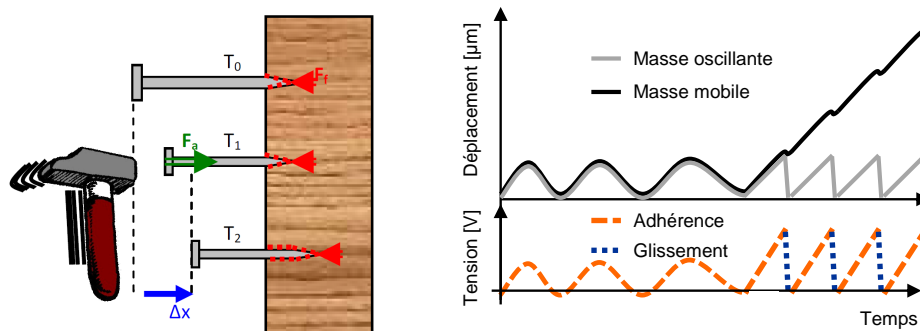
Figure 12 – Illustration du comportement acoustique des SPA. Chaque transition adhérence-glissement génère un pic d'accélération équivalent à un coup de marteau qui propage des vibrations dans toutes la structure et qui irradie acoustiquement.

Afin d'adresser cette problématique vibro-acoustique, la première étape a été d'identifier le principal contributeur acoustique, entre l'actionnement et le frottement, pour ensuite proposer des solutions de réduction du bruit. Dans les SPA, l'actionnement s'est révélé être le plus bruyant. Il n'était donc pas possible d'envisager des solutions sans affecter les performances moteurs. Ainsi, toutes les solutions proposées ont été mises en vis-à-vis des performances mécaniques telles que la force et la vitesse.

Parmi les solutions proposés, l'isolation par l'extérieur à été rapidement mis de côté car elle requiert de connaître la structure dans laquelle le moteur sera intégré, ce qui n'est pas toujours possible. De même, ce n'était pas forcément cohérent avec la logique de miniaturisation des moteurs.

L'amortissement élastique a été mis de côté également car il impactait la raideur de l'actionneur. Ainsi, au lieu de générer des pas, l'effort généré par l'actionneur contribuait plus à déformer l'amortisseur.

Une troisième piste d'amélioration a consisté à faire évoluer le signal d'actionnement vers un signal ne générant pas de pic d'accélération. Un signal quasi-dent-de-scie (Quasi-SawTooth, QST) existait déjà dans la littérature pour exciter les fréquences de résonance des moteurs ultrasonores (Eq.1, Morita et al., 2012).

$$V_{QST\ signal}(t) = A[sin(\omega t + \varphi) + \frac{1}{3}sin(2(\omega t + \varphi) + \Phi) + B] \qquad (1)$$

Avec ω, la pulsation du signal, A l'amplitude de tension divisée par la norme de la somme des sinus. φ et B, les déphasage et offset nécessaires pour que le signal commence et termine à 0V (et ainsi éviter des pics d'accélérations à l'allumage de l'alimentation). Φ, le déphasage entre les deux sinus pour faire apparaitre le signal QST.

De plus, un temps mort a été ajouté entre deux actionnements afin de (i) laisser du temps au système pour amortir les oscillations libres générées et (ii) dissocier la fréquence acoustique de la fréquence d'actionnement (Fig.13). En effet, augmenter cette période de temps mort diminue d'autant la fréquence acoustique vers une fréquence à laquelle l'oreille est moins sensible.
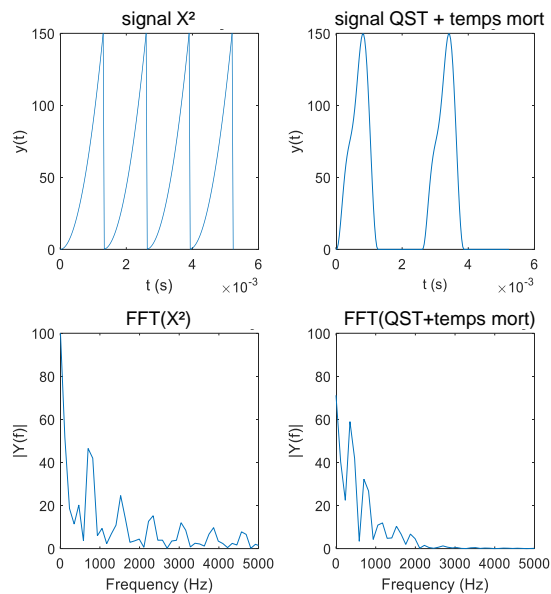
Figure 13 – Signaux d'actionnement d'origine (x^2) et optimisé acoustiquement (QST+temps mort). L'énergie du second signal est concentrée dans les basses fréquences auxquelles l'oreille humaine est moins sensible.

L'utilisation de ce signal a permis une réduction drastique du bruit (80dBA→61dBA) mais a également grandement impacté les performances du moteurs (Fig.14). En effet, alors qu'avec le signal d'origine, le moteur testé était capable de générer une vitesse à vide de 7.5mm/s et 2N de force, le signal QST+temps mort génère 1.5mm/s et 0.5N de force. Cela s'explique par l'absence de pic d'accélération. Pour y remédier partiellement, un troisième pulsation a été ajoutée au signal QST précédent, ce qui a permis de se rapprocher d'un signal dent de scie. Ce signal, appelé QST-3f, a pu générer une vitesse de 7.5mm/s et une force de 1N, sans trop augmenter le niveau de bruit (64dBA).
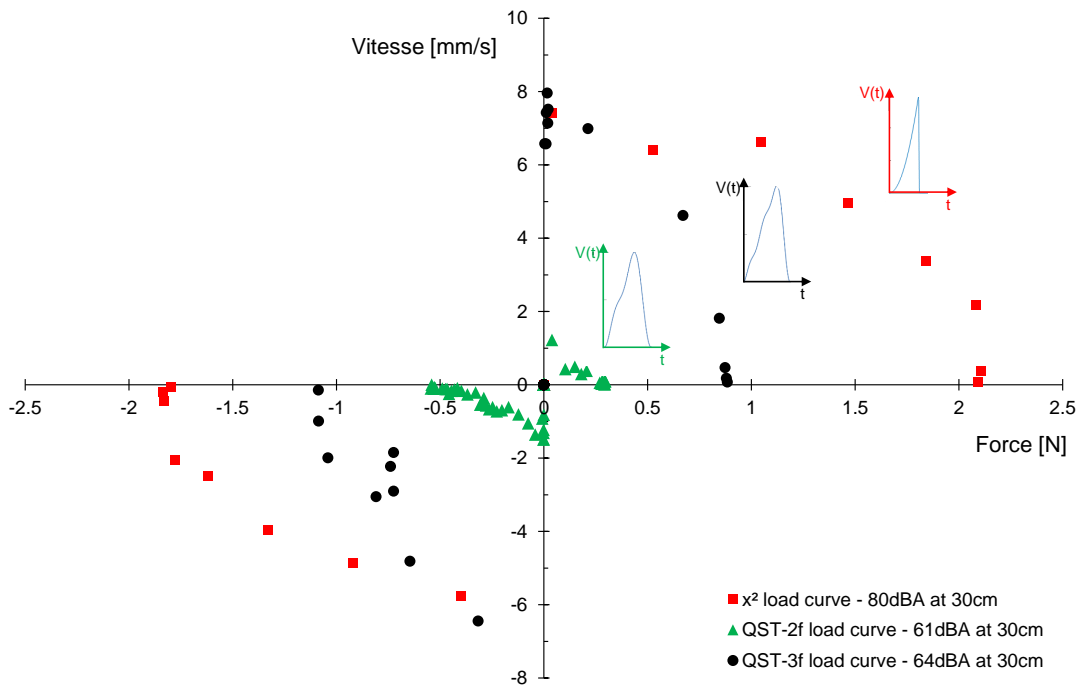
Figure 14 – Courbe de charge d'un SPA avec les signaux d'origine x^2, puis QST-2f et QST-3f. Bien que les performances acoustiques du signal QST-2f sont bonnes, les performances mécaniques sont trop diminuées. En comparaison, le signal QST-3f génère des vitesses et des efforts cohérents sans trop augmenter le niveau acoustique.

L'intérêt de la solution précédente est qu'elle est applicable quelque soit le SPA. Cependant, le bruit n'a pas été complètement supprimé, ce qui reste gênant pour certaines applications. Pour y remédier, une dernière solution a été proposée: concevoir un SPA ultrasonore. Cette solution a été implémentée avec succès en se basant sur la littérature (Morita et al., 2012). Le moteur est complètement silencieux et génère une vitesse de l'ordre de 20mm/s. Cependant, les efforts générés restent faibles. Ainsi, ce moteur va constituer une des principales perspectives de ces travaux afin de comprendre cette faible génération d'efforts ainsi que pour décrypter les sollicitations tribologiques associés à ce mécanisme.

Conclusion générale

Pour résumer, les SPA génèrent des vibrations asymétriques converties en déplacement par frottement grâce au phénomène d'adhérence-glissement. Ces vibrations et ce frottement soulèvent des problématiques liées au bruit et à l'usure. Pour y répondre, ces travaux étudient *les comportements tribologique et vibratoire de ces moteurs.*

Dans un premier temps, un tribomètre pion-plan actionné par un SPA a été développé. Il a permis d'observer les écoulements de $3^{\text{ème}}$ corps *in-situ* et en fonctionnement. Ces observations directes, couplées à des analyses *post-mortem* ont permis de décrypter les sollicitations tribologiques, pilotés principalement par l'abrasion des fibres de verre piégés dans la couche de $3^{\text{ème}}$ corps qui se forme rapidement à la surface du composite. En intervertissant les interfaces de frottement, la durée de vie du moteur a été multipliée par dix. De même, remplacer les fibres de verre par des fibre de carbone dans la matrice polymère à permis de réduire l'usure générée.

Dans un second temps, des analyses numérique et expérimentale ont été proposées afin de mieux appréhender le comportement vibratoire des SPA. Le modèle à constantes localisées 1-D a été modifié en une version hybride, constantes localisées-FEM. Ce modèle reflète mieux le comportement vibratoire des SPA car il peut prendre en compte des vibrations dans toutes les directions de l'espace et qui peuvent impacter l'actionnement. Ce modèle est également plus versatile car il permettra de simuler des structures de SPA qui n'ont pas encore été imaginées. De même, les tests expérimentaux menés ont également permis de déterminer que l'actionnement est le principal contributeur acoustique. Après avoir testé différentes solutions, une modification du signal à permis de réduire le niveau de bruit de seize dBA.

Méthodologie de design des SPA

Dans un premier temps, ces travaux de thèse se sont concentrés sur les aspects tribologique et vibratoire des moteurs SPA. A partir des différentes simulations et essais réalisés, une méthodologie de design a également été formulée. Cette méthodologie est divisée en deux étapes: le design mécanique et l'estimation des performances (Fig.15).
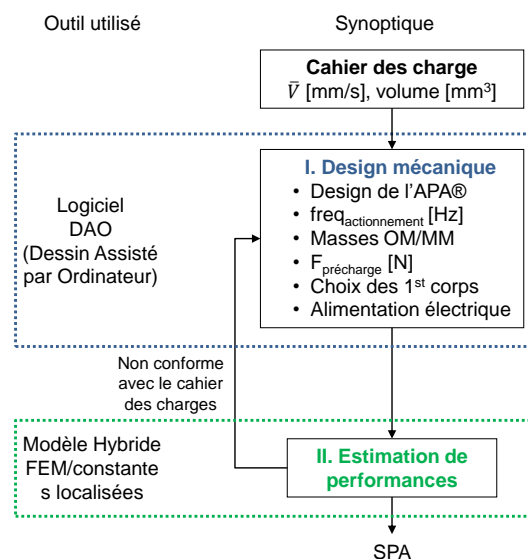

Figure 15 – Synoptique de conception d'un SPA.

xix

Conception mécanique — Quelques jalons, introduit ci-dessous, pourront guider la conception des SPA et s'assurer de la cohérence du cahier des charges vis-à-vis, par exemple, du *volume* et de la *vitesse* envisagés.

- Tout d'abord, la vitesse finale du moteur va dépendre directement de la *conception de l'APA®*. En effet, la vitesse est approximativement égale au produit de l'amplitude vibratoire de l'actionneur par la *fréquence d'actionnement*. De même, cette fréquence d'actionnement doit être inférieure aux fréquences de résonance du moteur afin que leur effet soit négligeable. Ainsi, la raideur et l'amplitude vibratoire de l'actionneur donnent les premiers éléments de dimensionnement du volume final du moteur. Il faut également déterminer si diminuer le niveau acoustique est prioritaire. Le cas échéant, l'utilisation du signal QST-3f permettra d'adresser cette problématique mais engendrera également une baisse des performances. De plus, la raideur de l'actionneur devra être d'autant plus importante puisque le signal QST-3f dissipe son énergie majoritairement dans les basses fréquences.

- Dans un second temps, il faut considérer le transfert d'énergie à travers l'interface de frottement. Ce transfert dépend à la fois des *masses oscillantes* et *mobiles* ainsi que de la *force de précharge*. En se basant sur les investigations tribologiques, un coefficient de frottement de 0.5 peut être utilisé. Ces informations permettent de dimensionner la force que doit générer l'actionneur afin qu'elle soit supérieure à la force de frottement envisagé, afin de pouvoir déclencher la transition adhérence-glissement. Notons également que la fonction précharge va également piloter le volume final du moteur. De même, notons que pour diminuer la dissymétrie des performances, l'axe de poussée de l'actionneur doit être au plus proche de l'axe de poussée de la force de frottement.

Au delà des performances mécaniques, il est nécessaire de rappeler quelques points clés à propos du *choix des 1er corps.*

- Tout d'abord, l'orientation des interfaces impacte les performances tribologiques. Afin d'atteindre une durée de vie importante avec des performances répétables, il est nécessaire que le 1er corps qui "voit" le plus de frottement soit en Ti-6Al-4V revêtu. Si un volume d'usure faible est également recherché, il sera intéressant de considérer le remplacement des fibres de verre dans la matrice polymère par des fibres de carbone.

- De même, dans ces travaux, la pression de contact a été calculé avec les équations de Hertz. Une valeur d'environ 10MPa a été adoptée au début de chaque test. Cette pression de contact pourra être conservée dans les futurs conceptions. Elle pilotera la conception de la géométrie des 1er corps et donc le volume final du SPA. Finalement, il est important de rappeler que l'usinage des 1er corps doit se faire à sec, sans huile de coupe, afin d'éviter que du lubrifiant soit introduit dans le contact frottant pendant le fonctionnement.

En parallèle, les choix mécaniques de conception pilotent également le choix de la céramique piézoélectrique et, par extension, celui de *l'alimentation électrique.* En effet, la fréquence d'actionnement sera limitée par la capacité électrique de la céramique et par la limitation en courant de l'alimentation choisie.

Estimation des performances — A partir des jalons précédents, si le cahier des charges est cohérent, le dessin du moteur peut être réalisée rapidement. Ensuite, le modèle hybride va permettre d'estimer ses performances finales. Premièrement, l'analyse fréquentielle par FEM va permettre de s'assurer de la valeur des fréquences de résonance, dépendant de la raideur de l'actionneur. Cela permettra également de bien choisir la fréquence d'actionnement. La formulation de la fonction de transfert permet ensuite de rapidement déterminer la vitesse du moteur; Si le pré-dimensionnement a été fait correctement, il ne devrait rester que quelques ajustements à effectuer, par exemple pour optimiser le suivi de la consigne adhérence-glissement. Dans un futur proche, il serait également intéressant d'utiliser cette méthode pour optimiser les SPA par le biais d'un algorithme génétique (Ha et al., 2005), mais les jalons indiqués plus haut permettront déjà de concevoir efficacement les prochains *SPA*.
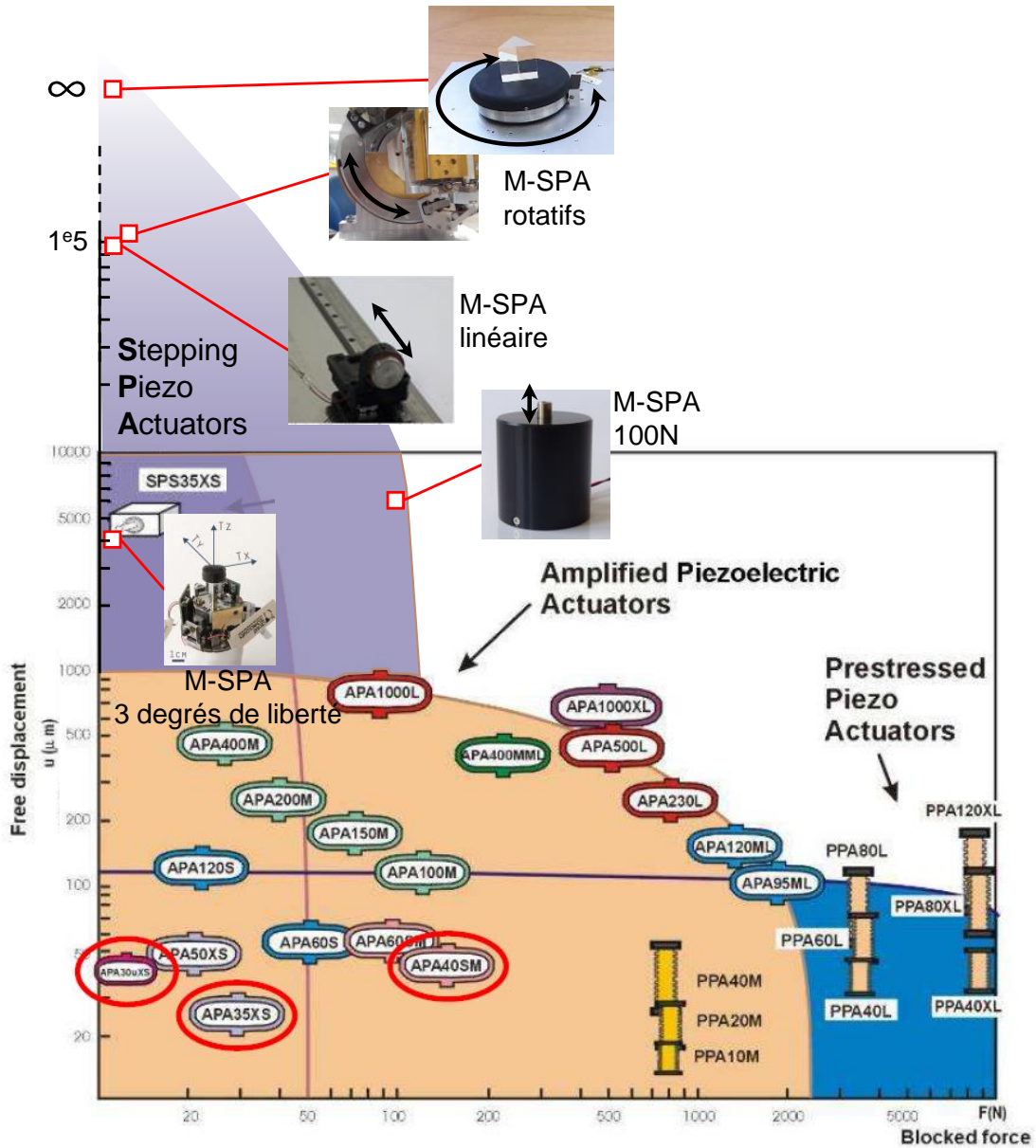
Développements innovants

Si le tribomètre a été initialement développé pour décrypter les sollicitations tribologiques, sa configuration de contact pion-plan s'est révélé pertinente pour concevoir des SPA. En effet, comme la distance entre le point de contact frottant et le centre de poussée de l'actionneur ne varie pas, contrairement à la configuration arbre-pince, la course du moteur n'est plus limitée et ne dépend que du guidage de la structure à entrainer (Fig.16). Au delà d'un potentiel de course plus longue, cette configuration facilite également la conception de mécanismes rotatifs, voire de mécanismes à plusieurs degrés de libertés. Ainsi, quatre moteurs basés sur cette structure ont été développés pendant ces travaux (Fig.17).
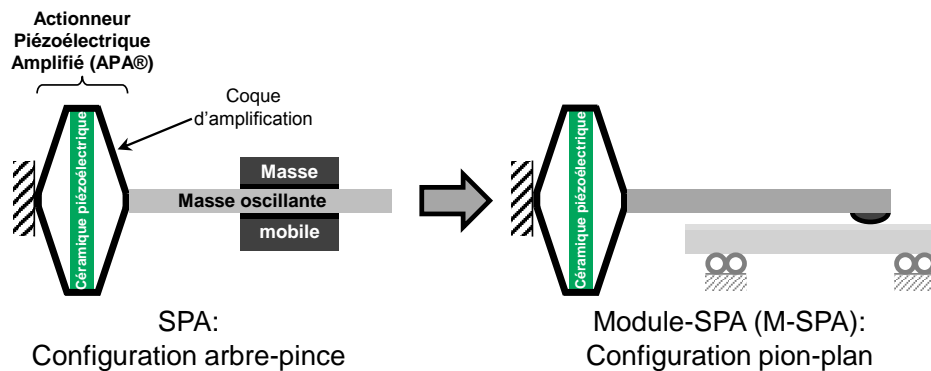
Figure 16 – SPA en configuration pion-plan. Cette configuration permet d'actionner un mécanisme déjà guidé quel que soit la course nécessaire.

Perspectives

Au début de ces travaux, les objectifs étaient d'améliorer les performances tribologique et vibratoire des SPA. Pour ce faire, il fallait d'abord comprendre ce moteur. Ainsi, la réalisation de différents tests et simulations ont permis de mieux saisir leurs subtilités et ont conduit à des améliorations pratiques telles que l'augmentation de la durée de vie et la réduction du bruit. Néanmoins, ce travail a également soulevé d'autres questions qui devraient être étudiées pour poursuivre leur amélioration. Cinq points méritent, à mon avis, une attention particulière. Certains de ces points sont

Figure 17 – Développements innovants basés sur la structure M-SPA viennent compléter la gamme des moteurs Cedrat Technologies. Les M-SPA adressent les applications longue course.

déjà à l'origine du projet européen Elvisa qui doit transporter les SPA vers les phases d'industrialisation.

Le premier point concerne les tests en environnement sévère. En effet, tous les tests menés pendant cette thèse ont été faits dans l'air à température et humidité ambiante. Or, certaines applications en ambiances contraignantes: vide, froid ou amagnétique pourrait également bénéficier des SPA. Ainsi, il sera intéressant de reproduire l'analyse tribologique introduite ici dans ces environnements.

Le second point concerne la dissymétrie des vitesses dans les directions aller-retours d'actionnement. Cette dissymétrie pourrait être abordée expérimentalement en implémentant une mesure d'effort, par exemple avec un ressort monté en série avec une cellule de charge.

Le troisième point provient des analyses des sollicitations tribologiques. De telles analyses restent qualitatives. Pour être quantitatif, la rhéologie des débits $3^{\text{ème}}$ corps devrait être étudiée, par exemple avec de la modélisation numérique Éléments Finis/Éléments discrets (FEM/DEM).

Le quatrième point repose sur les résultats acoustiques. Comme ils sont actionnés par un signal électrique dont la fréquence est dans une plage audible, le SPA actuel fait définitivement du bruit. Les limites de réduction de ce bruit semblent être atteintes dans ce travail. Pour surmonter cette limite, il pourrait être intéressant de poursuivre les travaux sur les SPA ultrasonores.

Enfin, le cinquième et dernier point est basé sur la structure "simple" des SPA. En effet, dans ces moteurs, l'impact de l'actionnement sur le frottement (et inversement) est direct. Ainsi, il pourrait être intéressant d'optimiser ce système tribologique non plus passivement - avec un choix pertinent de matériaux frottants - mais de manière active - en agissant en temps réel sur un système contrôlé des débits de $3^{\text{ème}}$ corps (Fig.18). On parlerait alors de système non plus mécatronique mais *tribotronique* (Glavatskih and Höglund, 2008).
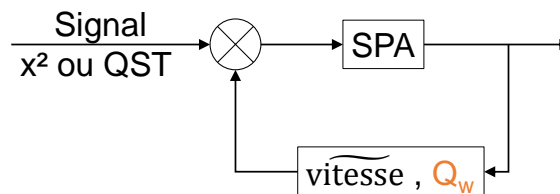
Figure 18 – Concept *tribotronique*: optimisation des performances tribologiques par l'intermédiaire d'une boucle de contrôle des débits de $3^{\text{ème}}$ corps.

FOLIO ADMINISTRATIF

THESE DE L'UNIVERSITE DE LYON OPEREE AU SEIN DE L'INSA LYON

NOM: DUBOIS   DATE de SOUTENANCE: 11 octobre 2017

Prénom: Fabien

TITRE: Tribological and vibratory approaches for amplified piezoelectric inertia motors.

NATURE: Doctorat   Numéro d'ordre : 2017LYSEI087

École doctorale: Mécanique – Énergétique – Génie civil – Acoustique (MEGA)

Spécialité: Génie Mécanique

RÉSUMÉ:

SPA are amplified piezoelectric inertia motors. They operate by converting asymmetrical vibrations into µ-displacements by means of friction, through stick-slip. These vibrations and this friction raise issues related to wear and noise. So, the present work investigates both *the tribological and vibratory behaviours of these motors*. First, a pin-on-pad tribometer, actuated by a SPA, was developed. It led us to observe, *in-situ* and in operation, interfacial solid flows: the 3rd body. These direct observations carried out in conjunction with *post-mortem* analyses resulted in decrypting the tribological solicitations and in increasing by ten the lifetime of the motors. Second, numerical and experimental considerations have been proposed to better grasp the vibratory behaviour of SPA. The existing lumped model was modified to a more versatile hybrid lumped-FEM model. The experimental tests made it possible to determine the main acoustic contributor and to reduce the noise level by sixteen dBA. Finally, this dual - tribology/vibratory - approach provided a better understanding of the SPA intricacies. In particular, it led to develop innovative structures such as a motor with three degrees of freedom and two rotary motors.

MOTS-CLÉS: SPA piezoelectric inertia motors - *In-situ* observations of a friction contact - Tribological circuit and 3rd body flows - Hybrid lumped-FEM modelling - Noise reduction.

Laboratoire de recherche: Laboratoire de Mécanique des Contacts et des Structures (LaMCoS), CNRS, UMR5259

Directeurs de thèse: BERTHIER, Yves   DR CNRS, LaMCoS, Lyon
                     SAULOT, Aurélien   Dr. HDR, MCF INSA, LaMCoS, Lyon

Président de jury:

Composition du jury:		
DENAPE, Jean	Pr. ENIT, LGP, Tarbes	Rapporteur
BREGUET, Jean-Marc	Dr., PDG Alemnis AG, Thun, Suisse	Rapporteur
ROUCHON, Jean-François	Pr. ENSEEIHT, LAPLACE, Toulouse	Examinateur
BOHER, Christine	Dr. HDR, MCF Mines, ICA, Albi	Examinateur
STOICA, Gina	Pr., Université Polytechnique, Bucarest, Roumanie	Examinateur
BELLY, Christian	Dr., Cedrat Technologies, Meylan	Examinateur
CLAEYSSEN, Frank	Dr., DG Cedrat Technologies, Meylan	Invité
SAULOT, Aurélien	Dr. HDR, MCF INSA, LaMCoS, Lyon	Directeur de thèse
BERTHIER, Yves	DR CNRS, LaMCoS, Lyon	Directeur de thèse